

Structural dynamics  
of a photoexcited dicopper(I) complex  
probed with ultrafast  
X-ray and optical techniques

Maria Naumova

Fakultät für Naturwissenschaften  
Universität Paderborn

A thesis submitted for the degree of  
*Doktor der Naturwissenschaften*

Paderborn 2017

Gutachter der Dissertation:

Prof. Dr. Gerald Henkel  
Prof. Dr. Michael Rübhausen

Gutachter der Disputation:

Prof. Dr. Gerald Henkel  
Prof. Dr. Michael Rübhausen  
Prof. Dr. Matthias Bauer

Vorsitzender des Promotionsausschusses:

Prof. Dr. René Wilhelm

Datum der Disputation:

13.07.2017

## Abstract

Experimental techniques using X-rays, such as absorption and emission spectroscopies and solution scattering, are a powerful tool in material research due to their sensitivity to geometric and electronic structure of the investigated system. Furthermore, these methods can be applied to study samples in solution, which is especially important for monitoring reactions *in situ* in biochemical applications and catalysis. Extension of X-ray methods into the pump-probe regime, where the sample system is probed after excitation by a pump photon, happened in recent years and opened new possibilities for investigation of structures of short-living photoexcited states. In this thesis a combination of ultrafast X-ray and optical techniques was applied to study the structural dynamics in a photoexcited binuclear copper complex with tetramethylguanidine and bridging disulfide ligands  $[\text{Cu}_2(\text{TMGphS}-\text{SphTMG})_2]^{2+}$  ( $\text{Cu}_2(\text{NSSN})_2$ ). This complex stems from biomimetic research of active sites of copper enzymes involved in electron transfer. In the context of structural responses to electronic excitations within biologically relevant Cu/N/S systems, coordinated disulfide groups offer ideal conditions as electron sinks due to their empty antibonding sigma orbitals. In the course of this study certain aspects of the electronic and structural dynamics of the photoexcited MLCT state of  $\text{Cu}_2(\text{NSSN})_2$  in solution were elucidated. In particular, the femtosecond optical transient spectroscopy revealed three distinct timescales constants of 650 fs, 10 ps and >100 ps, which were assigned as internal conversion to the ground state ( $S_n \rightarrow S_0$ ), intersystem crossing  $^1\text{MLCT} \rightarrow ^3\text{MLCT}$ , and structural changes in the triplet state and its subsequent relaxation to the ground state, respectively. Experimental data collected with both X-ray techniques were in agreement with the DFT-predicted structure for the triplet state. Direct energy space fitting of transient extended X-ray absorption fine structure (EXAFS) data confirmed shortening and elongation of certain Cu-N and Cu-S bonds with precision on the order of 0.01 Å. The best fit of the transient WAXS data is achieved for the structure where, as predicted by the DFT calculations, one of S-S bonds is cleaved, and the copper-sulfur cycle opens up with the Cu-S-S-Cu torsion angle change of 52°. These results widen the knowledge on electronic and structural dynamics of photoexcited copper-sulfur complexes and demonstrate the potential of combining the pump-probe X-ray absorption and scattering for studies on photoinduced structural dynamics in copper-based coordination complexes.

## Zusammenfassung

Experimentelle Techniken mit Röntgenstrahlung bieten große Möglichkeiten in der Materialforschung. Dabei ist die Röntgenabsorptionsspektroskopie (XAS) gegenüber lokalen Strukturen besonders sensibel. Die Röntgenemissionsspektroskopie (XES) ist hingegen sensitiv auf atomare Spins. Die beiden Techniken können auf feste, flüssige und gasförmige Proben angewendet werden. Dies ist besonders wichtig für die *in situ* Überwachung von Reaktionen in biochemischen Anwendungen und Katalyse. Pump-Probe-Experimente, bei denen die Probe zunächst von einem Anregungspuls angeregt und deren photoangeregte Zustände anschließend mit Röntgenpulsen untersucht wird, erweitern diese Techniken um das zeitaufgelöste Regime. Dies eröffnet Möglichkeiten zur Untersuchung der Struktur kurzlebiger, photoinduzierter Zustände. Eine weitere struktursensitive und zeitaufgelöste Technik ist die zeitaufgelöste Weitwinkel-Röntgen-Streuung (TR-WAXS), mit welcher Moleküle in Lösung untersucht werden können.

Kupfer-Diimin-Komplexe waren unter den ersten Proben, welche mittels zeitaufgelöster Röntgenabsorptionsspektroskopie untersucht wurden. Diese Arbeit erweitert diese Forschung auf einen zweikernigen Kupferkomplex koordiniert mit Disulfidbrücken und Tetramethylguanidinliganden. Diese Verbindung ist für einen Cu(I)/N/S-Komplex außergewöhnlich stabil in atmosphärischer Umgebung und zeigt ein interessantes, durch Chlorid-Ionen vermitteltes, Gleichgewicht mit der Cu(II)-Thiolat-Form.  $\text{Cu}_2(\text{NSSL})_2$  weist gewisse Ähnlichkeiten zu Kupfer-Diimin, wie zum Beispiel die Koordination durch  $sp^2$  Stickstoffatome. Gleichzeitig bewirken die Anwesenheit von zwei Kupferatomen sowie die zusätzliche Koordination durch Schwefel spezifische Wechselwirkungen, die die angeregte Zustandsstruktur beeinflussen. Um die photoinduzierten Strukturänderungen innerhalb des solvatisierten Komplexes direkt zu beobachten, wurde dieser mittels zeitaufgelöster Röntgenabsorptions- und emissionsspektroskopie, sowie Weitwinkel-Röntgen-Streuung im Pikosekundenbereich untersucht. Ergänzend wurde die Zeitentwicklung elektronisch angeregter Zustände im Femtosekundenbereich durch transiente UV/Vis Absorptionsspektroskopie untersucht. Mittels dichtefunktionaltheoretischer (DFT) Berechnungen wurden molekulare Geometrien und elektronische Strukturen des Grundzustandes, sowie zweier Metall-zu-Ligand-Ladungstransfer-Zustände (MLCT) mit Singulett- ( $^1\text{MLCT}$ ) und Triplettkonfiguration ( $^3\text{MLCT}$ ) berechnet. Durch Kombination dieser Techniken konnten wesentliche Aspekte der elektronischen und strukturellen Dynamik des photoangeregten MLCT-Zustandes von gelöstem  $\text{Cu}_2(\text{NSSL})_2$  aufgedeckt werden. Durch transiente UV/Vis-Femtosekunden-Spektroskopie konnten drei verschiedene Anregungen bestimmt werden: die innere Konversion (IC) in den Grundzustand ( $S_n \rightarrow S_0$ ) mit einer Zeitkonstanten von 650 fs, der Übergang von  $^1\text{MLCT} \rightarrow ^3\text{MLCT}$  (Intersystem Crossing) mit einer Zeitkonstanten von 10 ps, sowie eine strukturelle Änderung im Triplettzustand und deren anschließende Relaxation in den Grundzustand mit einer Zeitkonstanten  $>100$  ps. Durch die beiden Röntgentechniken (XAS und WAXS) gewonnene Daten stimmten mit den theoretischen DFT-Vorhersagen für die Struktur des Triplettzustandes überein. Direkte Energieraum Anpassungen transientser EXAFS (Extended X-Ray Absorption Fine Structure Spectroscopy) bestätigte die Ergebnisse bezüglich Verkürzung und Verlängerung bestimmter Cu-N- und Cu-S-Bindungen mit einer Präzision gegen  $0,01 \text{ \AA}$ . Die Besten Resultate transientser WAXS-Daten wurden für diejenige Struktur erreicht, bei der durch DFT-Berechnungen eine der S-S-Bindungen aufgebrochen und der Kupfer-Schwefel-Zyklus geöffnet ist, während sich der Cu-S-S-Cu-Torsionswinkel um  $52^\circ$  ändert. Die Ergebnisse dieser Arbeiten erweitern den bisherigen Kenntnisstand über die Photophysik in Kupfer-Schwefel-Komplexen und zeigen das große Potential der Kombination von Röntgenspektroskopie- und streutechniken, sowie optischer Ultrakurzzeitspektroskopie für die Untersuchung photoinduzierter Struktur- und elektronischer Dynamik in kupferbasierten Koordinationskomplexen auf.



# Contents

<b>1</b>	<b>Introduction</b>	<b>1</b>
<b>2</b>	<b>Copper: chemical properties and biological relevance</b>	<b>3</b>
2.1	Introduction	3
2.2	Electronic structure and coordination geometries of copper	3
2.3	Copper enzymes for electron transfer	6
2.4	Thiolate-disulfide equilibrium	7
<b>3</b>	<b>Photophysical properties of transition metal complexes</b>	<b>9</b>
3.1	General aspects of photophysics of transition metal complexes	9
3.2	Photophysical properties of copper complexes	11
3.3	Structural dynamics upon photoexcitation in copper complexes	13
<b>4</b>	<b>Experimental X-rays techniques</b>	<b>14</b>
4.1	X-ray absorption spectroscopy (XAS)	16
4.1.1	X-ray absorption fine structure	16
4.1.2	X-ray absorption near edge structure (XANES)	16
4.1.3	Extended X-ray absorption fine structure (EXAFS)	19
4.1.4	Experimental setup for X-ray absorption spectroscopy	21
4.2	X-ray emission spectroscopy (XES)	22
4.2.1	Experimental setup for high-resolution X-ray emission spectroscopy	22
4.3	Wide-angle X-ray scattering (WAXS)	23
4.4	Pump-probe time-resolved X-ray techniques	26
<b>5</b>	<b>Photoinduced structural dynamics of a dicopper-disulfide complex <math>\text{Cu}_2(\text{NSSN})_2</math></b>	<b>27</b>
5.1	Physical and chemical properties of $\text{Cu}_2(\text{NSSN})_2$	27
5.1.1	Synthesis, characterisation and structure discussion	27
5.1.2	Electronic structure in the ground state	28
5.1.3	Excited states	29
5.1.4	Choosing the solvent	32
5.1.5	Photostability of the complex	35
5.2	Transient UV-vis absorption spectroscopy	36
5.2.1	Experiment description	36
5.2.2	Spectral evolution	37
5.2.3	Kinetic analysis	40
5.2.4	Summary	42
5.3	Transient X-ray absorption spectroscopy	43
5.3.1	Experiment description	43
5.3.2	Estimation of excited state fraction in the laser-illuminated volume	44
5.3.3	Ground state EXAFS	45

5.3.4	Transient XANES . . . . .	48
5.3.5	Transient EXAFS . . . . .	53
5.3.6	Excited state kinetics . . . . .	61
5.3.7	Summary . . . . .	65
5.4	Transient wide-angle X-ray scattering and transient X-ray emission spectroscopy	67
5.4.1	Experiment description . . . . .	67
5.4.2	Transient X-ray emission spectroscopy . . . . .	68
5.4.3	Transient wide-angle X-ray scattering . . . . .	71
5.4.4	Summary . . . . .	77
5.5	Discussion of the photocycle of $\text{Cu}_2(\text{NSSL})_2$ . . . . .	80
<b>6</b>	<b>Summary, conclusions and outlook</b>	<b>83</b>
6.1	Summary and conclusions . . . . .	83
6.2	Outlook . . . . .	85
	<b>Acronyms</b>	<b>88</b>
	<b>Chemical nomenclature</b>	<b>90</b>
	<b>Bibliography</b>	<b>91</b>
	<b>Acknowledgments</b>	<b>109</b>

# Chapter 1

## Introduction

Transition metal (TM) complexes play an important role in both nature and technology. Photochemistry and photophysics of TM compounds have been in the focus of fundamental and applied research since decades [Sch04]. As a result, photocatalytical reactions using TM complexes became an important branch of modern chemical technology [Mal09]. Copper, in particular, plays a big role both in technology and in chemistry of life. Compared to transition metals of the 5th and 6th periods copper is more environmentally friendly and economically viable material for photosensitisers and photocatalysts [SSC08]. At the same time copper is found in active centres of many enzymes, whose functions include electron transfer (ET), oxygen binding, activation, and reduction [Ror04; Sol+14], and others. Since long time scientists strive to reproduce and study structure and function of the active site of enzymes, in particular, copper ET centres, based on small synthetic compounds [Sol+04; BRP05]. Research in this field contributed immensely to the knowledge on these chemical systems.

Experimental tools using X-rays offer great possibilities in material research. Among experimental techniques X-ray absorption spectroscopy (XAS), in particular, is sensitive to local structure, and X-ray emission spectroscopy is sensitive to atomic spins. These techniques can be applied to samples in any medium, such as solid, liquid or gas, which is especially important for monitoring reactions *in situ* in biochemical applications and catalysis. Extending X-ray methods into the pump-probe regime, where the sample system is probed after excitation by a pump photon, opens new possibilities for investigation of structures of short-living photoinduced states. Due to their importance, TM complexes became the object of structural studies directly following the development of these methods. Materials studied with pump-probe X-ray absorption and/or emission spectroscopies include Cu diimine complexes [Che+03; Pen+13; Fra+14; Dic+17], spin crossover Fe complexes [Gaw+07; Bor+13], as well as compounds of Ru [Gaw06; Van+15], Ir [Bri17], Os [Zha+16], Pt [Vee+09], Re [El +13], Co [Can+15]. Sensitivity of XAS to the oxidation state of the element was used to study kinetics of Photosystem II (Mn K-edge) [Hau05].

In this thesis we applied pump-probe X-ray and optical methods to study photoinduced structural dynamics in a binuclear copper complex with disulfide bridges and tetramethylguanidine ligands  $[\text{Cu}_2(\text{TMGphS-SphTMG})_2]_2^+$  ( $\text{Cu}_2(\text{NSSN})_2$ ). This compound is unusually stable in ambient conditions for a Cu(I)/N/S complex and demonstrates an interesting chloride-mediated equilibrium with Cu(II)-thiolate form [Neu+12]. Light pulses can be used to excite a charge transfer band in this complex, causing the change of oxidation state of copper from (+1) to (+2). The combination of picosecond time-resolved X-ray absorption spectroscopy (XAS), X-ray emission spectroscopy (XES) and wide-angle X-ray scattering (WAXS) was used to access the structural and electronic changes in the complex originating due to this charge transfer. Additionally, femtosecond transient absorption in UV-Vis energy range was used to address the relaxation dynamics at ultrafast timescales. Density functional theory (DFT) calculations were

used to predict molecular geometries and electronic structures of the ground and excited states.  $\text{Cu}_2(\text{NSSN})_2$  bears certain similarity to copper-diimines, extensively studied by pump-probe XAS, such as coordination by  $sp^2$  nitrogen atoms. At the same time, the presence of two copper atoms as well as additional coordination by sulfur cause specific interactions influencing the excited state structure. In particular, in the context of structural responses to electronic excitations within biologically relevant Cu/N/S systems, coordinated disulfide groups offer ideal conditions as electron sinks due to their empty antibonding sigma orbitals. Investigating the effect of this interaction will contribute to the emerging field of structural dynamics studies and to knowledge of biologically-relevant ET-coupled structural changes.

**Thesis outline.** In chapter 2 general aspects of chemistry of copper are addressed. Details of photophysical properties of TM compounds with focus on copper complexes are presented in chapter 3. X-rays and their interaction with matter are addressed in chapter 4. Chapter 5 is devoted to the objective of this thesis – the study of structural dynamics in a dicopper(I)-disulfide complex. In section 5.1 preparative studies in the ground state are reported and the choice of the solvents for the following pump-probe experiments is justified. In further sections three pump-probe experiments are reported. Section 5.2 presents the results of the transient absorption in UV-Vis experiment. Section 5.3 follows up with transient X-ray absorption spectroscopy. Finally, transient wide-angle X-ray scattering combined with X-ray emission spectroscopy are presented in section 5.4. Section 5.5 summarises the results by the discussion of the photocycle resulting from this combined study. The main conclusions and an outlook for future are presented in chapter 6.

## Chapter 2

# Copper: chemical properties and biological relevance

This chapter introduces electronic structure of copper and the role of *d* orbitals for its coordination geometry. Insight into the biological role of copper is given with focus on proteins relevant for electron transfer. Finally thiolate-disulfide interconversion in nature as well as model systems demonstrating copper(I)-disulfide/copper(II)-thiolate interconversion are addressed.

### 2.1 Introduction

Copper played an important role in both evolution of life on earth and development of human culture. In the evolution of life on Earth copper first became important after oxygen started to accumulate in the atmosphere causing solubilisation of copper(II) sulfide minerals [IB13]. Nowadays on the order of 3000 copper-containing enzymes are known, which are distributed over all domains of life. However, they are mainly found in the aerobic organisms [DBW11]. Copper enzymes are involved in ET, O<sub>2</sub> binding, activation and reduction, NO<sub>2</sub> and N<sub>2</sub>O reduction, and substrate activation [Sol+14]. In the history of human civilisation copper metal has been recognized and used extensively since prehistoric times – probably around 5000 B.C. [Con06]. A period of extensive use of the metal in production of tools, currency and weapons is often referred to as the Copper Age. The Bronze Age followed around 2500 B.C. when it was discovered that addition of tin to copper improves the strength of the material [Con06]. Nowadays copper is the most common material for electric wires due to its good electric conductivity and relatively low price. Metallic copper on substrates as well as numerous copper compounds are used as catalysts both in lab and industry (see, for example, reviews [BC04; Ale+08; Jer+09; Gaw+16]). High-temperature cuprate superconductors can be cooled to superconductivity using liquid nitrogen (instead of liquid helium required for normal superconductors), which makes them an important material for building powerful electromagnets [Cha00]. Application of copper complexes as organic light-emitting diodes (OLEDs) and photosensitisers will be further addressed in the section 3.2.

### 2.2 Electronic structure and coordination geometries of copper

Copper belongs to the transition metals, which are elements whose atom has a partially filled *d* sub-shell, or which can give rise to cations with an incomplete *d* sub-shell [MW97]. The presence of partially-filled *d* orbitals (shown on Fig. 2.1) to a big extent determines the properties of TM complexes: they take part in the formation of chemical bonds and determine coordination geometry of the system. In the periodic table of elements copper is located in group 11 together

with silver and gold. As a metal it has  $[\text{Ar}]3d^{10}4s^1$  electronic structure. Typical oxidation states of Cu are +1 and +2; +3 is rare, and +4 exists, but is quite exotic [Con06; Sin+15].

Coordination polyhedra of copper and other TM compounds can be discussed in terms of crystal field theory (CFT) [Ber10]. This theory makes several assumptions: it regards the interaction of the central atom (CA) and ligands as purely electrostatic; ligands are regarded as "structureless" charge sources, whereas the CA is considered with its detailed electronic structure. The main effect that ligands have on the states of the CA is splitting of its energy levels. In a spherically symmetric electric field  $d$  orbitals of the CA would have equal energies. In a coordination compound the field symmetry is determined by positions of ligands. The energy of orbitals whose lobes are located closer to ligands is higher than the energy of orbitals located further away. As a result,  $d$  orbitals are split in energy as shown in Fig. 2.2 for tetrahedral, octahedral and square-planar coordination.

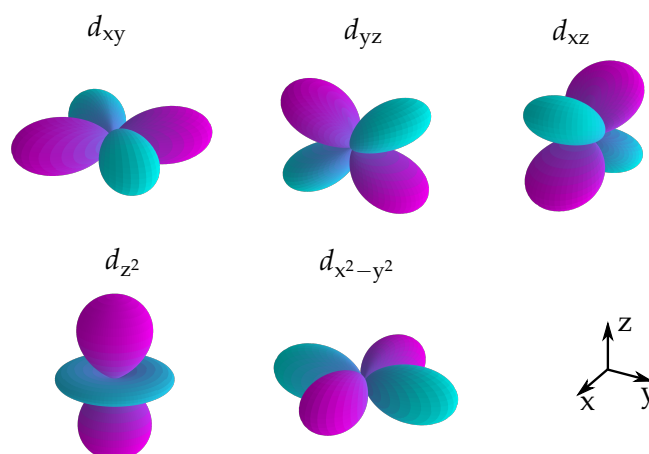


**Figure 2.1:**  $d$  orbitals calculated for a hydrogen atom.

The preferred coordination geometry depends on the electronic structure of the CA and therefore on its oxidation state.  $\text{Cu}^{+1}$  has a full  $3d^{10}$  shell and is a soft (easily polarisable) cation which readily coordinates soft ligands, such as phosphorus and sulfur, also nitrogen, and to lesser extent halogenes (Cl, Br, I) and oxygen. Due to a fully occupied  $3d$  level  $\text{Cu}^{+1}$  does not have strong preferences in coordination geometry:  $d$  orbitals are split in the field of ligands, but no structural distortion would result in the energy gain for the  $d^{10}$  subshell. Therefore in an unconstrained system ligands are usually distributed in space as far from each other as possible, resulting in linear, trigonal or tetrahedral coordination for two, three and four ligands respectively [Con06]. In tetrahedral geometry the orbitals are split into two levels:  $d_{z^2}$  and  $d_{x^2-y^2}$  have lower energy than  $d_{xy}$ ,  $d_{yz}$  and  $d_{xz}$  (Fig. 2.2).

$\text{Cu}^{+2}$  has a  $3d^9$  subshell. It is a less polarisable cation than  $\text{Cu}^{+1}$ , and its coordination chemistry is dominated by nitrogen- and oxygen-donating ligands, followed by chloride and sulfur-containing species [Con06].  $\text{Cu}^{+2}$  normally has higher coordination numbers than  $\text{Cu}^{+1}$ , most typically four to six. For an octahedral, i.e. six-coordinated complex,  $d_{xy}$ ,  $d_{yz}$  and  $d_{xz}$  have lower energies than  $d_{z^2}$  and  $d_{x^2-y^2}$  which have their lobes along metal-ligand bonds (see Fig. 2.1 and 2.2). For a  $d^9$  system in an ideal octahedral coordination three electrons would occupy two degenerate  $d$  orbitals. In this situation the Jahn-Teller theorem becomes relevant, which states that if a nonlinear system has degenerate energy levels in the ground state, this state will be unstable, and the deformations leading to removal of degeneracy will appear [Ber75]. As a result of this instability six-coordinated  $\text{Cu}^{+2}$  complexes are distorted from octahedral towards

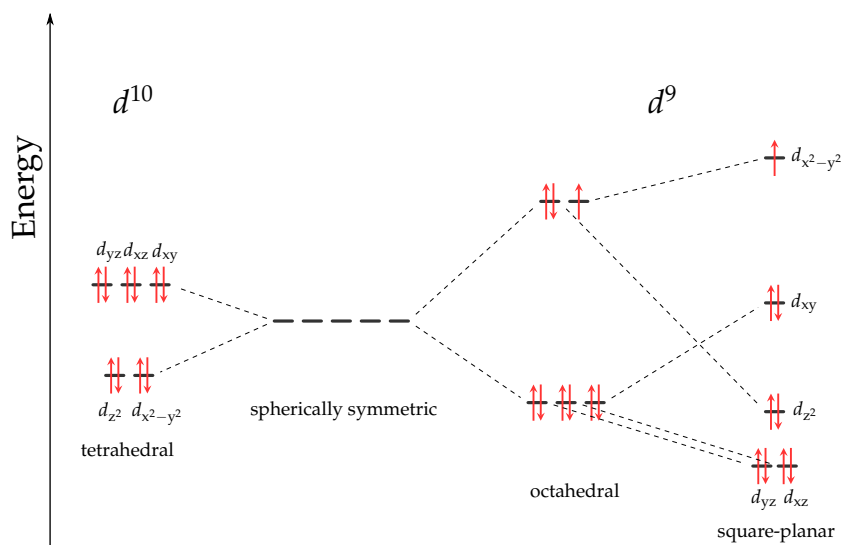
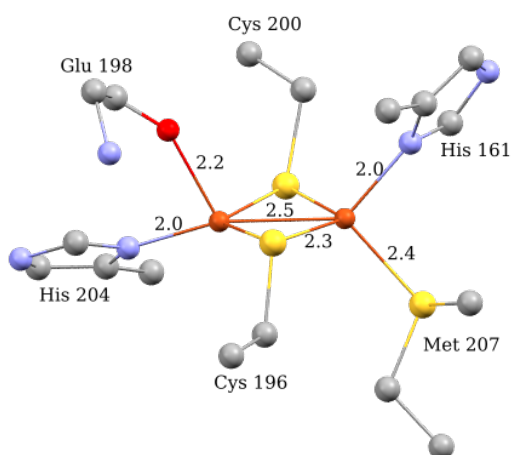


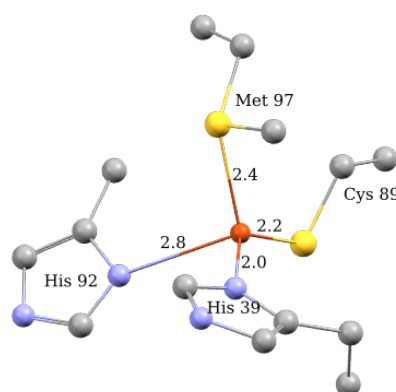
**Figure 2.2:** Scheme of crystal field splitting of  $d$  orbitals for  $d^{10}$  in tetrahedral coordination (characteristic for  $\text{Cu}^{+1}$ ) and  $d^9$  in octahedral and square-planar coordination ( $\text{Cu}^{+2}$ ).

tetragonal coordination, with four shorter equatorial bonds and two longer axial bonds (or one for five-coordinated complexes). This distortion causes further splitting of the  $d$  orbitals in energy and therefore disappearance of the degeneracy. Complexes with two shorter axial bonds and four longer equatorial bonds exist, but are more rare. Four-coordinate tetrahedral and planar complexes are also known [Con06]. Apart from static distortion caused by the Jahn-Teller effect some  $\text{Cu}^{+2}$  complexes demonstrate non-rigid geometries (copper-ligand distances observed in a crystallographic experiment depend on the temperature) and plasticity effect (different geometries can be stable at the same external conditions) [Gaž+76; Hat84]. This behaviour can be explained by the pseudo-Jahn-Teller effect [Ber75; Ber10]. The Born-Oppenheimer approximation cannot be applied to describe the electronic properties of the  $d^9$  configuration of the  $\text{Cu}^{+2}$  ion in an orbitally degenerate electronic ground state. The vibronic potential energy surface (PES) has to be considered, which has a shape of a warped "Mexican hat" with several minima corresponding to structural distortions along different coordinates [Hat84]. The system can be in a state of degenerate dynamic equilibrium switching between these minima; or some influence (such as ligands; conditions of crystallisation – pH, temperature; external pressure) can stabilise the system in one of these minima. Due to these electronic effects  $\text{Cu}^{+2}$  complexes demonstrate a high versatility of crystallographic structures.

CFT explains some important optical, magnetic, and thermodynamic properties of TM complexes. However, its main limitation is the assumption that the nature of bonding in a TM system is a purely electrostatic interaction between the central atom and the ligands. Therefore it does not take into account the nature of ligands, which is necessary for description of the electronic structure of the system and its further photophysical properties. An extension of CFT, which takes into account the nature of bonding between the central atom and the ligands is the ligand field theory (LFT). This theory describes the formation of molecular orbitals (MO) from the atomic orbitals of ligands and CA [Ber10]. This description is especially relevant for the discussion of photophysical properties involving ligand orbitals, as will be addressed in chapter 3.



(a) Structure of  $\text{Cu}_A$ -centre of bovine heart cytochrome *c* oxidase in fully oxidised state from [Aoy+09]



(b) Structure of Type I Cu centre of the double mutant D44A D45A Plastocyanin from *Phormidium laminosum* from [Fro+09]

## 2.3 Copper enzymes for electron transfer

In the chemistry of life copper plays an important role being a part of many essential metalloenzymes. Among various active sites of copper, the mononuclear Type I blue Cu site and the binuclear  $\text{Cu}_A$  site (Fig. 2.3a) participate in the electron transfer processes.  $\text{Cu}_A$  is a structural motif found in the enzyme cytochrome *c* oxidase, a terminal oxidase of the breathing chain in mitochondria of eukariotic cells and some aerobic bacteria, and in nitrous oxide reductase in denitrifying bacteria. It contains an almost flat rhombic  $\text{Cu}_2\text{S}_2$  core (referred to as "diamond core"). Copper ions are coordinated each by a histidine nitrogen and sulfur atoms from two cysteine residues. Additionally, depending on the particular enzyme, they can be supported by weakly coordinating ligands such as thioether sulfur of methionin and carbonyl oxygen from isoleucine, histidine and glutamate residues [Iwa+95; Tsu+95; Sou00]. The Type I centre is found in the family of so-called blue copper proteins. Two most common examples are plastocyanine and azurine. In these copper enzymes copper ion has a trigonal coordination by two histidines and a cysteine residue (with copper being slightly out of  $\text{Hys}_2\text{Cys}$  plane). In various proteins of this family the copper can be additionally weakly coordinated with one or two residues forming a trigonal (bi)pyramid [GF83; Syk85; NAB86; Kar+91; Zai+96; Duc+98].

Both these active centres are able to mediate long-range ET processes with rates on the order of  $10^3 - 10^5 \text{ s}^{-1}$  [SSM96; DeB+01; BRP05; Sol+14]. These rates are unusually high, because normally ET reactions involve a significant reorganisation energy due to both internal changes in structure, following the changes in electron configuration, and reorganisation of the surrounding solvent matrix, following the change in the dipoles of the redox system [Ror04]. In particular in an unconstrained  $\text{Cu}(+2/+1)$  system, ET would involve a change in both coordination geometry and number, as well as in bond lengths, resulting in high internal reorganisation energies. On the other hand, as discussed in section 2.2, the spherically symmetric  $d^{10}$  electronic configuration of  $\text{Cu}^{+1}$  should not exhibit a strong preference for a specific geometry, and  $\text{Cu}^{+2}$  complexes demonstrate flexibility in their geometries. These factors may facilitate ET in constrained copper systems. Two main hypotheses were proposed in order to explain the nature of unusually fast ET in these copper enzymes. According to the "entatic state" concept by Vallee and Williams [VW68; Wil95] the local protein environment imposes a certain coordination on the metal centre which is intermediate between two redox states. This way the ground state geometry resembles the transition state geometry during the ET, and thus the Marcus reorganisation energy  $\lambda$  [MS85] is small and ET rates are large. At the same time the idea that high copper-ligand covalency,

and not strained geometry, is responsible for stabilisation of electronic states was developed by Solomon [SL93; SLR98; Gam+98] and Rydes [Ryd+96; Ols+98]. Both blue copper site and  $\text{Cu}_A$  contain short and highly covalent Cu-thiolate bonds. For  $\text{Cu}_A$  the redox-active molecular orbital (RAMO) is highly delocalised, and the unpaired spin of the  $\text{Cu}^{1.5}\text{Cu}^{1.5}$  state is located to a larger extent on the two bridging sulfur atoms (46 %) than on the two coppers (44 %) [DeB+01]. In this respect the polarisable nature of sulfur serves to tune electronic properties and reactivity of the active sites [Sol+14; YBT05].

Catalytic active sites of metalloenzymes inspired work of synthetic chemists striving to reproduce structure and/or function of the enzymes with synthetic low molecular weight compounds. A variety of copper complexes with sulfur-containing ligands were isolated and characterised, including models for the dinuclear  $\text{Cu}_A$  site. Most of the synthesized complexes contain monovalent dicopper(II) bis( $\mu$ -thiolato) species and can not be brought into the mixed valent state [Hou+95; Bra+96; INF01; UTI02; Ura+05; Ram+06; Roy+09; Neu+12]. Still, several groups succeeded in synthesizing multivalent species with delocalised charge  $\text{Cu}_2^{1.5}\text{S}_2$  [HYT96; Gen+11; Neu+11]. Although many of the compounds synthesized in biomimetic research do not reproduce the sought properties of real biochemical objects, research in this field contributed immensely to the knowledge on these particular chemical systems. Difficulties in reproducing certain properties of metalloenzymes demonstrate that fine details of molecular and electronic structure can have a decisive effect on the properties of the system and reaction pathways, driving further investigations in this field.

## 2.4 Thiolate-disulfide equilibrium

Thiolate-disulfide equilibrium is relevant for diverse processes in chemistry of life, such as protein folding and stability, regulation of gene expression, catalytic activity and protection against oxidative damage [Fah77; Gil95; GGJ03]. For example, glutathione (GSH) is an abundant enzyme involved in many cellular processes; in particular, it reacts with a wide spectrum of cellular oxidants, this way protecting cells from free radicals. Its function is realised by reaction of the free -SH group with a radical; GSH is then oxidised into GSSG disulfide form, which can then be recovered back into the reduced form by the enzyme glutathione-disulfide-reductase [Sie99; Jac+03]. Another important process involving thiolate-disulfide interconversion is the formation of disulfide bridges forming secondary and tertiary protein structure. In addition to the redox-active function, the thiolate group forms coordinate bonds with a wide range of metal ions such as iron, zinc, cadmium, mercury, cobalt, and copper. These metal ions can affect the redox properties of the thiolate [Jac+03]. In particular, it was suggested that disulfide-thiolate conversion is involved in process of copper delivery to  $\text{Cu}_A$  by Sco proteins [Ban+11].

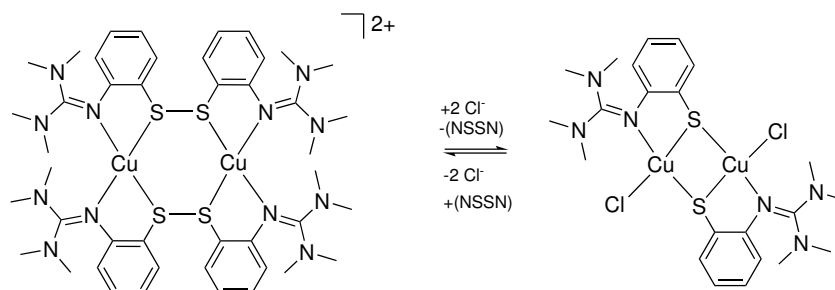


**Figure 2.4:** Chloride-mediated disulfide-thiolate equilibrium reported in [Neu+12].

Research of dinuclear copper thiolate complexes and their interconversion had led to a discovery of redox equilibrium between copper(II)- $\mu$ -thiolate and copper(I)-disulfide species. Some systems were demonstrated where this equilibrium is mediated by halide ions [UTI02;

[Neu+12]. Both publications report reversible copper(I)-disulfide/copper(II)-thiolate interconversion mediated by addition or removal of chloride ions. The  $\text{Cu}^{+1}$ -disulfide complex from [Neu+12] (Fig. 2.4) was investigated in this work. Another study of copper-thiolate-disulfide equilibrium was reported in [Ord+14]. The authors found a system where, depending on the solvent and temperature, either  $\text{Cu}_2^{+2}\text{S}_2^{-2}$  or  $\text{Cu}_2^{+1}\text{S}_2^{-1}$  is formed upon addition of  $\text{Cu}^{+1}$  ions to the ligand (Fig. 2.5).

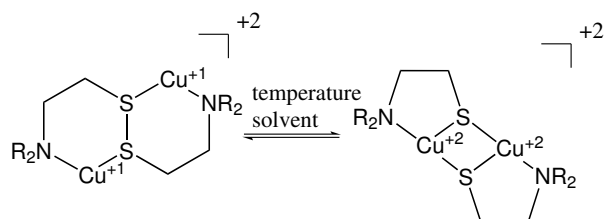


**Figure 2.5:** Disulfide-thiolate equilibrium reported in [Ord+14].

Investigation of such equilibrium systems may lead to deeper understanding of copper-sulfur redox processes in biological systems, as well as influence of metal ions on disulfide-thiolate equilibrium in general.

## Chapter 3

# Photophysical properties of transition metal complexes

This chapter introduces the photophysical properties of transition metal complexes with focus on copper. Recent advances in knowledge about structural dynamics in copper complexes are summarised.

### 3.1 General aspects of photophysics of transition metal complexes

Photophysical and photochemical properties of TM complexes are extensively studied due to their relevance to some biological processes and various applications in technology [Sch04]. Many special photophysical features of TM complexes originate from the existence of various types of excited states of different orbital origin and localization within the molecule, as well as high density of states. Possible excited states include [Vlč00]:

- charge transfer states, such as metal-to-ligand charge transfer (MLCT), where an electron is excited from a metal-centred orbital to a ligand-centred orbital, or vice-versa (ligand-to-metal charge transfer (LMCT));
- metal-centered (MC) transitions between  $d$  orbitals that are possible in transition metals with partially filled  $d$  orbitals;
- ligand-centered (LC) transitions which happen between the orbitals of the ligand.

The processes of photoexcitation and consequent relaxation in a molecule are normally presented in the form of Jablonski diagrams as shown in Fig. 3.1. For organic molecules, the photoexcited behaviour is often discussed in terms of relaxation processes clearly separated in time and energy [KM05]. However, for TM complexes such a simplified description is often not possible. Due to a high density of states, TM complexes typically have several electronic configurations with similar energy. These configurations will generally mix and give rise to several electronic excited states accessible in a narrow energy range [Bal01]. These excited states can be of different character and can interact with each other. As a result, the relaxation pathway of the system often depends on the excitation energy. Besides that, many TM complexes are active in redox reactions in the ground state as well as in excited states [Bal01]. The spin-orbit coupling is significant for transition metals, and, unlike organic molecules, TM systems undergo efficient intersystem crossing (ISC), often on ultra-fast time scales [Vee+11]. All these factors make study of photophysics and photochemistry of TM complexes challenging, but interesting for fundamental science and perspective for technology, where TM complexes with desirable photophysical properties can be designed. The connection between excited-state chemistry and

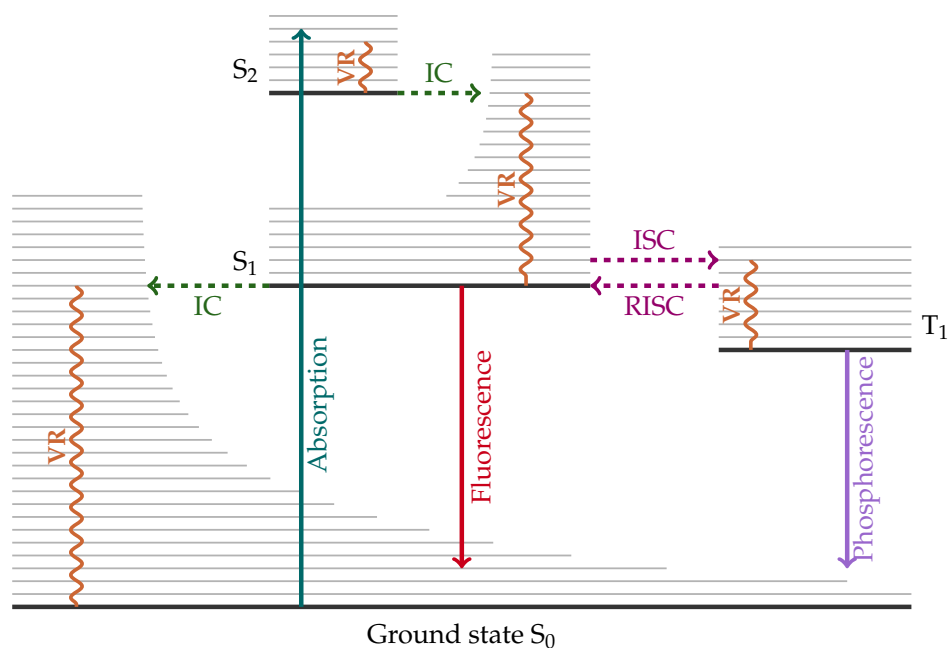


**Figure 3.1:** Jablonski diagram showing photoexcitation and following relaxation processes. Shown are non-radiative processes – vibrational relaxation (VR), internal conversion (IC), intersystem crossing (ISC), reversed intersystem crossing (RISC), and radiative processes – fluorescence and phosphorescence. Figure modified from [Sal09].

ET reactivity enables us to study the charge-transfer processes relevant for biochemistry driven by light pulses.

## 3.2 Photophysical properties of copper complexes

Photoexcited states of  $\text{Cu}^{+1}$  complexes have been studied extensively with relation to their emissive or photosensitising properties [Arm+07; Mal09]. Mostly copper complexes with N- and P- ligands were investigated, sometimes with halogen coligands.  $\text{Cu}^{+2}$  complexes normally do not demonstrate attractive photophysical properties, because the lowest excited states are often metal-centred, since a  $d-d$  transition is possible for the  $3d^9$  configuration, and deactivate via ultrafast non-radiative processes [Arm+07]. In the following section the current knowledge about photophysics of  $\text{Cu}^{+1}$  complexes is summarised.

### Photoabsorption (optical spectra)

In the absorption spectra of  $\text{Cu}^{+1}$  complexes the lowest-lying absorption band is normally a metal-to-ligand charge transfer transition from a highest-occupied molecular orbital (HOMO) with strong Cu  $3d$  contribution to a ligand-centred lowest-unoccupied molecular orbital (LUMO). For ligands with  $\pi$ -bonds, such as pyridine and related compounds, the LUMO often is the  $\pi^*$  of the aromatic ring [BM78]. At the same time, ligand-centered transitions ( $\pi\pi^*$ ) close in energy are also possible with some ligand systems [Hsu+11], as well as halogen-to-ligand charge transfer (XLCT) transitions [Zin+13]. The copper complex investigated in this work,  $\text{Cu}_2(\text{NSSN})_2$ , has its LUMO located on the  $\sigma^*$  orbital of the disulfide bridge. As a result the lowest transition in the absorption spectrum is a MLCT  $\text{Cu}\rightarrow\text{S}$ , as shown in Fig. 3.2.

### Relaxation of the excited state

Light pulse absorption happens on the time scale of 1 fs, which is faster than the characteristic time of nuclear motion, and as a result the created excited state has different electronic, but the same molecular structure as the ground state (Frank-Condon (FC) principle). Such system is far from equilibrium, and the excess energy is dissipated via a complex convolution of several processes happening on ultrafast time scales, such as vibrational relaxation (VR) and internal conversion (IC)  $S_n \rightarrow S_1$ . VR is the loss of vibrational excitation energy by a molecular entity through energy transfer to the environment caused by collisions, whereas IC refers to an isoenergetic radiationless transition between two electronic states of the same spin multiplicity [MW97]. These processes are accompanied by structural changes leading to  $S_{1,relaxed}$  and adjustment of the solvation sphere according to the new charge distribution in the system [VI00; MFC15]. The common view of excited-state relaxation as a sequence of steps that are distinguished in time and energy can not be applied for these processes.

After the system relaxed to the  $S_1$  state, it can return to the ground state via emissive (fluorescence) or non-emissive (IC)  $S_1 \rightarrow S_0$  transition. A competing process is intersystem crossing (ISC) to the triplet state  $S_1 \rightarrow T_1$ . ISC denotes a radiationless process involving a transition between two electronic states with different spin multiplicity [MW97]. ISC  $S_n \rightarrow T_m$  is also possible, followed by IC  $T_m \rightarrow T_1$ . The real relaxation path can only be discussed in terms of PES of the system, as demonstrated in [ITT07] for  $\text{Cu}(\text{dmp})_2$ . The efficiency and the rate of ISC is determined by the value of spin-orbit (SO) constant ( $\zeta_{\text{Cu}} = 857\text{cm}^{-1}$  [Ber+16]), as well as by the molecular structure, electronic levels and structural changes which take place after the photoexcitation [Vee+11]. Time scales of ISC were reported to be 2 to 27 ps for different copper complexes [MFC15; ITT07; Ber+16; Dic+17]. It is interesting to note that these times are much longer than what is observed for many other TM complexes, which normally undergo ISC at  $<200$  fs [VI00; For06]. The relative efficiency of IC  $S_1 \rightarrow S_0$  versus ISC  $S_1 \rightarrow T_1$  can be quite different for different compounds. For example, [Hua+15] found the yield of 14 % ISC and 86 % IC for non-emissive  $[\text{Cu}(\text{phen})_2]^+$ , while [Dic+17] observed a 1:1 ratio between these two competing processes for phosphorescent  $\text{Cu}(\text{TMGqu})_2$ .

After ISC to  $T_1$  the system can return to the ground state following the non-radiative (ISC) or radiative pathway (phosphorescence). Typical triplet emission decay times ( $T_1 \rightarrow S_0$ ) are on the order of 100  $\mu\text{s}$  up to a few ms [Yer+11]. Some complexes show prompt fluorescence,

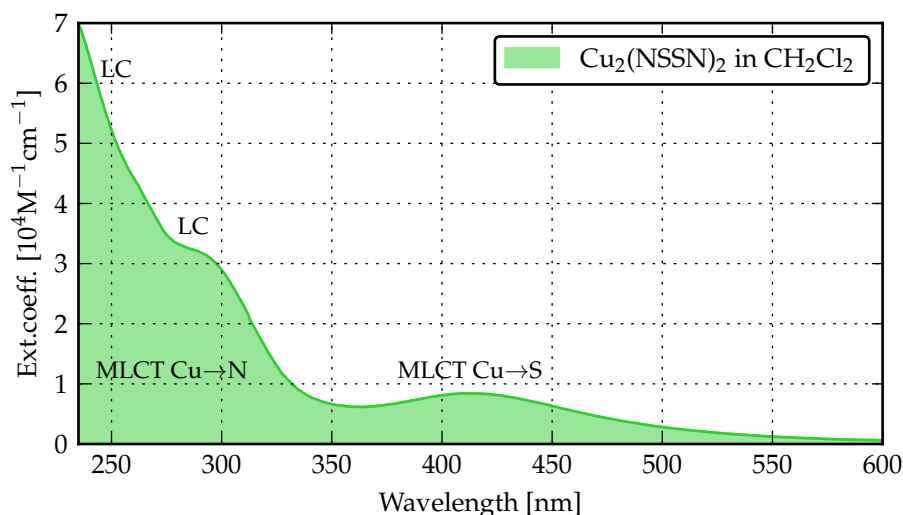


**Figure 3.2:** UV-vis absorption spectrum of  $\text{Cu}_2(\text{NSSN})_2$  in  $\text{CH}_2\text{Cl}_2$ . Band assignment performed based on [Neu09] and the DFT calculations presented in this work.

however, strong singlet emission is normally only observed in cases when the singlet state gets repopulated from the triplet if the energy gap between  $S_1$  and  $T_1$  is on the order of  $k_B T$  [CT14]. This process is normally called reversed intersystem crossing (RISC), and the emission from the repopulated singlet is referred to as thermally activated delayed fluorescence (TADF). It is quite efficient for some copper complexes [CT14]. In emission spectra it manifests itself as emission bands with small Stokes shifts characteristic for fluorescence, lifetimes which fall between fluorescence and phosphorescence, and gradual red-shift and increase of emission lifetimes upon cooling [CY15].

#### Functional materials based on copper complexes

There are two major material classes where photophysical and photochemical properties of copper complexes are applied: organic light emitting diodes (OLEDs) and photosensitisers. Copper complexes are promising alternatives to noble-metals compounds used in these applications due to their lower price, higher abundance and lower impact on the environment [SS15]. An OLED is a light-emitting diode where the emissive electroluminescent layer is a film of an organic compound [GRP06]. Some  $\text{Cu}^{+1}$  complexes with P-coordination synthesised in recent years demonstrate the desired combination of high quantum yields and moderately long lifetimes (tens of  $\mu\text{s}$ ) due to the TADF effect, making them suitable candidates for OLEDs [Dea+10; Che+13; Lei+13; Gne+15; CY15; Ber+16]. Photosensitisers are compounds that are excited upon absorption of a visible light photon and transfer their photoexcited electrons to an acceptor, for example the anode of a solar cell [Gon+17]. Copper complexes often have a strong absorption in the blue part of the visible spectrum, and were investigated in this regard as materials for dye-sensitised solar cells and for photocatalytic water reduction [Lin+10; Luo+12; Fra+14; San+14; SS15].

#### Photophysics of copper complexes with sulfur ligands

Copper complexes with sulfur ligands were synthesised and studied extensively (see chapter 2), but their photophysical properties remain largely unknown. There are some examples of luminescence studies, such as works on multicopper(I) arenethiolates [Kno+92] and Cu-substituted  $\text{Zn}_7$ -metallothionein [Gas+88]. [Kno+92] presents several tricopper complexes with  $\text{Cu}_3\text{S}_3$  and  $\text{Cu}_3\text{S}_2\text{C}$  rings and discusses their photophysical properties as a function of relative orientation of the aryl group (Ar) and the lone-pair electrons on sulfur of the neighboring SAR groups. The emission that is observed for one of the complexes can be described as happening

from two levels with  $14.5 \text{ cm}^{-1}$  separation, with  $6 \mu\text{s}$  and  $300 \mu\text{s}$  decay times. The authors state that it could be either TADF or emission from two triplet levels resulting from zero-field splitting. Low number of publications addressing luminescence properties of Cu/S systems shows that there is still a big field for investigations in this class of materials.

### 3.3 Structural dynamics upon photoexcitation in copper complexes

In this work we concentrate on structural changes that accompany photoinduced charge transfer. These changes can be directly monitored by means of transient X-ray absorption spectroscopy (trXAS) (see chapter 4). Copper compounds were among the first to be investigated with this developing technique, in particular  $\text{Cu}(\text{dmp})_2$  and other Cu bisphenantrolines [Che+02; Che+03; SSC08; Loc+10; Pen+13; Cap+14; MFC15; Cap+15], as well as Cu bichinchoninic acid ( $\text{N}_{\text{qu}}$  coordination) [Fra+14] and  $\text{Cu}(\text{TMGqu})_2$  ( $\text{N}_{\text{qu}}$  and  $\text{N}_{\text{TMG}}$  coordination) [Dic+17]. These trXAS studies, supported by time-resolved optical spectroscopies and DFT calculations, show that upon photoexcitation of these compounds the oxidation state of copper changes from +1 to +2, which is accompanied by flattening of the coordination polyhedron and shrinking of Cu-N distances to the values characteristic for  $\text{Cu}^{+2}$  analogues (when they are known, like in [Che+03; Dic+17]). Despite extensive studies on Cu bisphenantrolines, there is still discussion about interpretation of the results, especially in the question of exciplex formation (solvent coordination in the excited state). Some researches state that the acetonitrile molecule is coordinated in the excited state at the distance as short as nitrogens of the ligand ( $\sim 2 \text{ \AA}$ ) [Che+03; SSC08]. However, some recent trXAS experiments and molecular dynamic simulations on the model complex suggest the lack of complexation and rationalise the lifetime shortening by decrease in  $^3\text{MLCT}$  energy and ISC yield in donating solvents [Pen+13]. The extensive research of excited states in copper complexes added a lot to the contemporary understanding of the structural degrees of freedom in TM complexes and was a grounding base for this work.

## Chapter 4

# Experimental X-rays techniques

This chapter provides the theoretical background necessary to understand the X-ray techniques applied in this work. First, an introduction into interaction of X-rays with matter is given. X-ray absorption and emission spectroscopies are discussed, with a focus on copper compounds. X-ray scattering is described in relevance with pump-probe time-resolved wide-angle X-ray scattering applied to solutions.

X-rays are electromagnetic radiation with energies approximately between 0.1 and 100 keV. When an X-ray photon interacts with an atom, it can be scattered or absorbed. The photoabsorption process is accompanied by excitation of an electron [AM11]. The scattering process can be elastic or inelastic. Each of these processes is characterised by its cross-section, and the total cross-section is a sum of contributions from all processes  $\sigma_{tot} = \sigma_{el} + \sigma_{inel} + \sigma_{abs}$  (Fig. 4.1). For Cu at the photon energy of around 10 keV the cross-section of absorption exceeds that of other processes. In this work we used X-ray techniques based on both absorption and elastic scattering.

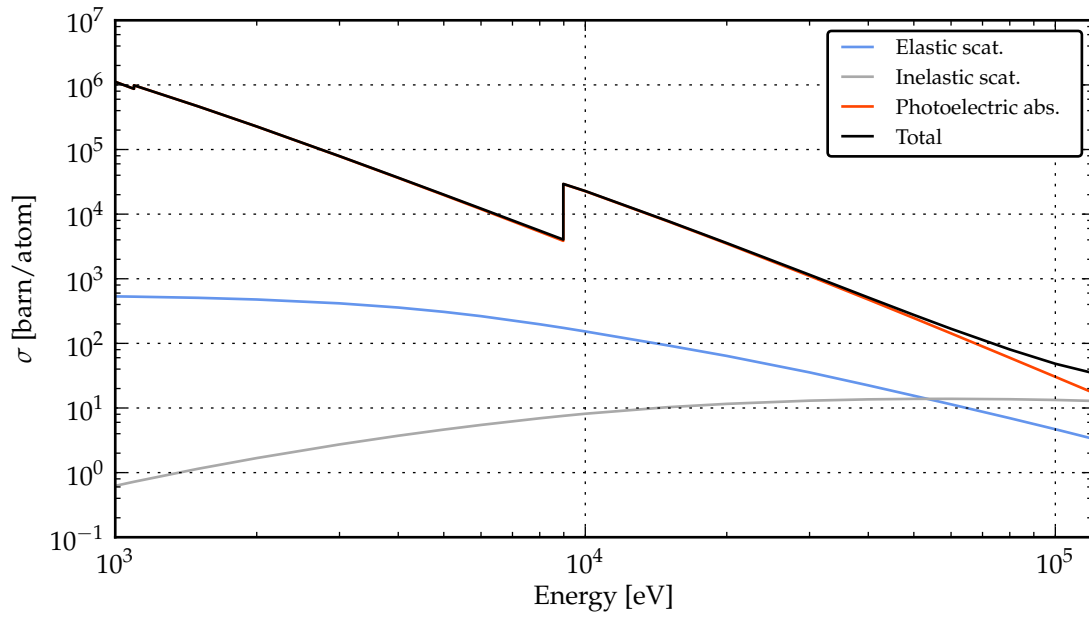


Figure 4.1: Atomic X-ray interaction cross-sections of Cu for different processes (data from [NIS])

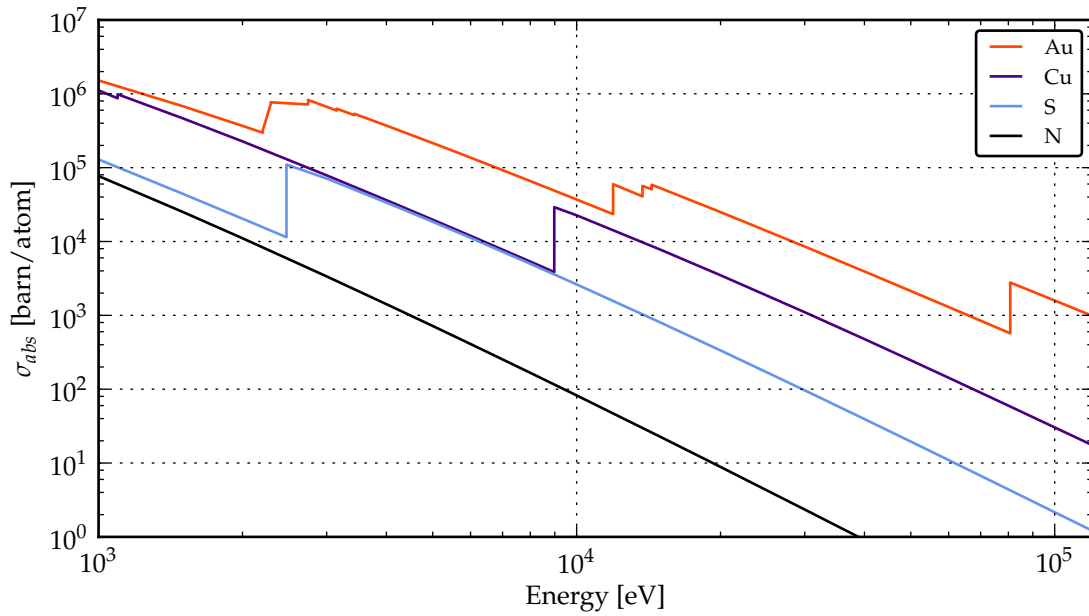


Figure 4.2: Atomic X-ray absorption cross-sections of different elements (data from [NIS])

## 4.1 X-ray absorption spectroscopy (XAS)

Far from resonant photon energies the absorption cross-section of X-rays drops with approximately  $E^{-3}$  dependence [AM11] (Fig. 4.1, 4.2). When the energy of an incoming X-ray photon approaches the energy of a bound electron on one of the subshells, the probability of photon absorption strongly increases. This part in the spectrum is referred to as an absorption edge. Upon photoabsorption the electron is excited, either to an empty bound orbital, or to the continuum above the ionisation potential [Pen05]. The energy of core electrons strongly depends on the atomic number  $Z$  and is therefore a unique spectral signature of an element.

Absorption edges are named according to the main quantum number  $n$ , like K for  $n=0$ , L for  $n=1$ , M for  $n=2$ , etc (Fig. 4.3). For the K-edge, only one subshell ( $1s$ ) exists. For the L-edge, electrons are distributed on  $2s$  and  $2p$  subshells. Due to spin-orbit coupling,  $2p$  subshell is additionally split in two. As a result, there are three L-edges:  $L_I$ ,  $L_{II}$  and  $L_{III}$ , which correspond to the absorption from  $2s$ ,  $2p_{1/2}$  and  $2p_{3/2}$  subshells, respectively. For M shell 5 subshells exist:  $3s$ ,  $3p_{1/2}$  and  $3p_{3/2}$ ,  $3d_{3/2}$  and  $3d_{5/2}$ . In this work, the absorption spectroscopy was performed on the Cu K-edge.

### 4.1.1 X-ray absorption fine structure

When the energy of an X-ray photon  $h\nu_{ph}$  exceeds the energy of a bound electron  $E_{subshell}$  the electron is emitted from the atom. Its kinetic energy is equal to the difference between the absorbed photon energy and the energy of the subshell:  $E_{kin} = h\nu_{ph} - E_{subshell}$ . It is commonly expressed in terms of the photoelectron wavenumber  $k$ :

$$k = \sqrt{\frac{2m_e E_{kin}}{\hbar^2}} \quad (4.1)$$

where  $m_e$  is the mass of an electron.

An absorption spectrum of a noble gas does not show oscillations in the post-edge region. However, when the absorbing atom is embedded into matter the photoelectron propagates as a spherical wave and scatters on the neighbouring atoms, creating an interference pattern in the absorption beyond the edge, which is called the "fine structure" [AM11]. The part of the spectrum that includes the edge and first  $\sim 30$ -50 eV above it is called X-ray absorption near edge structure (XANES) (Fig. 4.4). In this region the kinetic energy of the electron is low, and it is strongly affected by the potential energy surface of the material. Besides that, the electron mean free path grows at low  $k$  values. As a result, multiple scattering (MS) significantly contributes to the interference pattern [RA00]. This part of the spectrum is very sensitive to 3D structural and electronic information. It is challenging to model it quantitatively. When the photoelectron kinetic energy is sufficiently high ( $E_{kin} > 30$ -50 eV) single scattering events dominate. At the same time, MS events still contribute in this energy range, but at these energies they can be theoretically treated similarly to single scattering paths [RA00]. This region of the spectrum contains 1D information about distances between the absorbing and scattering atoms. It is called extended X-ray absorption fine structure (EXAFS) (Fig. 4.4).

### 4.1.2 X-ray absorption near edge structure (XANES)

The XANES region can be separated into two regions: pre-edge + edge, where photon absorption happens due to transition to bound orbitals; and post-edge, where the electron is excited to the (quasi-)continuum and propagates as a spherical wave.

In the pre-edge region of K-edge spectra of  $3d$  TM complexes dipole-forbidden quadrupole-allowed  $1s \rightarrow 3d$  transitions can be observed. For copper, this transition is only possible for

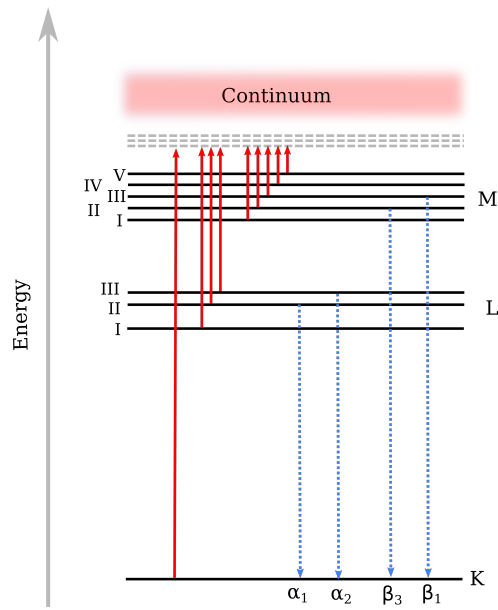


**Figure 4.3:** Scheme of the atomic energy levels. Red lines: photoabsorption process. Roman numbers indicate the nomenclature used to label the X-ray absorption edges of the elements. Blue lines: the core-hole is filled with an electron from a higher-lying subshell. Orbitals with quantum number  $n \geq 3$  are omitted for clarity. Dashed gray lines represent empty valence orbitals. Based on [Jen99; AM11].

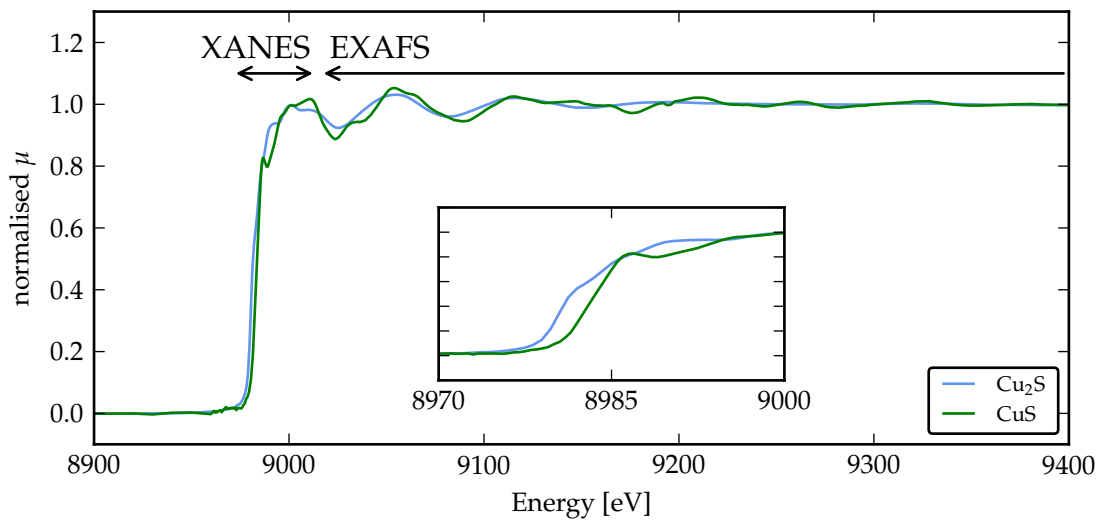


**Figure 4.4:** X-ray absorption spectra of  $\text{Cu}_2\text{S}$  and  $\text{CuS}$ . XANES and EXAFS regions are marked. The inset zooms into the edge region in order to highlight the edge shift between  $\text{Cu}^{+1}$  and  $\text{Cu}^{+2}$ . Data taken from the database of XAS data [XAF].

the oxidation states +2 or higher and occurs at 8978-8981 eV. Due to the quadrupole character this transition is very weak; however, in the result of mixing between  $p$  orbitals of ligands with both  $3d$  and  $4p$  orbitals of copper, hybrid orbitals with Cu  $4p$  contribution are formed, which strongly increases the transition probability [HS12]. This mixing increases upon distortion of the coordination polyhedra from square-planar in the direction of tetrahedral resulting in the increase of the peak intensity [SKY92]. The peak position was shown to shift to higher energies for  $\text{Cu}^{+2}$  complexes with higher ligand field [Sar+08], as well as upon increase of the oxidation state of copper to +3 [Sar+07].

The ab-initio calculations of the XANES part of the spectrum are mostly qualitative or semi-quantitative. There is a number of software packages which can calculate edge and near edge structure, such as Feff [Ank+98]; MXAN [BLN02]; FPMS [Hat+10; Hat]; MSNano [Krü]; FDMNES [BJ09]. A different approach to analysis of XANES spectra is empirical: the information about the oxidation state and coordination of the absorbing atom can often be extracted from the edge position and shape by comparing it with spectra of known compounds. For copper a number of works focusing on correlations between the edge shape and the electronic structure of the system have been published [San+84; Smi+85; Kau+87; SKY92; Ran+00; Sar+08; Sar+11; HS12]. XANES spectra are routinely used to identify the oxidation state of Cu in catalysis [Gio+14; Bor+15], in new synthetic complexes [Dok+09; Aqu+11; Neu+11; Neu+12; But+12; Bur+14; Sin+15], as well as in biological samples [Kau+87; Win91; Sol+14; Arc+16].

The strong absorption on the copper K-edge happens due to the dipole-allowed  $1s \rightarrow 4p$  transition. Energies of  $4p_x$ ,  $4p_y$  and  $4p_z$  orbitals and therefore the position and shape of the absorption edge depend on the coordination environment [HS12].

For  $\text{Cu}^{+1}$  with  $3d^{10}$  configuration no pre-edge  $1s \rightarrow 3d$  transition is possible. For two-coordinate linear  $\text{Cu}^{+1}$  complexes the energy of the  $4p_z$  orbital is increased, and  $4p_{x,y}$  is localized in space and at lower energy, which results in a sharp peak at  $\sim 8984$  eV due to the  $1s \rightarrow 4p_{x,y}$  transitions. The addition of a third ligand to the  $\text{Cu}^{+1}$  splits the degeneracy of the  $4p_x$  and  $4p_y$  levels. It results in a split feature with lower intensity. For four-coordinated copper all three  $4p$  orbitals have increased energy because of ligands, and the edge feature is at higher energy and can also be broad. A XANES spectrum of the copper complex investigated in this work  $\text{Cu}_2(\text{NSSN})_2$ , shown in Fig. 5.18, demonstrates a quite sharp and strong (0.8 of edge jump) feature with a maximum at 8985.5 eV and, hidden on its rise, there is a shoulder at lower energy ( $\sim 8982.3$  eV, which is better visible in the first derivative spectrum). [Kau+87] reports several four-coordinated Cu complexes with ( $\text{N}_4$ ) and ( $\text{N}_3\text{O}$ ) coordination which all show an edge peak at 8985.5 eV with the normalized absorption amplitude of  $0.72 \pm 0.06$ . The spectrum of a ( $\text{S}_4$ ) complex has a shoulder at 8986.6 eV with intensity of 0.8, and in addition a smaller shoulder at 8983.8 eV. The authors suggest that the peak shift and the shoulder are due to high covalency of the ( $\text{S}_4$ ) ligand. Our case with ( $\text{N}_2\text{S}_2$ ) coordination is in agreement with these observations.

For  $\text{Cu}^{+2}$  compounds, the edge position is shifted to higher energies compared to  $\text{Cu}^{+1}$  due to increased charge on copper causing a higher binding energy of  $1s$  electrons (as is demonstrated on Fig. 4.4 for  $\text{Cu}_2\text{S}$  and  $\text{CuS}$ ). For some  $\text{Cu}(\text{N}_4)$  complexes this shift (measured at the half height of the rising edge) was found to be 3-3.5 eV [Che+02; Hof+14], but can be smaller for more covalent Cu-ligand bonds [Kau+87]. As in the case of  $\text{Cu}^{+1}$  compounds, ligands play a big role in the position and shape of the edge. For example, Cu-ligand bonds with high covalency demonstrate stronger absorption at low energies [Kau+87].  $\text{Cu}^{+2}(\text{N,S})$  complexes reported by [Aqu+11] confirm this observation, as well as  $\text{Cu}^{+2}(\text{N},2\text{S},\text{Cl})$  from [Neu+12]. The rising edge shape of  $\text{Cu}^{+2}$  compounds is often featureless. However, XANES spectra of some of them demonstrate a two-electron ligand-to-metal shake-down transition [HS12]. The origin of this effect is the change in energies of copper  $d$  orbitals due to the core hole from the  $1s \rightarrow 4p$  transition. If the half-occupied  $3d_{x^2-y^2}$  orbital becomes lower in energy than valent orbitals of ligands, then a LMCT transition becomes possible, when  $3d_{x^2-y^2}$  gets filled by an electron

from the ligand. A  $1s \rightarrow 4p$ +LMCT transition happens at lower energy than the  $1s \rightarrow 4p$ , and sometimes is a dominating excitation channel [Cha+05].

In summary, it is not easy to predict the edge shape of a photoexcited copper complex: the ligand field and possible presence of the shake-down transition both have strong influence on the absorption edge of  $\text{Cu}^{+2}$  compounds. Even for structurally quite similar complexes the edge shapes of  $\text{Cu}^{+2}$  can be very different (see, for example, [Sar+08; Aqu+11]). In order to account for the LMCT shake-down transition an ab-initio calculation has to include two-electron processes as done in [Cha+05].

### 4.1.3 Extended X-ray absorption fine structure (EXAFS)

The EXAFS region starts at  $E_{kin} > 30\text{-}50$  eV and extends as long as oscillations can still be registered – in a conventional experiment in transmission mode the spectrum is normally measured up to  $E_{kin} \sim 1000$  eV. In this region single-scattering events dominate, which greatly simplifies the analysis. Normally bond lengths between absorbing atom and first and second shells can be determined with precision on the order of  $\sim 0.02$  Å, and with good data quality for the first shell below  $0.01$  Å even in time-resolved experiments as shown in [Gaw+09; Van+15; Zha+16].

In order to extract the pure EXAFS signal the data reduction can be performed as presented in Fig. 4.5. First the pre-edge and post-edge are fitted with polynomials (pre-edge normally as a linear function).  $\mu(E)$  can be represented as a sum of the step-like absorption spectrum of the isolated atom  $\mu_0(E)$  and the oscillatory part of the spectrum  $\chi(E)$  that originates due to photoelectron scattering and carries the structural information. In order to extract  $\chi(E)$  the atomic-like background  $\mu_0(E)$  is subtracted (eq. 4.2), and the edge jump is normalised to 1 at the edge position  $E_0$ .  $E_0$  is normally chosen at the maximum of the first derivative of the edge or at the half of the edge jump (Fig. 4.5a). The position of  $E_0$  is fitted in the following analysis.

$$\chi(E) = \frac{\mu(E) - \mu_0(E)}{\mu_0(E_0)} \quad (4.2)$$

In the next step the energy of the photoelectron is converted to electron wavenumber  $k$  by applying eq. 4.1 for  $E_{kin} = E - E_0$  (Fig. 4.5c). In order to emphasise weak oscillations at higher energies the data are normally weighted by powers of  $k$  and treated further as  $\chi(k) \cdot k^2$  or  $k^3$  (Fig. 4.5c). The Fourier-transform of  $\chi(k)$  gives pseudo radial distribution function  $\chi(R)$  (Fig. 4.5d). It is possible to fit the data either in  $k$  or in  $R$ -space.

The EXAFS function  $\chi(k)$  can be expressed as a sum of contributions of all scattering paths. The following equation was developed in [SSL71; Ste74] for modelling EXAFS data:

$$\chi(k) = S_0^2 \sum_j N_j |f_j(k)| \sin(2kR_j + \phi_j(k)) \frac{e^{-2R_j/\lambda(k)} e^{-2\sigma_j^2 k^2}}{kR_j^2}. \quad (4.3)$$

The main part of this equation is  $\sin(2kR_j)$  – this is the oscillatory term which carries the structural information, where  $R_j$  is the scattering path length.  $\phi(k)$  is the phase shift introduced when the photoelectron passes through the potential of the absorbing and scattering atoms.  $S_0^2$  is the amplitude reduction factor, which takes into account inelastic loss processes. Its typical value is in the range of 0.7-1.  $N_j$  stands for the scattering path degeneracy.  $|f_j(k)|$  is the back-scattering amplitude, which depends on the back-scattering atom. For atoms with close  $Z$  values, like O and N, the shapes of  $|f_j(k)|$  are very similar, and these elements cannot be distinguished in the EXAFS fit. Several damping factors in this equation take account of EXAFS being only a local probe.  $1/kR_j^2$  describes the propagation of the electron as outgoing and scattered spherical wave. The damping factor  $e^{-2R_j/\lambda(k)}$  describes the electron mean free path  $\lambda(k)$ . The factor  $e^{-2\sigma_j^2 k^2}$  originates from displacements of atoms due to structural and thermal disorder, where  $\sigma_j^2$  is the

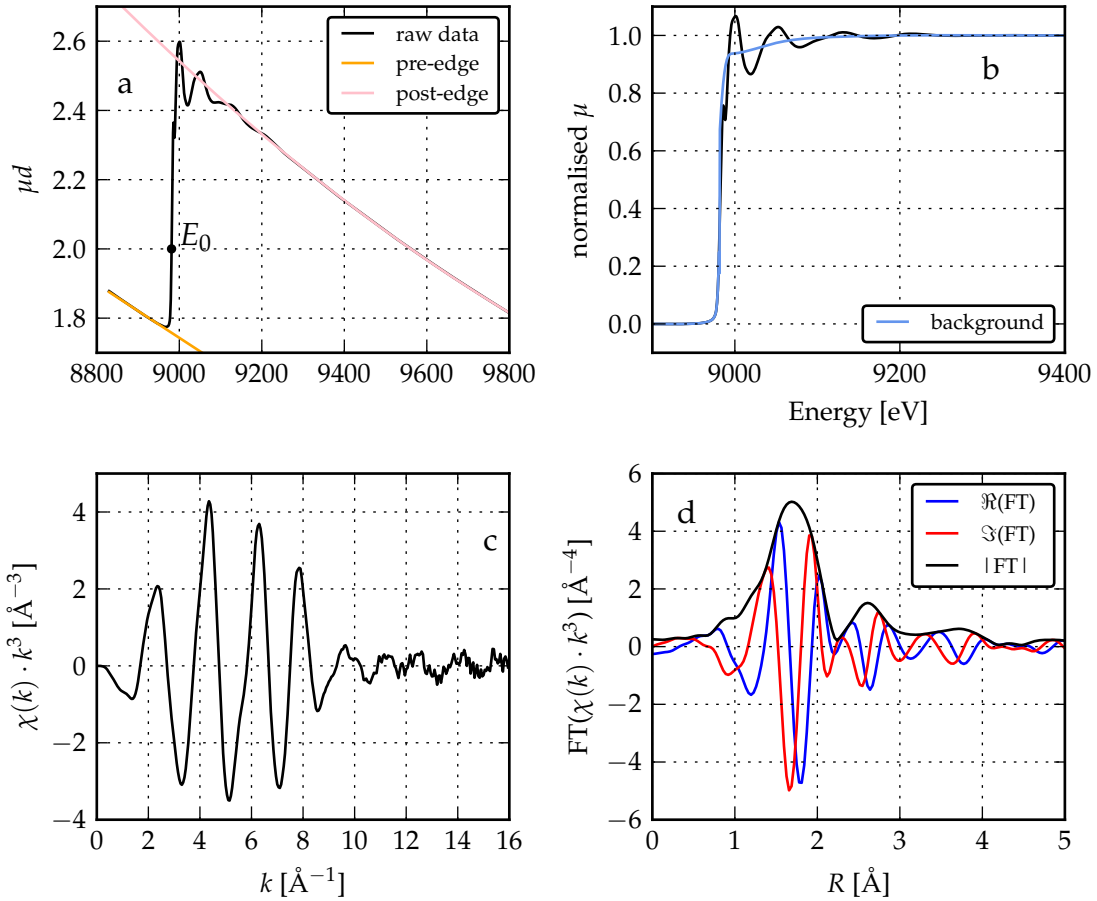


**Figure 4.5:** X-ray absorption spectrum of  $\text{Cu}_2(\text{NSSN})_2$  measured in transmission in a solid. (a) shows the raw spectrum, pre-edge, post-edge and the  $E_0$  at the maximum of the first derivative of the rising edge (8981.2 eV). (b) shows the normalised spectrum with the background, determined in Athena[RN05]. (c) shows the extracted  $\chi(k) \cdot k^3$ . (d) shows Fourier transformed  $\chi(k) \cdot k^3$  for  $k=3-16$  Å (real part, imaginary part and the magnitude).

mean square deviation of the distance between scattering atom and absorber. It is normally called the Debye-Waller factor.<sup>1</sup>

Of all these factors,  $|f_j(k)|$  and  $\phi(k)$  have to be calculated externally or extracted from a measurement of a reference compound. Nowadays the theory level allows to calculate them reliably for quantitative analysis [Ank+98]. The structural parameters  $N$ ,  $R$  and  $\sigma$  can then be fitted. Although the original EXAFS formula described only single-scattering events, the same formula can be generalized to represent the contribution from MS events [NBD86; RA90]. Taking into account MS events is necessary for accurate calculations when not only the first shell, but also further shells are fitted.

There is a number of software packages for EXAFS data reduction and analysis. In this work the Demeter package (Athena and Artemis) was used [RN05], as well as ExCurve [Bin98]. ExCurve has some features especially suitable for working with biological compounds and molecular complexes, like the database of typical radicals and ability to move and rotate several atoms together as fixed units during the fit. An example of a software package which fits directly raw data without preliminary data reduction is GNXAS [Cic09]. A big amount of literature is published about EXAFS, among which [New04] is a good basic introduction into EXAFS theory, experiment and analysis. [KHR08] thoroughly goes into details of choice of parameters for the data reduction and the fit.

#### 4.1.4 Experimental setup for X-ray absorption spectroscopy

A typical X-ray absorption setup is presented at Fig. 4.6. Normally an X-ray source with high intensity and broad photon energy range is used, such as a synchrotron light source. The incoming beam is then monochromatised, and the scan is performed over photon energies from approximately -200 to 1000 eV throughout the absorption edge. The incident and the transmitted intensity are measured ( $I_0$  and  $I_1$ , respectively), and the absorption coefficient is then calculated according to the Lambert-Beer law as  $\mu = 1/d \cdot \ln(I_0/I_1)$ ,  $d$  is the sample thickness. Often  $\mu d$  is used for analysis, without extraction of  $\mu$ . Normally a reference sample (a sample containing the measured element with the tabulated spectrum, for example, a metal foil) is placed between  $I_1$  and one more ion chamber,  $I_2$ , and its transmission is measured simultaneously with the sample. The reference spectrum is then used for the energy calibration.

The measurements in transmission mode work well for thin samples with high content of the absorbing element. In case when the sample is too thick to be penetrated by X-rays or on the contrary too diluted to absorb enough photons for a good signal over  $I_0$  background, it is not possible to measure XAFS in transmission. In this case X-ray fluorescence is a measurement technique of choice [New04] (for the physical origin of X-ray fluorescence see the next section). The intensity of the emitted fluorescence can be proportional to the intensity of the incident beam  $\mu(E) \sim I_f/I_0$  for some conditions, such as a thin sample limit ( $\mu d \ll 1$ ) or a thick, dilute sample limit ( $\mu d \gg 1$  and  $\mu_x \ll \mu_{tot}$ , where  $\mu_x$  is absorption by the element of interest and  $\mu_{tot}$  is the total absorption). When these conditions are not satisfied, the dependency is more complicated due to fluorescence self-absorption [BB05].

A fluorescence detector collects not only fluorescence photons emitted by the element of interest, but also fluorescence of other elements in the solution and scattered radiation. The contribution of scattering can be quite significant. For samples with low concentration of the absorbing atom it can dominate the spectrum. Since elastic scattering is strongly suppressed at  $90^\circ$  to the incident beam in the horizontal plane due to polarisation of the synchrotron radiation, detectors are normally placed perpendicular to the incident beam as shown at Fig. 4.6 [New04].

---

<sup>1</sup>The term "Debye-Waller factor" originates from crystallography where it denotes a displacement of atom in space, whereas in EXAFS it quantifies variation in distance between the scattering atom and the absorbing atom.

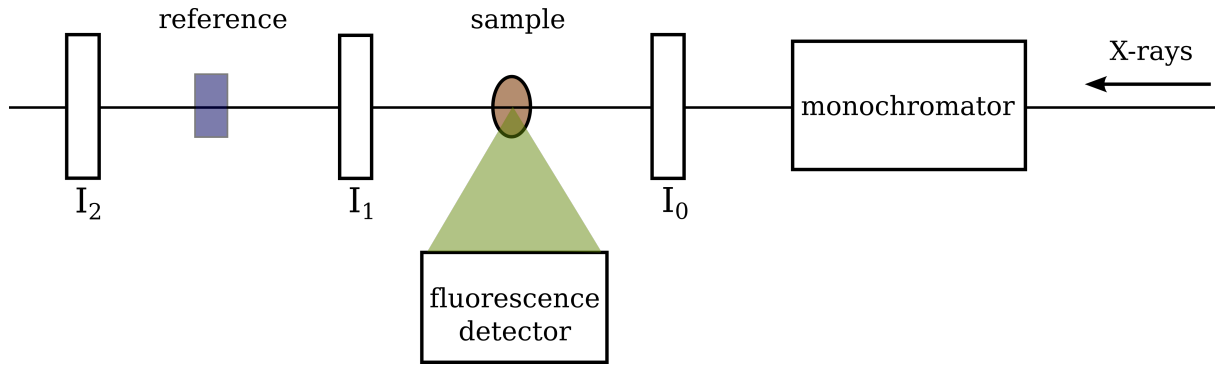


**Figure 4.6:** A scheme of an X-ray absorption experiment.  $I_0$ ,  $I_1$ ,  $I_2$  refers to ionisation chambers which measure transmitted intensity.

## 4.2 X-ray emission spectroscopy (XES)

Absorption of an X-ray photon leaves a core-hole in the atom. This state is not stable, and the hole is promptly ( $\sim 1$  fs) filled by an electron from one of the upper shells. The excess in energy can be released in a form of a photon. This process is called X-ray fluorescence. Alternatively this energy can be passed to one of the electrons in the atom which will be then expelled from its shell. This process is called Auger decay. For light elements Auger decay is a dominating core-hole decay channel; the fluorescence yield  $\phi_{fl}$  relative to Auger decay yield  $\phi_{Au}$  increases with the atomic number  $Z$ . For copper  $\phi_{fl}(1s) = 0.44$  [Kra79].

X-ray fluorescence lines in spectroscopy are commonly named following the Siegbahn notation [Jen+91; Jen99]. Each series name is determined by the final level of the transition (K, L, M, ...), and a particular transition within a series is specified with a greek letter index in the order of intensity decrease as  $\alpha$ ,  $\beta$ ,  $\gamma$ , ... .  $K\alpha$  and  $K\beta$  transitions are shown in Fig. 4.3).

In this work we registered spectra of  $K\alpha$  lines of copper. Due to spin-orbit coupling, the  $2p$  level is split into two. This splitting results in two  $K\alpha$  transitions:  $K\alpha_1$  ( $2p^{3/2} \rightarrow 1s$ ) and  $K\alpha_2$  ( $2p^{1/2} \rightarrow 1s$ ). This spin-orbit interaction is strong for the  $K\alpha$  lines (appr. 20 eV, see Fig. 4.7) and  $<1$  eV for the  $K\beta$  lines [BG09]. Due to twice bigger degeneracy of  $2p^{3/2}$  compared to  $2p^{1/2}$ ,  $K\alpha_1$  shows approximately twice bigger intensity than  $K\alpha_2$ .

### 4.2.1 Experimental setup for high-resolution X-ray emission spectroscopy

X-ray emission spectrum can be measured directly with an energy dispersive detector (Fig. 4.6), such as solid state Si or Ge detectors [LS13]. Energy resolution of such detectors for Si and Ge is on the order of one to several hundreds eV at 5-10 keV. With such resolution it is not possible to distinguish  $K\alpha_1$  and  $K\alpha_2$  and study fine features in emission spectra. Much higher resolution can be achieved by dispersing X-rays before detection. Normally such setup is realised by placing a sample, a dispersive crystal and a detector on a circumference of a circle (called Rowland circle, Fig. 4.8). Radiation emitted by the sample reaches the surface of the analyser crystal and is energetically dispersed. When emitted X-rays with the wavelength  $\lambda$  fall at a crystal with lattice spacing  $d$  at a specific angle  $\theta$ , only those X-rays that satisfy Bragg's Law  $n\lambda = 2d \sin \theta$  are reflected, and a narrow energy band is passed on to the detector. Focusing can be achieved by making the analyser crystal cylindrically bent (von Hamos geometry) or spherically bent (Johann or Johansson geometry) [Bau14]. In Von Hamos geometry the whole emission spectrum is registered in one shot with a position-sensitive detector. In Johann geometry the Bragg angle and therefore the energy is scanned by moving the analyser crystal and the point detector along the circumference of the Rowland circle. In this work a spherically bent Si(111) crystal in Johann geometry was used. Point detectors may be non-energy dispersive or can have energy

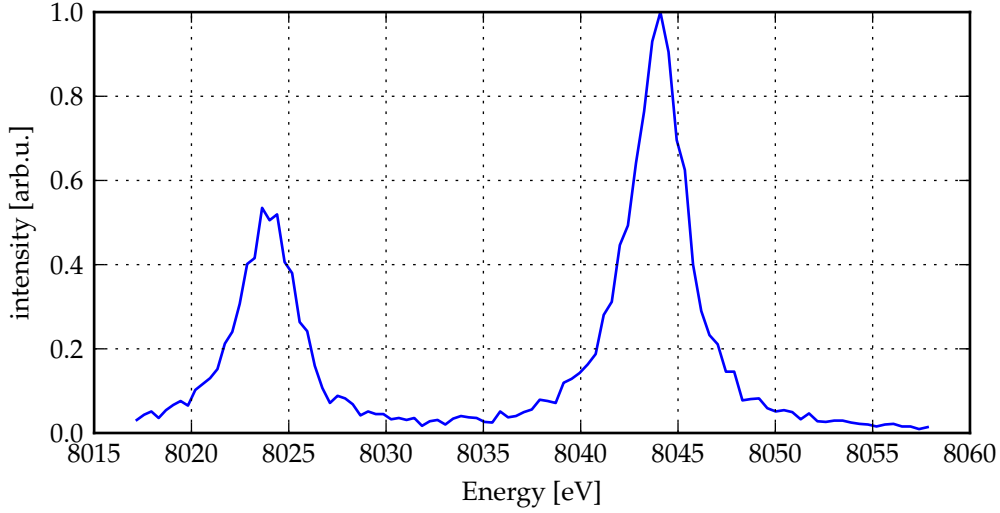


Figure 4.7: Emission spectrum of  $\text{Cu}_2\text{O}$ :  $K\alpha_1$  and  $K\alpha_2$ .

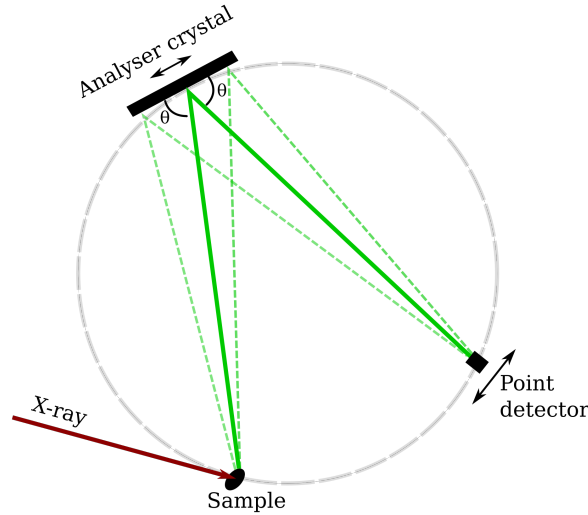


Figure 4.8: High resolution X-ray emission spectroscopy setup in Johann geometry.

resolution, such as an silicon drift detector (SDD) with a multichannel analyser as it was used in the experiment in this work. Additional energy resolution of the detector serves to reject the contribution of elastically scattered X-rays of higher energy.

### 4.3 Wide-angle X-ray scattering (WAXS)

Apart from photoelectric absorption, the second strongest interaction of hard X-rays with matter is elastic scattering. The photon interacts with electrons of an atom and is deflected from its original direction without loss of energy. The connection between the scattering amplitude of the X-ray wave  $A(\mathbf{q})$  and the electron density of the sample  $\rho_e(\mathbf{r})$  as a function of the 3D coordinate  $\mathbf{r}$  in Born approximation is given by eq. 4.4 [Ihe+10]:

$$A(\mathbf{q}) = \int \rho_e(\mathbf{r}) \exp(-i\mathbf{q} \cdot \mathbf{r}) \, d\mathbf{r}, \quad (4.4)$$

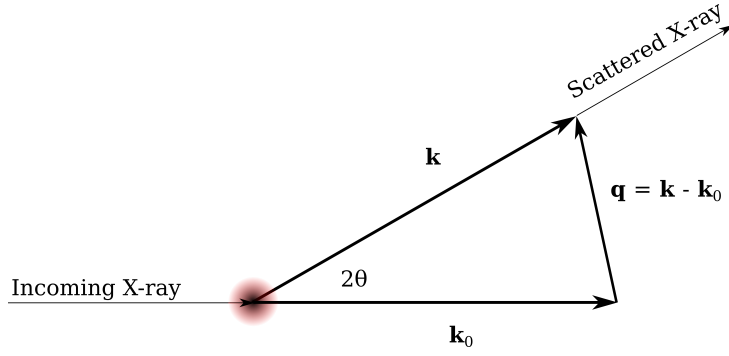


**Figure 4.9:** Schematic illustration of the scattering process. Incident X-rays are scattered by the sample.  $\mathbf{q}$  is the momentum transfer between the incident ( $\mathbf{k}_0$ ) and the elastically scattered ( $\mathbf{k}$ ) waves. Adopted from [Ihe+10].

where  $\mathbf{q}$  is the momentum transfer between the incident ( $\mathbf{k}_0$ ) and the elastically scattered ( $\mathbf{k}$ ) waves (Fig. 4.9):  $\mathbf{q} = \mathbf{k} - \mathbf{k}_0$ .

As shown in eq. 4.4, the scattering amplitude is the Fourier-transform of the electron density. Therefore if  $A(\mathbf{q})$  is known, the electron density  $\rho_e(\mathbf{r})$  can be calculated as its inverse Fourier-transform:

$$\rho_e(\mathbf{r}) = \frac{1}{(2\pi)^3} \int A(\mathbf{q}) \exp(i\mathbf{q} \cdot \mathbf{r}) d\mathbf{q}. \quad (4.5)$$

However, the information about the phase of the scattered wave is lost upon detection. In the experiment the intensity of scattered X-rays is measured, which is the modulus square of the amplitude:

$$S(\mathbf{q}) \sim |A(\mathbf{q})|^2 \quad (4.6)$$

At the same time, in contrast to X-ray diffraction from crystals, in the case of liquid scattering there is no lattice or long range order, and the molecules are oriented randomly. As a result, the measured signal is isotropically averaged, and we observe scattering intensity  $S$  as a function of  $q = |\mathbf{q}|$ . The 3D electron density as a function of  $\mathbf{r}$  cannot be reconstructed, but only the 1D pair distribution function as a function of distance between atoms  $r$  (for X-rays with coherence length on the order of interatomic distances).

$S(q)$  can be expressed as a sum of contributions of all atoms in solution. For the case of a liquid a convenient way to do it is to introduce the pair distribution function  $g_{ij}(r)$  between atom types  $i$  and  $j$  so that  $4\pi r^2 g_{ij}(r) dr$  is the probability of finding a  $j$ -type atom at the distance  $r$  from an  $i$ -type atom. The scattering intensity can then be expressed as

$$S(q) = \sum_i N_i f_i^2(q) + \sum_i \sum_{i \neq j} \frac{N_i N_j}{V} f_i(q) f_j(q) \int_0^\infty (g_{ij}(r) - 1) \frac{\sin(qr)}{qr} 4\pi r^2 dr, \quad (4.7)$$

where the indices  $i$  and  $j$  include all atom types,  $N_i$  is the number of  $i$ -type atoms,  $V$  is the volume of the sample and  $f_i$  is the atomic form-factor of atom type  $i$ . The atomic form-factor is the Fourier transform of the charge distribution in the atom [AM11]. Atomic form-factors of different elements are tabulated in the International tables for crystallography [IUC].

A liquid solution is a mixture of a minor component (solute) and a major component (solvent). Thus the total scattering from a solution can be classified into three types of contributions: the scattering from the solute alone ( $S(q)_{\text{solute}}$ ), the scattering from the solute–solvent interferences ( $S(q)_{\text{cage}}$ ) and the scattering from the solvent alone ( $S(q)_{\text{solvent}}$ ) [Ihe+10].

$$S(q) = S(q)_{\text{solute}} + S(q)_{\text{cage}} + S(q)_{\text{solvent}} \quad (4.8)$$

In case of working with diluted solutions where the solute is investigated, the contribution of the solvent is dominating as the molar ratio of the solvent to solute molecules is very large, typically of the order of  $10^4$ . It is therefore often impossible to extract the structural information on the solute unambiguously just from the static solution scattering. At the same time, if the scattering experiment is performed on a photoexcited solute, the difference scattering signal from the solute may dominate or be of similar strength as the difference signal contributions from the solvent and the solvation shell. Such experiments are usually performed using the pump-probe method (see section 4.4), where the solute molecules are photoexcited with an ultrashort laser pulse. Upon photoexcitation molecules undergo structural changes or a photochemical process, and scattering pattern at different time delays between the pump laser pulse and the probe X-ray pulse is measured. This technique is sensitive to solute structural changes, solvation shell rearrangements and the bulk solvent temperature and density and was successfully applied to study small molecules and molecular complexes [Kim+06; Chr+09; Ihe09; Sal+10; Kim+12; Kim+].

For the pump-probe experiment the observed difference intensity can be decomposed into three distinct terms: the solute-only term, the solvent-only term and the cage term describing the structural rearrangements in the solvation shell as in eq. 4.8:

$$\Delta S(q, t) = \Delta S(q, t)_{\text{solute}} + \Delta S(q, t)_{\text{cage}} + \Delta S(q, t)_{\text{solvent}} \quad (4.9)$$

For the analysis the components of this equation can be grouped into two parts - solute-related contribution and contribution of the solvent bulk.

The solvent component  $\Delta S(q, t)_{\text{solvent}}$  can be estimated via MD (molecular dynamics) or QM/MM (quantum mechanics/molecular mechanics) simulations or measured in a separate reference solvent heating experiment [Ihe+10; Kjæ+13]. One way to perform such an experiment is to excite the solvent vibrational bands with IR photons. Another approach, which was used in this work, is to measure transient scattering on a solution of a substance whose photoexcited state lifetime is much shorter than the X-ray pulse length, as proposed in [Kjæ+13]. This way on the 100 ps time scale of the synchrotron-based experiment all absorbed energy is transferred to the solvent, and pure solvent response is measured. The calculated or measured solvent response is then used in the fit of the transient WAXS data from the sample.

The  $\Delta S(q, t)_{\text{solute}}$  term is usually calculated using the equation 4.7 for the molecular structure obtained using the DFT methods as a starting guess. Then either analysis on the different candidate structures or structural optimization using geometrical transformation methods is performed.

$\Delta S(q, t)_{\text{cage}}$  is estimated using a molecular dynamics approach and is often not considered as it mostly contributes the low- $q$  scattering region of the difference signal, and the contribution is typically much weaker as compared to the solute term.

In contrast to the element-specific X-ray absorption techniques, the non-resonant elastic scattering is sensitive to all atoms in the illuminated solution. Therefore, if the solute ground state and the intermediates do not behave as rigid molecules with well defined structure, the isotropic averaging over various molecular species and orientations smears the signal features thus decreasing the structural sensitivity. Still, choosing a proper analysis framework, information of the complementary techniques (XES, XAS) and chemically justified considerations it is possible to discriminate certain structural models on the base of the best fit.

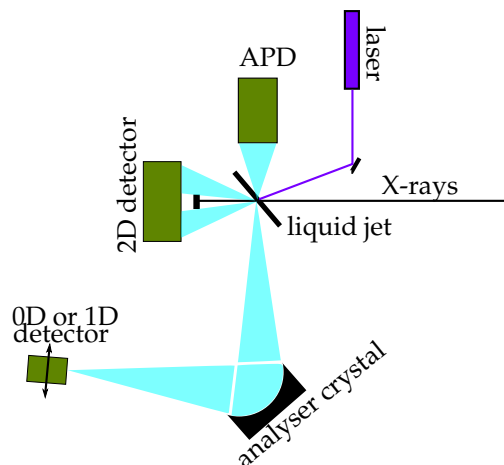


**Figure 4.10:** Scheme of a setup for combined pump-probe XAS, XES and WAXS measurements. Drawing based on [Bri17].

#### 4.4 Pump-probe time-resolved X-ray techniques

Pump-probe experiments are performed in order to access changes caused in a system upon photoexcitation by a laser pulse. In X-ray techniques the photoexcited system is probed by an X-ray pulse after a certain time-delay. The temporal resolution of this experiment is determined by the X-ray pulse length and is on the order of 70-100 ps for synchrotron light sources and down to 1-10 fs for free electron lasers.

A scheme of an experimental setup which represents several pump-probe X-ray techniques used in this work is given at Fig. 4.10. Pump and probe beams are overlapped on the sample, which is delivered via a liquid jet or a flow capillary. Steady state and laser-excited spectra are acquired alternately. The laser-excited spectrum (pumped spectrum (PS)) contains contributions of both ground state (GS) and excited state (ES). The relative contribution of the ES spectrum is called excited state fraction  $f$ . Knowledge of  $f$  is crucial for the data analysis since it is necessary in order to reconstruct the excited state (ES) spectrum:

$$ES = \frac{PS - GS}{f}. \quad (4.10)$$

Time-resolved X-ray techniques developed in the last fifteen years following the development in synchrotrons, lasers and electronics. First transient XAS experiments were established [Che01; Sae+03; Gaw+05], as well as transient WAXS [Ihe05; Chr+09]. More photon-hungry transient X-ray emission spectroscopy (trXES) methods followed soon after [Van+10].

Combining several pump-probe methods in one experiment can have a great advantage. XANES probes empty valent orbitals, whereas certain X-ray emission lines originate from occupied valent orbitals. TrWAXS is sensitive to the changes in the whole system (sample+solution), whereas transient XAS registers only changes in the local environment of the absorbing atom. Fitting several data sets with the same unknown parameters makes the analysis more reliable. In particular, excited state fraction can be obtained in one experiment and used for the analysis of the other data set.

## Chapter 5

# Photoinduced structural dynamics of a dicopper-disulfide complex $\text{Cu}_2(\text{NSSN})_2$

This chapter reports the objective of this thesis: the study of the structural dynamics upon photoexcitation in a dicopper complex with guanidine and disulfide ligands  $\text{Cu}_2(\text{NSSN})_2$ .

### 5.1 Physical and chemical properties of $\text{Cu}_2(\text{NSSN})_2$

In this section the investigated copper complex  $\text{Cu}_2(\text{NSSN})_2$  is described and its structure is compared with published structures of copper complexes with nitrogen and sulfur coordination. Electronic structures of ground and excited states are discussed based on density functional theory (DFT) calculations. The choice of solvents for the experiments is justified and photostability issues in different solvents are addressed.

#### 5.1.1 Synthesis, characterisation and structure discussion

The investigated copper complex was for the first time synthesised by Dr. Adam Neuba, research group of Prof. Gerald Henkel, Paderborn University, as described in [Neu09; Neu+12]. The substance was characterised with elemental analysis, UV-vis and Fourier transform infrared (FT-IR) spectra, single crystal X-ray diffraction and XAS (as a solid and in solution). The crystal structure is available online in the Cambridge Crystallographic Data Centre [Neu11].

The structure of the complex is shown in Fig. 5.1. It is a binuclear  $\text{Cu}^{+1}$  complex, the complex cation  $[\text{Cu}_2(\text{NguaS}-\text{SNgua})_2]_2^+$  (further referred to as  $\text{Cu}_2(\text{NSSN})_2$ ) consists of two copper atoms, which are connected by two disulfide bridges into a six-member ring in twist conformation. Two sulfur atoms take part in forming a tetrahedral coordination polyhedron together with two nitrogen atoms from tetramethylguanidine (TMG) ligands. TMG has strong donor properties, strong basicity and is a part of various ligand systems [Neu+15; Hof+14]. The overall structure of the molecule has  $D_2$  symmetry. The compound was synthesised with two counter-anions –  $\text{OTf}^-$  and  $\text{PF}_6^-$ .

The critical parts of the complex for its photoreactivity are Cu-N and Cu-S bonds. Below typical bond lengths in Cu/N/S complexes are reviewed, and  $\text{Cu}_2(\text{NSSN})_2$  is discussed in this frame. The coordinating nitrogen of the TMG ligand has imine character. The Cu-N distance (av. 2.02 Å) is close to Cu-pyridine coordination (2.01-2.07 Å) [WOS74; Che+03] and shorter than typical for amine coordination  $\text{Cu}^{+1}-\text{NR}_3$  (2.16(9) Å) [Amb+99]. Several examples of copper complexes existing for both  $\text{Cu}^{+1}$  and  $\text{Cu}^{+2}$ , like  $\text{Cu}(\text{dmp})_2$  [Che+03] and the complexes reported

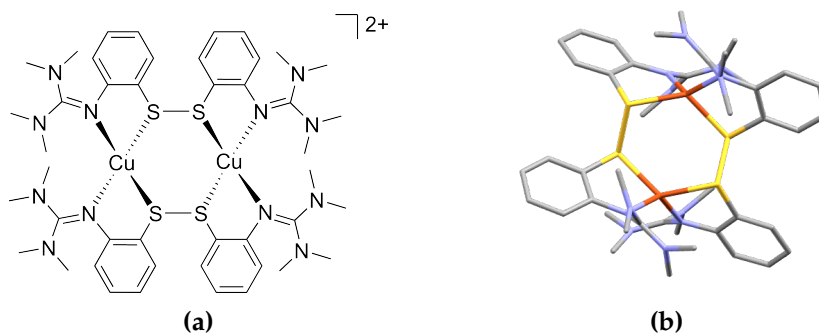


**Figure 5.1:** Scheme (a) and crystallographic structure (b) of  $[\text{Cu}_2(\text{NguaS-SNgua})_2](\text{OTf})_2$ . Legend: Cu - orange, S - yellow, N - violet, C - grey. Hydrogens are omitted for clarity.

in [Hof+14] and [Amb+99], all have shorter Cu-N bond length for  $\text{Cu}^{+2}$  than for  $\text{Cu}^{+1}$ . The same trend is observed when  $\text{Cu}^{+2}$  is created by photoexcitation of  $\text{Cu}^{+1}$  [Che+03; Dic+17]. For  $\text{Cu}^{+1}$ -disulfide coordination the Cu-S distance were reported to be 2.20-2.27 Å [INF01], 2.24-2.25 Å [Oht+00] and 2.30-2.37 Å [WOS74].  $\text{Cu}_2(\text{NSSN})_2$  with the Cu-S bond lengths of 2.28-2.30 Å falls into this range.  $\text{Cu}^{+2}$  complexes tend to have 4+1 or 4+2 coordination with axial bonds elongated due to pseudo-Jahn-Teller distortion [Ber10]. For  $\text{Cu}^{+2}$ -disulfide bonds in axial coordination the span of covered Cu-S bond lengths is 2.68 to 3.28 Å in [Thi+74; Miy+80; Bra+90; Nic+93; Gon+16]. For a  $\text{Cu}^{+2}$ -disulfide linkage with a rare case of seemingly equal six Cu-ligand bonds [Fox+00] Cu-S is within 2.46-2.57 Å, which is longer than characteristic for  $\text{Cu}^{+1}$ -disulfide. However for  $\text{Cu}^{+2}$  with equatorially bound radical disulfide ( $\text{S}_2^{\bullet-}$ ) a much shorter distance of 2.27 Å was reported [YBT05]. For several complexes of  $\text{Cu}^{+1}$  and  $\text{Cu}^{+2}$  with the same aliphatic thiolate  $\text{NS}_3$  ligands  $\text{Cu}^{+1}$ -S bonds were reported to be 2.26 Å, whereas  $\text{Cu}^{+2}$ -S - 2.37-2.38 Å [Amb+99].

Based on this literature study, we may expect shortening of Cu-N bonds and elongation of Cu-S distances in the excited state. However, the DFT calculations for  $\text{Cu}_2(\text{NSSN})_2$  (see below) show that upon photoexcitation in the blue part of the visible spectrum the electron is transferred to the antibonding  $\sigma^*$  PhS-SPh MO, which will increase the negative charge on the S-S bridge. This can make S-S a stronger coordinating ligand than it was in the ground state and cause shortening of Cu-S bonds.

### 5.1.2 Electronic structure in the ground state

The calculations used in this work were performed by Martin Rohrmüller from the group of Prof. W.G. Schmidt, Paderborn university. The calculations were carried out using the implementation of gaussian 09 [Fri+09]. The most frequently used hybrid functional B3LYP [LYP88; Bec93; Bec99] and for comparison also a pure GGA PW91 [Per+92] and the meta hybrid functional TPSSh [Tao+03] were applied. Excitations and geometrically relaxed excited states were addressed with time-dependent density functional theory (TDDFT) [SSF98] by solving the Casida equations [Cas+98], which had to be solved within every step of a geometric relaxation of the specific excited-state. A computationally feasible cc-pVDZ [Dun89] basis set was used for the TDDFT calculations. Triple- $\zeta$  basis Def2-TVZP [WA05; Wei06] was used for evaluation of excitation spectra. Both used basis sets included polarization functions. Additionally, a continuum solvent model [TMC05] was used to examine the influence of different solvents [Sca+06]. Vibrational frequencies were checked for the ground state to ensure a true minimum. These concepts have been shown to result in reliable excited-state properties for a system within the copper-sulfur or related copper-oxygen chemistry [Roh+15; Wit+16].

Calculations performed with different potentials all show similar electronic structure. The

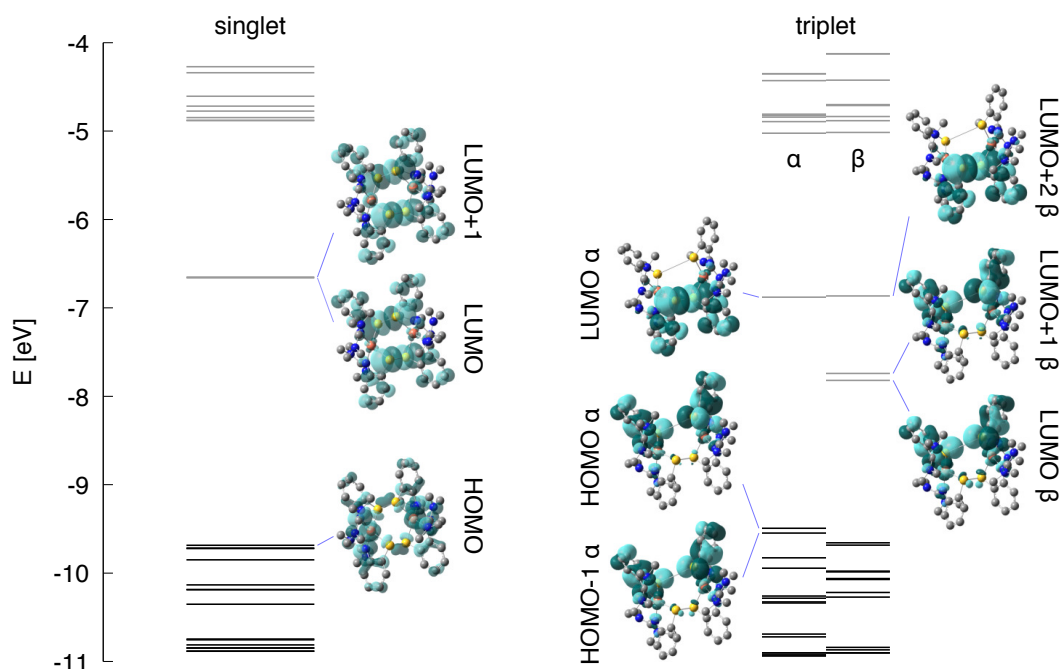


**Figure 5.2:** Molecular orbital spectra of  $S_0$  (left) and  $T_1$  (right) in their equilibrium structures respectively. Occupied states are depicted black, unoccupied – gray. The figure is a courtesy of M. Rohrmüller.

complex has two close-lying LUMO orbitals with strong  $S-p$  contribution that are significantly lower in energy than LUMO+2 and further orbitals. They account for a broad absorption band centered at 415 nm where transitions from HOMO and HOMO- $n$  (with strong Cu  $3d$  contribution) happen to LUMO and LUMO+1. The overall shape of the experimental UV-vis absorption spectrum matches well with the calculation, although the calculated spectrum is shifted to lower energies (Fig. 5.3). The transitions in the UV are ligand-centred, such as  $C=N$   $n \rightarrow \pi^*$  and  $\pi \rightarrow \pi^*$ , as well as  $Cu \rightarrow TMG$  MLCT.

The calculation results confirm that the lowest-lying absorption band for the complex is a MLCT, and in order to drive the charge transfer in pump-probe experiments, the excitation was performed with 343 and 400 nm wavelength photons.

The calculation of the molecular structure was performed with relaxed geometry with  $D_2$  symmetry and the B3LYP potential. The calculated structure matches well with interatomic distances in the ligands, but Cu-N, Cu-S and S-S distances are elongated (see Table 5.1). The calculation done with including the solvent (DFB) resulted in slight shortening of distances (less than 0.01 Å). At the same time including the solvent leads to better match between experiment and theory in the UV part of the absorption spectrum (see Fig. 5.3).

### 5.1.3 Excited states

As a benchmarking study, the calculations of the possible excited state singlet structures (without including spin-orbit coupling) were performed for all significant excitation channels in MLCT range, resulting in thirteen excited state structures. The calculated structures originating from different excitation channels significantly differ from each other geometrically and energetically. All structures have in common a strong S-S bond elongation for one or both S-S bonds because the electron is excited to the antibonding orbital of the disulfide bridge. The relevant bond-distance changes for different singlet excited state structures are gathered in Table 5.2.

With the temporal resolution of the transient synchrotron-based experiments (70-100 ps) we

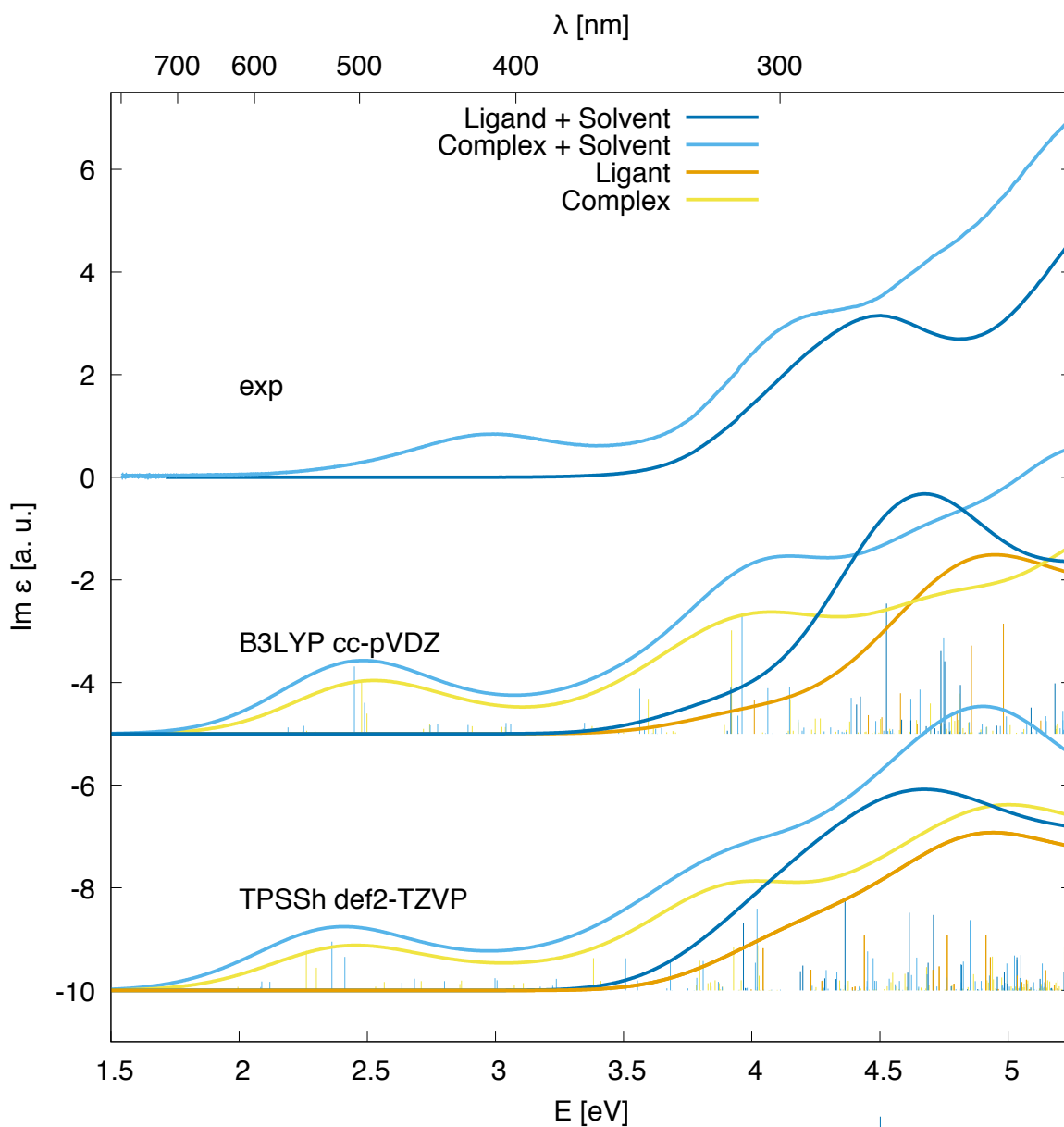


**Figure 5.3:** Comparison of experimental and DFT-calculated UV-vis absorption spectra for  $\text{Cu}_2(\text{NSSN})_2$  and the pure ligand NSSN. The figure is a courtesy of M. Rohrmüller.

**Table 5.1:** Selected bond lengths for  $\text{Cu}_2(\text{NSSN})_2$

Bond	Crystallography, Å	DFT, Å	dR(DFT-cryst.), Å
Cu-N	2.013, 2.013, 2.022, 2.037, av = 2.021	2.101	0.080
Cu-S	2.275, 2.297, 2.280, 2.301, av = 2.288	2.395	0.107
S-S	2.126, 2.137 (free lig.: 2.044), av = 2.132	2.256	0.124
Cu-Cu	3.941	4.321	0.380
S-C	1.764, 1.771, 1.784, 1.794, av = 1.778	1.784	0.006
N- $C_{ph}$	1.364, 1.388, 1.390, 1.400, av = 1.386	1.405	0.019
N- $C_{img}$	1.343, 1.344, 1.348, 1.359, av = 1.349	1.339	-0.010
$C_{ph}$ - $C_{ph}$	1.396, 1.412, 1.412, 1.424, av = 1.411	1.394	0.017

**Table 5.2:** Cu-N and Cu-S bond length changes between excited states (singlet  $S_n$  and lowest triplet  $T_1$ ) and ground state [ $\text{\AA}$ ]. Index  $j$  in  $N^j/S^j$  refers to the ligand number: ligands 1 and 2 coordinate one copper site, ligands 3 and 4 – the other one. The last two columns show changes in the distances between the copper atoms and in two disulfide groups.

ES	$N^1$	$S^1$	$N^2$	$S^2$	$N^3$	$S^3$	$N^4$	$S^4$	Cu-Cu	S-S
$S_1$	-0.01	-0.01	0.01	-0.11	-0.14	-0.06	-0.06	0.33	0.24	0.91, -0.05
$S_2$	-0.15	-0.17	-0.14	-0.17	-0.15	-0.17	-0.15	-0.17	0.59	1.23, 1.24
$S_3$	0.02	-0.07	0.02	-0.07	-0.07	0.03	-0.07	0.03	-0.14	0.34, 0.34
$S_6$	-0.01	-0.03	-0.01	-0.03	-0.01	-0.02	-0.01	-0.02	0.02	0.28, 0.28
$S_7$	-0.05	-0.03	-0.03	0.09	-0.01	-0.08	0.01	0.05	0.42	0.64, -0.02
$S_9$	-0.03	-0.07	-0.03	-0.07	-0.03	-0.07	-0.03	-0.07	0.16	0.52, 0.52
$S_{10}$	-0.04	-0.03	0.00	-0.02	-0.04	-0.03	0.00	-0.02	0.02	0.07, 0.54
$S_{13}$	-0.02	0.03	0.02	-0.10	-0.13	-0.06	-0.08	0.33	0.31	-0.05, 0.84
$S_{15}$	0.00	0.00	0.01	-0.09	-0.14	-0.05	-0.07	0.31	0.25	0.84, -0.05
$S_{16}$	-0.01	-0.08	0.01	0.05	-0.05	-0.03	-0.03	0.09	0.38	-0.01, 0.62
$S_{17}$	-0.04	-0.05	0.09	-0.02	-0.04	-0.05	0.09	-0.02	-0.02	0.56, 0.01
$S_{26}$	0.01	-0.06	0.06	0.01	0.01	-0.06	0.06	0.01	0.03	0.64, 0.01
$S_{38}$	0.03	-0.07	0.03	-0.07	0.03	-0.07	0.03	-0.07	0.14	0.49, 0.49
$T_1$	-0.04	0.03	0.03	-0.13	-0.04	0.03	0.03	-0.13	0.54	2.86, -0.01

expect that we will only observe the complex after it underwent ISC to the triplet state as it normally happens for copper complexes on a faster time-scale ( $< 30$  ps) [ITT07; MFC15; Ber+16]. The orbital spectra of the relaxed triplet  $T_1$  are compared to the singlet  $S_0$  in Fig. 5.2. Single occupation of one antibonding sulfur  $\sigma^*$  leads to the S-S bond breaking (see Fig. 5.4). The other S-S bond is slightly shortened, and there are symmetric changes on both copper atoms. On the side where S-S bond breaks, Cu-S bond shortens and Cu-N bond elongates. On the contrary, for the NSSN ligand for which the S-S bond remains intact, the Cu-S bond elongates and Cu-N bond shortens. In comparison with Cu-bisphenanthroline complexes [Pen+13] quite small flattening of the coordination polyhedron occurs – the angle between ligand chelate planes changes from  $89^\circ$  to  $77^\circ$  on both coppers.

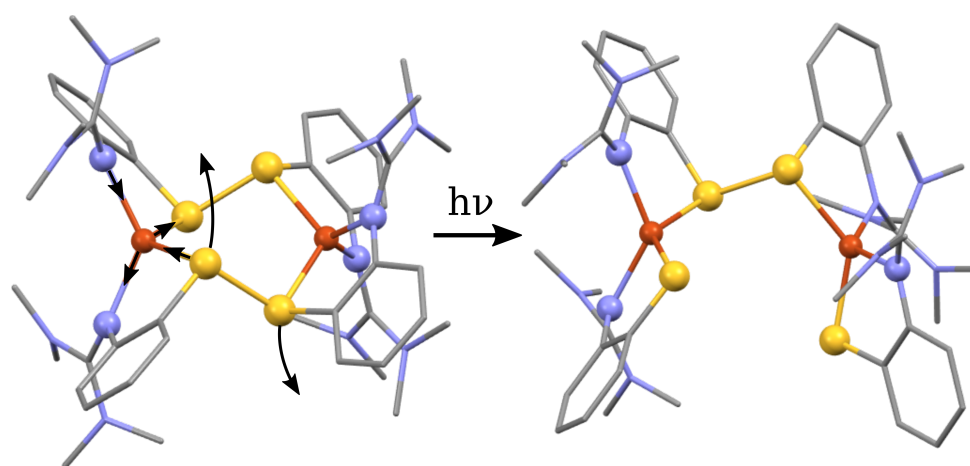


**Figure 5.4:** DFT-calculated ground state and the lowest triplet state. The changes in the triplet state are symmetric on both copper atoms. Hydrogen atoms are omitted for visual clarity.

### 5.1.4 Choosing the solvent

For performing pump-probe experiments with  $\text{Cu}_2(\text{NSSN})_2$  a matching solvent needed to be chosen. After testing different solvents the decisive criteria were found. The solvent has to be:

1. polar (because otherwise the substance will not dissolve);
2. aprotic (because tetramethylguanidine nitrogens are strongly basic, and therefore easily get protonated);
3. non-coordinating (because a coordinating solvent will decompose the complex by exchanging S at Cu);
4. the solvent should allow performing pump-probe experiments in an open jet meaning that it has to be non-hazardous for health, and the boiling temperature is also important.

The behaviour of  $\text{Cu}_2(\text{NSSN})_2$  in all tested solvents is summarised in the Table 5.3.

Aprotic solvents with high donor ability (expressed by donor number (DN), taken from [SSR95]), such as **DMF** (DN = 26.6) or **DMSO** (DN = 29.8), decompose  $\text{Cu}_2(\text{NSSN})_2$  within minutes. Solvents which have acidic protons, such as **methanol** and **isopropanol**, demonstrate the same behaviour. In **acetone** (DN = 17.0) and **butanone** the shape of the absorption spectrum of freshly prepared solution depends on the concentration: upon dilution the spectral weight of the MLCT band diminishes compared to absorption in UV. Absorption spectra also evolve with time: intensity of MLCT decreases within hours and days. The more diluted the solution is, the stronger relative MLCT band decay is. In order to check if this effect is caused by the coordination ability of the C=O group or by acidity of  $\alpha$ -C ( $\text{pK}_a=19-20$ ) the complex was added to **pivalone** (di-tert-butyl ketone), which does not have acidic protons. However it does not dissolve in it.

In **acetonitrile** (DN = 14.1) the MLCT transition band is present, and like with acetone and butanone its relative intensity decreases upon dilution (Fig. 5.5). However the spectral shape does not evolve with time, which means that there is only fast-establishing dynamic equilibrium and no long-term changes in the solution. Probably lower acidity than for ketones ( $\text{pK}_a = 25$ ) and lower DN plays a decisive role here. At the low concentration the complex is mostly dissociated, and the higher the concentration is, the more intact complex is present in the solution. This statement is supported by comparison of EXAFS spectra of the solid complex and its 10 mM solution in  $\text{CH}_3\text{CN}$  (see Fig. 5.15), which shows that the substances in solid and solution are identical.

A class of solvents that matches the necessary chemical criteria (polar, aprotic, non-coordinating) are haloalkanes. Indeed the UV-vis absorption spectra of the complex in **dichloromethane** have the same shape for all investigated concentrations as demonstrated on Fig. 5.6. However DCM evaporates strongly ( $T_b = 40^\circ\text{C}$ ) and is too toxic to be used in an open jet for pump-probe experiments. A less toxic solvent with higher boiling temperature ( $T_b = 92^\circ\text{C}$ ) is **1,2-difluorobenzene** [OTo+89]. The shape of UV-vis absorption spectra in this solvent also does not depend on the concentration.

As a result, the following solvents were chosen for the experiments:

1. acetonitrile (ACN) from Carl Roth, 99.98 %, Ultra LC-MS, for luminescence and transient absorption (TA); from Sigma-Aldrich, anhydrous, 99.8%, for trXAS;
2. dichloromethane (DCM), HPLC grade, non-stabilised, from Carl Roth (stored under inert atmosphere), for luminescence and TA;
3. 1,2-difluorobenzene (DFB), 98 %, from Thermo Fisher Scientific, Acros Organics and ChemPur, for trXAS, transient wide angle X-ray scattering (trWAXS) and trXES.

**Table 5.3:** Behaviour of the complex in different solvents

Solvent	Comments	Complex behaviour
Dichloromethane	non-stabilized, solution prepared both in the air and in the inert atmosphere	stable
1,2-difluorobenzene	98 % purity, solution prepared in air	stable
Acetonitrile	solutions prepared both in air and in the inert atmosphere	MLCT band intensity (relative to absorption in the UV) depends on the concentration, the UV-vis spectrum doesn't change with time
Acetone	HPLC-grade, oxygen-free	quite stable, but MLCT slowly decays within days, and its relative intensity depends on concentration
Butanone	analytical grade, both air-equilibrated and degassed were tested (the solutions were prepared in air)	similar to acetone, but the decay of MLCT is more pronounced
Tetrahydrofurane	HPLC-grade, solution prepared in the inert atmosphere	MLCT disappears within hours
Dimethylsulfoxyde, dimethylformamide, isopropanol, methanol	solutions prepared in air	MLCT disappears within minutes
Ethylacetate		hardly dissolves
Di(t-butyl)ketone	does not have acidic protons	does not dissolve
Water, diethylether, cyclohexane		does not dissolve

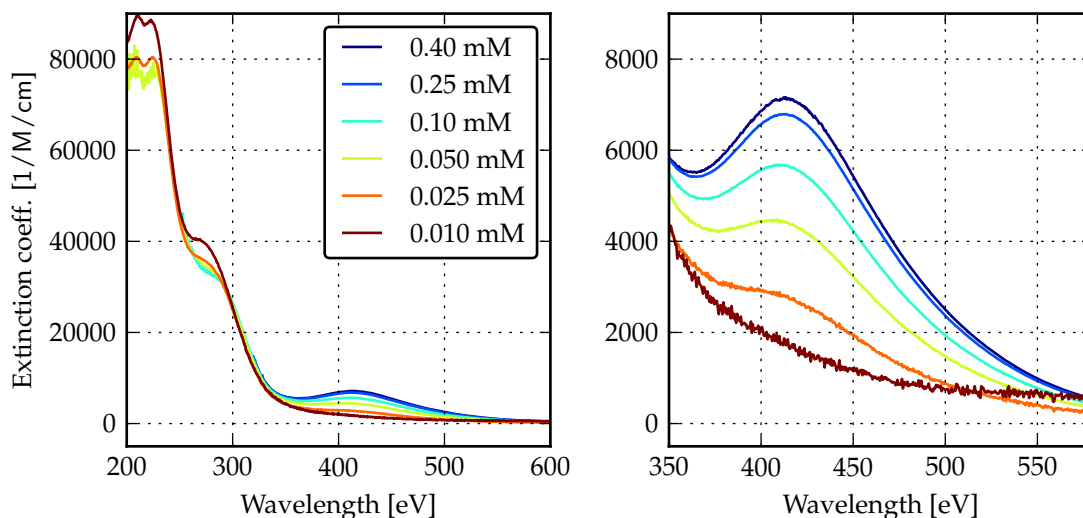


**Figure 5.5:** Absorption spectra of  $\text{Cu}_2(\text{NSSN})_2$  in  $\text{CH}_3\text{CN}$  for different concentrations. The extinction coefficients are calculated by dividing measured optical density by the concentration of the complex. Upon dilution the absorption band at 415 nm disappears, at the same time absorption in the UV increases. The right figure shows zoom into the MLCT region.

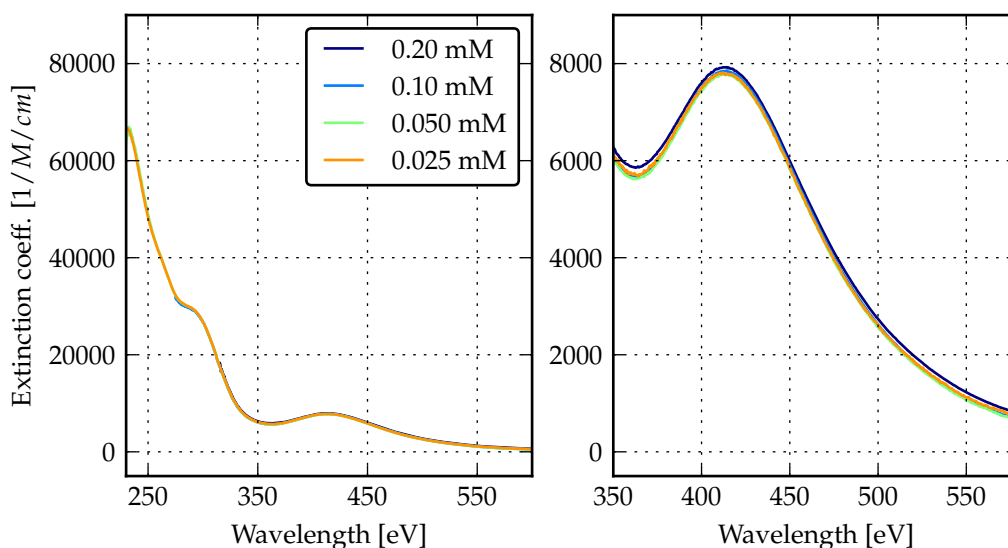


**Figure 5.6:** Absorption spectra of  $\text{Cu}_2(\text{NSSN})_2$  in  $\text{CH}_2\text{Cl}_2$  for different concentrations (recalculated into the extinction coefficients). The concentration does not have effect on the spectra shape. The right figure shows zoom into the MLCT region.

Experiments in ACN were carried out with the highest concentration possible for the particular experimental conditions. All solvents were used as purchased.

### 5.1.5 Photostability of the complex

A special attention should be given to photostability of the complex. Pump-probe techniques use powerful laser pulses that aim to transfer a significant part of the molecules into the excited state, which can result in the fast accumulation of photoproducts in the solution.

The stability of the complex during measurements was checked by comparing UV-vis spectra before and after experiments. For XAS the stability of the system could also be monitored by comparing the shape of the X-ray absorption edge from different scans. For the measurements with low pulse energies (nJ), such as were used for the luminescence measurements, the complex is stable in all three used solvents at excitation wavelengths 365, 375, 400 and 410 nm. Illumination with 300 nm caused radiation damage in the DFB solution. Laser excitation with  $\mu\text{J}$  pulses in pump-probe measurements with 343 and 400 nm wavelengths does not cause radiation damage of the complex in ACN. However, DFB solutions show radiation damage: both laser pulses and X-rays caused bleach of the MLCT transition accompanied by increase of absorption in the UV. In the XAS spectra it manifested itself as decrease in the intensity of the edge peak at 8985.5 eV and by changes in the pseudo radial distribution function  $\chi(R)$ . This radiation damage does not result in new absorption bands in the visible range – on the contrary, the visible MLCT band is bleached, and new absorption bands appear in the UV range. Since the photoproducts do not absorb in the visible range, they should not contribute to transient signals in any experiment.

## 5.2 Transient UV-vis absorption spectroscopy

In order to get a better insight into the ultrafast processes in the photoexcited complex, femtosecond transient absorption experiments were carried out upon excitation at 400 nm, as reported in this section.

### 5.2.1 Experiment description

The experiments were performed in ELI-beamlines laser facility in Dolní Břežany, Czech Republic, together with Dr. Mateusz Rebarz. The TA setup was based on an amplified Ti:sapphire laser (Astrella, Coherent). The oscillator (Vitara, Coherent) was pumped by a 5 W CW semiconductor laser (Verdi, Coherent) and delivered ultrashort pulses ( $<35$  fs) with energy of 25 nJ at repetition rate of 80 MHz and wavelengths of 800 nm. These pulses were amplified in a regenerative amplifier (Astrella, Coherent) pumped by a 38 W, 1 kHz intracavity frequency-doubled Nd:YLF laser (Revolution, Coherent). The final output delivered pulses characterised by 33 fs duration at 800 nm wavelength with total energy 6.5 mJ/pulse at 1 kHz repetition rate. The majority of the output energy of the fundamental beam was frequency doubled by the second harmonic generation (SHG) in a 0.3 mm thick barium betaborate (BBO) crystal in order to generate pump pulses at 400 nm wavelength. The pump pulses at the sample position had total energy about 2.5  $\mu$ J and a diameter about 0.4 mm. The remaining energy (a few  $\mu$ J) of the fundamental beam was used to generate a white light continuum, which served as the probe beam, by focusing on a 2 mm thick CaF<sub>2</sub> rotating plate. The white light continuum pulses were characterised by a broad spectral range of 340 - 750 nm. In order to prevent distortions in kinetics due to the rotational depolarisation effect [Lak06], the pump-probe polarisation was set at the magic angle (54.7°). The probe pulses were delayed in time relative to the pump pulse using an optical delay line (M-IMS1000LM Linear Stage, Newport). The probe and pump beams were focused and overlapped on the quartz sample cell with 1 mm path length. In order to protect the sample from the remaining fundamental beam with 800 nm wavelength, a solution of a dye absorbing at wavelengths longer than 670 nm was used as a filter. The transmitted light of the probe was focused onto the entrance slit of a prism spectrograph and recorded by charge-coupled device (CCD) camera (HA S7030-1006, 1024 x 64 px, Hamamatsu). The shot to shot readout of CCD camera was synchronised with the laser amplifier by an electronic system (Entwicklungsbuero Stresing) and pump on/off cycles were obtained by the chopper placed in the pump beam working at 500 Hz and synchronised with the laser amplifier. All the pump off and pump on recorded spectra were transferred to the computer via PCI interface and the transient absorption spectra were computed. The data from all the scans were averaged. For the background removal the average value from two first spectra (-100 and -50 ps) was subtracted from all the spectra.

The transient spectra were recorded in the spectral range 350 – 670 nm and timescale 0 – 1 ns for solutions of Cu<sub>2</sub>(NSSN)<sub>2</sub>(PF<sub>6</sub>)<sub>2</sub> and Cu<sub>2</sub>(NSSN)<sub>2</sub>(OTf)<sub>2</sub> in 1,2-difluorobenzene (DFB), acetonitrile (ACN) and dichloromethane (DCM). The samples were dissolved at a concentration of 4 – 6 · 10<sup>-4</sup> M corresponding to optical density (OD) of ~ 0.4 – 0.6 at the pump wavelength in a 1 mm cuvette. UV-vis spectra of the solutions were registered before and after the measurements to control the stability of the samples. The solution of Cu<sub>2</sub>(NSSN)<sub>2</sub>(OTf)<sub>2</sub> in DFB, used for initial alignment, demonstrated significant radiation damage (reduction of intensity of the absorption band at 410 nm by half), therefore the incident pump energy for the measurements was reduced to 2.5  $\mu$ J. Further measurements were performed with this pulse energy, and UV-vis absorption spectra for Cu<sub>2</sub>(NSSN)<sub>2</sub>(PF<sub>6</sub>)<sub>2</sub> before and after the measurements are shown in Fig. 5.7. The ACN solution does not demonstrate any changes after the experiment; the radiation damage in DFB and DCM solutions is negligible.

Due to dispersion of light going through any material, the red part of the white light continuum, which was used as a probe, propagates faster than the blue. Several sources of this

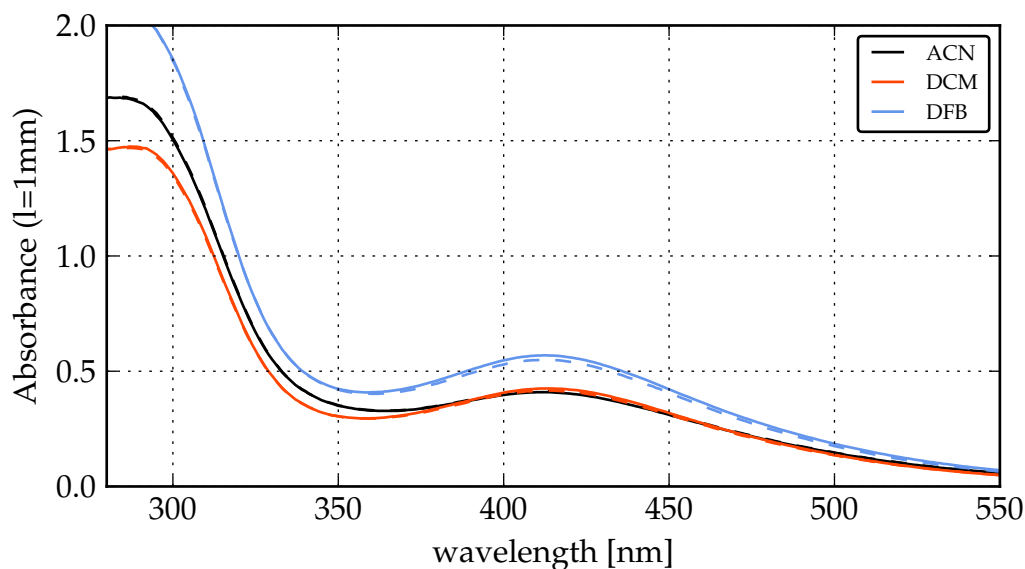


**Figure 5.7:** UV-vis absorption spectra of  $\text{Cu}_2(\text{NSSN})_2(\text{PF}_6)_2$  before and after the measurements in different solvents. Solid line: before the measurements, dashed line: after.

dispersion in the beam path include the  $\text{CaF}_2$  plate, which creates the continuum, several filters, and the quartz cell of the cuvette. All these materials introduce the group velocity dispersion (GVD) effect. As a result, the real time-offset is different for different wavelengths and the registered spectra are not correct. Thus, every kinetic trace had to be shifted to obtain the equivalent timescale for all the wavelengths. The GVD effect was estimated from pure solvent measurements. When light pulses propagate through the solvent, the transient absorption spectra demonstrate positive and negative bands which originate from two photon absorption (pump + probe) and/or Raman scattering. Taking the positions of the corresponding peaks for several different wavelengths, time delay as a function of wavelength was obtained. The time delays were then adjusted for all wavelengths to the same value of  $t_0$ .

## 5.2.2 Spectral evolution

Among several measured samples the dataset for the solution of  $\text{Cu}_2(\text{NSSN})_2(\text{PF}_6)_2$  in DFB (shown in Fig. 5.8 and top left in Fig. 5.10) was chosen for the detailed analysis due to the best signal to noise (S/N) ratio. This dataset was obtained as the average value of 16 scans and is representative for the whole series. Other sample solutions were measured in sets of 3 scans for comparison and they exhibit very strong similarities. The evolution of the studied spectra can be roughly divided into four distinct steps.

In **step 1** the transient spectrum is created upon photoabsorption. Judging by DFT calculations and the experimental ground state absorption spectrum of the studied complex (Fig. 5.7), the excitation at 400 nm corresponds to one of the higher singlet excited states  $S_n$ . The absorption tail goes up to  $\sim 600$  nm, and excitation to  $S_1$  should be located at longer wavelengths. A femtosecond pulse excitation leads to the formation of a spectrum composed of three characteristic bands. Directly after the photoexcitation the spectra are distorted by solvent effects, and at 0.45 ps the first clear spectrum is observed as shown in Fig. 5.8A. The region around the pump wavelength of 400 nm is removed from the spectrum because the data in this region are obscured by the strong scattering of the pump. A strong negative band appears around 430 nm, which is the region of the ground state  $^1\text{MLCT}$  absorption as shown in Fig. 5.7. This effect is called ground state bleaching (GSB). In principle, GSB should be a mirror view

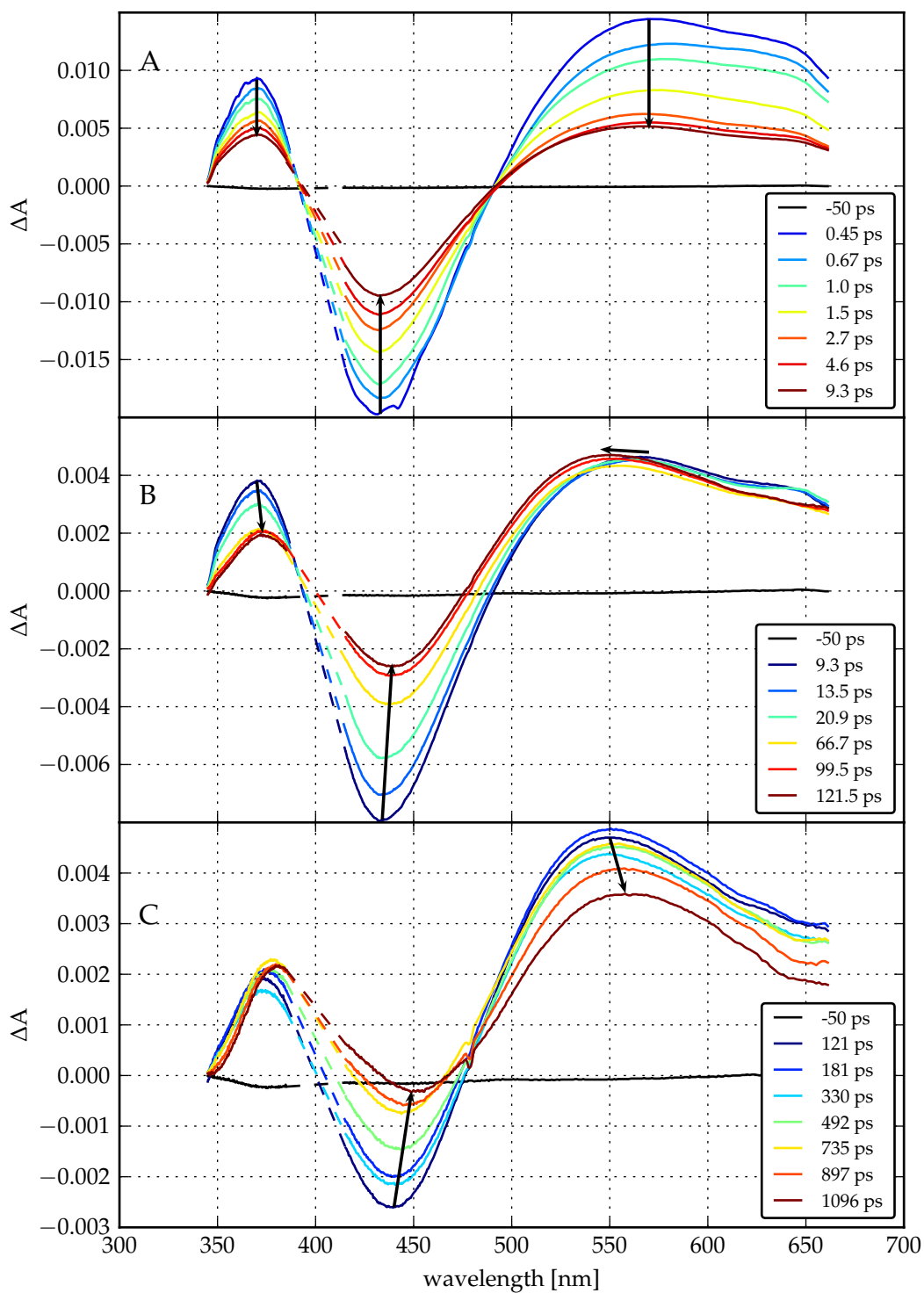


**Figure 5.8:** Transient absorption spectra of  $\text{Cu}(\text{NSSN})_2(\text{PF}_6)_2$  in DFB recorded at different time delays after femtosecond excitation at 400 nm. Dashed lines connect two parts of spectra separated by strong signal of the laser pump beam.

of the ground state absorption, but can be superimposed with broad positive ES absorption bands. As a consequence, the negative ground state (GS) band (430 nm) is slightly shifted in comparison to the GS absorption (410 – 420 nm).

Another negative band which can appear in a transient spectrum is stimulated emission (SE). If emission is very weak such a band can be completely obscured by the positive ES absorption. In addition, the emission from the initially excited state can be only slightly redshifted from the absorption (small Stokes shift), so such band can be merged with the GS band. However, no emission was detected in the steady state luminescence experiment. It should be mentioned that  $\text{Cu}_2(\text{NSSN})_2$  can demonstrate femtosecond emission, but a time-resolved fluorescence experiment such as fluorescence up-conversion would be necessary to detect such a weak and ultrashort emission. Even if  $\text{Cu}_2(\text{NSSN})_2$  shows such emission, it is not clearly manifested in the transient absorption spectra. The positive band with maximum at 370 nm as well as featureless broad absorption extending above 500 nm are ascribed to excited states absorption (ESA).

**Table 5.4:** Time constants obtained by global fit analysis of transient absorption spectra for  $\text{Cu}_2(\text{NSSN})_2$  with  $\text{PF}_6$  and OTf counter ions in different solvents.

Solvent	Counter-anion	$\tau_1$ / ps	$\tau_2$ / ps
DFB	$\text{PF}_6$	$0.65 \pm 0.03$	$10.6 \pm 1.8$
	OTf	$0.70 \pm 0.09$	$12.5 \pm 3.1$
ACN	$\text{PF}_6$	$0.53 \pm 0.06$	$7.9 \pm 1.0$
	OTf	$0.61 \pm 0.05$	$11.1 \pm 1.8$
DCM	$\text{PF}_6$	$0.47 \pm 0.11$	$7.4 \pm 2.1$
	OTf	$0.94 \pm 0.21$	$12.7 \pm 5.0$

In **step 2** decay of all bands and especially strong recovery of the GS band are observed. During first few picoseconds all the bands decrease simultaneously (Fig. 5.8A) by about 60 % in intensity without significant shifts and shape variations revealing ultrafast deexcitation to the ground state with time constant of about 650 fs (see the kinetic analysis below). This process can be radiative (fluorescence) or non-radiative (internal conversion). It shows that the conformation in the higher excited singlet states reveals strong vibronic coupling with the ground state of the complex.

In **step 3** (see Fig. 5.8B) we observe further recovery with a weak red shift of the GS band, accompanied by the blueshift of the broad ES band. Thus a decay of GS band can be caused (at least partially) by the increasing overlap with strong positive ES band. The time constant of about 10 ps, corresponding to this decay, points to ISC to the triplet  $^3\text{MLCT}$  state, as ISC in various homoleptic and heteroleptic copper complexes was found to happen within 2 – 30 ps [Sid+03; ITT07; Iwa+11; San+14; Dic+17].

In **step 4** further spectral evolution exhibits a redshift of all bands and decrease of intensity with time constant  $>100$  ps. This step can be ascribed to the beginning of further structural changes in the triplet state and radiationless decay to the ground state. The limited accuracy for this decay time constant is due to the limited pump-probe time delay ( $\sim 1$  ns) accessible in our experiments which cannot be extended to the whole kinetics. This slower process was further observed in transient XAS and WAXS experiments.

This spectral discussion was done for the solution of  $\text{Cu}_2(\text{NSSN})_2(\text{PF}_6)_2$  in DFB. Other investigated solutions in DFB, DCM and ACN demonstrate similar behaviour.

Apart from IC and ISC, vibrational relaxation (VR) in the excited state and ground states can contribute to the observed signal. This phenomenon can take place in quite wide timescale (100 fs to 100 ps) depending on the complex structure and on the solvent. For TM complexes IC, VR and rearrangement of the solvation sphere are typically convoluted and only the average time constant for all these processes is observed [Vlč00]. For many TM complexes ultrafast ISC

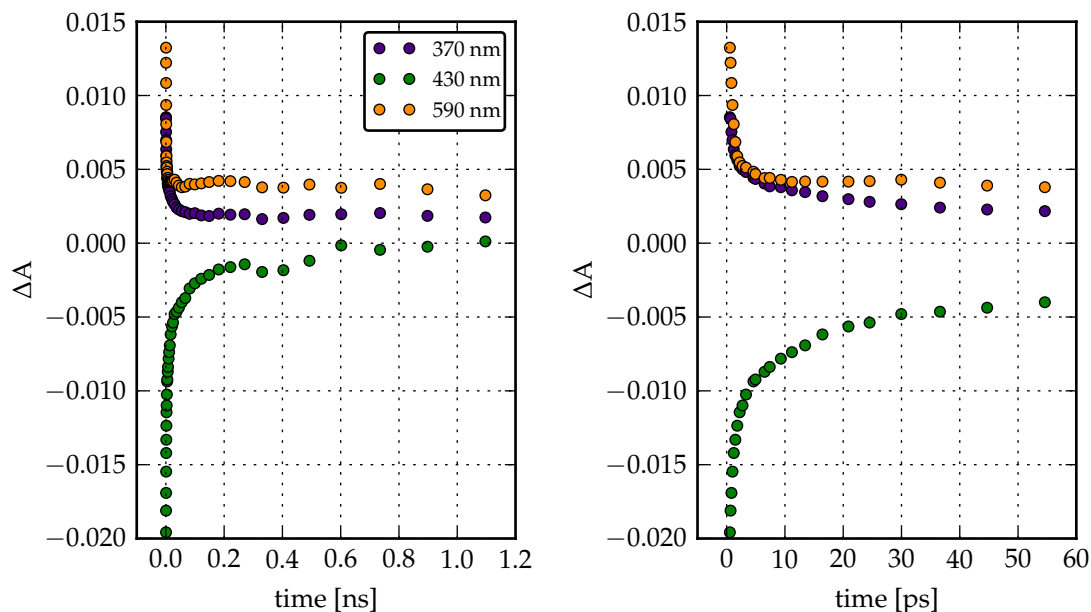


**Figure 5.9:** Transient absorption kinetics of  $\text{Cu}_2(\text{NSSN})_2(\text{PF}_6)_2$  in DFB probed at 370, 430 and 590 nm. The right plot zooms into shorter time scale.

takes place on the timescale below 1 ps, as for  $\text{Ru}(\text{bpy})_3$  [Dam97], but for copper compounds this process was found to happen on a significantly longer time scale [MFC15]. In order to disentangle the individual ultrafast processes the set of additional purposeful experiments would have to be done. To distinguish VR from other processes a fs-ps pump-probe IR experiment can be performed as demonstrated in [Dic+17]. Alternatively vibrational populations can be accessed by means of time-resolved Raman spectroscopy [Miz97]. On the other hand, ascribing the observed 10 ps process as ISC could be supported by further monitoring the populated state in a ns TA experiment performed on a degassed and an oxygenated solution. Oxygen serves as an efficient triplet excited state quencher and therefore should accelerate the decay of the triplet state [Lak06]. However, such an effect is clearly pronounced only with lifetimes of at least several tens of ns (exceeding characteristic diffusion times), and the pump-probe X-ray measurements on  $\text{Cu}_2(\text{NSSN})_2$  demonstrated decay times on the order of 1 – 2 ns (see sections 5.3 and 5.4), what indicates the presence of faster quenching mechanisms.

### 5.2.3 Kinetic analysis

Several kinetic traces at wavelengths corresponding to GSB and ESA spectral features are shown in Fig. 5.9. The real time resolution of the experiment is determined by the cross correlation of the pump and probe pulses at the sample. The Raman scattering or two photon absorption in the solvent exists only as long as pump and probe pulses overlap. For a kinetic trace at 485 nm only a positive signal was observed in the transient spectrum. It was fitted with the Gaussian function, and FWHM was found to be 116 fs. This is the real time resolution of the experiment. In order to analyse kinetics at time scales close to the time resolution, the decay function has to be convolved with this cross-correlation function. However, in our case strong and irregular signal from the solvents obscure the sample signal in the first  $\sim 0.5$  ps after the excitation. We have not analysed this time interval further and only took into account the data at time delays longer than 450 fs. Thus a simple multiexponential model could be used for fitting kinetic traces.

In order to get reliable time constants the global fitting procedure was applied. In this approach kinetic traces at selected wavelengths were fitted with several global decay constants.

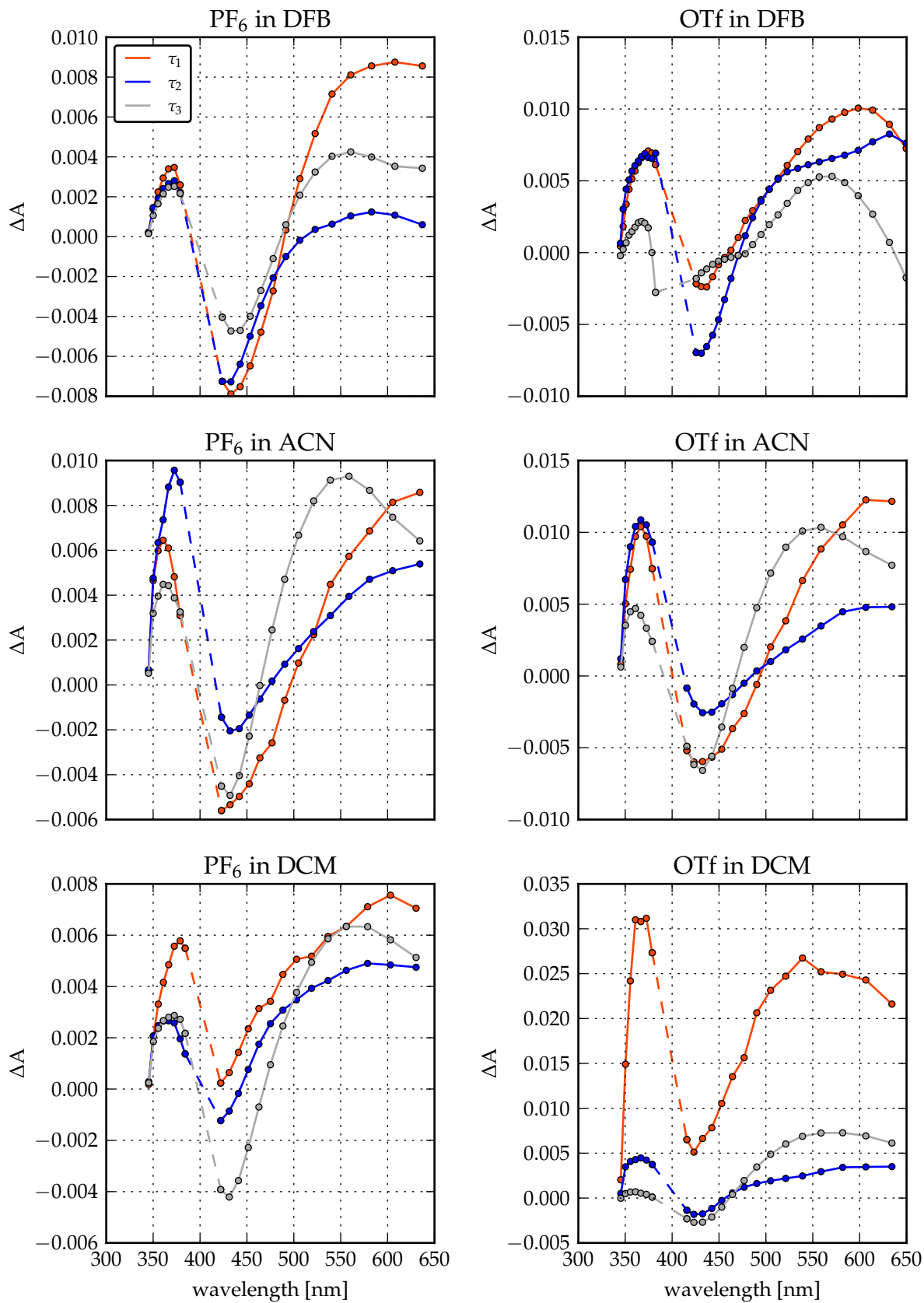


**Figure 5.10:** Decay associated spectra from transient absorption of  $\text{Cu}_2(\text{NSSN})_2(\text{PF}_6)_2$  and  $\text{Cu}_2(\text{NSSN})_2(\text{OTf})_2$  in DFB, ACN and DCM obtained by global fit analysis with multi-exponential functions. Time constants are given in Table 5.4.

The analysis revealed the existence of three steps (steps 2 – 4, as discussed before) characterised by three different time constants, which for all experimental solutions are gathered in Table 5.4. The decay-associated spectra extracted from the global fit are shown in Fig. 5.10. These differential spectra have similar shapes for all decay components, expressed in GSB and ESA.

#### 5.2.4 Summary

The transient absorption in UV-vis gave us an insight into the evolution of photoexcited  $\text{Cu}_2(\text{NSSN})_2$  with 120 fs resolution. Solutions of  $\text{Cu}_2(\text{NSSN})_2$  with  $\text{OTf}^-$  and  $\text{PF}_6^-$  counter anions in ACN, DCM and DFB could all be globally fitted with three exponential decays. Two fast decay processes demonstrate similar time constants for all solvents and were assigned as IC to the ground state and ISC to  $^3\text{MLCT}$ . The much slower third time constant could not be precisely determined with the existing delay line and corresponds to non-radiative ISC from  $^3\text{MLCT}$  back to the ground state. This longer timescale is further investigated in pump-probe X-ray experiments as reported in sections 5.3 and 5.4. To the best of our knowledge, the results presented in this chapter provide the first femtosecond time-resolved study on the dinuclear copper complexes.

## 5.3 Transient X-ray absorption spectroscopy

This section will discuss the analysis of the data collected in steady-state and picosecond transient X-ray absorption spectroscopy experiments.

### 5.3.1 Experiment description

#### Steady state measurements

The Cu K-edge X-ray absorption spectrum of the solid  $\text{Cu}_2(\text{NSSN})_2(\text{OTf})_2$  was measured by the group of Prof. M. Bauer, Paderborn University. The spectrum was measured at ANKA synchrotron in Karlsruhe, Germany. The sample was mixed with boron nitride and measured in transmission mode simultaneously with a copper foil as a reference. Three scans were acquired and merged.

The Cu K-edge X-ray absorption spectrum of the 10 mM solution of  $\text{Cu}_2(\text{NSSN})_2(\text{OTf})_2$  in ACN was measured at beamline BM23 of ESRF synchrotron in Grenoble, France together with the group of Prof. M. Bauer. The X-ray beam was monochromatised by a Si(111) double-crystal monochromator. The sample was measured in fluorescence mode with a 13 pixel Ge detector from Canberra. Two scans were acquired and merged. The energy calibration was performed by setting the maximum of the first derivative of the reference spectra to 8979.0 eV.

#### Pump-probe time-resolved measurements

Transient X-ray absorption measurements were performed at beamline P11 of Petra III synchrotron, Hamburg, Germany, in the course of three experiments. The measurement in ACN in January 2014 was performed with the setup as described in [Sch13; Dic13; Gör14] in single photon counting mode (limited to  $10^4$  ph/s). This measurement mode allowed us to see transient XANES, but in the EXAFS energy range no oscillations could be observed. Afterwards the setup was upgraded as reported in [Goe+16]. The scheme of the setup is shown in Fig. 5.11. In the course of the upgrade the detection in single photon counting mode was changed to integrating mode (possible count rates  $> 10^8$  ph/s). The description of the upgraded setup is given below, and particular parameters of each experiment are provided in Table 5.5.

**Table 5.5:** Experimental details of transient XAS experiments.

date	Sample, concentration, solvent	jet parameters	Laser pulse energy
Jan'14	10 mM $\text{Cu}_2(\text{NSSN})_2(\text{PF}_6)_2$ in ACN	cylindrical, 300 $\mu\text{m}$	7.1 $\mu\text{J}$
Oct'15	5 mM $\text{Cu}_2(\text{NSSN})_2(\text{PF}_6)_2$ in ACN	cylindrical, 300 $\mu\text{m}$	3.0 $\mu\text{J}$
Jun'16	5 mM $\text{Cu}_2(\text{NSSN})_2(\text{OTf})_2$ in DFB	flat, 100 $\mu\text{m}$	0.6 $\mu\text{J}$

Pump-probe experiments were performed with 40 bunch mode of Petra III, which delivers a 70-100 ps X-ray pulse every 192 ns. The X-ray beam for the experiment is monochromatised with a Si(111) crystal (energy resolution  $dE/E = 1.3\text{E-}4$ ). The beam is further focused by a Kirkpatrick-Baez (KB) mirror system. The XAS setup is installed directly behind the KB-system at a distance of 72.3 m from the source. The X-ray spot size on the sample position is on the order of 10  $\mu\text{m}$ . The X-ray beam first passes through a silicon photodiode to register the incident flux  $I_0$  and further through a small aperture in the middle of an on-axis microscope before interacting with the sample. The sample is delivered by a liquid jet system, which is mounted on a translational motor stage. For X-ray fluorescence detection two avalanche photodiodes (APDs [Bar+06]) from FMB Oxford (APD001 model) are mounted at an angle of ninety degrees with respect to the incident beam. The pump laser pulses are guided to the sample by a set of mirrors (M) and focused by a lens located ca. 200 mm in front of the sample position. In addition

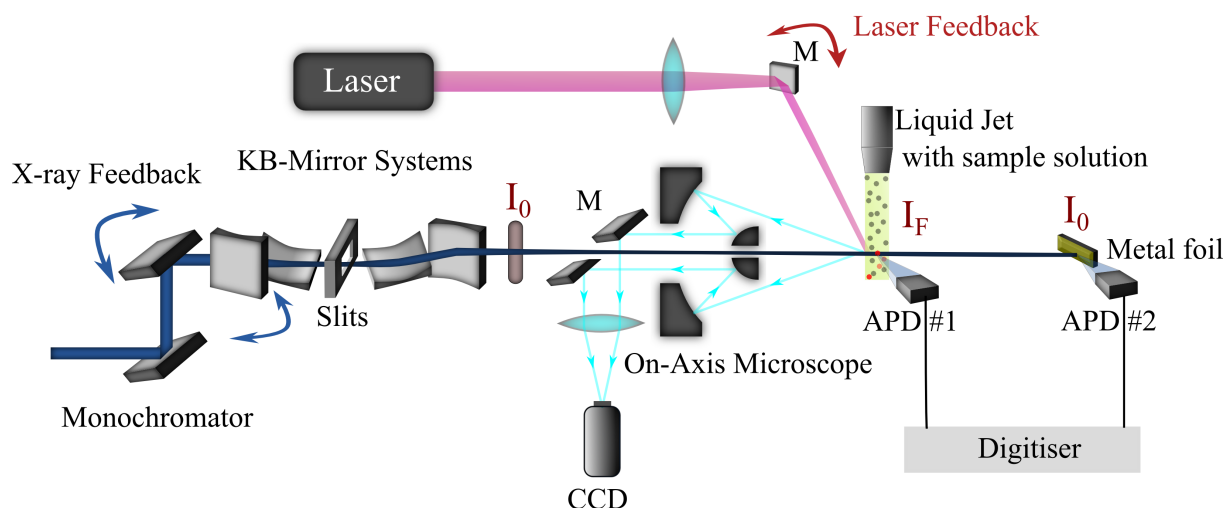


**Figure 5.11:** A scheme of the pump-probe X-ray absorption spectroscopy setup at beamline P11 of Petra III. Modified from [Goe+16].

to monitoring the incident beam intensity  $I_0$  the normalisation is performed by measuring scattering from a metal foil placed several cm behind the jet. This way the same X-ray bunch is used for the data collection and for the normalisation, which allows to reduce the noise coming from different intensities of different bunches. APDs can be covered with Mo conical shieldings with 1 mm opening in order to decrease the contribution of elastically scattered X-rays. The voltage signals from the APDs are fed into a fast digitiser (model ADQ412AC, 12 bit, 2/4GS) from SP Devices for processing. The corresponding firmware and software has been developed by the EuropeanXFEL (Advanced Electronics Group, Control & Analysis Software Group, and the FXE Group) [Bri+16]. For the excitation of the sample a femtosecond pulsed PHAROS laser system from Light Conversion is used. The laser is based on a Yb:KGW crystal which generates light with 1030 nm wavelength. Further harmonics can be generated producing light at 515, 343 and 257 nm. In this work the excitation was performed with 343 nm light pulses. The laser oscillator is synchronised to the master frequency of the synchrotron (500 MHz reference radio frequency). The laser amplifier operates with 65 KHz frequency which corresponds to half of the Petra III round trip frequency (130 KHz). The pump laser beam and the probe X-ray beam are spatially overlapped on the liquid jet with the sample solution.

With this upgraded setup the measurements on 5 mM solution of  $\text{Cu}_2(\text{NSSN})_2(\text{OTf})_2$  in ACN in October 2015 were performed. Transient EXAFS data were acquired that are analysed in the following subsections. In June 2016 transient XAS measurements were performed on the solution of  $\text{Cu}_2(\text{NSSN})_2(\text{OTf})_2$  in DFB. In order to be able to perform the measurements, the laser power on the jet had to be reduced by one order of magnitude compared to the power used in the first ACN measurement. It probably accounts for smaller focal spot of the laser and therefore higher energy density on the sample in case of the DFB solution. The transient data in this set have much higher noise level compared to the measurements in ACN as shown in Fig. 5.19. A possible reason for it could be radiation damage of  $\text{Cu}_2(\text{NSSN})_2$  in DFB.

### 5.3.2 Estimation of excited state fraction in the laser-illuminated volume

In order to assure that the pump-probe measurements reported below are performed in the linear regime (no multiphoton excitations) one has to compare the number of photons in a laser pulse and the number of molecules in the illuminated volume. In order to be safely in the linear regime, the number of photons in the illuminated volume  $N_{ph}$  should be significantly less than the number of molecules  $N_{mol}$ . As a rule of thumb the condition  $N_{ph} < 10 \cdot N_{mol}$  can be used.

The number of photons in a laser pulse can be calculated as

$$N_{ph} = E_{pulse} / E_{ph}, \quad (5.1)$$

where  $E_{pulse}$  is the total pulse energy and  $E_{ph}$  is the energy of one photon. For trXAS of  $\text{Cu}_2(\text{NSSN})_2$  in ACN, which is analysed in the following sections, the laser power measured before the jet was 200 mW, and the laser frequency was 65 KHz, which results in  $E_{pulse} = 3.1 \mu\text{J}$ . The energy of a photon with  $\lambda = 343 \text{ nm}$  expressed in Joules equals  $5.8 \cdot 10^{-19} \text{ J}$ . This gives number of photons per laser pulse  $N_{ph} \approx 5.3 \cdot 10^{12}$ .

The number of molecules in the illuminated volume  $V$  can be found as

$$N_{mol} = N_A \cdot v = N_A \cdot c \cdot V, \quad (5.2)$$

where  $N_A$  is the Avogadro number ( $6.02 \cdot 10^{23} \text{ mol}^{-1}$ ) and  $c$  is concentration. The size of the laser spot on the jet was set to be approximately equal to the jet diameter ( $300 \mu\text{m}$ ). For the calculation we assume that the diameter of the laser spot was in the range of  $100 \mu\text{m} < d < 300 \mu\text{m}$ . For a cylindrical jet and a cylindrical beam the illuminated volume can be approximated as common volume of two circular cylinders with the jet radius  $R$  and beam radius  $r$  with their axes intersecting at right angles. For  $R = r$  the common volume equals  $V = 16/3R^3$ ; for  $r = 1/3R$   $V = 0.6747R^3$  [Hub65]. This estimations gives the number of molecules in the illuminated volume as  $6.9 \cdot 10^{12} < N_{mol} < 54.2 \cdot 10^{12}$ .

In order to calculate the absorption of the laser beam by a cylindrical jet one would have to integrate over all penetration thicknesses of the beam through the jet. However, as an approximation it can be assumed that the laser beam travels through a flat (rectangular) jet of the same cross-section as the cylindrical jet. It would then have a thickness  $h = \pi R^2 / 2R = 236 \mu\text{m}$ . According to the Lambert-Beer law the transmitted light intensity is  $I = I_0 \cdot 10^{-OD}$ , where  $OD = \epsilon ch$  is optical density, or absorbance<sup>1</sup>. With the extinction coefficient  $\epsilon = 10^4 \text{ M}^{-1} \text{ cm}^{-1}$ , concentration  $c = 5 \text{ mM}$  and  $h = 236 \mu\text{m}$ ,  $OD = 1.18$ , and  $I/I_0 = 0.066$ . It means that 93.4% of photons, or  $5.0 \cdot 10^{12}$  out of  $5.3 \cdot 10^{12}$ , are absorbed in the jet. This calculation shows that for the laser spot size on the jet of  $\sim 300 \mu\text{m}$ , the  $N_{ph}^{abs} \approx 0.1 \cdot N_{mol}$  (the excited state fraction in the laser-illuminated volume is appr. 10%), which satisfies the linear regime condition.

### 5.3.3 Ground state EXAFS

For the analysis of the transient EXAFS data first the steady state EXAFS spectrum had to be analysed. The non-structural fitting parameters obtained from the ground state fit were further used for modelling of the EXAFS of the excited state.

Several fitting approaches were pursued in order to assure reliable results:

- EXAFS data (solid OTf<sup>-</sup> and 10 mM acetonitrile solution) were analysed using Athena and Artemis [RN05] software packages, the fitting was performed with the D<sub>2</sub>-symmetric DFT structure as a model, varying structural parameters. The aim was to obtain a D<sub>2</sub>-symmetric structure with the interatomic distances matching the EXAFS data. DFT bond lengths Cu-N and Cu-S are appr. 10% longer than the crystallographic values from an X-ray diffraction (XRD) experiment, and EXAFS fit confirms the crystallographic structure. The DFT model was modified according to the fit results, however, a lot of manual changes in the molecule were required for that, and it was not possible to discriminate between some models with structural differences in shells further than 3 Å. Due to these uncertainties the preference was given to the crystallographic structure as the model. Although it is not strictly symmetric, it is a structure obtained from a high precision experiment. The EXAFS

<sup>1</sup>In UV-vis spectroscopy it is conventional that the extinction coefficient is calculated for the decimal base, and not the exponential.

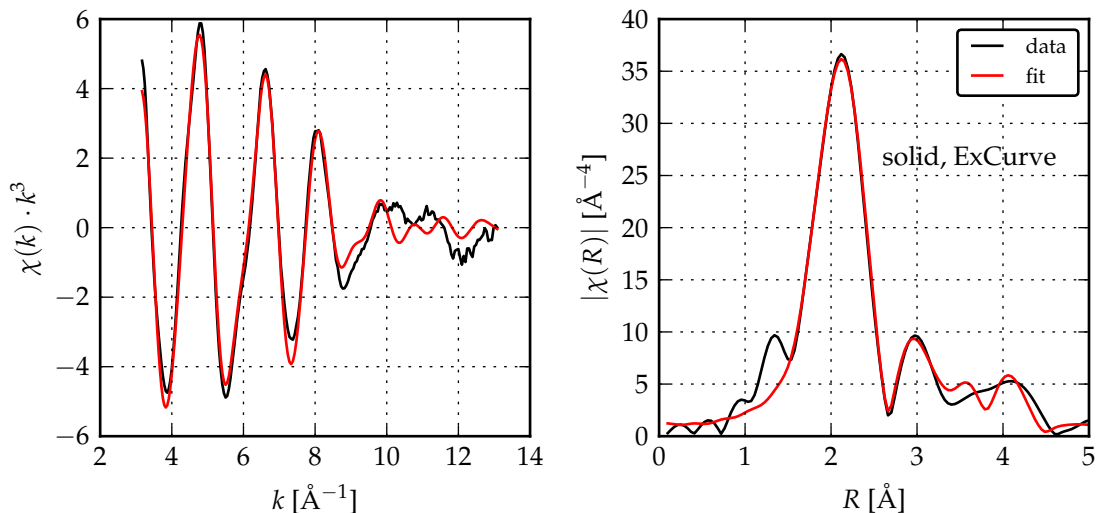


**Figure 5.12:** Fit of EXAFS of solid  $\text{Cu}_2(\text{NSSN})_2(\text{OTf})_2$  performed with ExCurve. N, S, C, S, Cu shells were included; number of atoms, distances to shells and  $\sigma^2$  were fitted.

data could be adequately fitted with the crystallographic model without fitting structural parameters as presented below.

- EXAFS data (solid  $\text{OTf}^-$  and 10 mM acetonitrile solution) were analysed using ExCurve [Bin98] software. Scattering atoms were added shell by shell, and their number, distance to the absorber and  $\sigma^2$  were fitted. Five shells were included: N, S, C, S, Cu. Since there was no 3D model, only single scattering paths were considered.  $C_{\text{TMG}}$  and  $N_{\text{TMG}}$  were not considered in the fit, because they could not be fitted with reasonable parameters. The fitting was performed together with Roland Schoch from the group of Prof. Matthias Bauer, Paderborn university. The results are presented in Fig. 5.12 and 5.13, and the parameters are gathered in Table 5.6.
- EXAFS data (solid  $\text{OTf}^-$ ) were analysed with Athena and Artemis [RN05]. The same shells were included into the fit as in ExCurve (N,S,C,S,Cu). Crystallographic structure was used as a model, structural parameters were fitted. Using the 3D model allowed to additionally include multiple scattering paths. The results are shown in Fig. 5.14, and the parameters are given in Table 5.6.

Athena and ExCurve both yield similar results that confirm the crystallographic structure. The distances to the coordinating atoms (N and S) match within errorbars for two software packages; for further shells there are some discrepancies due to contribution of multiple scattering paths taken into account in the Artemis fit.

- Finally, EXAFS data (solid  $\text{OTf}^-$ ) were analysed with Athena and Artemis [RN05], using the crystallographic structure as a model without varying structural parameters. This fitting result was used for transient EXAFS modelling. The relevant analysis parameters are given below.

The data reduction was performed in Athena [RN05], the background was removed using the implemented Autobk algorithm with parameters  $R_{\text{bkg}} = 1.1$  and  $k = 3$ . The extracted EXAFS signal  $\chi(k)$  was fitted with horae Artemis [RN05], using Feff85L [Ank+98].

The fitting was done in  $k$ -space for  $k = 3 - 16 \text{ \AA}^{-1}$ . Strong multiple-scattering paths were included. All distances were kept fixed, because the structure was further used as the base for the construction of the excited state structures. Energy shift  $E_0$ , amplitude reduction

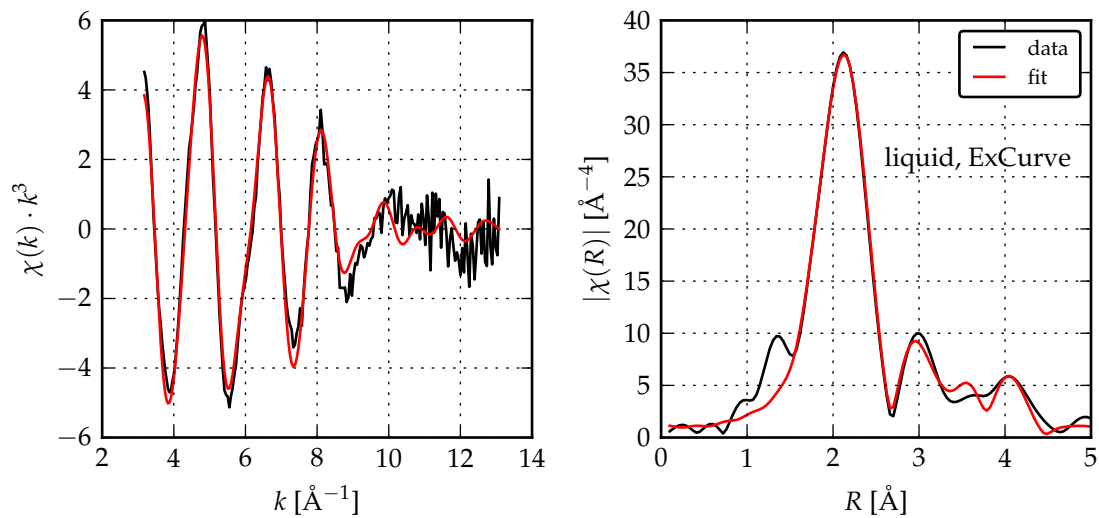


**Figure 5.13:** Fit of EXAFS of 10 mM acetonitrile solution of  $\text{Cu}_2(\text{NSSN})_2(\text{OTf})_2$  performed with ExCurve. N, S, C, S, Cu shells were included; number of atoms, distances to shells and  $\sigma^2$  were fitted.

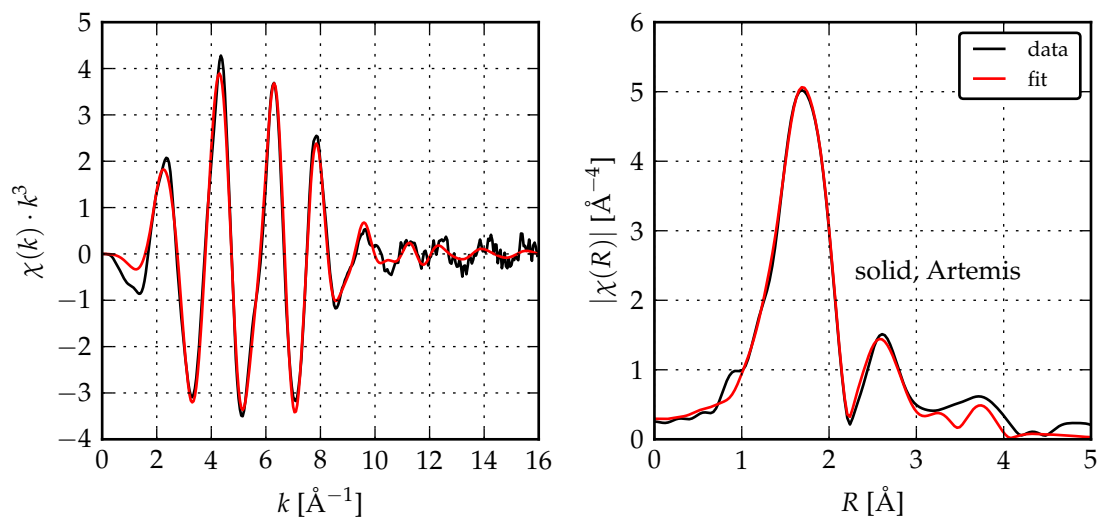


**Figure 5.14:** Fit of EXAFS of solid state  $\text{Cu}_2(\text{NSSN})_2(\text{OTf})_2$  performed with Artemis. N, S, C, S, Cu shells were included; distances to shells and  $\sigma^2$  were fitted. The number of atoms was taken from the crystallographic data and was not refined. Fit was performed in  $k$  space for  $k = 3 - 15.5 \text{ \AA}^{-1}$ .

**Table 5.6:** Comparative results of EXAFS fitting performed in Artemis and ExCurve. For details see text.

		Solid, ExCurve	Liquid, ExCurve	Solid, Artemis	Cryst. distance [Å]
$E_0$ [eV]		$2.8 \pm 2.2$	$2.9 \pm 2.5$	$-2.6 \pm 1.2$	
$S_0^2$		1	$1.07 \pm 1.15$	$0.9999 \pm 0.0002$ (restrained by 1)	
N	N	$1.9 \pm 1.2$	$1.7 \pm 2.2$	2	2
	R [Å]	$2.00 \pm 0.03$	$1.99 \pm 0.04$	$2.017 \pm 0.015$	$2.021 \pm 0.010$
	$\sigma^2$ <sup>a</sup>	$0.021 \pm 0.007$	$0.021 \pm 0.009$	$0.009 \pm 0.001$	
S	N	$2.3 \pm 1.2$	$2.4 \pm 3.1$	2	2
	R [Å]	$2.26 \pm 0.02$	$2.25 \pm 0.02$	$2.276 \pm 0.009$	$2.288 \pm 0.011$
	$\sigma^2$	$0.024 \pm 0.007$	$0.021 \pm 0.009$	$0.0109 \pm 0.0008$	
C	N	$3.4 \pm 1.4$	$2.8 \pm 3.8$	6	6
	R [Å]	$2.90 \pm 0.02$	$2.90 \pm 0.02$	$2.87, 2.95, 3.00 \pm 0.02$	2.898-3.067
	$\sigma^2$	$0.021 \pm 0.009$	$0.018 \pm 0.009$	$0.012 \pm 0.002$	av. = 2.964
S	N	$1.7 \pm 0.8$	$1.7 \pm 2.7$	2	2
	R [Å]	$3.51 \pm 0.03$	$3.50 \pm 0.03$	$3.57 \pm 0.03$	3.400-3.659
	$\sigma^2$	$0.025 \pm 0.011$	$0.025 \pm 0.013$	$0.016 \pm 0.004$	av. = 3.530
Cu	N	$1.0 \pm 0.8$	1	1	1
	R [Å]	$3.96 \pm 0.03$	$3.95 \pm 0.04$	$4.02 \pm 0.03$	3.941
	$\sigma^2$	$0.025 \pm 0.011$	$0.025 \pm 0.015$	$0.013 \pm 0.004$	

<sup>a</sup>  $\sigma^2$  values from ExCurve should be divided by 2 to be compared with Artemis

factor  $S_0^2$  and "Debye-Waller factors"  $\sigma^2$  were fitted. Since fitted value of  $S_0^2$  was close to 1.0 (within error bar) and it correlated strongly with the  $\sigma^2$  of the first shell, it was fixed at  $S_0^2 = 1.0$  for the final fit, resulting in  $N_{ind} = 25$  (number of "independent points" which is an estimation of the informational content of the data, calculated by the fitting software) for  $N_{par} = 8$  fitting parameters. The list of used scattering paths and the fitting parameters are presented in Table 5.7, the experimental data and fits plotted in  $k$ - and  $R$ -space are shown in Fig. 5.17. The atoms used in the EXAFS fit are marked on the Fig. 5.16. As the input to Feff8.5L the following parameters were important: FOLP 0 1.1; AFOLP; SCF 5. 1. The overlap factor (FOLP) for the central atom was changed from 1.15 to 1.1, because the Feff calculation could not proceed with the default value of 1.15. The self-consistent potential (SCF flag in the Feff input file) was used because it is supposed to give a better estimation of  $E_0$ , at the cost of significantly slower calculations. The energy shift was found to be  $\Delta E_0 = -0.2$  eV with Feff8.5 with SCF in comparison to  $\Delta E_0 = 6$  eV for Feff6 without SCF.

### 5.3.4 Transient XANES

Fig. 5.18 shows the edge region of the Cu K-edge absorption spectrum of the complex. The edge position (maximum of the first derivative at 8981.2 eV) and shape (intensive shoulder at 8985.5 eV, assigned as  $1s \rightarrow 4p$  transition) correspond to a four-coordinated  $\text{Cu}^{+1}$  [Kau+87; HS12].

Upon photoexcitation with 343 nm light pulses strong changes are observed in the XANES spectrum. The transient signal (Fig. 5.18) has a double minimum corresponding to the disappearance of the two edge shoulders caused by the edge shift to higher energies for  $\text{Cu}^{+2}$ . This fact was used to estimate the excited state fraction as described below. At the same time a small positive preedge feature emerges at 8978 eV which in literature is assigned to be  $1s \rightarrow 3d(+4p)$  transition which is characteristic for  $\text{Cu}^{+2}$  with coordination distorted from a centrosymmetric one [SKY92; MDD12; HS12]. The transient obtained on a DFB solution shows the same fea-

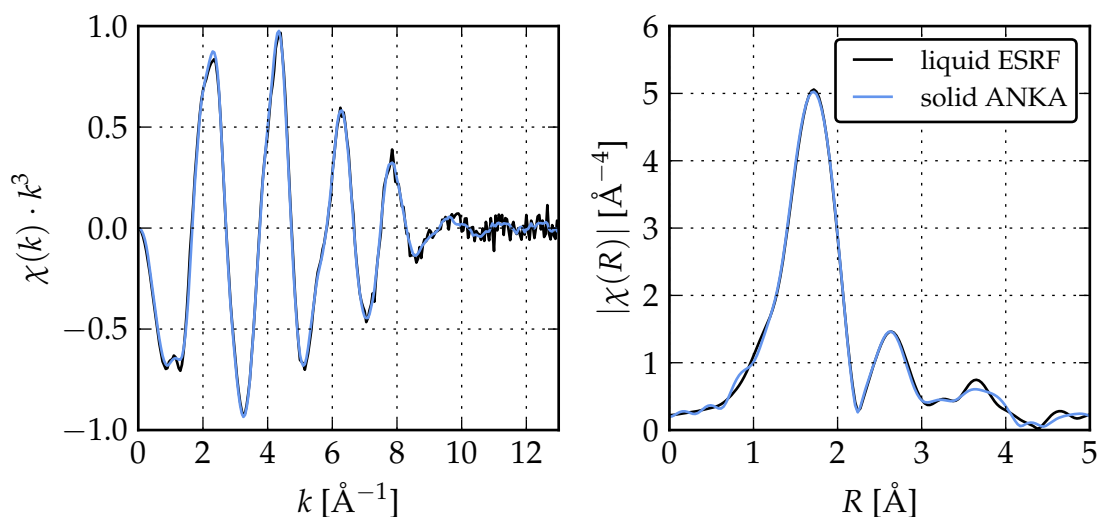


Figure 5.15: Comparison between EXAFS of solid  $[\text{Cu}_2(\text{NSSN})_2](\text{OTf})_2$  and its 10 mM solution in ACN.

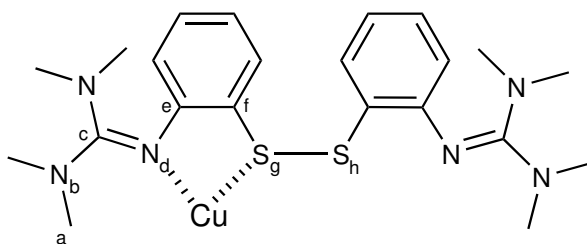


Figure 5.16: Atoms indicated in the EXAFS fitting results (table 5.7).

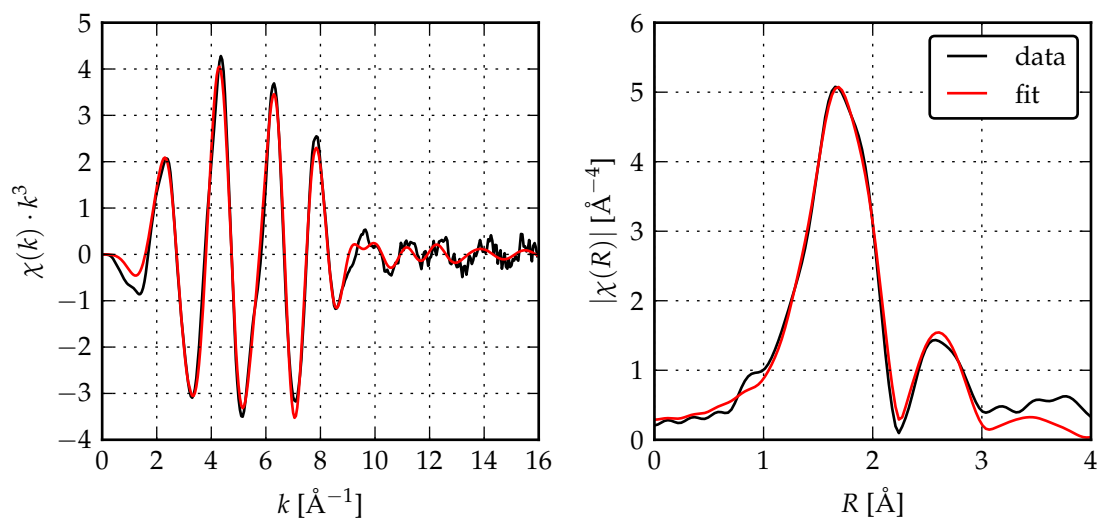
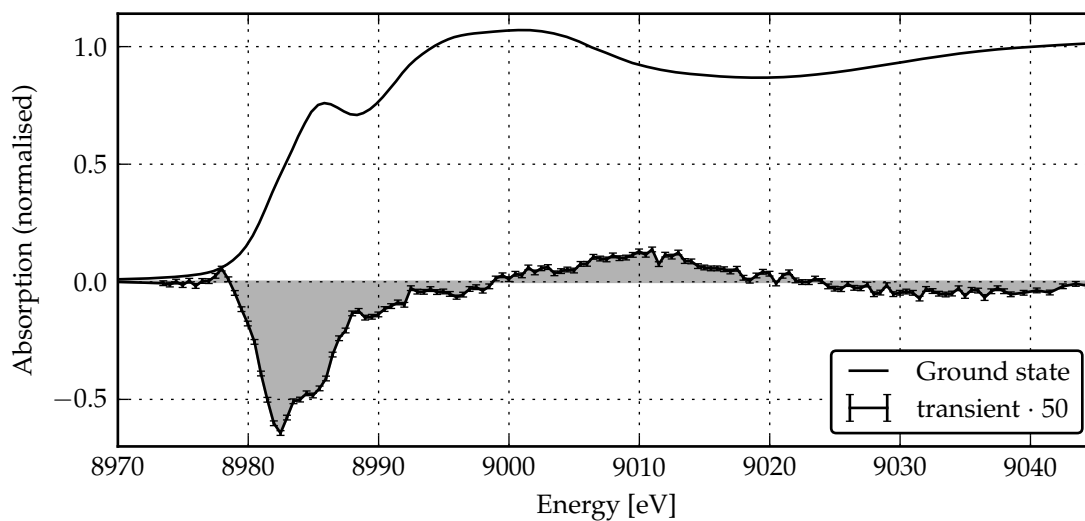


Figure 5.17: EXAFS data and fit in  $k$ - and  $R$ -space of the solid sample of  $\text{Cu}_2(\text{NSSN})_2(\text{OTf})_2$  used for further transient EXAFS analysis. Fit was performed in  $k$  space for  $k = 3 - 16 \text{ \AA}^{-1}$ .

**Table 5.7:** The list of scattering paths included in the EXAFS fit and the fitting results. The amplitude reduction factor was fixed at  $S_0^2 = 1$ , the energy shift was found to be  $E_0 = -0.2 \pm 0.4$  eV.

Scattering path	$\sigma^2$ [ $\text{\AA}^2$ ]	fitting parameter
Cu-N <sub>(d)</sub>	$0.0079 \pm 0.0008$	sig1
Cu-S <sub>(g)</sub>	$0.0109 \pm 0.0006$	sig2
Cu-C <sub>(c,e,f)</sub>	$0.0087 \pm 0.0016$	sig3
Cu-C <sub>(e)</sub> -C <sub>(f)</sub>	$0.0087 \pm 0.0016$	sig3
Cu-N <sub>(d)</sub> -C <sub>(e,c)</sub>	$0.007 \pm 0.004$	sig_ms
Cu-N <sub>(d)</sub> -C <sub>(e,c)</sub> -N <sub>(d)</sub>	$0.016 \pm 0.004$	sig1·2
Cu-N <sub>(b)</sub> ,Cu-C <sub>(a)</sub>	$0.030 \pm 0.016$	sig4
Cu-N <sub>(d)</sub> -C <sub>(f)</sub>	$0.0083 \pm 0.0009$	sig1/2+sig3/2
Cu-N <sub>(d)</sub> -N <sub>(b)</sub>	$0.019 \pm 0.007$	sig1/2+sig4/2
Cu-S <sub>(g)</sub> -C <sub>(f)</sub>	$0.0098 \pm 0.0008$	sig2/2+sig3/2
Cu-S <sub>(h)</sub>	$0.017 \pm 0.013$	sig5
Cu-Cu	$0.021 \pm 0.013$	sig6



**Figure 5.18:** Ground state X-ray absorption spectrum of solid  $\text{Cu}_2(\text{NSSN})_2$  and transient spectrum of 5 mM solution in ACN).

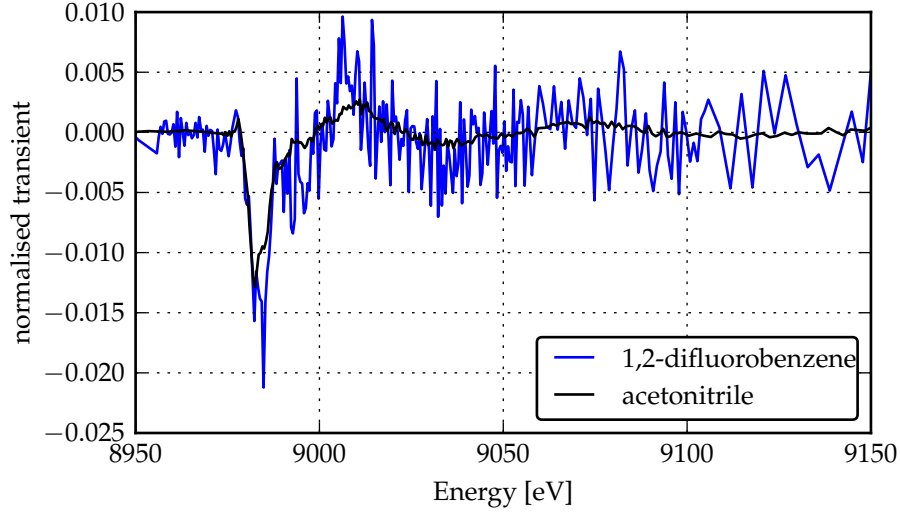


**Figure 5.19:** Transient X-ray absorption spectra in ACN and in DFB. Each transient is normalised to the corresponding edge jump, therefore their amplitudes reflect the excited state fractions.

tures as the transient in ACN, but the S/N ratio for DFB is much lower, and it is hard to do a quantitative comparison (Fig. 5.19).

### Estimation of the excited state fraction in the X-ray absorption spectrum

The laser-pumped spectrum (PS) has contributions of both ground state (GS) and excited state (ES) spectra. In order to extract the ES spectrum, the knowledge of its relative contribution (excited state fraction  $f$ ) is necessary. In order to estimate it, the following procedure was performed. The edge shape for the GS spectrum was modelled as a sum of an error function and two pseudo-voigt peaks centred at 8982.4 eV (pVoigt1) and 8985.4 eV (pVoigt2) as shown in Fig. 5.20. With the ES fraction  $f_i$  the excited state spectrum  $S_i$  can be calculated out of GS spectrum and transient (Tr) as

$$S_i = GS + \frac{\text{Tr}}{f_i}. \quad (5.3)$$

For the sought fraction  $f_x$  the spectrum  $S_i$  turns into the ES spectrum:

$$\text{Tr} = f_x \cdot (ES - GS). \quad (5.4)$$

Upon change from  $\text{Cu}^{+1}$  to  $\text{Cu}^{+2}$  the absorption edge shifts to higher energies. Due to this edge shift there should be no or only small absorption by  $\text{Cu}^{+2}$  at 8982.4 eV (pVoigt1). We can use this fact and find  $f$  for which the amplitude of pVoigt1 would be zero.

Combining equations 5.3 and 5.4 results in

$$S_i = GS + \frac{ES - GS}{f_i} \cdot f_x, \quad (5.5)$$

and after normalising the amplitude of  $S_i$  by GS in

$$\frac{S_i}{GS} = 1 - f_x \cdot \left(1 - \frac{ES}{GS}\right) \cdot \frac{1}{f_i}. \quad (5.6)$$

Equation 5.6 describes the dependence of  $S_i$  (normalised by GS) as a function of  $f_i$ . For each  $S_i$  the edge was modelled using the same model as for the GS, keeping the position and the

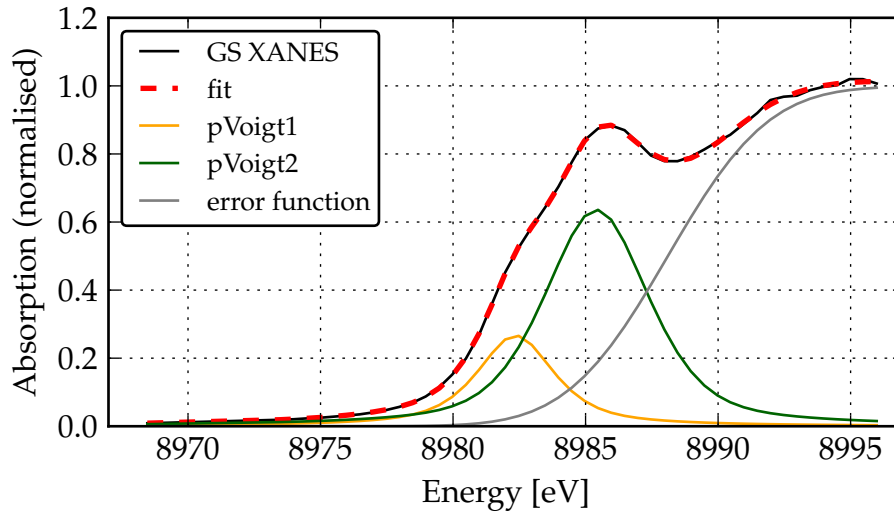


Figure 5.20: Modeling of the absorption edge as a sum of two pseudo-voigt functions and an error-function.

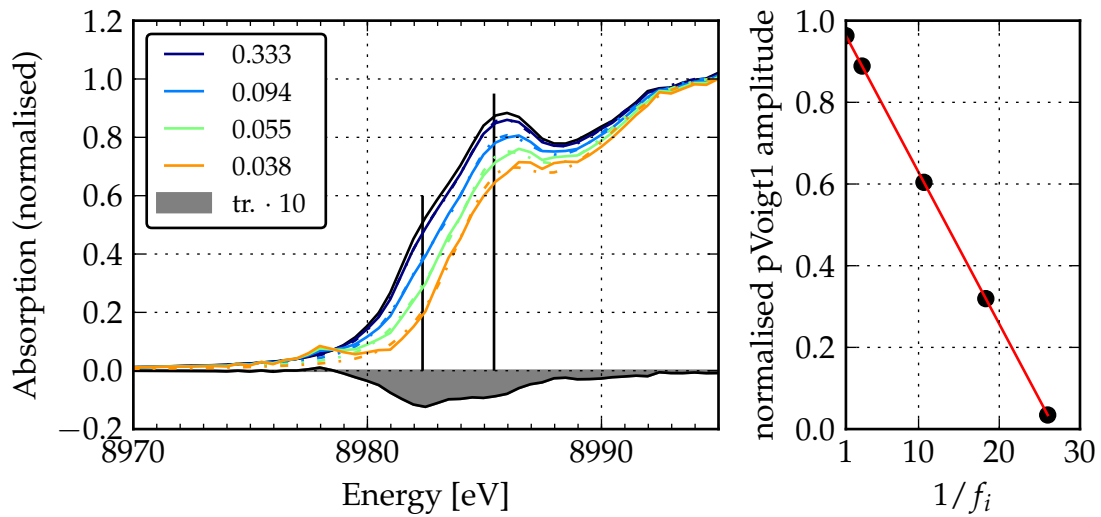
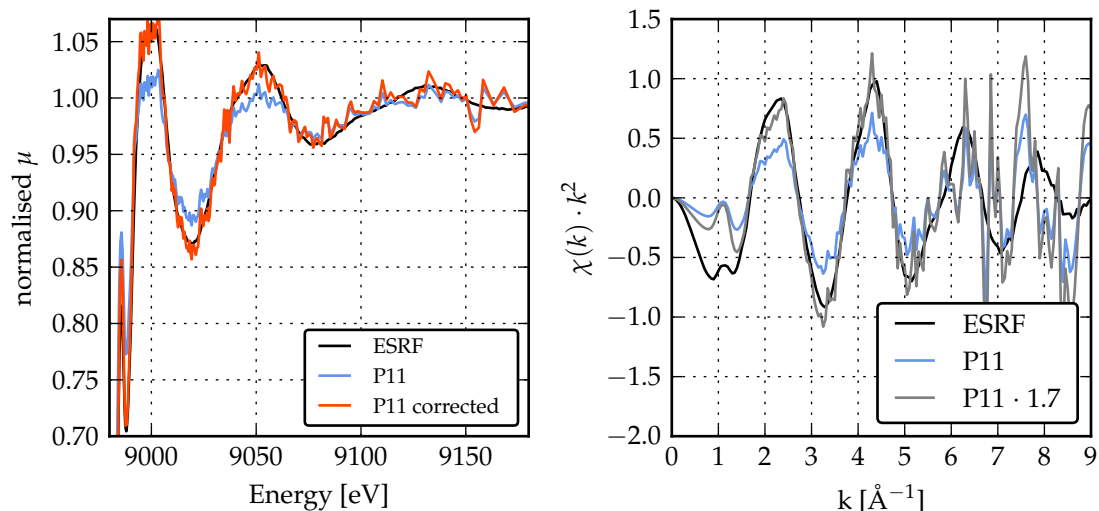


Figure 5.21: Left plot: modeling of edges of calculated  $S_i$  spectra. The solid lines show  $S_i$  for different excited state fractions  $f$ , dashed lines of the same color represent the fits. The widths and positions of the edge peaks were kept fixed to the fitted GS values, amplitudes were fitted. Right plot: linear regression of the amplitude of the edge peak at 8982.4 eV as the function of the excited state fraction.



**Figure 5.22:** Comparison of X-ray absorption spectra from the pump-probe experiment (measured at P11 beamline) and a static experiment (measured in ESRF). Left: self-absorption correction was performed on the P11 data in Athena software, resulting in a good match between the two data sets. Right: EXAFS data from P11 and ESRF in  $k$ -space.

width of pVoigt1 and pVoigt2 fixed and fitting their amplitudes as shown in Fig. 5.21 (left). The fitted amplitude of pVoigt1 and its linear regression is plotted in Fig. 5.21 (right). The slope of the linear regression of this data set is  $-f_x \cdot (1 - \frac{ES}{GS})$ . If there is no absorption in the excited state at 8982.4 eV, then  $ES = 0$ ,  $(1 - \frac{ES}{GS}) = 1$  and the slope of eq. 5.6 is equal to  $-1/f_x$ . If in the excited state the amplitude of an edge peak is non-zero (which would be the case for pVoigt2, because there is  $\text{Cu}^{+2}$  absorption at this energy), then  $(1 - \frac{ES}{GS}) < 1$  and the slope gives the lower border estimation for the excited state fraction. For pVoigt1 the linear regression results in  $f_x = 0.037$ . However, since there are two copper atoms in the molecule, the electron density loss upon photoexcitation is divided between them, and a more realistic estimation for the excited state fraction would be a factor of two larger, 0.074. It corresponds to 50 % decrease in the intensity of pVoigt1. This should be the lower-border estimation of the excited state fraction.

### 5.3.5 Transient EXAFS

#### Extraction of the transient EXAFS data

The ground and laser-pumped X-ray absorption spectra collected during the pump-probe experiment show EXAFS oscillation damping and high noise level compared to the GS spectrum obtained in a static EXAFS experiment at ESRF (see Fig. 5.22). As possible reasons for the oscillation damping two effects were considered: fluorescence self-absorption and the detector (avalanche photodiode (APD)) dead time. Fluorescence self-absorption should not have a strong effect: the mass percentage of copper in a 10 mM ACN solution is (assuming the density of the solution being equal to the density of the solvent):

$$\frac{m_{\text{Cu}}}{m_{\text{solution}}} = \frac{c_{\text{Cu}} \cdot M_{\text{Cu}}}{c_{\text{complex}} \cdot M_{\text{complex}} + \rho_{\text{solvent}}} = 0.0075.$$

This concentration of the absorbing atom falls into the diluted sample approximation and should not show self-absorption effects in the X-ray absorption spectrum [New04]. Other samples with the same copper concentration measured at this setup with different alignment did not demonstrate oscillations damping. This leaves us with the assumption that the saturation

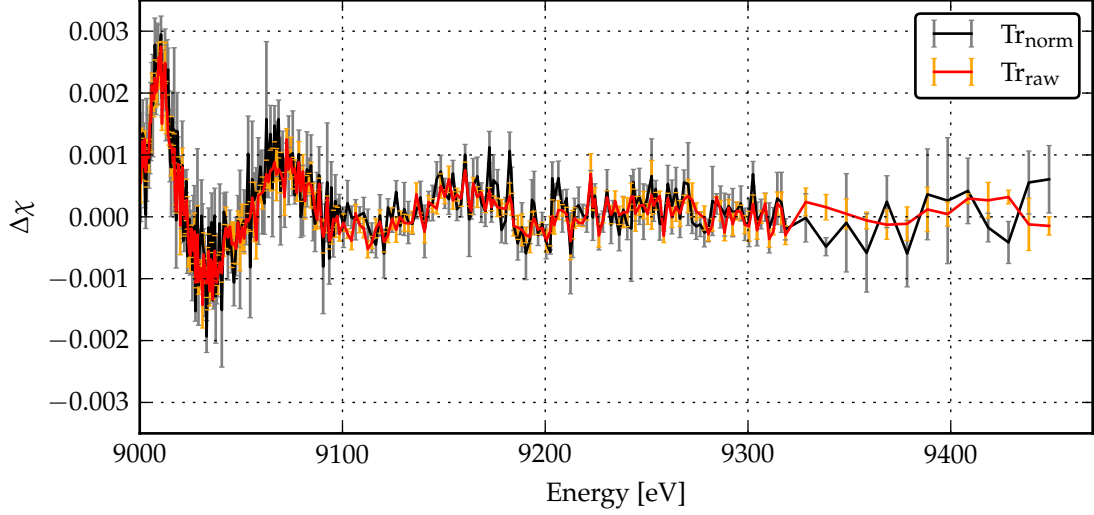


**Figure 5.23:** Comparison between  $\text{Tr}_{\text{raw}} = \text{pumped}_{\text{raw}} - \text{unpumped}_{\text{raw}}$  and  $\text{Tr}_{\text{norm}} = \text{pumped}_{\text{norm}} - \text{unpumped}_{\text{norm}}$ . For the details see text. Both transients are divided by the corresponding edge jump.

of the detector caused this effect. It has not been analysed further because we do not have an estimation for the count rate during the experiment. Judging by [Bar+06], in order to cause dead-time effects the count rate should have been higher than  $10^7$  ph/s. [Bri+16] estimated for a similar setup that the dead time effects are observed only with the count rate  $\gg 10^8$  ph/s. Self-absorption correction module in Athena software [RN05] was used in order to correct for the damping. The correction was performed on the data normalised by incident intensity  $I_0$ . Even though the reason for damping is different, applying this correction results in a good match between corrected data and a static spectrum as shown in Fig. 5.22 (left).

Despite the high noise level in the normalised GS spectrum, the transient spectrum obtained by subtracting normalised steady-state (unpumped) from normalised laser-pumped spectrum  $\text{Tr}_{\text{norm}} = \text{pumped}_{\text{norm}} - \text{unpumped}_{\text{norm}}$  shows clear oscillations even in the regions where the steady-state and laser-pumped spectra are dominated by noise. What is more, the transient calculated by subtraction of raw signals, not normalised by  $I_0$ ,  $\text{Tr}_{\text{raw}} = \text{pumped}_{\text{raw}} - \text{unpumped}_{\text{raw}}$  demonstrates higher S/N ratio than  $\text{Tr}_{\text{norm}}$  as demonstrated in Fig. 5.23. The fact that the transient has lower noise than the steady state and laser-pumped spectra points to the fact that there are other noise sources in addition to the inherent shot noise of the X-ray beam. The possibility to extract the transient data despite noisy steady-state and laser-pumped spectra underlines the advantage of the data collection scheme in this experiment: the data for unpumped / pumped channels are collected alternately for each Laser Off / Laser On cycle at 65 kHz. This way certain external factors which may have effect on the spectrum, such as X-ray beam position, ring current intensity, jet thickness, sample concentration, do not change significantly within one cycle of data collection. The transient data do not suffer from these modulations, which, however, can increase the noise in the actual ground state and pumped spectra. Since  $\text{Tr}_{\text{raw}}$  had higher S/N ratio than  $\text{Tr}_{\text{norm}}$ , it was used as the experimental data in the further data analysis, and is further referred to as  $\text{Tr}_{\text{exp}}$ , or  $\Delta\chi_{\text{exp}}$ . In order to compensate for the damping effect  $\text{Tr}_{\text{exp}}$  was scaled by a factor of 1.7. This factor was obtained by scaling the analysed GS spectrum to the spectrum from a static experiment in  $k$ -space as shown in Fig. 5.22 (right). The error in estimating this scaling coefficient only affects the value of the ES fraction extracted in the further data analysis.

## Analysis

The analysis was based on fitting of the transient EXAFS spectrum directly in energy space by minimisation of the square residual function between a series of simulated transient EXAFS spectra and the experimental data as proposed in [Gaw+09]. This approach was successfully applied to study photoexcitation-driven structural changes in spin-crossover Fe complexes [Gaw+09; Ass16] and a dimetal Pt complex [Vee+09]. An advantage of the energy space transient EXAFS fitting is that the ES fraction is one of the fitting parameters, and no preliminary knowledge of it is necessary. What is more, in our experiment the quality of the GS spectrum was too low to analyse EXAFS. In this approach we could base the ground state fit on an external data set (high-quality static solid state EXAFS spectrum). The steps of the analysis were the following.

### 1. Ground state EXAFS fit

In this analysis approach transient EXAFS spectra are calculated as difference between EXAFS spectra for excited state models and the ground state. Therefore, the ground state EXAFS spectrum of  $\text{Cu}_2(\text{NSSN})_2$  had to be fitted. The ground and laser-pumped X-ray absorption spectra collected during the pump-probe experiment show EXAFS oscillation damping and too high noise level to be analysed. Therefore, we decided to use a steady-state EXAFS spectrum for the ground state fit. The transient EXAFS data are obtained on a solution, and it would be reasonable to base the analysis on a steady-state EXAFS spectrum of the solution. However, EXAFS spectra of liquid and solid samples look identical (see Fig. 5.15), and the solid sample has higher S/N ratio. For this reason the spectrum of the solid  $\text{Cu}_2(\text{NSSN})_2(\text{OTf})_2$  measured at ANKA was taken as the base for the GS fit. The fitting procedure and results were presented in section 5.3.3.

### 2. Calculating $\chi(k)$ for the ground state

In order to have  $\chi(k)$  for GS and ES calculated in the identical way,  $\chi^{\text{GS}}(k)$  was calculated externally by using Feff8.5L for the crystallographic structure using the fitting parameters of the GS. Five modules of Feff have been executed (*pot*, *xsph*, *fms*, *path*, *genfmt*), and the generated list.dat file was modified by removing all paths which were not taken into account in the fit and setting the  $\sigma^2$  for all relevant paths to the GS fit values. With this modified list.dat the sixth module *ff2x* has been run to generate  $\chi^{\text{GS}}(k)$ .

### 3. Constructing excited state structures and calculating $\chi^{\text{ES}}(k)$

Excited state structures were constructed as follows. Brute-force generation of possible ES structures would need investigation of too many structures. Because of two copper atoms and four Cu-N/Cu-S bonds, there are eight independent parameters even if the ligands are moved as fixed units. Therefore, we based the search of the ES structures on the DFT calculation results. As discussed previously in section 5.1.3, only the triplet state should be observed with the temporal resolution of the transient XAS experiment (70-100 ps). Since the DFT-calculated GS structure had longer Cu-N and Cu-S bond lengths than the crystallographic model (see Table 5.1), the calculated DFT structures ( $S_0$  and  $T_1$ ) could not be used for the fit as they are. Therefore, we decided to construct the ES structures out of the crystallographic structure. In order to do it, relative changes (ratios) between the DFT-calculated Cu-N and Cu-S distances in  $T_1$  and  $S_0$  were applied to corresponding bonds in the crystal structure. The ligand part of the molecule can be separated into four equal parts, each including tetramethylguanidine, phenyl and one sulfur of the disulfide bridge. (On the Fig. 5.16 the separation line would go between two sulfur atoms.) For each copper, the paths which significantly contribute to the EXAFS signal, and therefore were used for the fit, all belong to such a ligand half except for contributions by two

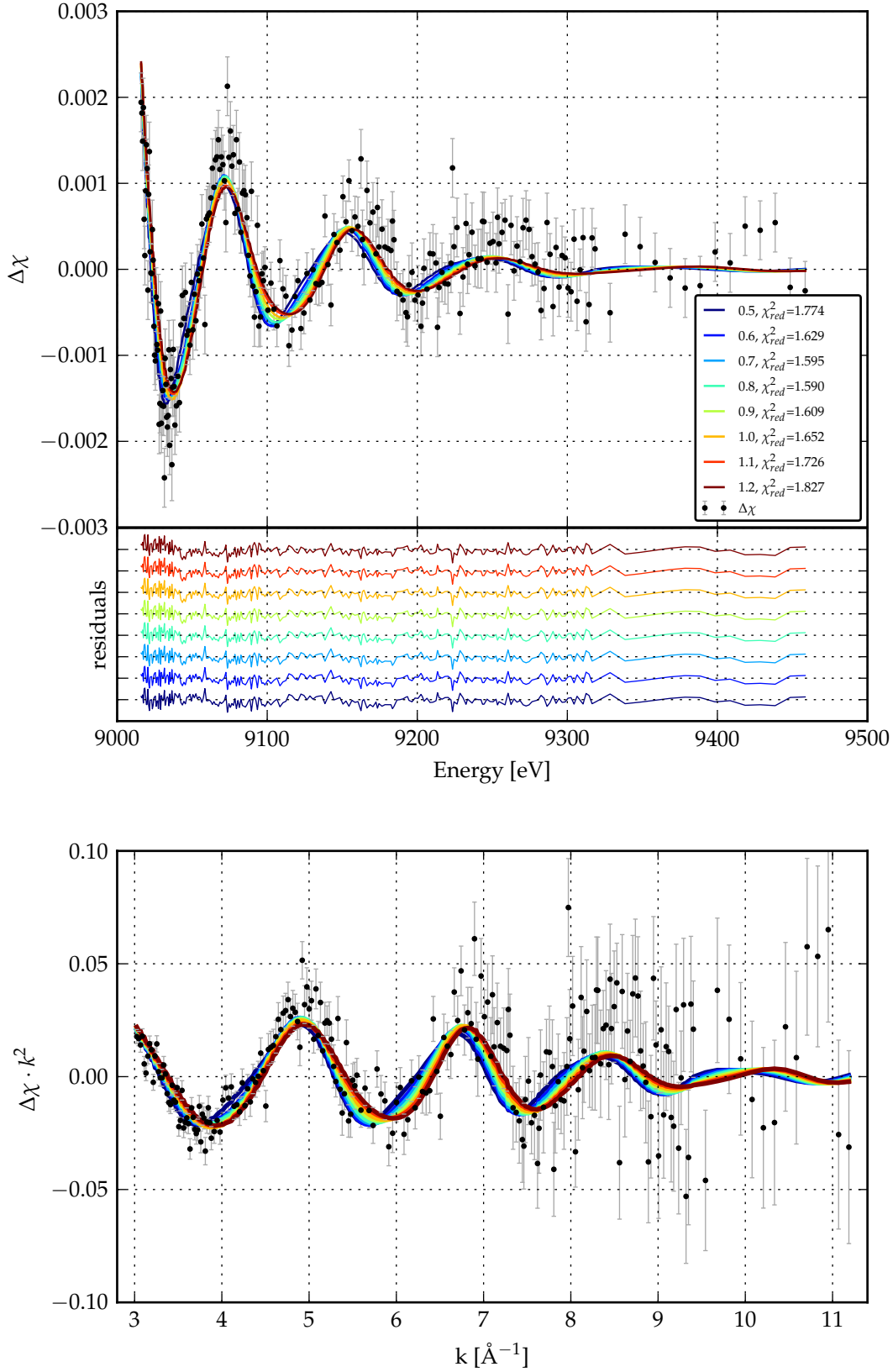


**Figure 5.24:** Best fits of transient EXAFS data for structures along the  $S_0^{cr} \rightarrow T_1^{cr}$  transformation path. Top: energy space. Bottom: recalculated into  $k$ -space with  $E_0 = 8981.08$  eV (ground state value). The fitting parameters are collected in Table 5.8.

second-shell sulfur atoms (3.4 – 3.7 Å) and the second copper (3.9 Å). Therefore, for the construction of the ES these four parts could be moved independently as fixed units. As the first step the ligand unit was moved in the Cu-S-N plane along the Cu-N vector to the aimed Cu-N distance. In the second step the ligand was rotated in the same plane around the coordinating N-atom until the necessary Cu-S distance was reached. The structural modifications were performed on both copper atoms independently, without changing the Cu-Cu distance. The structure obtained this way was denoted as  $T_1^{cr}$ . In order to perform the structural refinement additional ES structures were constructed along the transformation path  $S_0^{cr} \rightarrow T_1^{cr}$  with  $\Delta R = 0.5 - 1.2$  relative bond lengths changes (where  $T_1^{cr}$  corresponds to  $\Delta R = 1.0$ ).

In the calculated triplet structure one of the S-S bonds breaks, and two parts of the molecule rotate around the remaining S-S bond away from each other. A convenient way to evaluate the degree of rotation is the dihedral angle Cu-S-S-Cu. In the crystallographic structure this angle is  $52^\circ$  and  $57^\circ$ , whereas in the calculated  $S_0$  (GS) structure it is  $70^\circ$ . In the triplet state  $T_1$  it grows to  $98^\circ$ . Due to the cycle breaking the contribution of Cu-Cu scattering to EXAFS in the excited state should be very weak, since the displacement from the average Cu-Cu distance will be much higher than in the GS. The same is valid for that one of the second-shell sulfur atoms which moves away from copper upon rotation. These two scattering paths were excluded from the calculation. With these prerequisites  $\chi^{ES}(k)$  was calculated for each copper atom separately and later summed up.

#### 4. Statistical analysis

The theoretical transient in energy space can be constructed as  $\Delta\chi_{calc}(E) = f \cdot (\chi^{ES}(E, E_0^{ES}) - \chi^{GS}(E, E_0^{GS}))$ .  $E_0$  is the energy that corresponds to  $k = 0$ .  $E_0^{GS}$  was obtained in the GS fit. However,  $E_0^{ES}$  is unknown. The chemical shift between the excited and ground states  $dE = E_0^{ES} - E_0^{GS}$  can be estimated from the shift of the X-ray absorption edge position. Upon photoinduced MLCT in copper complexes the K-edge absorption edge shifts to higher energies due to the change of the electronic density on copper. For some  $Cu(N_4)$  complexes this shift (measured at the half of the edge jump) was found to be 3-3.5 eV [Che01; Hof+14; Pen+13]. For the investigated complex and its  $Cu^{+2}$ -chloride-thiolate derivative the shift is 1.8 eV [Neu+12]. The smaller value compared to  $Cu(N_4)$  complexes can be explained by higher covalency of Cu-S bonds compared to Cu-N [Kau+87]. Since there are two copper atoms in the molecule which potentially can have different  $E_0$  in the excited state, the energy shift has to be varied for both, and it is expected to have a positive value up to 3.5 eV. However, the changes on both copper atoms in the calculated  $T_1$  are identical, and therefore the chemical shifts for them should be equal:  $dE = dE_1 = dE_2$ . Thus, for each ES model  $\chi^{ES}(k)$  was recalculated into  $\chi^{ES}(E, E_0^{GS} + dE)$  with  $dE$  varied from -1 to 4 eV with 0.1 eV step.

Another parameter that has to be fitted is the ES fraction. We estimated the lower border for it to be  $f = 0.037$ , and the expected value to be  $f = 0.074$ . However, the presence of two copper sites makes it difficult to predict the edge position and shape of the ES spectrum, and  $f$  was varied as an independent parameter from 3% to 15% with 0.5% step. For each parameter set ( $\Delta R, dE, f$ )  $\Delta\chi_{calc}(E)$  was calculated and compared to  $\Delta\chi_{exp}(E)$ . The goodness of match between the calculation and the experiment was evaluated by calculating  $\chi_{red}^2$  according to the following equation:

$$\chi_{red}^2 = \frac{1}{N-1} \cdot \Sigma \left( \frac{f \cdot \Delta\chi_{calc}(\Delta R, dE, f) - \Delta\chi_{exp}}{stderr} \right)^2, \quad (5.7)$$

where  $N$  is the number of points in the experimental spectrum,  $stderr$  is the standard error for experimental values.

**Table 5.8:** Best fit results for structures along  $S_0^{cr} \rightarrow T_1^{cr}$  transformation path. The fits are plotted in Fig. 5.24

$S_0^{cr} \rightarrow T_1^{cr}$	$f$	$dE$	$\chi_{red}^2$
0.5	0.135	0.7	1.774
0.6	0.120	1.4	1.629
0.7	0.105	1.5	1.595
0.8	0.095	1.5	1.590
0.9	0.080	1.9	1.609
1.0	0.070	2.2	1.652
1.1	0.060	2.5	1.726
1.2	0.055	2.7	1.827

The standard deviation at each energy point  $j$  of the spectrum could be estimated as

$$stddev_j = \sqrt{\frac{1}{n_j-1} \cdot \sum_{i=1}^{n_j} (x_{ij} - \bar{x}_j)^2},$$

where  $x_{ij}$  is an independent measurement at point  $j$ ,  $n_j$  is the number of measurements ( $n_j = 3$  or  $6$  for different parts of the spectrum). However, due to the small value of  $n$ , values of the standard deviation differed strongly from point to point, thus making some spectral points during the  $\chi_{red}^2$  calculation much more (orders of magnitude) significant than others. This is not physically reasonable, because we expect approximately the same number of photons coming to the detector at all EXAFS energies. For this reason the standard deviation for each experimental data point was taken to be the same and was calculated as the mean value of standard deviations for all measurement points  $stddev = \frac{1}{N} \sum_{j=1}^N stddev_j$ . The standard error, or the standard deviation of the mean,

was then calculated for each spectral point as  $stderr_j = stddev / \sqrt{n_j}$ .<sup>2</sup>

## Results and discussion

Experimental data and the best fit results for each ES structure are presented in Fig. 5.24; the best fit parameters are gathered in Table 5.8. The global minimum of  $\chi_{red}^2$  is achieved for  $S_0^{cr} \rightarrow T_1^{cr}$  transformation path parameter  $\Delta R = 0.8$ , chemical shift  $dE = 1.5$  eV and ES fraction  $f = 0.095$ . The contour plot in Fig. 5.25 covers parameter values for all three parameters for which  $\chi_{red}^2$  is within  $3\sigma$  from the global  $\chi_{red}^2$  minimum.

The  $\chi_{red}^2$  surface on the space of  $(dE, f, \Delta R)$  parameters has quite shallow minimum along the **structural dimension**  $\Delta R$  due to the fact that shorter bond lengths result in a better match in the low-energy part of  $\Delta\chi_{exp}$ , whereas longer bond lengths – in the higher energy part. As a result, structures with  $\Delta R = 0.8 \pm 0.2$  produce fit with  $\chi_{red}^2$  within  $3\sigma$  from the global minimum for certain parameter combinations of  $dE$  and  $f$ . This range of  $\Delta R$  corresponds to the following bond lengths changes: Cu-N =  $-0.035(9)$  and  $+0.020(5)$  Å, Cu-S =  $+0.026(7)$  and  $-0.10(2)$  Å (see Fig. 5.44a). Although the minimum in the  $\chi_{red}^2$  is quite shallow on the scale of the investigated structural parameters (relative error of bond length change of appr. 25%), it should be noted that on the absolute scale the analysis demonstrates the precision on sub-pm level. This precision is achieved due to strict structural constraints: the system moves along one structural coordinate, which is  $S_0^{cr} \rightarrow T_1^{cr}$ .

The fit results in reasonable values of non-structural parameters  $dE$  and  $f$ . The **chemical shift** was found to be  $dE = 1.5_{-0.5}^{+1.2}$  eV (as can be seen on Fig. 5.25), in agreement with  $dE < 3.5$  eV

<sup>2</sup>For small sample statistics a possible approach for estimation of error bars is using the Student t-factor. In this case it would result in introducing additionally factor of 1.386 and 1.156 to error bars of the data points with  $n = 3$  or  $6$ , respectively. Normally error bars for X-ray transient experiments are calculated by error propagation out of error bars for ground and pumped spectra, which are often calculated as shot noise. However, in this experiment the spectra were dominated by other noise sources.

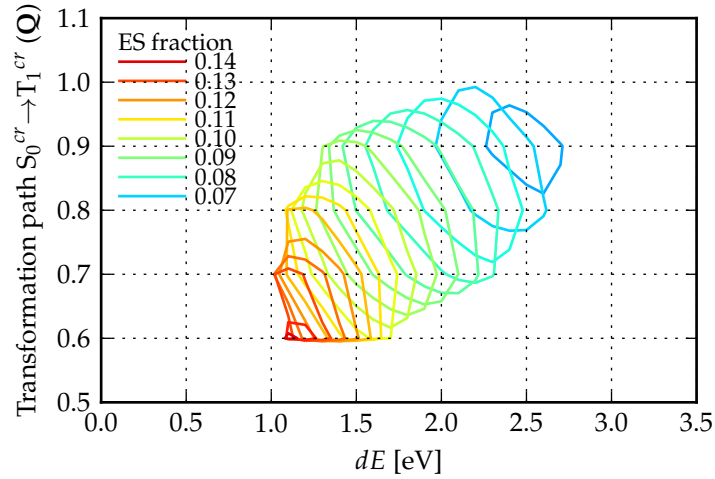


**Figure 5.25:** Contour plots marking  $3\sigma$  deviation from global minimum of  $\chi_{red}^2$  on the field of  $(dE, \Delta R)$  parameters. Different colours stand for different excited state fractions. Only every second  $f$  is labelled for visual clarity.

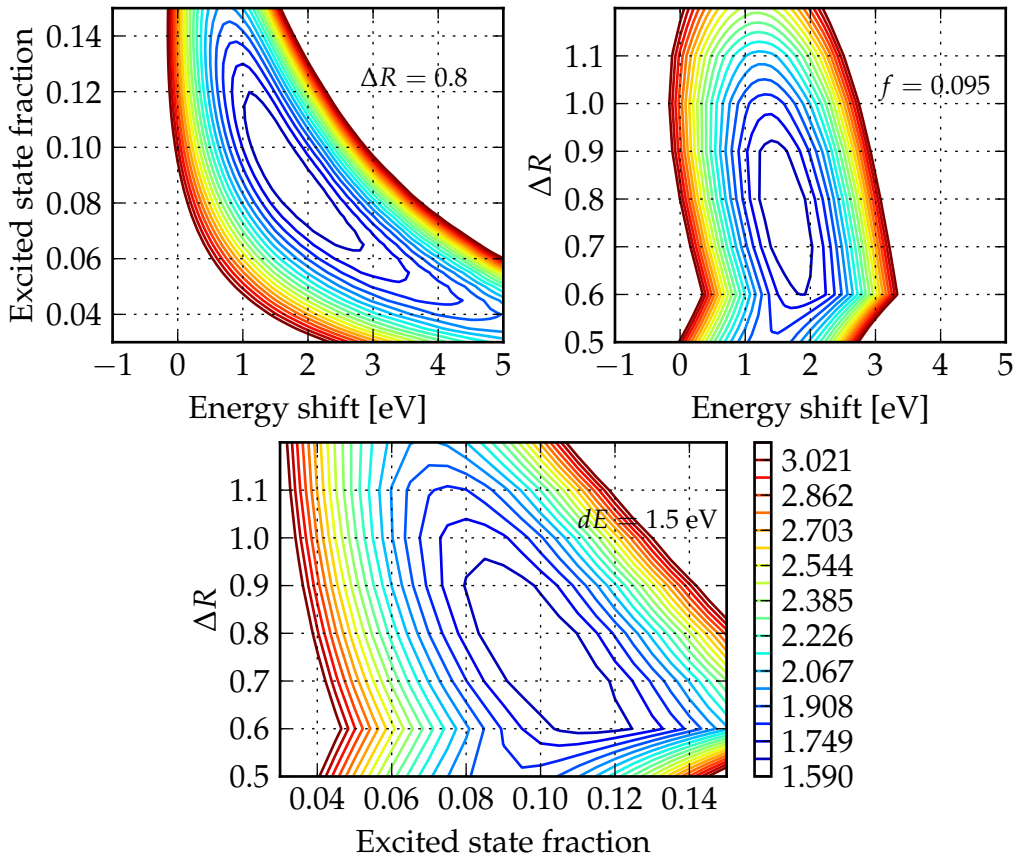


**Figure 5.26:** Contour plots showing correlations between fitting parameters ES fraction  $f$ , chemical shift  $dE$  and  $S_0^{cr} \rightarrow T_1^{cr}$  transformation path parameter  $\Delta R$ . On each plot one parameter is fixed as labelled, and  $\chi_{red}^2$  is plotted as a function of remaining two parameters. The parameters corresponding to the global minimum of  $\chi_{red}^2$  are taken. Contours are given in steps corresponding to 5% of  $\chi_{red}^2$  minimum.

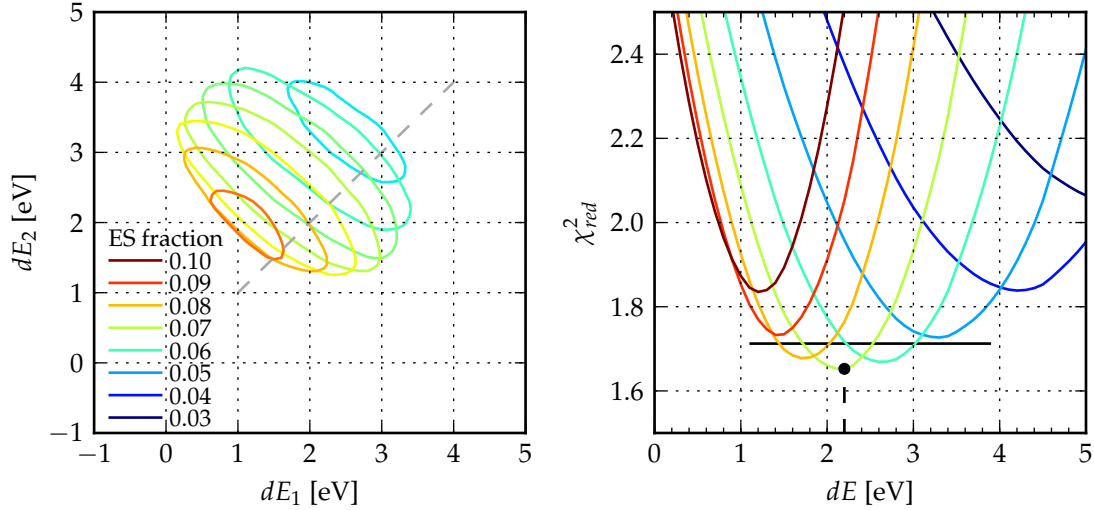


**Figure 5.27:** Plots illustrating  $\chi_{red}^2$  calculated on  $(dE_1, dE_2, f, \Delta R = 1.0)$  parameter space. Left: contour plots on  $(dE_1, dE_2)$  space showing  $3\sigma$  deviation from the global minimum of  $\chi_{red}^2$  for different excited state fractions.  $\text{Min}(\chi_{red}^2) = 1.64$  at  $f = 0.070$ ,  $dE_1 = 2.8$  eV,  $dE_2 = 1.4$  eV. The dashed gray line marks  $dE_1 = dE_2$  line. Only every second  $f$  is labelled for clarity. Right plot:  $\chi_{red}^2$  as a function of energy shift plotted along the  $dE_1 = dE_2$  line.  $\text{Min}(\chi_{red}^2) = 1.65$  at  $dE = 2.2$  eV and  $f = 0.070$ . The horizontal black line denotes  $3\sigma$  level for global minimum of  $\chi_{red}^2$ .

expected for a  $\text{Cu}^{+1} \rightarrow \text{Cu}^{+2}$  transition. The **excited state fraction** was found to be  $f = 9.5^{+5.5}_{-3.0}\%$ , close to 7.4%, predicted from the analysis of the XANES region. Errorbars for both parameters are given at  $3\sigma$  level from  $\chi_{red}^2$  analysis. Fig. 5.26 shows correlation plots for  $dE$ ,  $f$  and  $\Delta R$  parameters.

In addition to the structural refinement, the effect of having independent energy shifts on copper atoms ( $dE_1$  and  $dE_2$ ) was investigated:  $\chi_{red}^2$  was calculated for  $(dE_1, dE_2, f, \Delta R = 1.0)$ . For identical copper sites and symmetric changes in the excited state one can expect the mirror symmetry of  $\chi_{red}^2$  relative to  $dE_2 = dE_1$  axis. However, as can be seen in Fig. 5.27 the symmetry axis is rather  $dE_2 = dE_1 + 1$  eV. The possible reason for it is the fact that the modelling was based on the crystal structure, which demonstrates certain variance in Cu-N ( $2.021 \pm 0.010$  Å) and Cu-S ( $2.288 \pm 0.011$  Å) bond lengths. This structural asymmetry could result in asymmetry of  $\chi_{red}^2$  relative to the  $dE_2 = dE_1$  axis.

In order to test the structural sensitivity of the transient EXAFS data,  $\chi_{red}^2$  was calculated for all TDDFT-predicted singlet structures (presented in section 5.1.3). The structures were constructed following the same principle as was used to construct  $T_1^{cr}$ : ligands were moved as whole units, and relative changes in Cu-N and Cu-S bond lengths were applied to the crystallographic structure. Further structural refinement was not performed. Since some of the singlet structures had asymmetric changes on copper atoms,  $dE_1$  and  $dE_2$  were varied independently. Parameters corresponding to the global minimum of  $\chi_{red}^2$  for each singlet structure are presented in Table 5.9. Most of singlet structures result in worse  $\chi_{red}^2$  than the triplet structure and/or unreasonable values of  $dE$  or  $f$ . However, two structures,  $S_7^{cr}$  and  $S_{16}^{cr}$ , which structurally are almost mirror images of each other (with asymmetric changes on copper atoms), demonstrate good fits with reasonable energy shifts and ES fraction. These results show that there are different structures on the multidimensional space of structural parameters that result in a good fit of the data with reasonable non-structural parameters. Based on the transient EXAFS fit only it would not be possible to discriminate between  $T_1^{cr}$  and  $S_7^{cr}/S_{16}^{cr}$ . In this case potential structures can be discriminated by prior physical knowledge (we expect

**Table 5.9:** Best fit parameters for the structures constructed based on TDDFT calculations of the excited singlets (see text for details). The chemical shift  $dE_1$  and  $dE_2$  was varied from -6 to 6 eV with 0.5 eV step size. Fitting parameters for the triplet structure performed in the same conditions are given for comparison.

Structure	$dE_1$	$dE_2$	$f$	$\chi_{red}^2$
$S_1^{cr}$	3.5	3.5	0.035	2.27
$S_2^{cr}$	-6.0	-2.0	0.030	1.48
$S_3^{cr}$	0.0	1.0	0.105	1.54
$S_6^{cr}$	-1.0	2.5	0.110	1.93
$S_7^{cr}$	2.5	1.5	0.095	1.60
$S_9^{cr}$	-1.0	1.0	0.065	1.77
$S_{10}^{cr}$	-1.5	1.0	0.140	1.80
$S_{13}^{cr}$	4.5	4.0	0.035	2.33
$S_{15}^{cr}$	4.0	3.5	0.035	2.23
$S_{16}^{cr}$	1.5	2.5	0.100	1.60
$S_{17}^{cr}$	3.0	4.0	0.050	2.23
$S_{26}^{cr}$	4.0	4.5	0.055	2.22
$S_{38}^{cr}$	3.0	4.0	0.045	2.19
$T_1^{cr}$	2.5	1.5	0.070	1.65

that intersystem crossing takes place within the temporal resolution of the experiment), and by studying the same sample system with another pump-probe technique sensitive to structural changes, such as transient wide-angle X-ray scattering, as described in section 5.4. On the base of this transient EXAFS study we could not reliably probe the distance between two copper atoms and relative movement of two parts of the molecule in the excited state, because the distances between an absorbing copper and the ligand system of the second copper are too large to be reliably fitted. However, transient WAXS study was sensitive to these structural changes.

### 5.3.6 Excited state kinetics

Kinetic traces were registered during three transient XAS experiments:

- for 10 mM ACN solution of  $\text{Cu}_2(\text{NSSN})_2(\text{PF}_6)_2$  at 8985.0 eV
- for 5 mM ACN solution of  $\text{Cu}_2(\text{NSSN})_2(\text{OTf})_2$  at 8982.3 eV
- for 5 mM DFB solution of  $\text{Cu}_2(\text{NSSN})_2(\text{OTf})_2$  at 8985.8 eV.

All these traces were taken at the energies corresponding to the strongest negative transient. The kinetic data were modelled with equation 5.19, derived in the next subsection. The model is a convolution of the function describing time-dependent concentrations of species, contributing to the transient, with the Gaussian X-ray probe pulse. The fitting parameters include  $\tau_1$  and  $a_1$  – exponential decay constant and amplitude;  $a_2$  – a constant offset;  $\sigma_{pr}$  – full width at half maximum (FWHM) of the X-ray probe pulse. Additionally in some cases an offset  $y_0$  was added to the equation in order to take into account non-zero values at negative delay times. The fitting results for all solutions are summarised in Table 5.10.

Two ACN measurements both demonstrate a single-exponential decay down to a constant offset. For the 10 mM solution the measurement was done up to the time of 40 ns (Fig. 5.28). For the 5 mM ACN solution the data were collected only up to 6 ns (Fig. 5.29a). Therefore, we assumed that the system behaves in the same way as for the 10 mM measurement, and fitted it with the same model of a monoexponential decay to a constant offset. The fast decay components

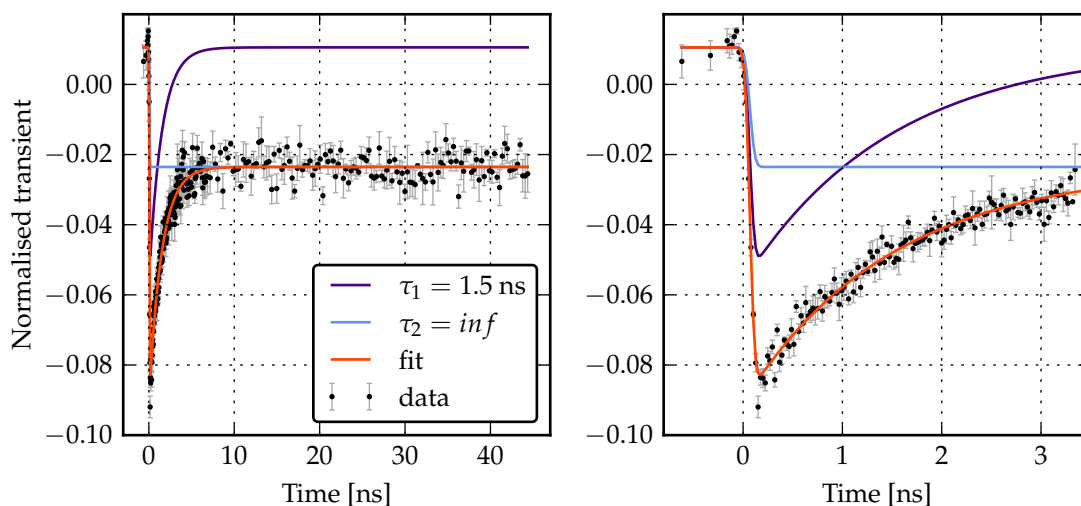
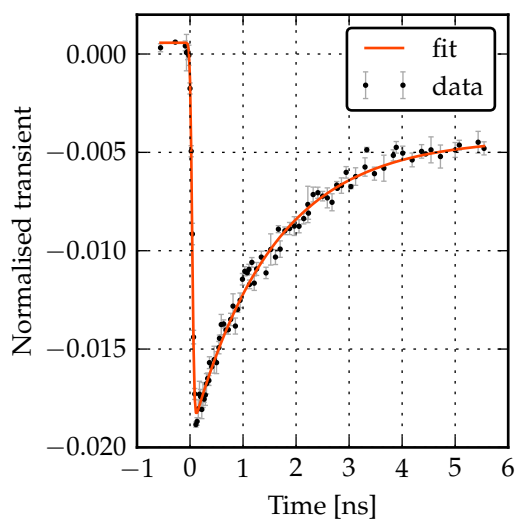
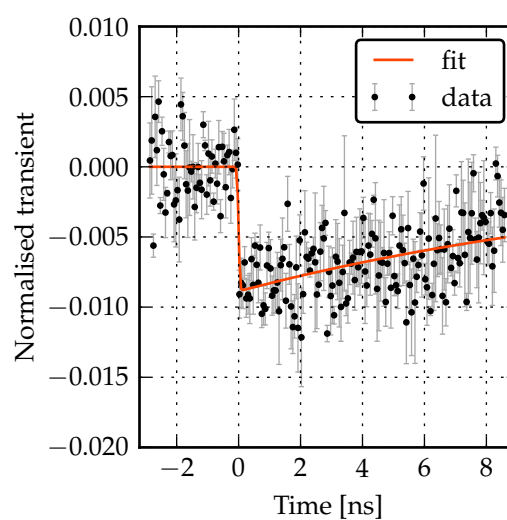


**Figure 5.28:** Normalised transient signal for 10 mM ACN solution at 8985.0 eV as a function of time delay between the pump and the probe pulses. Fitting performed with eq. 5.19. The left plot shows the full decay, the right plot is zoom into the first nanoseconds.



**(a)** 5 mM solution in ACN, 8982.3 eV.



**(b)** 5 mM solution in DFB, 8985.8 eV

**Figure 5.29:** Normalised transient signal as a function of time delay between the pump and the probe pulses. Fitting performed with eq. 5.19.

**Table 5.10**

	$\tau_1$ [ns]	$a_1$	$a_2$	$a_1/a_2$	$\sigma_{pr}$ [ns]
10 mM ACN	$1.46 \pm 0.03$	$-0.0164 \pm 0.0002$	$-0.0089 \pm 0.0003$	$1.86 \pm 0.08$	$0.039 \pm 0.003$
5 mM ACN	$1.53 \pm 0.04$	$-0.01487 \pm 0.00011$	$-0.00485 \pm 0.00013$	$3.1 \pm 0.1$	$0.031 \pm 0.002$
5 mM DFB	$15 \pm 2$	$-0.0160 \pm 0.0007$	-	-	0.037 (fixed)

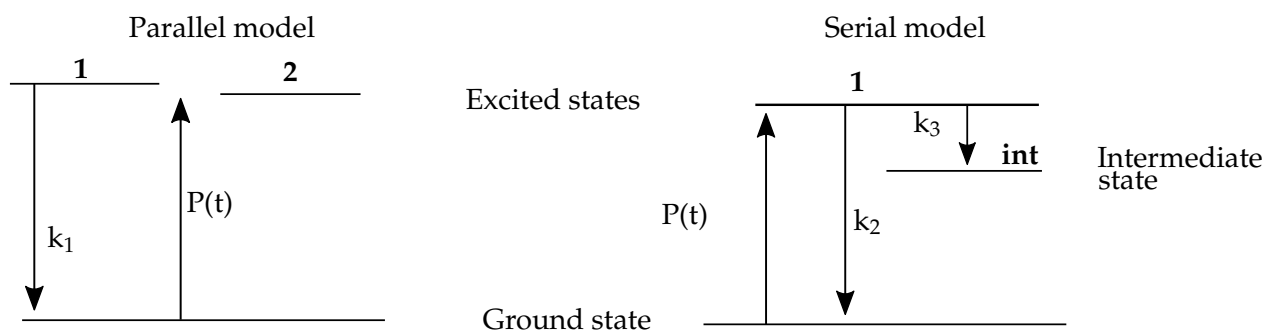


**Figure 5.30:** Schematic illustration of two excitation models.

Parallel model: the excitation populates two states **1** and **2**. State **1** decays with the rate constant  $k_1$ , state **2** does not decay.

Serial model: the excitation populates state **1**, which decays to the ground state with the rate constant  $k_2$  and to the intermediate state **int** with the rate constant  $k_3$ . State **int** does not decay further.

match very well between the two measurements. The constant offset may correspond to a photochemical reaction in the excited state, which prevents the return of the system to the ground state (oxidation state of copper stays (+2)). However, there were no signs of radiation damage in ACN solutions. Thus, it could be a species long-living on the time scale of the experiments (several tens of ns), but eventually transforming back into the original ground state.

The 5 mM solution of  $\text{Cu}_2(\text{NSSN})_2(\text{OTf})_2$  in DFB caused difficulties during the experiment: the solvent was evaporated easily by the jet and the collected transient signal was very noisy. In this and other experiments it was found out that  $\text{Cu}_2(\text{NSSN})_2$  in this solvent is not stable if illuminated by powerful laser and/or X-ray pulses. The observed decay is shown in Fig. 5.29b. It demonstrates much longer lifetime than for the ACN solution (Fig. 5.29b). No offset is visible within the noise level. The decay could be fitted with the lifetime of  $\tau_1 = 15 \pm 2$  ns. It is possible that for the DFB solution the main deexcitation happens faster than 70-100 ps time resolution and only the constant offset is observed. However, fitting the data with  $\tau_1 = \text{inf}$  resulted in 20% increase in reduced  $\chi^2$  compared to  $\tau_1 = 15$  ns. On the other hand, the kinetics measured on a 400 nm pumped DFB solution in a wide-angle X-ray scattering (WAXS) experiment, described in section 5.4, demonstrated kinetic behaviour very similar to ACN solutions with lifetime of  $2.9 \pm 0.7$  ns. It is possible that for the transient XAS measurements in the DFB solution, due to smaller laser spot and/or excitation with 343 nm light pulses (compared to 400 nm for the WAXS experiment), the slow component, possibly corresponding to a photochemical reaction, dominates over the reversible relaxation.

### Modelling of the excited state kinetics

The model for the decay fitting is based on the assumption that the pump instantaneously excites electrons from a ground state into an excited state, and the electrons in the excited state subsequently relax back to either ground state or an intermediate state **int** at a typical time  $\tau$  (rate constant  $k$ ) after excitation. The progression of the decay suggests two well-separated lifetimes. Two models may be assumed: the two independent decay channels (parallel model) or subsequent decay of a fast-living state into the long-living state (serial model) as shown in Fig. 5.30. This modelling assumes that the contribution to the trXAS signal is the same for all excited or intermediate states. We see only excited states with Cu(+2), because the transient signal originates from the edge shift to higher energies, and we assume that different excited states, as long as they have the oxidised copper in them, have the same edge positions.

#### Parallel model

This model describes the case of two excitation channels into excited states **1** and **2**. State **1**

decays to the ground state with the constant  $k_1$ , and **2** lives infinitely long in the time scale of the experiment. The populations of the excited states  $N_1, N_2$  can be described as

$$\frac{dN_1}{dt} = -k_1N_1 + c_1P(t) \quad (5.8)$$

$$\frac{dN_2}{dt} = c_2P(t) \quad (5.9)$$

where  $P(t)$  is the pump pulse. For the Gaussian laser pulse with width  $\sigma_{pu}$

$P(t) = \frac{1}{\sqrt{2\pi}\sigma_{pu}} e^{-\frac{t^2}{2\sigma_{pu}^2}}$ , and coefficients  $c_1$  and  $c_2$  include the pump intensity and excitation yield of the states **1** and **2**.

Solving these differential equations results in

$$N_1 = 1/2 \cdot c_1 \cdot e^{\sigma_{pu}^2 \cdot k_1^2 / 2} \cdot \operatorname{erfc}\left(\frac{\sigma_{pu} \cdot k_1}{\sqrt{2}} - \frac{t}{\sqrt{2}\sigma_{pu}}\right) \cdot e^{-k_1 t}, \quad (5.10)$$

$$N_2 = 1/2 \cdot c_1 \cdot \operatorname{erfc}\left(-\frac{t}{\sqrt{2}\sigma_{pu}}\right), \quad (5.11)$$

where  $\operatorname{erfc}$  is complementary error function.  $\sigma_{pu} \cdot k_1 \sim 10^{-4}$ , therefore  $e^{\sigma_{pu}^2 \cdot k_1^2 / 2} \approx 1$ .

The next step would be to convolve the excited state population with the probe X-ray pulse. Since the probe pulse (70-100 ps) is much longer than the pump pulse (180 fs) we can neglect the width of the latter and approximate the excited state population with Heaviside step function  $\theta(t)$ :

$$N_1 = c_1\theta(t)e^{-k_1 t} \quad (5.12)$$

$$N_2 = c_2\theta(t) \quad (5.13)$$

The contribution of both excited states to the signal is then:

$$N_1 + N_2 = c_2\theta(t)\left(1 + \frac{c_1}{c_2} \cdot e^{-k_1 t}\right). \quad (5.14)$$

### Serial model

This model describes the case when the excitation happens into excited state **1** which decays to the ground state with rate constant  $k_2$  and to the intermediate state **int** with the constant  $k_3$ . The intermediate state does not decay further. The rate of depopulation of **1** is  $k_1 = k_2 + k_3$ .

The populations of the excited state  $N_1$  and the intermediate state  $N_{int}$  can be described as

$$\frac{dN_1}{dt} = -(k_2 + k_3)N_1 + c_1P(t) = -k_1N_1 + c_1P(t) \quad (5.15)$$

$$\frac{dN_{int}}{dt} = k_2N_1 \quad (5.16)$$

If we solve eq. 5.16 with  $N_1$  taken from eq. 5.12, we obtain

$$N_{int} = c_1 \frac{k_2}{k_1} \theta(t) (1 - e^{-k_1 t}), \quad (5.17)$$

$$N_1 + N_{int} = c_1 \theta(t) \frac{k_2}{k_1} \left(1 + \frac{k_1 - k_2}{k_2} e^{-k_1 t}\right). \quad (5.18)$$

Comparison of the equations 5.14 and 5.18 shows that the models have essentially the same time dependence and cannot be distinguished based on the fit only without prior physical knowledge. In both cases the faster decay is the rate of disappearance of the excited state **1**. Interpretation of amplitudes would be different for the two models. Since there is no indication which model to choose and they have the same mathematical structure, only the parallel model was used further.

The convolution of the excited states populations (parallel model) with the probe signal  $Pr = b_1 \cdot \frac{1}{\sqrt{2\pi}\sigma_{pr}} e^{-\frac{t^2}{2\sigma_{pr}^2}}$  results in the equation

$$dXAFS = 1/2 \cdot c_1 \cdot b_1 \cdot \operatorname{erfc}\left(\frac{\sigma_{pr} \cdot k_1}{\sqrt{2}} - \frac{t}{\sqrt{2}\sigma_{pr}}\right) \cdot e^{-k_1 t} + 1/2 \cdot c_2 \cdot b_1 \cdot \operatorname{erfc}\left(-\frac{t}{\sqrt{2}\sigma_{pr}}\right) \quad (5.19)$$

Eq. 5.19 was used to fit the lifetime data. The relative amplitude of the two contributions was different in two experiments with ACN ( $c_1/c_2 = 3.1 \pm 0.1$  and  $1.86 \pm 0.08$ ), which points to the parallel model rather than serial, because different laser intensity can have influence on the created photoexcited products and less effect on their decay.

### 5.3.7 Summary

The transient X-ray absorption spectroscopy (XAS) experiments were performed in order to obtain quantitative information about structural changes in the coordination polyhedra of copper atoms in  $\text{Cu}_2(\text{NSSN})_2$  upon photoexcitation. The data were acquired at the pump-probe XAS setup at beamline P11 of Petra III. While this work was in progress an upgrade was performed resulting in an experimental setup where data of transient EXAFS quality could be collected [Goe+16]. The data analysis approach was based on comparison of the experimental transient with transients calculated for different ES models directly in energy space. The ground state EXAFS spectrum was modelled with the crystallographic structure. The same structure was used to construct excited state structures by modifying it in a way the DFT calculations predict for the lowest triplet state  $T_1$ . Fitting of the data directly in energy space has several benefits. Small systematic errors in the ground state structure and in the excited state structure, derived from it, may cancel each other to some extent, while the difference between two structures matters. Besides that, the fraction of the excited state in the spectrum is one of the fitting parameters, as well as the chemical shift of the absorbing element. What is more, the analysis could be based on fitting the ground state EXAFS data obtained in a static experiment, where the data quality permitted us to perform the fit up to  $k = 16$ . The analysis shows that DFT makes a realistic prediction of changes in coordination bond lengths for the triplet state. The best fit structures are those at 0.6 – 1.0 of the transformation path  $S_0^{cr} \rightarrow T_1^{cr}$ , corresponding to the following bond lengths changes: Cu-N = -0.035(9) and +0.020(5) Å, Cu-S = +0.026(7) and -0.10(2) Å. The best fit is achieved with reasonable excited state fraction and chemical shift:  $f = 9.5_{-3.5}^{+5.5} \%$  (close to the value of  $f = 7.4 \%$  estimated from the absorption edge shift analysis) and  $dE = 1.5_{-0.5}^{+1.5} \text{ eV}$  (expected for  $\text{Cu}^{+1} \rightarrow \text{Cu}^{+2}$ ). In addition to the triplet structure, the experimental transient was fitted with predicted excited singlet structures. All singlet structures, except of one, cannot adequately model the experimental data. This fact demonstrates that transient EXAFS has structural sensitivity, however, on the space of possible geometries there are different solutions that result in good fits with reasonable non-structural parameters. Such structures can be discriminated based on prior physical knowledge and by addressing the structural changes in

a different experiment. Transient EXAFS demonstrated high sensitivity to the changes in the local structure, however, for the triplet state of  $\text{Cu}_2(\text{NSSN})_2$  the DFT calculations predict not only changes in the coordination of copper, but also relative movement of two halves of the molecule, which EXAFS could not probe. This structural degree of freedom could be addressed in the transient wide-angle X-ray scattering experiment, as reported in section 5.4.

Since photoexcitation causes strong changes in the sulfur electronic density and coordination, an interesting experiment for this molecular system would be a pump-probe transient XAS experiment on sulfur K-edge. Such measurements on sulfur, performed on small organic molecules, were reported recently for the first time [Och+17; Kui+17]. Such an experiment should provide a direct way to monitor changes in S-S bond in this system.

## 5.4 Transient wide-angle X-ray scattering and transient X-ray emission spectroscopy

The transient wide-angle X-ray scattering (WAXS) together with transient X-ray emission spectroscopy (XES) measurements were performed in February 2016 at beamline ID09b of the ESRF synchrotron, Grenoble, France, together with Dr Dmitry Khakhulin. The description of the pump-probe setup at beamline ID09b can be found in [Wul+02].

Conducting an experiment where different measurement techniques are performed on the same sample system makes the data analysis more reliable by providing higher information content with the same number of degrees of freedom (unknown parameters). In our experiment transient WAXS was performed in order to probe the structural changes in the system upon photoexcitation, while the aim of acquiring transient X-ray emission spectra was to verify the oxidation state change of copper and give a direct information about the excited state fraction.

### 5.4.1 Experiment description

The scheme of the experimental setup is shown in Fig. 5.31. The sample was prepared as a 4 mM solution of  $[\text{Cu}_2(\text{NSSN})_2](\text{OTf})_2$  in DFB. The sample solution was delivered via a 300  $\mu\text{m}$ , flat sheet jet from a sapphire nozzle providing a flow speed of approximately 3 m/s to ensure the complete sample exchange between consecutive pump-probe events at 1 kHz repetition rate of the experiment. The solution was regularly refilled with the new solvent to compensate for the evaporation. The excitation was performed using 400 nm frequency doubled output of Ti:sapphire amplified system (Legend Elite, Coherent Inc.) with 1 kHz frequency and  $\sim 1$  ps pulse length (FWHM). To avoid non-linear absorption and saturation effects the laser pulse energy was set to a low value of 20  $\mu\text{J}$ . Single X-ray pulses (100 ps FWHM, 18 keV, 3% bandwidth pink beam) generated from the U17 undulator were selected using a mechanical chopper system to reduce the repetition rate to 1 kHz. The size of the laser spot on the sample was measured using a pinhole and determined to be 120  $\mu\text{m} \times 150 \mu\text{m}$  (h $\times$ v). The size of X-ray beam was 90  $\mu\text{m} \times 60 \mu\text{m}$  (h $\times$ v). The scattered X-rays were collected by a Rayonix MX170-HS CCD detector with 3840 $\times$ 3840 pixels in 2 $\times$ 2-pixel binning. The detector was placed 38 mm behind the liquid jet. A cylindrical tungsten beamstop of 1.5 mm diameter was used to block the direct beam in front of the detector. The 2D scattering images were collected for 18 different time delays between the laser and X-ray pulses in the range from -300 ps to 1  $\mu\text{s}$ . After every 3 images a reference image was taken at a nominal delay of -3 ns corresponding to the non-excited sample. All images were azimuthally integrated into 1D intensity curve  $S(q, t)$ . The signal intensity was corrected for the scattering angle dependences of the detector efficiency, of the sample absorption of X-rays, space angle coverage of the flat detector and the linear polarisation. The scattering contribution of DFB solvent to the total difference scattering signal was additionally measured in a separate time-resolved WAXS measurement with the same setup using the solution of an azobenzene dye (4-[(4-Bromophenyl)diazonyl]-N,N-diethylaniline, CAS 22700-62-5) as proposed in [Kjæ+13].

Cu  $K\alpha$  emission was registered with a 1 m diameter Rowland-circle spectrometer arranged in the horizontal plane with a Si(111) analyser crystal ((444) reflection) and a SDD with a multi-channel analyser to additionally suppress the elastic background. A He-filled tank was installed in the path of emitted X-rays to avoid absorption and scattering by air. The measurements were performed by scanning the analyser Bragg angle near 79° in order to span energy range of Cu  $K\alpha_1$  peak ( $\sim 8048$  eV). In total 35 scans were performed; certain spectral points were sampled 51 time.

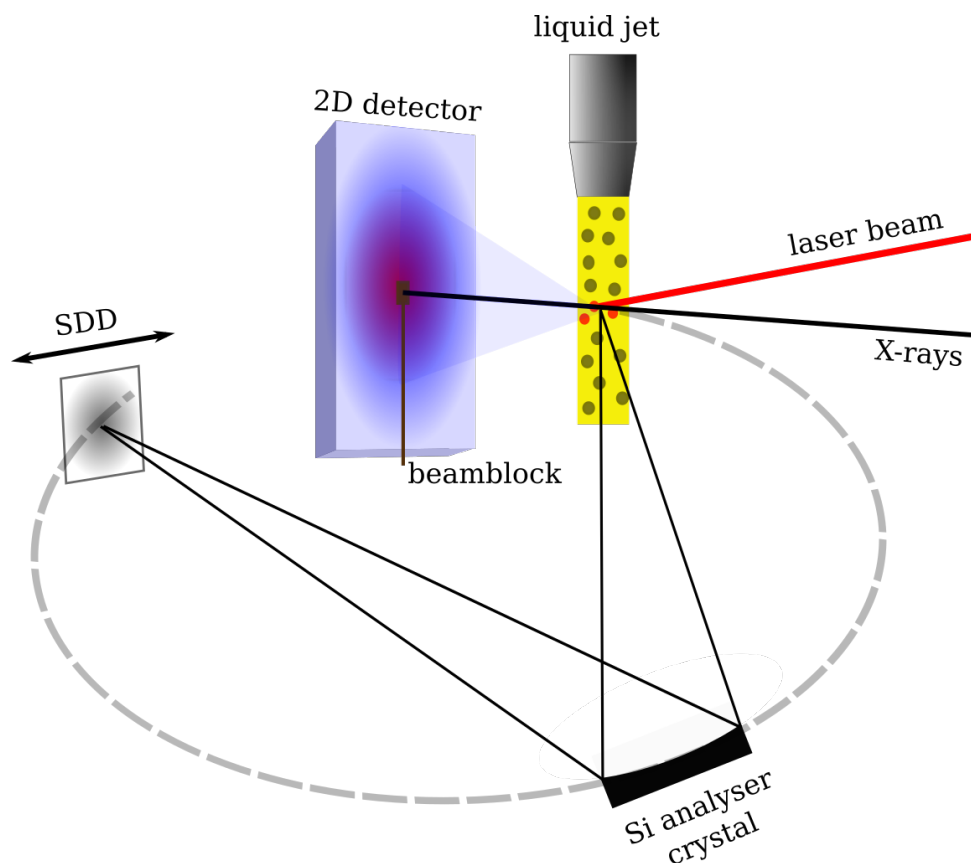
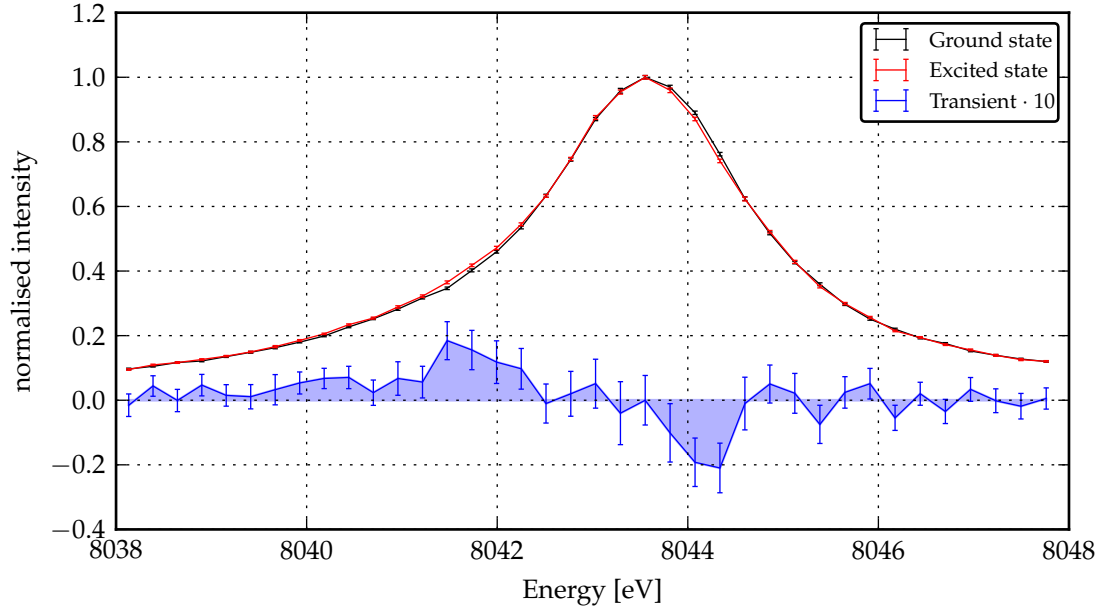


Figure 5.31: A scheme of pump-probe XES + WAXS setup at beamline ID09b in ESRF.

### 5.4.2 Transient X-ray emission spectroscopy

Upon MLCT transition in  $\text{Cu}_2(\text{NSSN})_2$  the change of the oxidation state of copper should cause changes in the X-ray emission spectrum. As shown in Fig. 5.32, upon photoexcitation the  $K\alpha_1$  peak widens and shifts slightly to lower energies. [Gla01] and [BG09] observe energy shift of  $K\alpha$  to lower energies upon increase in oxidation state in Mn compounds. For  $\text{Mn}^{+2} \rightarrow \text{Mn}^{+3}$  the energy shift was shown to be on the order of 0.2 eV and for  $\text{Mn}^{+2} \rightarrow \text{Mn}^{+4}$  – 0.5 eV. The width of  $K\alpha$  peaks was found to increase with the spin for compounds of Fe [Van+06] and Mn [Gla01]. The observed behaviour for copper is in line with these observations:  $\text{Cu}^{+1} \rightarrow \text{Cu}^{+2}$  ( $s=0 \rightarrow s=1/2$ ) results in a shift to lower energies and widening of the emission line.

If emission spectra of  $\text{Cu}^{+1}$  and  $\text{Cu}^{+2}$  are known, the excited state fraction can be obtained by scaling the experimental transient with the difference between them. Copper oxides  $\text{CuO}$  and  $\text{Cu}_2\text{O}$  were used as reference samples (see Fig. 5.33). However, using solid reference samples has a drawback: it is difficult to position the reference exactly at the position of the jet with the sample solution. Slightly different positions of the investigated samples cause small shifts in the line positions in the spectrum, and the energy shift between two references cannot be determined precisely. Another problem may be the degradation of solid references in the beam. A more reliable way to measure reference spectra would be to use liquid solutions which would be cycled in the same jet as the sample. Another important prerequisite in order to get an adequate reference spectrum is to use a substance chemically most similar to the sample under study. The widths of  $K\alpha_1$  for reference compounds are  $\text{FWHM}(\text{CuO}) = 3.19$  eV and  $\text{FWHM}(\text{Cu}_2\text{O}) = 2.92$  eV. As expected, the emission line of  $\text{CuO}$  is wider. However, the emission line of the investigated complex is slightly more narrow and has a different shape than for  $\text{Cu}_2\text{O}$ :  $\text{FWHM}(\text{Cu}_2(\text{NSSN})_2) = 2.78$  eV (see Fig. 5.33). Due to the differences in the shape of emission lines of  $\text{Cu}_2\text{O}$  and



**Figure 5.32:**  $K\alpha_1$  spectra of the ground and photoexcited states and the difference between them. Amplitudes of both are normalised to 1. For details of calculation of the errorbars see text.

$\text{Cu}_2(\text{NSSN})_2$ , the ground state spectrum of  $\text{Cu}_2(\text{NSSN})_2$  was used as the reference for  $\text{Cu}^{+1}$ . This way one unknown parameter is removed from the analysis: the energy scales of the transient and the ground state spectra are the same. The spectrum of  $\text{CuO}$  was used as the reference for the excited state.

When the theoretical transient is calculated, there are some unknowns which have to be taken into account: energy shift between the reference spectra  $dE$  and relative amplitude  $amp$  of  $\text{Cu}^{+2}$  emission line compared to  $\text{Cu}^{+1}$ . Since the exact position of the  $\text{Cu}^{+2}$  emission line relative to  $\text{Cu}^{+1}$  in this experiment was unknown, the  $\text{CuO}$  spectrum was shifted relative to the ground state spectrum between 0 and 3.5 eV. Zero energy shift was defined as the position at which centres of  $\text{Cu}^{+1}$  and  $\text{Cu}^{+2}$  emission lines coincide. The centre was defined as the point in the middle between two sides of a peak at the height of 0.6. Amplitudes of  $\text{Cu}^{+1}$  and  $\text{Cu}^{+2}$  emission lines are not necessarily the same. The area under the emission line should not change for different oxidation states, therefore we expect that the amplitude of a wider  $\text{Cu}^{+2}$  peak is lower than for  $\text{Cu}^{+1}$ . At the same time a laser pulse causes local heating of the sample which should result in the reduction of the solution density, causing additional decrease of the line amplitude. For the data reduction all acquired spectra were merged and maxima of both  $\text{Cu}^{+1}$  and  $\text{Cu}^{+2}$  lines were normalised to 1.0. For the fit the amplitude of  $\text{Cu}^{+2}$  was varied between 0.9 and 1.0. For all combinations of these parameters (energy shift  $dE$ , relative amplitude  $amp$ ) the theoretical transient was calculated, multiplied by the excited state fraction  $f$  (varied between 1% and 30%) and compared to the experimental transient. The goodness of match was evaluated with  $\chi_{red}^2$  parameter, which was calculated as

$$\chi_{red}^2 = \frac{1}{N-1} \cdot \sum \left( \frac{f \cdot \text{Tr}_{\text{calc}}(dE, amp, f) - \text{Tr}_{\text{exp}}}{stderr} \right)^2, \quad (5.20)$$

where  $N$  is the number of points in the spectrum. The standard error  $stderr$  for each point of the transient spectrum  $i$  was calculated as the standard error of the difference of ground and pumped states spectra  $stderr = \sqrt{stderr_{GS}^2 + stderr_{PS}^2}$ . The standard error for these spectra was calculated as  $stderr_i = stddev_i / \sqrt{n}$ , where  $n$  is the number of measurements,  $n = 35$

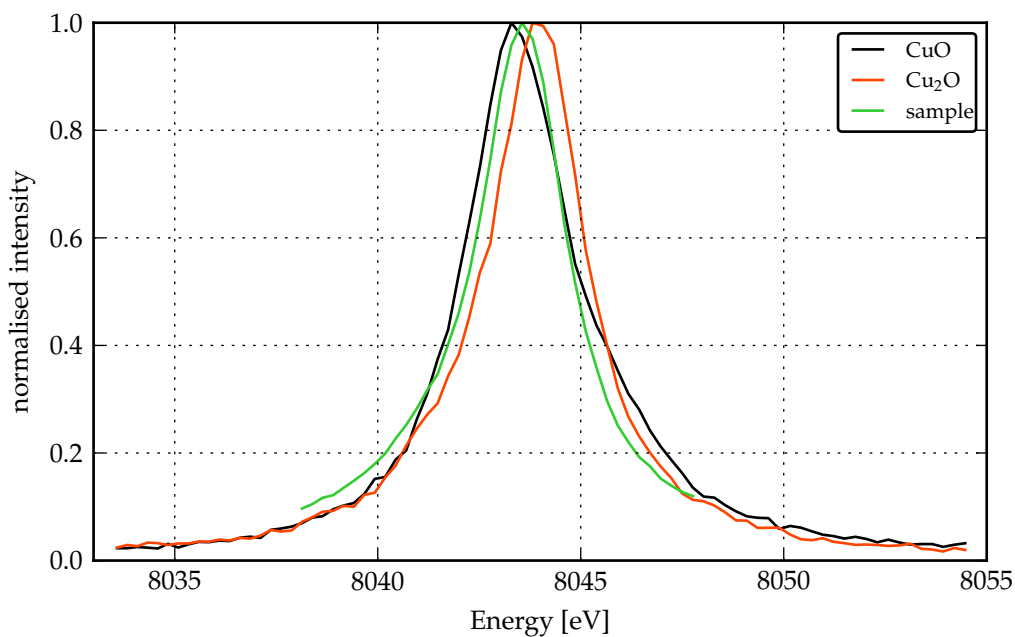


Figure 5.33: Spectra of copper oxides (references) and the sample  $\text{Cu}_2(\text{NSSN})_2$ .

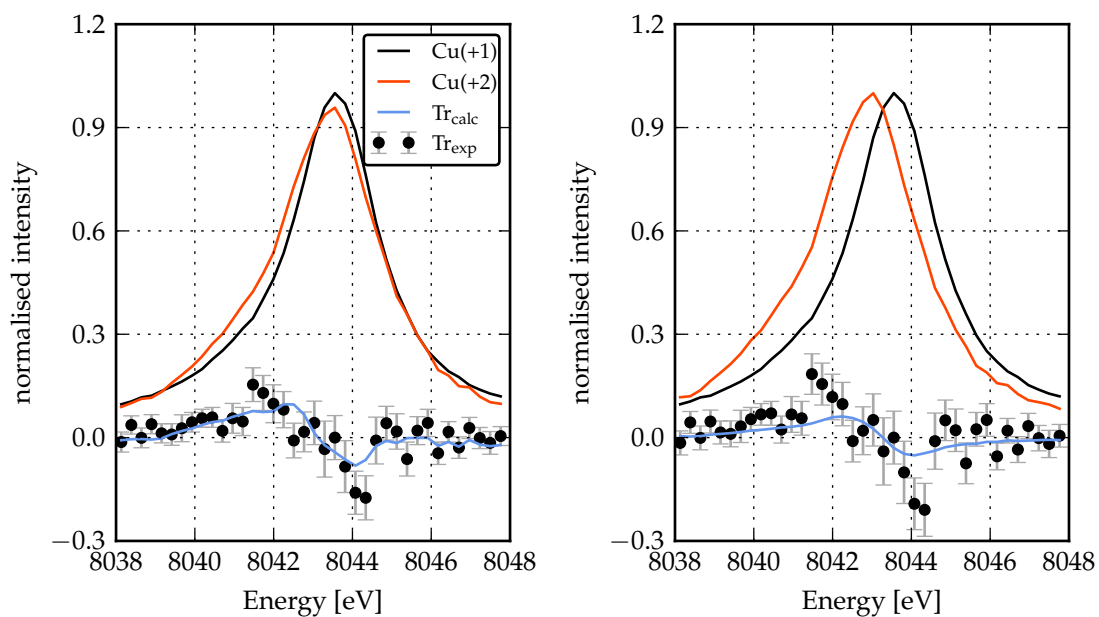
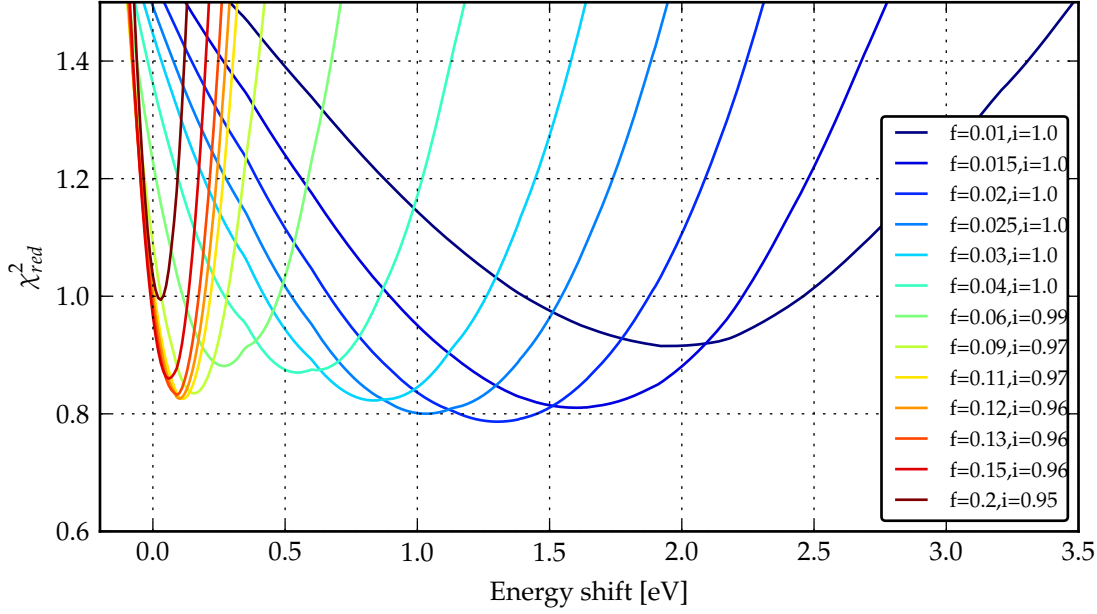


Figure 5.34: Two local minima on the space of unknown parameters of transient XES. For the details see text.

Right:  $\chi_{red}^2 = 0.77$  at  $f = 0.02$ ,  $\text{amp}(\text{Cu}^{+2}) = 1.00$ ,  $dE = 1.3$  eV. Experimental and calculated transients are scaled to 20%.

Left:  $\chi_{red}^2 = 0.83$  at  $f = 0.12$ ,  $\text{amp}(\text{Cu}^{+2}) = 0.96$ ,  $dE = 0.1\text{-}0.2$  eV. Experimental transient is scaled to 100%.



**Figure 5.35:**  $\chi_{red}^2$  as a function of energy shift between the ground state spectrum and the reference CuO. For each excited state fraction  $f$  the best relative amplitude  $amp$  is plotted ( $i$  in the legend).

or 51; the standard deviation of measured signal at each point was calculated as  $stddev_i =$

$$\sqrt{\frac{1}{n-1} \sum_{j=1}^n (I_{ij} - \bar{I}_i)^2}.$$

In this parameter space there are two local minima of  $\chi_{red}^2$  (see Fig. 5.34 and 5.35). The following parameters lie within 5% increase in local minima values of  $\chi_{red}^2$ :  $dE = 0.1 - 0.2$  eV and  $f = 9 - 15\%$ ; and  $dE = 0.9 - 1.7$  eV and  $f = 1.5 - 3\%$ . For both minima  $\chi_{red}^2 < 1$ , which could mean that the error bars are overestimated. In the reported  $K\alpha$  spectra for Mn and Fe the energy shift upon change of oxidation state is almost absent [Gla01; Van+06], which makes the first local minimum more reasonable. However, one should note that there are differences in the shape between the experimental and calculated transients, because shapes of  $K\alpha_1$  of CuO and excited state of the sample are not the same. Therefore, the shape of  $\chi_{red}^2$  map is distorted from the real picture. As an alternative approach to estimation of the ES fraction,  $f$  was calculated as the ratio of amplitudes of the experimental and calculated transients:  $f = \max(\text{Tr}_{\text{exp}}) / \max(\text{Tr}_{\text{calc}})$ . In this approach the shape of the calculated transient is not taken into account and only its amplitude matters. By shifting the CuO spectrum relatively to the ground state spectrum by 0.0 to 1.0 eV we obtained the value of  $f$  between 4 and 15%. Smaller energy shifts correspond to bigger excited state fractions. Since more precise estimation of  $f$  was not possible, it was fitted as an independent parameter when analysing transient WAXS data.

### 5.4.3 Transient wide-angle X-ray scattering

In order to follow photoinduced structural changes in the investigated complex, a pump-probe wide-angle X-ray scattering (WAXS) experiment was performed. Unlike transient EXAFS, transient WAXS is not a local probe and is sensitive to photoinduced changes in distances between all atoms in solution. In this method difference in the X-ray scattering between laser-excited and steady sample is measured. The experiment was carried out on  $\text{Cu}_2(\text{NSSN})_2(\text{OTf})_2$  solution in DFB with 400 nm photoexcitation. The difference scattering signal as a function of momentum transfer  $q$  at 100 ps delay is shown in Fig. 5.36. The momentum transfer

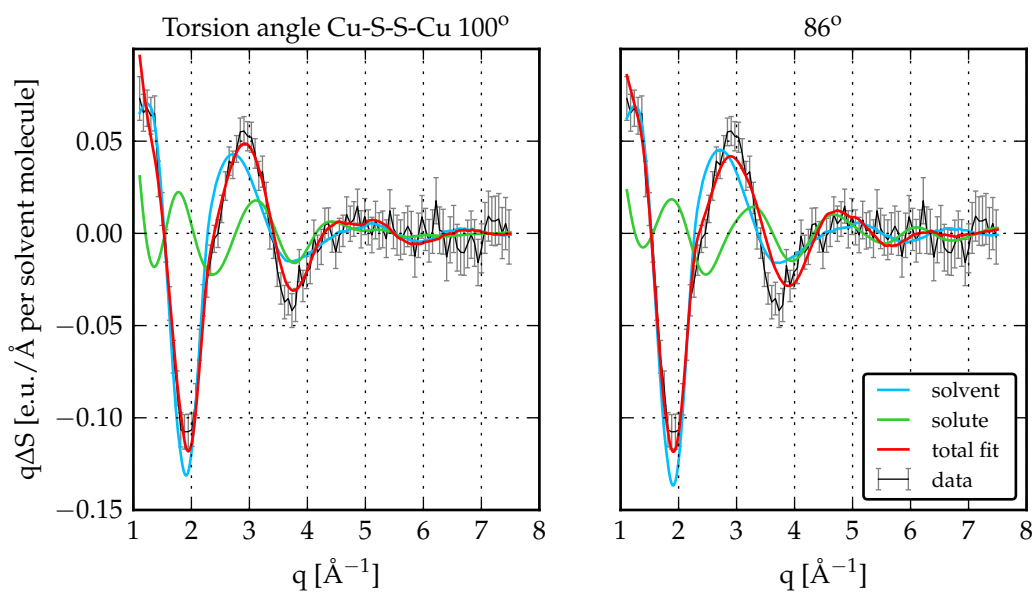


**Figure 5.36:** Difference scattering signal  $\Delta S(q)$  and best fits for two structures with different torsion angles Cu-S-S-Cu. Left: torsion angle  $100^\circ$ , in the vicinity of the global minimum of  $\chi_{red}^2$ . Right: torsion angle  $86^\circ$ . The main sensitivity of the fit is in the  $q = 2.5 - 4.5 \text{ \AA}^{-1}$ .

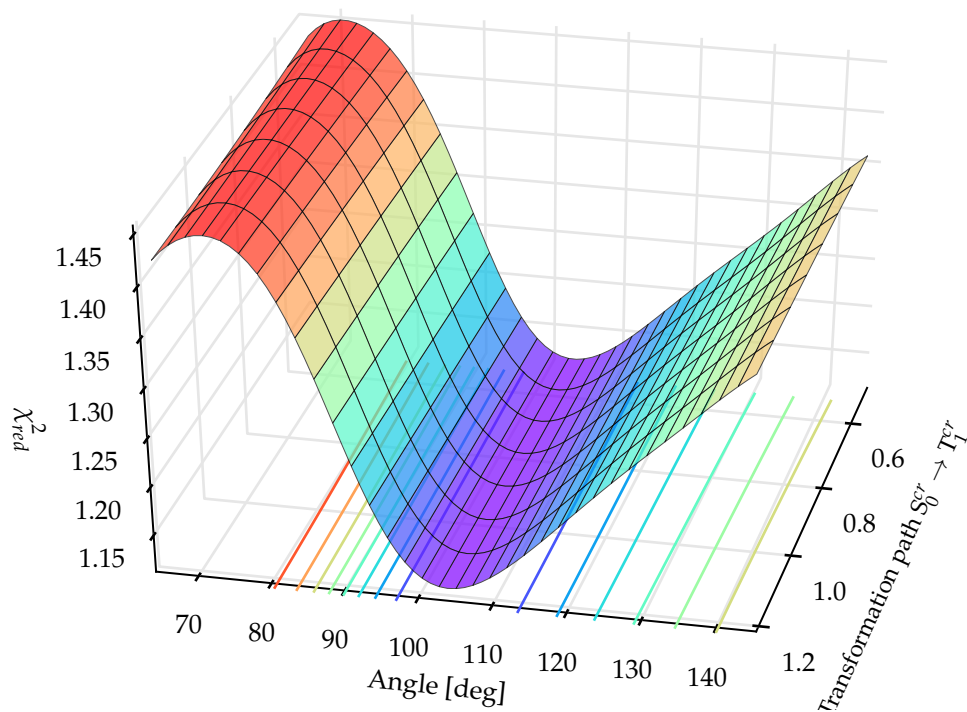


**Figure 5.37:**  $\chi_{red}^2$  for fitting of trWAXS data as a function of copper-ligand bond lengths (transformation path  $S_0^{cr} \rightarrow T_1^{cr}$ ) and torsion angle Cu-S-S-Cu (rotational angle between two parts of the molecule).

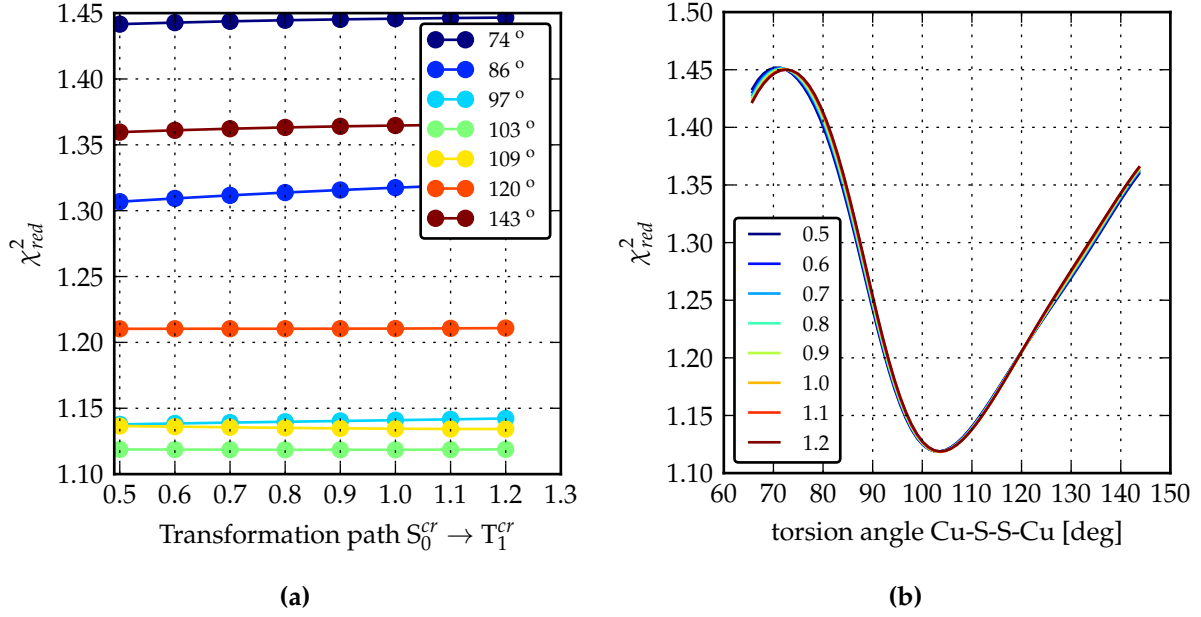


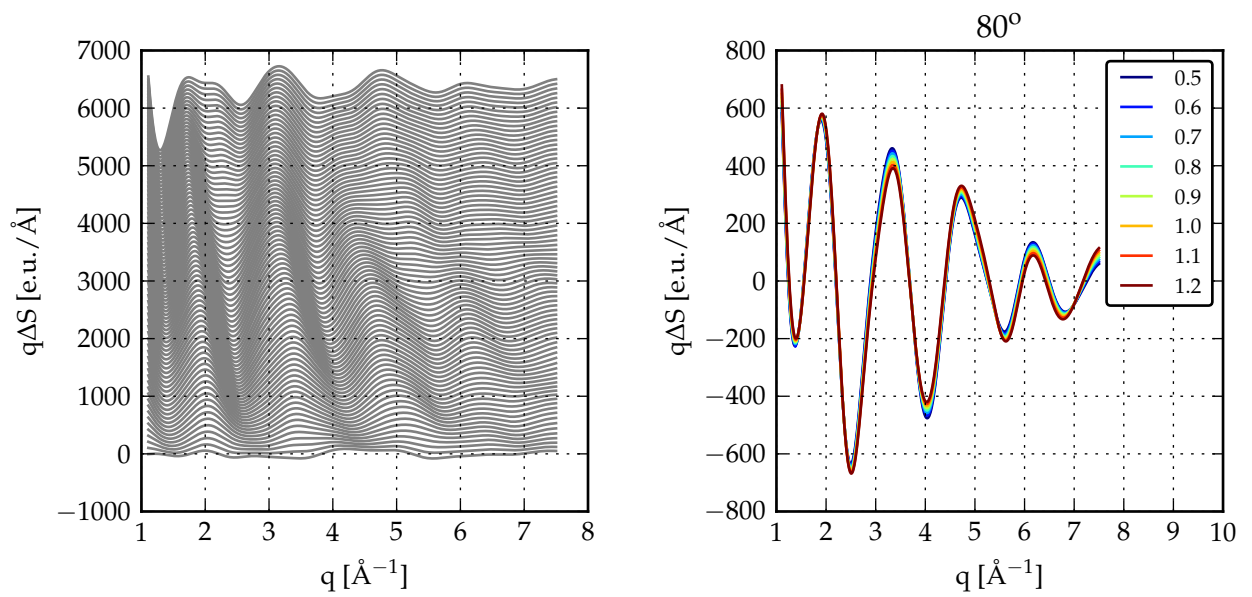
**Figure 5.38:** Slices of 3D  $\chi_{red}^2$  surface shown in Fig. 5.37. a)  $\chi_{red}^2$  as a function of coordination bonds lengths for certain values of Cu-S-S-Cu torsion angle; b)  $\chi_{red}^2$  as a function of the torsion angle for all investigated coordination bonds lengths.

$q = \frac{4\pi}{\lambda} \sin(\frac{2\theta}{2})$ , where  $\lambda$  is the X-ray wavelength and  $2\theta$  is the scattering angle. The data analysis was based on fitting the experimental transient spectrum with spectra calculated for different structural models. The fitting was performed with equation 5.21.

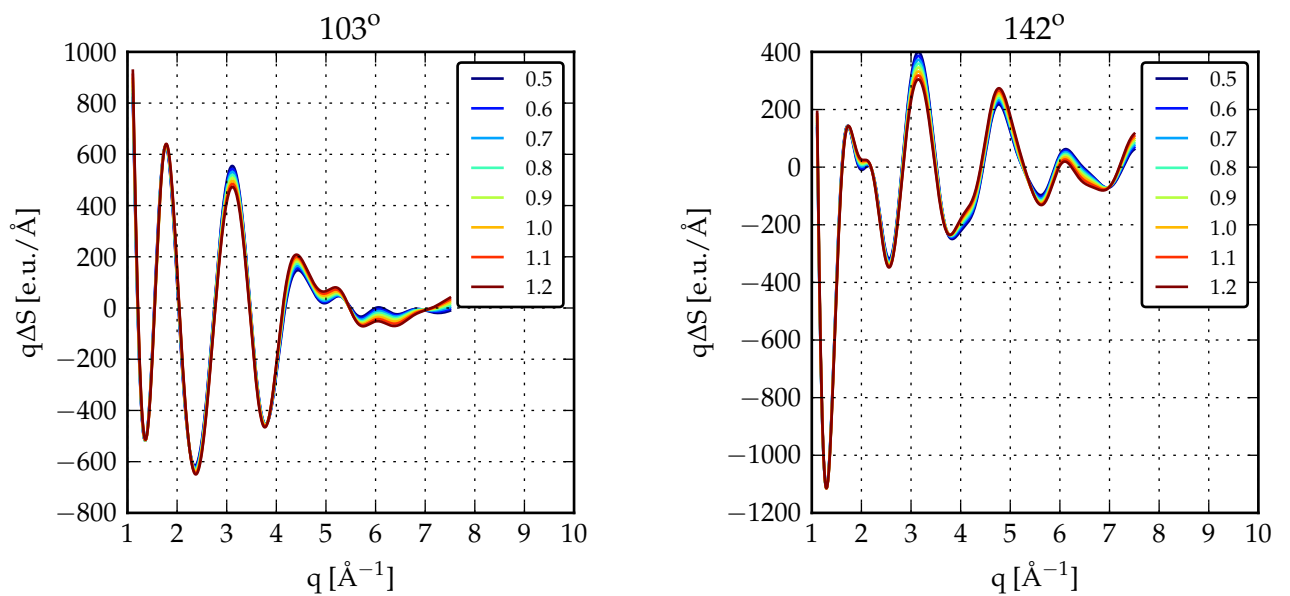
$$\Delta S(q, t)^{fit} = R \cdot f(t) \cdot \Delta S(q)_{solute}^{calc} + \left( \left( \frac{\partial S(q)}{\partial T} \right)_{\rho} \cdot \Delta T(t) + \left( \frac{\partial S(q)}{\partial \rho} \right)_{T} \cdot \Delta \rho(t) \right)_{solvent} \quad (5.21)$$

In this equation the first term in the sum represents the contribution from the structural changes in the solute, whereas the second accounts for changes in temperature and density of the solvent due to the deposited energy from relaxing solute molecules. The signal originating due to changes in solute-solvent interatomic distances ("cage term") was not taken into account in the present analysis as it is only expected to considerably contribute at lower values of  $q$  below  $1 \text{ \AA}^{-1}$ . The solute term  $\Delta S(q)_{solute}^{calc}$  is the calculated difference signal between the excited and ground states of the molecule.  $R$  is the molar ratio of solute to solvent molecules and  $f(t)$  is the excited state fraction. The differential terms  $\left( \frac{\partial S(q)}{\partial T} \right)_{\rho}$  and  $\left( \frac{\partial S(q)}{\partial \rho} \right)_{T}$  are the scattering responses of the solvent bulk to the ultrafast heating due to temperature increase and concomitant density decrease due to the thermal expansion [Cam+06]. The solvent-related differentials were obtained in a separate scattering measurement using the solution of an azobenzene dye as explained in section 4.3. The solute scattering signals for the ground and various excited structures were calculated according to eq. 4.7 and then convolved with the "pink" spectrum of the X-ray beam by computing a weighted sum of the scattering signals for 200 components equally spaced in energy over the entire spectrum.

Since transient WAXS is sensitive to the whole 3D structure of the molecule, in order to model excited state structures additional structural factors had to be taken into account. We could not apply only changes to copper-ligand distances, like for the transient EXAFS modelling, but also relative positions of two parts of molecule had to be considered. Following the DFT predictions for the triplet state,  $\Delta R \cdot S_0^{cr} \rightarrow T_1^{cr}$  structures (used for the transient EXAFS fit,  $\Delta R$



(a)  $\Delta S(q)_{solute}$  for structure 1.0  $S_0^{cr} \rightarrow T_1^{cr}$  with different torsion angles Cu-S-S-Cu. The angle linearly grows from bottom to top from  $52^\circ$  to  $142^\circ$ .



(b)

(c)

**Figure 5.39:** Difference solute signal as a function of  $q$  for fixed bond lengths and different torsion angles Cu-S-S-Cu (a) and fixed torsion angles Cu-S-S-Cu and different bond lengths (b,c,d).

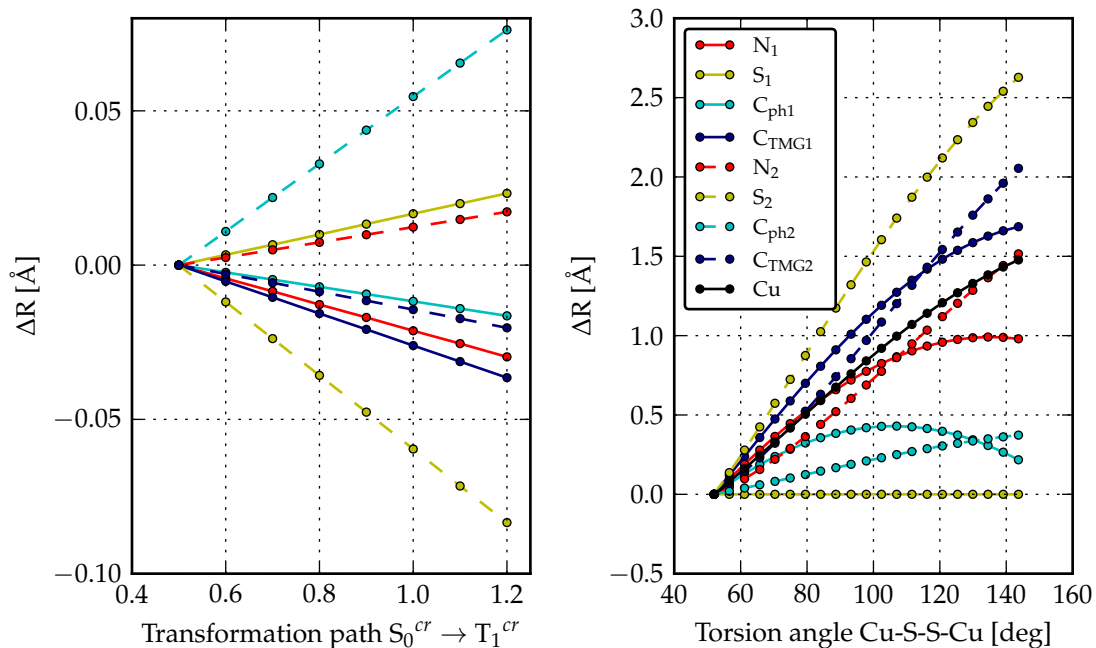


**Figure 5.40:** Margins of distance changes between certain atoms upon structural refinement. For details see text. Left: distance changes from  $Cu_1$  to certain atoms of  $Cu_1$  ligand system upon coordination sphere refinement: coordinating nitrogen and sulfur ( $N_1, N_2, S_1, S_2$ ), a carbon of phenyl group ( $C_{ph1}, C_{ph2}$ ), a carbon of TMG group ( $C_{TMG1}, C_{TMG2}$ ). Indices 1 and 2 denote two different ligands. Right: relative change of distance from  $Cu_2$  to the atoms shown on the left figure upon change of the torsion angle Cu-S-S-Cu. Additionally  $Cu_1$ - $Cu_2$  distance change is shown. From all distance changes the starting value is subtracted in order to bring them on the same scale.

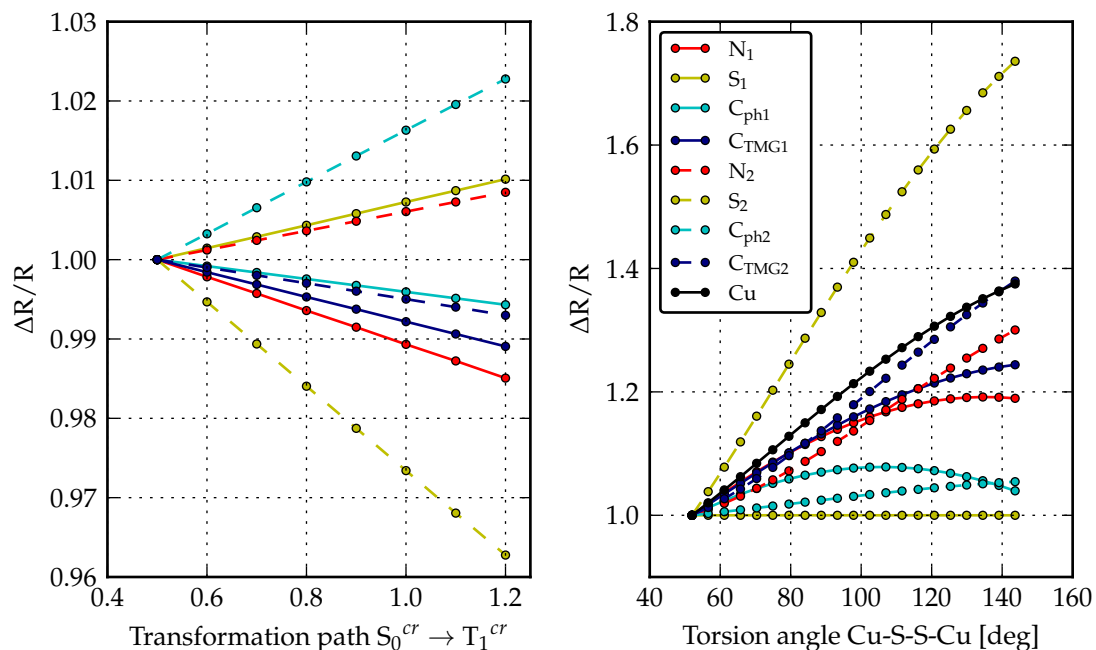


**Figure 5.41:** The same as in Fig. 5.40 shown in relative units: distance changes are normalised by dividing by the starting value.

= 0.5 – 1.2) were taken and one of the S-S bonds was used as a rotation axis for two halves of the molecule. For all combinations of Cu-ligand bond lengths and geometrically reasonable torsion angles Cu-S-S-Cu (from 52° as in the ground state to 144°, when ligands from two copper sites would hinder further movement of each other) the theoretical solute difference signal was calculated. The goodness of the fit was evaluated by calculating the  $\chi_{red}^2$  estimator following the equation:

$$\chi_{red}^2 = \frac{1}{N - p - 1} \sum_q \frac{(\Delta S(q, t)^{fit} - \Delta S(q, t)^{exp})^2}{\sigma^2}, \quad (5.22)$$

where  $N$  is the total number of  $q$  points,  $p$  is the number of fitting parameters,  $\sigma^2$  is the standard deviation for each data point,  $\Delta S(q, t)^{exp}$  is the experimental difference scattering and  $\Delta S(q, t)^{fit}$  is the theoretically predicted signal according to eq. 5.21 for a given set of the non-structural fitting parameters ( $f(t)$ ,  $\Delta T(t)$ ,  $\Delta\rho(t)$ ) and a given excited state structure defined by the two considered structural degrees of freedom. The sum in eq. 5.22 is calculated over all  $q$  points. To increase the statistical significance of the fits, all delays below 20 ns were fitted and the  $\chi_{red}^2$  values for them were averaged. A surface plot of  $\chi_{red}^2$  values on the space of structural parameters is shown in Fig. 5.37 while Fig. 5.38 represents different slices of  $\chi_{red}^2$  surface.

Fig. 5.39 demonstrates the effect of changing the Cu-ligand bond lengths along the transformation path  $S_0^{cr} \rightarrow T_1^{cr}$  and the Cu-S-S-Cu torsion angle on the shape of calculated solute difference scattering signal  $\Delta S(q)_{solute}^{calc}$ . The structural changes in the first coordination shell along the transformation  $S_0^{cr} \rightarrow T_1^{cr}$  do not have much influence on  $\Delta S(q)_{solute}^{calc}$  and their effect mostly manifests itself in the amplitude rather than in the phase of oscillations. Consequently the  $\chi_{red}^2$  value is hardly sensitive to this parameter (see Fig. 5.37): small changes in the signal amplitude are compensated by adjusting value of the ES fraction  $f(t)$  in the fitting procedure. On the other hand, the shape of  $\Delta S(q)_{solute}^{calc}$  signal strongly depends on the torsion angle, changing  $\chi_{red}^2$  from 1.12 to 1.45 for different angle values. The minimum of  $\chi_{red}^2$  was found at Cu-S-S-Cu torsion angle of 104°; angles between 98° and 109° result in fits within  $3\sigma$  confidence interval. It corresponds to torsion angle  $C_{ph}-S-S-C_{ph}$  of  $59^{+6}_{-5}$ , compared to 67° predicted by DFT for the triplet). The best-fit triplet structure is shown in Fig. 5.44b.

In order to illustrate why only one of the structural degrees of freedom has a strong effect on the fit, the distance changes between different pairs of atoms for both types of structural variations are plotted in figures 5.40 and 5.41. Fig. 5.40 shows the absolute changes, whereas Fig. 5.41 illustrates the relative changes. The changes are calculated relative to the starting structure (0.5  $S_0^{cr} \rightarrow T_1^{cr}$  and 52°). These plots show that variations in Cu-ligand bonds lengths result in maximum changes of interatomic distances of 0.08 Å, whereas the torsion angle variations cause changes in distances between some atoms of more than 1-2 Å. In particular, the Cu-Cu distance between two limit positions of torsion angle (52° to 144°) changes from 3.94 Å to 5.41 Å (37%), and for the cleaved S-S bond the distance between the sulfurs increases more than three times: from 2.19 Å to 6.86 Å. Therefore, the shape of  $\Delta S(q)_{solute}^{calc}$  exhibits much stronger dependence on the torsion angle variation within our range.

In order to follow the time evolution of the system, the transient signal at different delays between pump and probe pulses was registered. The best-fit structure (with the lowest  $\chi_{red}^2$ ) was used to fit the spectra at different delay times (Fig. 5.43). The fitting results demonstrates that the shape of the transient signal does not change with time, and excited state fraction extracted from these fits is plotted in Fig. 5.42. The maximum ES fraction at early delays reached approximately 0.09, which falls into the range estimated from the transient XES analysis (4 – 15 %). The fitting was performed with eq. 5.19 (exponential decay to an offset convolved with Gaussian profile of the X-ray pulse). The extracted lifetime was found to be  $2.9 \pm 0.7$  ns, which is longer than the lifetime extracted from transient XAS data in acetonitrile ( $1.53 \pm 0.04$  ns).

Comparing two fits in Fig. 5.36, it is important to note that structural sensitivity of the fit

**Table 5.11:** Torsion angle  $C_{\text{ph}}\text{-S-S-}C_{\text{ph}}$  of crystallised NSSN ligand and  $\text{Cu}_2(\text{NSSN})_2$  complex in comparison to values obtained from DFT (B3LYP cc-pVDZ).

structure	DFT	crystallographic
NSSN (ligand)	87°	85°
$\text{Cu}_2(\text{NSSN})_2$ ground state	95°	103°,108°
$\text{Cu}_2(\text{NSSN})_2$ triplet $T_1$	67°	$59^{\circ+6}_{-5}$ (fit)

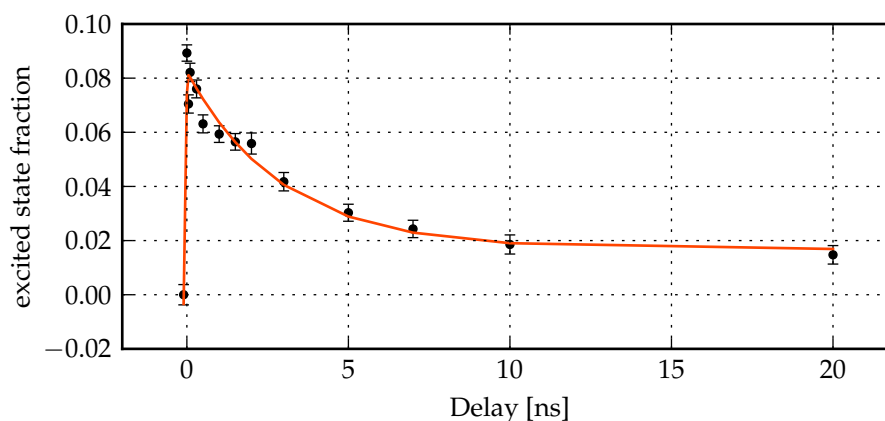


**Figure 5.42:** Excited state fraction  $f$  as a function of time delay between the pump and the probe pulses.  $f$  is extracted from fitting the solute contribution to the transient signal as shown in Fig. 5.43. Red line shows the fit with eq. 5.19, lifetime  $\tau = 2.9 \pm 0.7$  ns.

for this data set comes mainly from the  $q$ -range of  $2.5 - 4.5 \text{ \AA}^{-1}$ . At lower  $q$  the solvent signal dominates the spectrum, and starting from the  $q = 4.5 \text{ \AA}^{-1}$  no oscillations can be distinguished within the noise. In order to increase the structural sensitivity of the method, a stronger contribution of the solute signal compared to the solvent would be beneficial. It can be achieved by choosing a different solvent, such as ACN, and by increase of the excited state fraction. Furthermore, the part of the spectrum in the  $q$  range of  $0 - 1 \text{ \AA}^{-1}$  can be included into the fit if the cage term is modelled.

Since the theory predicts a significant change of torsion angle  $C_{\text{ph}}\text{-S-S-}C_{\text{ph}}$  between excited and ground states, it is interesting to address the value of this angle for free ligand NSSN and ground and excited states of  $\text{Cu}_2(\text{NSSN})_2$  and compare theoretical and experimental values (see Table 5.11). The DFT-calculated torsion angle  $C_{\text{ph}}\text{-S-S-}C_{\text{ph}}$  in the copper complex is larger than in the pure ligand:  $95^\circ$  vs  $87^\circ$ . For crystallographic structures the angle change is even bigger:  $105^\circ$  (averaged) vs  $85^\circ$ . For the photoexcited triplet state  $T_1$  DFT predicts decrease of the angle by  $28^\circ$  compared to the ground state – down to  $67^\circ$ . The best fit from trWAXS is achieved for the close-lying value of  $59^{\circ+6}_{-5}$ , which is achieved by rotation by  $52^\circ$  from the crystallographic ground state structure.

#### 5.4.4 Summary

This chapter reports the results of combined pump-probe X-ray emission spectroscopy and wide-angle X-ray scattering experiment. Photoexcitation of MLCT transition causes widening and slight shift ( $\sim$  tenth of eV) of the Cu  $K\alpha_1$  emission line to lower energies, which is in agreement with the observations reported for iron and manganese complexes. Copper oxides are not the most suitable references for X-ray emission spectra for the ground and excited states of  $\text{Cu}_2(\text{NSSN})_2$ : linewidth for  $\text{Cu}_2\text{O}$  is bigger than for  $\text{Cu}_2(\text{NSSN})_2$ . Despite that, the excited state fraction could be estimated as being 4 – 15 % by comparing the amplitudes of the calculated

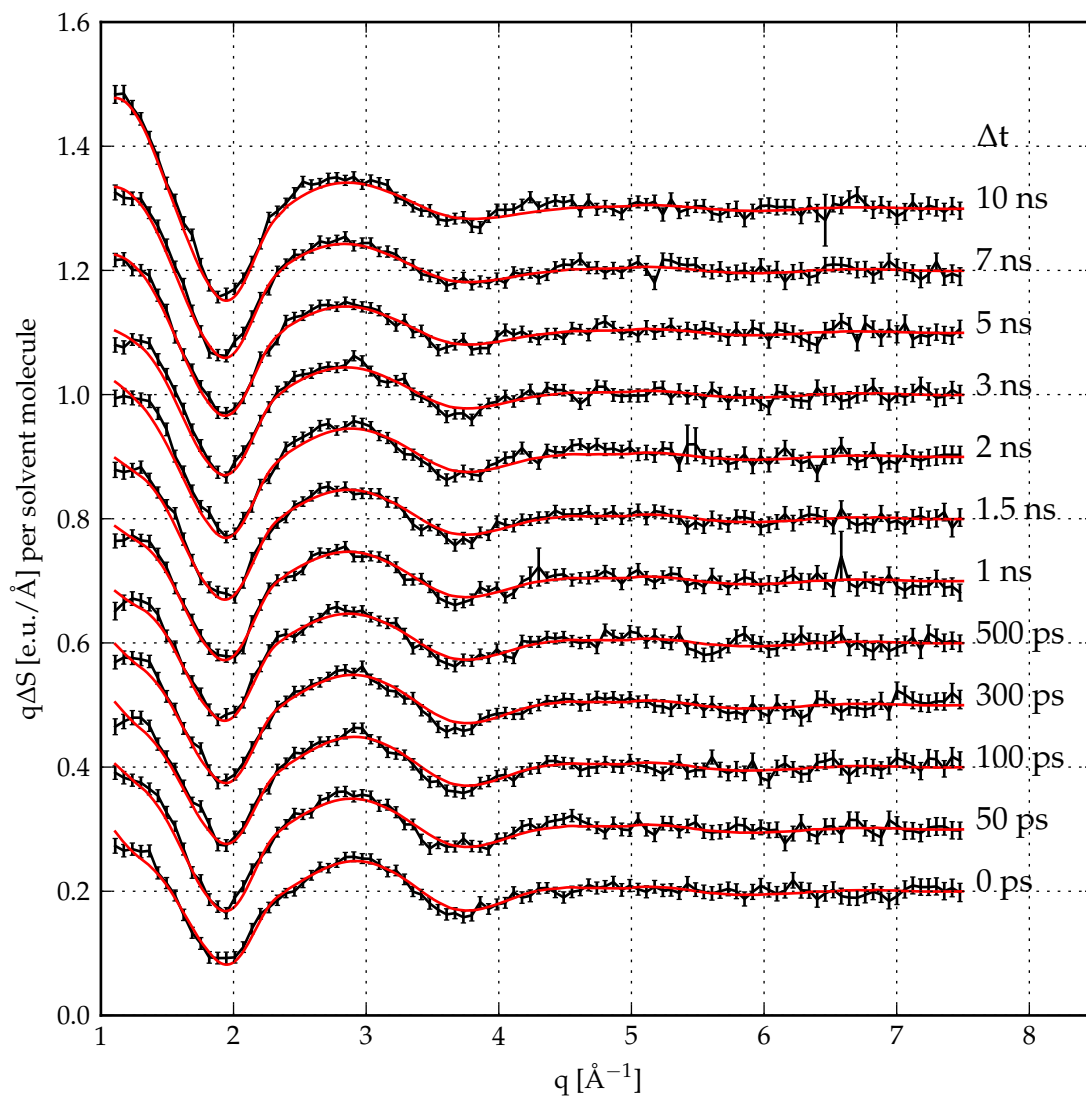


**Figure 5.43:**  $\Delta S(q)$  as a function of time delay between laser and X-ray pulses. Red lines show fits with eq. 5.21.

and the experimental transients. This range is in agreement with the value extracted from the trWAXS fit (9%). The analysis of the transient WAXS data demonstrates that in a compound like  $\text{Cu}_2(\text{NSSN})_2$ , with many atomic pairs of different origin building up the scattering signal, the fit is not so sensitive to small changes of bond lengths which happen in the coordination sphere of copper, however, it is sensitive to conformational changes in the molecule, when many atoms significantly change their relative positions. The experimental data are in agreement with DFT-predicted structure, when one of the S-S bonds breaks, causing increase in the torsion angle Cu-S-S-Cu, which was found to be  $104^{\circ+11}_{-9}$ . In contrast with trWAXS, changes in the first coordination shell of copper could be resolved in the transient EXAFS analysis as reported in section 5.3. The discussion of the structural dynamics based on the comparative analysis of both methods is presented in the next section.

## 5.5 Discussion of the photocycle of $\text{Cu}_2(\text{NSSN})_2$

This section summarises the steps of the photoinduced structural evolution of solvated  $\text{Cu}_2(\text{NSSN})_2$  based on the performed experiments and theoretical calculations.

The sample was excited with 343 nm photons for the transient EXAFS experiment and with 400 nm photons for the transient optical absorption and transient WAXS measurements. Both wavelengths drive the MLCT transition from an orbital with strong Cu 3d character to a sigma-antibonding orbital localised at disulfide bridges. Photons of both wavelengths excite the molecule to one of the higher excited states  $S_n$ : the MLCT absorption band has a maximum at 410 – 420 nm, whereas excitations to lower singlet states should happen in the red tail of the absorption band, which extends down to 600 nm. As probed by transient absorption spectroscopy in UV-vis, after photoexcitation with 400 nm photons > 60 % of molecules undergo radiationless deexcitation to the ground state with  $\sim 650$  fs lifetime. This ultrafast decay may also include competing IC  $S_n \rightarrow S_1$ . The remaining < 40 % of the excited species undergo further evolution with lifetime of 11 ps which we assign to be ISC to the triplet state. This assignment is based on the literature analysis (ISC on 2-30 ps timescale for monocopper complexes) and on further confirmation of the calculated triplet structure in transient EXAFS and transient WAXS experiments.

DFT calculations predict that, due to excitation of an electron to an antibonding orbital of disulfide bridges, one or both S-S bonds are significantly elongated in the excited singlets. In the lowest triplet state  $T_1$  ( $^3\text{MLCT}$ ), one of S-S bonds is cleaved and two parts of the molecule rotate around the remaining S-S bond away from each other: the torsion angle Cu-S-S-Cu increases from  $70^\circ$  to  $98^\circ$  while the torsion angle in the ligand  $\text{C}_{\text{ph}}\text{-S-S-C}_{\text{ph}}$  decreases from  $95^\circ$  to  $67^\circ$ . At the same time elongation and contraction of the coordination bonds Cu-N and Cu-S takes place: Cu-N by  $-0.044$  and  $+0.026$  Å; Cu-S by  $+0.035$  and  $-0.125$  Å. The coordination polyhedron flattens slightly: the angle between the chelate ligand planes changes from  $89^\circ$  to  $77^\circ$ . The DFT-calculated ground state structure shows good agreement with crystallographic data in intraligand distances, as shown in table 5.1, however, the Cu-ligand bond lengths are approx. 10 % longer than the those obtained in a XRD experiment. It shows that molecular complexes like the one investigated in this thesis still present challenges to theory. Despite the fact that DFT-calculated structures could not be directly used for the fit, the structure  $T_1^{\text{cr}}$ , constructed out of the crystallographic structure based on *differences* between calculated  $T_1$  and  $S_0$ , was successfully used as a structural model for both pump-probe X-ray techniques.

In the synchrotron-based pump-probe X-ray experiments providing 70 – 100 ps resolution only the triplet structure should be observed. In this work, the combination of transient EXAFS and transient WAXS provides access to different structural degrees of freedom of the excited state. EXAFS is a photoelectron technique, with the limitation of structural sensitivity up to a distance of 3 – 4 Å for low-symmetry molecular structures like  $\text{Cu}_2(\text{NSSN})_2$ . Contributions from the first and second coordination shells dominate the transient EXAFS signal. The Cu-Cu distance is 3.9 Å in the ground state and increases in the excited state. This is why, based on the transient EXAFS experiment only, we cannot conclude how the Cu-Cu distance changes in the excited state. WAXS, on the other hand, is based on elastic scattering of X-rays, and is sensitive to the changes in the whole structure and relative orientation of parts of the molecule within the volume of coherent illumination. The transient WAXS fit was not sensitive to the refinement of the coordination bond lengths. However, it showed strong sensitivity to the value of torsion angle Cu-S-S-Cu, since a change of this parameter causes strong changes in the distances between many atoms of the molecule. TrEXAFS yields the following Cu-ligand distance changes: Cu-N =  $-0.035 \pm 0.009$  and  $+0.020 \pm 0.005$  Å, Cu-S =  $+0.026 \pm 0.007$  and  $-0.095 \pm 0.024$  Å as shown on scheme 5.44a. From transient WAXS the torsion angle Cu-S-S-Cu was found to be  $104^\circ \pm \frac{6}{5}$  as shown on scheme 5.44b. The given errors correspond to  $3\sigma$  confidence level from  $\chi_{\text{red}}^2$  estimator. For both

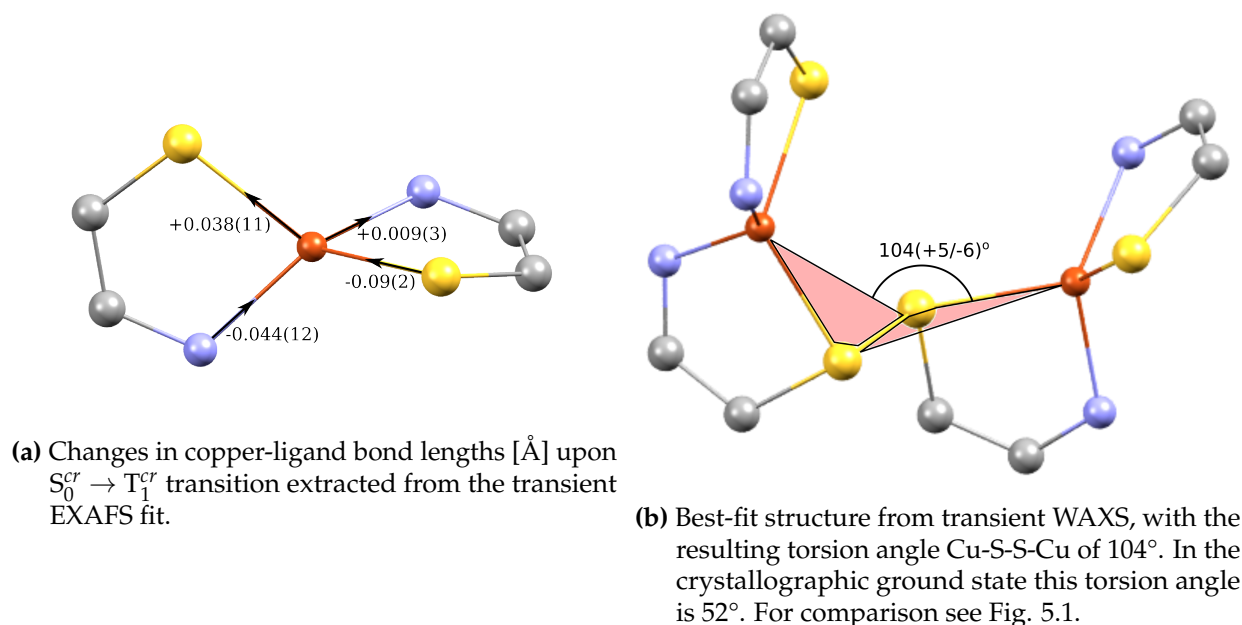


**Figure 5.44:** Best-fit structures from transient EXAFS and transient WAXS analysis.

techniques, modelling results in quite good fits with reasonable non-structural parameters, such as the excited state fraction and the chemical shift in transient EXAFS as well as the excited state fraction in transient WAXS.

It is important to note that our model uses a rather simplified structural parametrisation. Indeed, the ligands are moved as fixed units, and it is hard to parametrise relative orientation of different parts of the molecule, which is especially important for modelling WAXS data, which are sensitive to the 3D structure of the molecule. An additional uncertainty may originate due to the TMG unit of the molecule which has several sigma bonds C-C and C-N, around which rotation is possible to a certain degree. This simplification could be the reason for deviations between the calculated and the experimental data.

It should be noted that the performed experiments do not provide the direct proof that one of the S-S bonds is cleaved in the triplet state. An interesting experiment which would be able to probe this bond directly, is pump-probe transient XAS on the sulfur K-edge. Still, the analysis of the transient WAXS data shows that two parts of the molecule are rotated with respect to each other which is only possible if one of S-S bonds is cleaved.

The lifetime of the triplet state was measured in both X-ray experiments. For a solution at room temperature, the  $T_1 \rightarrow S_0$  transition follows the non-radiative pathway (no or very weak optical emission was observed in DCM and ACN). The solution of  $\text{Cu}_2(\text{NSSN})_2$  in ACN, as measured by transient EXAFS, demonstrates the lifetime of  $1.53 \pm 0.04$  ns, while transient WAXS measurements on DFB solution yield the lifetime of  $2.9 \pm 0.7$  ns. Comparison of both decays with the fits is given in Fig. 5.45. Since the resulting lifetimes are very similar, it seems that the influence of the solvent on the deexcitation of the triplet state is weak. This is quite remarkable, since donating solvents, like ACN, can significantly accelerate deexcitation of triplet states in copper complexes [Pen+13; Dic+17]. However, DFB is not a common solvent, and there is no data on lifetimes of copper complexes in it. For a more direct comparison of the lifetimes of  $\text{Cu}_2(\text{NSSN})_2$  in ACN and DFB a TA experiment in ns regime would be conclusive. In the literature about Cu-bisphenantroline complexes the question of solvent coordination in the excited state is widely discussed. The driving force for exciplex formation is flattening of coordination polyhedron and preference of Cu(II) for the 5- and 6-coordinated state. Transient EXAFS and TA measurements were performed in a coordinating solvent acetonitrile, which

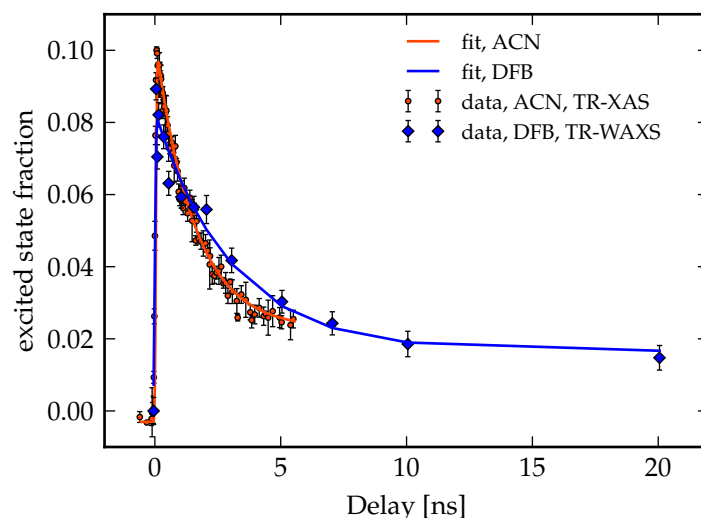


**Figure 5.45:** Time evolution of the excited state observed in transient XAS and transient WAXS experiments. Transient signals are normalised and plotted as a function of time delay between the pump and the probe pulses and fitted with equation 5.19 (+ constant offset to take into account non-zero values at the negative delays). Red: transient XAS in ACN at 8982.3 eV,  $\tau = 1.53 \pm 0.04$  ns. Green: excited state fraction extracted from transient WAXS signal in DFB,  $\tau = 2.9 \pm 0.7$  ns.

potentially could form an exciplex with excited  $\text{Cu}_2(\text{NSSN})_2$ . However, DFT predicts only small flattening of the copper coordination polyhedron – from  $89^\circ$  to  $77^\circ$  (angle between ligand chelate planes). It does not seem feasible that a solvent molecule could coordinate copper in this geometry. However, we have not addressed this question in more detail. Similar lifetimes of the triplet state for coordinating ACN and non-coordinating DFB also do not support the assumption of solvent coordination.

The next section summarises the results and concludes the thesis.

## Chapter 6

# Summary, conclusions and outlook

### 6.1 Summary and conclusions

X-ray absorption spectroscopy (XAS) is an element-specific technique which can visualise the local structure of an absorbing atom in all media. At the same time, X-ray emission spectroscopy (XES) is an efficient probe of an atomic spin. Recent development in synchrotrons, lasers and electronics allowed to extend these techniques into the pump-probe regime, making it possible to directly observe structures of short-living photoexcited states. In addition to spectroscopies, pump-probe wide-angle X-ray scattering (WAXS) can also be applied to solutions and is sensitive to structural changes of the solute, solvation shell rearrangements and the bulk solvent temperature and density. In this thesis pump-probe XAS, XES and WAXS were combined with transient absorption and luminescence in UV-vis and supported by DFT calculations in order to study photoinduced structural dynamics in a biochemically-relevant  $\text{Cu}_2(\text{NSSN})_2$  complex.

First, suitable solvents had to be identified for the experiments. The solvent had to be polar, aprotic and non-coordinating. Furthermore, low toxicity and high boiling temperature were required to make experiments using open jet under laser illumination. Because the absorption cross-section of X-rays strongly increases with the periodic number of an atom, solvents containing light atoms were preferable. 1,2-difluorobenzene (DFB) matches all these criteria.  $\text{Cu}_2(\text{NSSN})_2$  was also found to be stable in acetonitrile (ACN) in concentrated solutions, despite it being a donating solvent. These two solvents were used for the X-ray experiments. Dichloromethane (DCM) is more toxic and volatile, therefore, it was only used in optical spectroscopies for measurements in a cuvette.  $\text{Cu}_2(\text{NSSN})_2$  demonstrates different photostability in these solvents. There was no laser or X-ray damage registered in ACN solution at any measurements. However, for DFB solutions strong ( $\mu\text{J}$ ) laser pulses and X-ray radiation both caused damage, which manifested itself in UV-vis absorption spectra as reduction of metal-to-ligand charge transfer (MLCT) absorption band and increase of the absorption in the UV. Judging by this behaviour, the photoproduct does not absorb in the MLCT range, therefore, it should not contribute to the transient signals, which were analysed directly for all experiments. Interestingly, the sample demonstrates better photostability in DCM, which, like DFB, is a non-coordinating polar halogen-containing solvent. One possible reason for this could be impurities in the commercial DFB: the solvent in only is only available commercially with 98 % purity.

In order to predict molecular geometries and electronic structures of the ground state as well as photoexcited states, DFT calculations were conducted. Charge-transfer states with singlet and triplet multiplicities ( $^1\text{MLCT}$  and  $^3\text{MLCT}$ ) were calculated. The (TD-)DFT calculations predict that, due to the excitation of an electron to an antibonding orbital on disulfide bridges, one or both S-S bonds are significantly elongated in the excited singlet states. In the lowest triplet state  $T_1$  ( $^3\text{MLCT}$ ) one of the S-S bonds is cleaved, the copper-sulfur cycle opens up and two parts of the molecule rotate relative to each other around the remaining S-S bond. At the same time

elongation and contraction of the coordination bonds Cu-N and Cu-S takes place and the angle between the chelate ligand planes changes from 89° to 77°.

In order to get access to the evolution of the system at the fs-ps timescale, transient absorption in UV-vis was performed on the solutions of Cu<sub>2</sub>(NSSN)<sub>2</sub> in ACN, DCM and DFB. To the best of our knowledge, this is the first femtosecond time-resolved study on dinuclear copper complexes. With this method we identified that, upon photoexcitation to one of higher singlet states using 400 nm photons, Cu<sub>2</sub>(NSSN)<sub>2</sub> undergoes internal conversion (IC) to the ground state with the lifetime of ~650 fs ( $\geq 60\%$  of excited molecules) and intersystem crossing (ISC) to the triplet state <sup>3</sup>MLCT with ~11 ps ( $\leq 40\%$  of molecules). These two lifetimes do not show significant solvent dependence. No emission was observed in steady-state luminescence experiments in visible range. However, it is still possible that weak fs fluorescence competes with IC to the ground state.

In order to extract changes in bond lengths of copper coordination polyhedra in the excited state, transient XAS experiment was performed on ACN and DFB solutions. The DFB dataset showed high noise level and no structural information could be extracted. On the contrary, in ACN data of transient EXAFS quality could be obtained. In synchrotron-based pump-probe X-ray experiments providing 70-100 ps resolution, only the triplet structure should be observed. Modelling of the ground state EXAFS spectrum was performed with the crystallographic structure. An initial guess for the excited state triplet structure was constructed out of the crystallographic data based on DFT-predicted changes in Cu-N and Cu-S bond lengths in the triplet state. Some of the coordination bond length changes in this complex are on the order of conventional EXAFS fit errorbar (0.02 Å). Despite these small changes, fitting the data directly in the energy space along ground-triplet state structural distortion path resulted in determining distance changes with sub-pm precision: Cu-N = -0.035(9) and +0.020(5) Å, Cu-S = +0.026(7) and -0.10(2) Å. This high precision was possible due to only one structural degree of freedom refined in the fit – transformation path  $S_0^{cr} \rightarrow T_1^{cr}$ . This analysis approach also allowed us to extract non-structural parameters, such as excited state fraction and chemical shift. The chemical shift was found to be  $dE = 1.5_{-0.5}^{+1.5}$  eV, in agreement with the chemical shift expected for Cu<sup>+1</sup>→Cu<sup>+2</sup> transition and the excited state fraction was determined to be  $f = 9.5_{-3.5}^{+5.5}\%$ , which is close to the estimation from the transient data in the XANES region ( $\geq 7.4\%$ ).

Pump-probe WAXS is sensitive to photoinduced changes in interatomic distances in the whole solution. Thus, it was interesting to combine it with transient EXAFS with its local structure and chemical sensitivity. Pump-probe WAXS combined with XES was performed on a DFB solution. The latter were conducted in order to extract the excited state fraction and use it when fitting the WAXS data. The transient XES data demonstrate that in the photoexcited state the spin increases, as expected for the Cu<sup>+1</sup>→Cu<sup>+2</sup> transition. However, more suitable references than copper oxides would be necessary in order to unambiguously extract the excited state fraction. We estimated its value as  $f = 4 - 15\%$  and it was further fitted as an independent parameter in the WAXS analysis. While the distances between two Cu-centred halves of the molecule are too large to be reliably probed by transient EXAFS, transient WAXS showed sensitivity to the torsion angle Cu-S-S-Cu coupled to the rotation of two parts of molecule around the intact S-S bond. The torsion angle extracted from this data was found to be  $104_{-5}^{+6}$  (DFT: 98°), which corresponds to rotation by 52° from the ground state. At the same time, the WAXS fit was not sensitive to small changes in the coordination bonds lengths. Thus, structural data extracted from both EXAFS and WAXS show agreement with the calculations.

Previous research on the structural evolution in photoexcited copper bisphenantrolines was a grounding basis for the current study. In this work we extended this field by bringing a dicopper complex with biologically relevant copper-sulfur bonding into the focus of pump-probe X-ray and optical techniques. The long-term air and radiation stability makes Cu<sub>2</sub>(NSSN)<sub>2</sub> an interesting model to study reversible S-S bond cleavage. At the same time, photoexcitation

of an MLCT band models an electron transfer reaction, which is relevant for the biological function of certain Cu–S enzymes. For  $\text{Cu}_2(\text{NSSN})_2$  in particular, the charge transfer causes conversion from disulfide to thiolate, which is frequent in nature where it is found as one of the mechanisms of formation of the tertiary structure of proteins and protection of cells from oxidative stress. For this copper model system the disulfide–thiolate conversion can be achieved both by population of the antibonding orbital of the S–S bridge *via* photoexcitation and by chemical reaction with chloride ions. This work demonstrates that combining time-resolved X-ray absorption spectroscopy and wide-angle X-ray scattering has potential for studies of photoinduced changes in molecular systems in solution. This is one of the first studies where these two structurally-sensitive methods are applied together to investigate the photochemistry of a dinuclear copper complex providing insight into different structural aspects of its excited state.

## 6.2 Outlook

Certain aspects of the photocycle of  $\text{Cu}_2(\text{NSSN})_2$  could be further investigated with other time-resolved techniques. In particular, we do not have direct information about time scales of vibrational cooling: this phenomenon can take place in quite wide time scales (100 fs to 100 ps [Vil00]), depending on the complex, and it can be overlapped with other processes. One experimental technique sensitive to this process is fs pump-probe IR spectroscopy. For example, for a copper complex in [Dic+17], a combination of transient absorption spectroscopies in IR and UV-vis allowed to discriminate the lifetimes of ISC in the excited state and vibrational relaxation of the hot ground state. Another observable sensitive to the vibrational cooling is the ratio between Stokes and anti-Stokes regions in Raman spectra. Additional information that pump-probe Raman spectroscopy could provide about  $\text{Cu}_2(\text{NSSN})_2$  lies with its sensitivity to the S–S bond stretching vibration, which typically shows a strong signal at around  $500\text{ cm}^{-1}$ , while not being present in infrared spectra [BM73]. Bleaching of this spectral band after the photoexcitation should accompany ISC and therefore happen on the time scale of 10 ps. Transient Raman spectroscopy on this time scale should be possible with a pump-probe Raman setup recently built in our laboratory in the Center for free-electron laser science (CFEL) with a high-resolution UT-3 monochromator [Sch+05] and a microjet sample delivery system [Wet+16]. However, Raman scattering is typically very weak and extending it into the pump-probe regime is still very challenging. Another interesting question about photophysics of  $\text{Cu}_2(\text{NSSN})_2$  that could be addressed further is its luminescent properties. This complex is not emissive at the room temperature in a solution. This is not surprising, because normally strong structural changes in the excited state, as is the case with  $\text{Cu}_2(\text{NSSN})_2$ , cause increase in non-radiative decay rates [MFC15]. For this reason it would be interesting to measure luminescence of the complex as a solid: the rotation of two halves of the molecule should be hindered, which may affect its emissive properties.

In the field of X-ray spectroscopies,  $L_{\text{II,III}}$ -edge absorption spectra of 3d transition metals normally have sharper features and are easier to interpret quantitatively than K-edge spectra. These edges are formed by dipole-allowed  $2p\text{-}3d$  transitions and therefore probe valent  $d$  orbitals. K-edge spectroscopy of ligands also provides valuable information about metal-ligand bonds, because there the transitions also happen to valent orbitals, such as  $1s \rightarrow 2p$  for nitrogen and  $1s \rightarrow 3p$  for sulfur. Thus, by combining Cu L-edge and S K-edge XANES spectra, the Cu-ligand bond covalency in Cu/S/N compounds could be directly obtained [DeB+01; Sar+07]. In the field of time-resolved studies, pump-probe soft X-ray spectroscopies have already shown their potential in investigating photoexcited transition metal (TM) complexes on the TM L-edge [Hus+10; Hus+11; Wer+15] as well as the ligand K-edge [Kui+16]. Pump-probe XAS studies on sulfur K-edge, in particular, were recently reported for the first time for small organic molecules

[Och+17; Kui+17].

Ongoing development of pump-probe X-ray techniques shows that this field has big perspectives to answer questions in fundamental and applied research [MPC14; CZS14]. In addition to existing setups, new experimental stations are being opened, such as a planned pump-probe XAS and XES setup at beamline P64 of Petra III, which will be able to make the full use of high brilliance of Petra III. The Femtosecond X-ray Experiments (FXE) instrument at the European XFEL, dedicated to combined XAS, XES and WAXS, starts operation this year, and will combine ultra-high brilliance of X-rays with fs resolution, which brings scientists to the space- and timescale of elemental acts of chemical reactions.

# Publications list

- Peer-Review:

1. D. Göries, B. Dicke, P. Roedig, N. Stübe, J. Meyer, A. Galler, W. Gawelda, A. Britz, P. Geßler, N. Sotoudi, A. Beckmann, M. Schlie, M. Warmer, M. Naumova, Ch. Bressler, M. Rübhausen, E. Weckert, A. Meents. Time-resolved pump and probe x-ray absorption fine structure spectroscopy at beamline P11 at PETRA III. *Review of Scientific Instruments* 87 (2016), 053116.

- Submitted:

1. B. Grimm-Lebsanft, C. Brett, F. Strassl, D. Rukser, M. Biednov, F. Biebl, A. Hoffmann, M. Naumova, L. Akinsinde, D. Brückner, S. Herres-Pawlis, M. Rübhausen. A Cryostat for Low Temperature Resonance Raman Measurements on operando Oxygenated Bioinorganic Model Complexes.
2. B. Dicke, A. Hoffmann, J. Stanek, M. Rampp, B. Grimm-Lebsanft, A. Wetzel, F. Biebl, D. Rukser, B. März, D. Göries, M. Naumova, M. Biednov, S. Hofmann, P. Roedig, A. Meents, J. Bielecki, J. Andreasson, Ch. Bressler, K. Beyerlein, H. N. Chapman, W. Zinth, M. Rübhausen, S. Herres-Pawlis. Transferring the entatic state concept into photochemistry.

- In manuscript:

1. M. Naumova, Dm. Khakhulin, M. Rebarz, M. Rohrmüller, B. Dicke, M. Biednov, A. Britz, M. Kloz, N. Kretzschmar, A. Neuba, J. Ortmeier, R. Schoch, J. Andreasson, M. Bauer, Ch. Bressler, W.G. Schmidt, G. Henkel, M. Rübhausen. Structural dynamics upon photoexcitation-induced charge transfer in a copper(I) disulfide complex.

# Acronyms

**APD** avalanche photodiode 53

**CA** central atom 4, 5

**CCD** charge-coupled device 36, 67

**CFT** crystal field theory 4, 5

**DFT** density functional theory 27, 30, 37, 55, 65, 66

**DN** donor number 32

**ES** excited state 26, 39, 51, 54, 55, 57–60, 71, 76

**ESA** excited states absorption 39, 40, 42

**ET** electron transfer 1–3, 6, 10

**EXAFS** extended X-ray absorption fine structure 16, 17, 19, 21, 32, 43, 44, 48–50, 53, 55–58, 60, 61, 65, 73, 79–81

**FC** Frank-Condon 11

**FT-IR** Fourier transform infrared 27

**FWHM** full width at half maximum 61, 68

**GS** ground state 39, 51–55, 57

**GSB** ground state bleaching 37, 40, 42

**GVD** group velocity dispersion 37

**HOMO** highest-occupied molecular orbital 11, 29

**HPLC** high-performance liquid chromatography 32

**IC** internal conversion 11, 39, 80, 84

**ISC** intersystem crossing 9, 11, 13, 39, 40, 42, 80, 84, 85

**KB** Kirkpatrick-Baez 43

**LC** ligand-centered 9, 11

**LFT** ligand field theory 5

**LMCT** ligand-to-metal charge transfer 9, 18, 19

**LUMO** lowest-unoccupied molecular orbital 11, 29

**MC** metal-centered 9

**MLCT** metal-to-ligand charge transfer 9, 11, 13, 29, 32–35, 57, 68, 80, 83

**MO** molecular orbitals 5, 28

**MS** multiple scattering 16, 21

**OD** optical density 36, 45

**OLED** organic light-emitting diode 3, 12

**PES** potential energy surface 5, 11

**PS** pumped spectrum 26

**RISC** reversed intersystem crossing 12

**S/N** signal to noise 37, 51, 54, 55

**SDD** silicon drift detector 23, 67

**SE** stimulated emission 39

**SO** spin-orbit 11

**TA** transient absorption 32, 36, 40, 42, 81

**TADF** thermally activated delayed fluorescence 12, 13

**TDDFT** time-dependent density functional theory 28, 60, 61

**TM** transition metal 1–5, 9, 11, 13, 16, 39, 85

**trWAXS** transient wide angle X-ray scattering 32

**trXAS** transient X-ray absorption spectroscopy 13, 32, 45

**trXES** transient X-ray emission spectroscopy 26, 32

**VR** vibrational relaxation 11, 39, 40

**WAXS** wide-angle X-ray scattering 1, 25, 26, 39, 61, 63, 67, 68, 71, 80–82, 84

**XANES** X-ray absorption near edge structure 16–18, 26, 43, 48

**XAS** X-ray absorption spectroscopy 1, 2, 25–27, 35, 39, 43, 44, 55, 61, 63, 65, 66, 76, 81, 82, 84

**XES** X-ray emission spectroscopy 1, 25, 26, 67, 68, 70, 76, 84

**XRD** X-ray diffraction 45, 80

# Chemical nomenclature

**ACN** acetonitrile 35, 36, 39, 41–45, 49–51, 53, 61–63, 65, 77, 81, 82

**DCM** dichloromethane 32, 36, 39, 41, 42, 81

**DFB** 1,2-difluorobenzene 29, 35–44, 48, 51, 61–63, 67, 71, 81, 82

**DMF** dimethylformamide 32

**dmp** dimethylphenantroline 11, 13

**DMSO** dimethyl sulfoxide 32

**qu** quinoline 13

**TMG** tetramethylguanidine 13, 27, 29

**TMGqu** 8-(tetramethylguanidine)quinoline 11, 13

# Bibliography

- [Ale+08] A. Alexakis, J. E. Bäckvall, N. Krause, O. Pàmies, and M. Diéguez. “Enantioselective Copper-Catalyzed Conjugate Addition and Allylic Substitution Reactions”. In: *Chemical Reviews* 108 (2008), pp. 2796–2823. DOI: 10.1021/cr0683515.
- [AM11] J. Als-Nielsen and D. McMorrow. *Elements of Modern X-ray Physics. 2nd edition.* Wiley, 2011.
- [Amb+99] E. A. Ambundo, M.-V. Deydier, A. J. Grall, N. Aguera-Vega, L. T. Dressel, T. H. Cooper, M. J. Heeg, L. A. Ochrymowycz, and D. B. Rorabacher. “Influence of coordination geometry upon copper(II/I) redox potentials. Physical parameters for twelve copper tripodal ligand complexes”. In: *Inorg. Chem.* 38 (1999), pp. 4233–4242. DOI: 10.1021/ic990334t.
- [Ank+98] A. Ankudinov, B. Ravel, J. J. Rehr, and S. D. Conradson. “Real-space multiple-scattering calculation and interpretation of x-ray-absorption near-edge structure”. In: *Physical Review B* 58 (1998), pp. 7565–7576. DOI: 10.1103/PhysRevB.58.7565.
- [Aoy+09] H. Aoyama, K. Muramoto, K. Shinzawa-Itoh, K. Hirata, E. Yamashita, T. Tsukihara, T. Ogura, and S. Yoshikawa. “A peroxide bridge between Fe and Cu ions in the O<sub>2</sub> reduction site of fully oxidized cytochrome *c* oxidase could suppress the proton pump”. In: *Proceedings of the National Academy of Sciences* 106 (2009), pp. 2165–2169. DOI: 10.1073/pnas.0806391106.
- [Aqu+11] G. Aquilanti, M. Giorgetti, M. Minicucci, G. Papini, M. Pellei, M. Tegoni, A. Trasatti, and C. Santini. “A study on the coordinative versatility of new N,S-donor macrocyclic ligands: XAFS, and Cu<sup>2+</sup> complexation thermodynamics in solution.” In: *Dalton transactions (Cambridge, England : 2003)* 40 (2011), pp. 2764–77. DOI: 10.1039/c0dt01401j.
- [Arc+16] T. Arcos-López, M. Qayyum, L. Rivillas-Acevedo, M. C. Miotto, R. Grande-Aztatzi, C. O. Fernández, B. Hedman, K. O. Hodgson, A. Vela, E. I. Solomon, and L. Quintanar. “Spectroscopic and Theoretical Study of Cu(I) Binding to His111 in the Human Prion Protein Fragment 106-115”. In: *Inorganic Chemistry* 55 (2016), pp. 2909–2922. DOI: 10.1021/acs.inorgchem.5b02794.
- [Arm+07] N. Armaroli, G. Accorsi, F. Cardinali, and A. Listorti. “Photochemistry and Photophysics of Coordination Compounds: Copper”. In: *Top Curr Chem* 280 (2007), pp. 69–115. DOI: 10.1007/128\_2007\_131.
- [Ass16] T. A. Assefa. “Tracking chemical reactions with ultrafast X-ray spectroscopic and scattering techniques”. PhD thesis. Hamburg University, 2016.
- [Bal01] V. Balzani, ed. *Electron Transfer in Chemistry.* Wiley-Blackwell, 2001. DOI: 10.1002/9783527618248.
- [Ban+11] L. Banci, I. Bertini, G. Cavallaro, and S. Ciofi-Baffoni. “Seeking the determinants of the elusive functions of Sco proteins”. In: *FEBS Journal* 278 (2011), pp. 2244–2262. DOI: 10.1111/j.1742-4658.2011.08141.x.

- [Bar+06] A. Q. R. Baron, S. Kishimoto, J. Morse, and J.-M. Rigal. "Silicon avalanche photo-diodes for direct detection of X-rays". In: *Journal of Synchrotron Radiation* 13 (2006), pp. 131–142. DOI: 10.1107/s090904950503431x.
- [Bau14] M. Bauer. "HERFD-XAS and valence-to-core-XES: new tools to push the limits in research with hard X-rays?" In: *Phys. Chem. Chem. Phys.* 16 (2014), pp. 13827–13837. DOI: 10.1039/c4cp00904e.
- [BB05] C. H. Booth and F. Bridges. "Improved self-absorption correction for fluorescence measurements of extended x-ray absorption fine-structure". In: *Physica Scripta* T115 (2005), pp. 202–204.
- [BC04] I. P. Beletskaya and A. V. Cheprakov. "Copper in cross-coupling reactions". In: *Coordination Chemistry Reviews* 248 (2004), pp. 2337–2364. DOI: 10.1016/j.ccr.2004.09.014.
- [Bec93] A. D. Becke. "Density-functional thermochemistry. III. The role of exact exchange". In: *The Journal of Chemical Physics* 98 (1993), pp. 5648–5652. DOI: 10.1063/1.464913.
- [Bec99] A. D. Becke. "Exploring the limits of gradient corrections in density functional theory". In: *Journal of Computational Chemistry* 20 (1999), pp. 63–69. DOI: 10.1002/(SICI)1096-987X(19990115)20:1<63::AID-JCC8>3.0.CO;2-A.
- [Ber+16] L. Bergmann, G. J. Hedley, T. Baumann, S. Bräse, and I. D. W. Samuel. "Direct observation of intersystem crossing in a thermally activated delayed fluorescence copper complex in the solid state". In: *Science Advances* 2 (2016). DOI: 10.1126/sciadv.1500889.
- [Ber10] I. B. Bersuker. *Electronic structure and properties of transition metal compounds: introduction to the theory*. 2010. DOI: 10.1002/9780470573051.
- [Ber75] I. Bersuker. "The Jahn-Teller effect in crystal chemistry and spectroscopy". In: *Coordination Chemistry Reviews* 14 (1975), pp. 357–412.
- [BG09] U. Bergmann and P. Glatzel. "X-ray emission spectroscopy". In: *Photosynthesis Research* 102 (2009), pp. 255–266. DOI: 10.1007/s11120-009-9483-6.
- [Bin98] N. Binsted. *EXCURV98: CCLRC Daresbury Laboratory Computer Program*. CCLRC Daresbury Laboratory, Warrington, UK. 1998.
- [BJ09] O. Bunău and Y. Joly. "Self-consistent aspects of x-ray absorption calculations". In: *Journal of Physics: Condensed Matter* 21 (2009), p. 345501. DOI: 10.1088/0953-8984/21/34/345501.
- [BLN02] M. Benfatto, S. D. Longa, and C. R. Natoli. "The MXAN procedure: a new method for analysing the XANES spectra of metalloproteins to obtain structural quantitative information". In: *Journal of Synchrotron Radiation* 10 (2002), pp. 51–57. DOI: 10.1107/s0909049502018137.
- [BM73] E. J. Bastian and R. B. Martin. "Disulfide vibrational spectra in the sulfur-sulfur and carbon-sulfur stretching region". In: *The Journal of Physical Chemistry* 77 (1973), pp. 1129–1133. DOI: 10.1021/j100628a010.
- [BM78] M. T. Buckner and D. R. McMillin. "Photoluminescence from copper(I) complexes with low-lying metal-to-ligand charge transfer excited states". In: *Journal of the Chemical Society, Chemical Communications* (1978), p. 759. DOI: 10.1039/c39780000759.

- [Bor+13] E. Borfecchia, C. Garino, L. Salassa, T. Ruiu, D. Gianolio, X. Zhang, K. Attenkofer, L. X. Chen, R. Gobetto, P. J. Sadler, and C. Lamberti. "X-ray transient absorption structural characterization of the <sup>3</sup>MLCT triplet excited state of *cis*-[Ru(bpy)<sub>2</sub>(py)<sub>2</sub>]<sup>2+</sup>." In: *Dalton transactions* 42 (2013), pp. 6564–71. DOI: 10.1039/c3dt32865a.
- [Bor+15] E. Borfecchia, K. A. Lomachenko, F. Giordanino, H. Falsig, P. Beato, A. V. Soldatov, S. Bordiga, and C. Lamberti. "Revisiting the nature of Cu sites in the activated Cu-SSZ-13 catalyst for SCR reaction". In: *Chem. Sci.* 6 (2015), pp. 548–563. DOI: 10.1039/C4SC02907K.
- [Bra+90] M. L. Brader, E. W. Ainscough, E. N. Baker, A. M. Brodie, and D. A. Lewandoski. "Copper(II)-promoted oxidation of mercaptocarboxylic acids. The characterization of disulphide- and oxalate-containing products. Crystal structures of [(Cu(bipy)(2,2'-dtdp))<sub>n</sub>].3nH<sub>2</sub>O and [(Cu(bipy)(3,3'-dtdp))<sub>n</sub>].2nH<sub>2</sub>O (bipy = 2,2'-bipyridine, dtdp = dithiodipropionate)". In: *J. Chem. Soc., Dalton Trans.* (1990), pp. 2089–2094. DOI: 10.1039/DT9900002089.
- [Bra+96] N. D. J. Branscombe, A. J. Blake, A. Marin-Becerra, W.-S. Li, S. Parsons, L. Ruiz-Ramirez, and M. Schröder. "Synthesis and structure of tetranuclear zinc(II) and binuclear copper(II) complexes of a dithiolate compartmental macrocyclic ligand: a model for the binuclear Cu<sub>A</sub> site in cytochrome c oxidase and N<sub>2</sub>O reductase". In: *Chem. Commun.* (1996), pp. 2573–2574. DOI: 10.1039/cc9960002573.
- [Bri+16] A. Britz, T. A. Assefa, A. Galler, W. Gawelda, M. Diez, P. Zalden, D. Khakhulin, B. Fernandes, P. Gessler, H. S. Namin, A. Beckmann, M. Harder, H. Yavaş, and C. Bressler. "A multi-MHz single-shot data acquisition scheme with high dynamic range: pump-probe X-ray experiments at synchrotrons". In: *Journal of Synchrotron Radiation* 23 (2016), pp. 1409–1423. DOI: 10.1107/s1600577516012625.
- [Bri17] A. Britz. "Ultrafast X-ray Spectroscopies of Transition Metal Complexes Relevant for Catalysis". PhD thesis. Hamburg University, 2017.
- [BRP05] C. Belle, W. Rammal, and J. L. Pierre. "Sulfur ligation in copper enzymes and models". In: *Journal of Inorganic Biochemistry* 99 (2005), pp. 1929–1936. DOI: 10.1016/j.jinorgbio.2005.06.013.
- [Bur+14] A. S. Burlov, A. I. Uraev, D. A. Garnovskii, K. A. Lyssenko, V. G. Vlasenko, Y. V. Zubavichus, V. Y. Murzin, E. V. Korshunova, G. S. Borodkin, S. I. Levchenkov, I. S. Vasilchenko, and V. I. Minkin. "Synthesis, XAFS and X-ray structural studies of mono- and binuclear metal-chelates of N,O,O(N,O,S) tridentate Schiff base pyrazole derived ligands". In: *Journal of Molecular Structure* 1064 (2014), pp. 111–121. DOI: 10.1016/j.molstruc.2014.02.019.
- [But+12] K. Butsch, A. Klein, S. Nitsche, K. Stirnat, J. R. Hawke, E. J. L. McInnes, and M. Bauer. "Generation and characterisation of the phenoxyl-radical containing Cu(II) complex [Cu(triaz)<sub>2</sub>]<sup>+</sup> (triaz<sup>-</sup> = O, N chelating triazole-phenolate)". In: *Dalton Transactions* 41 (2012), p. 11464. DOI: 10.1039/c2dt31369c.
- [Cam+06] M. Cammarata, M. Lorenc, T. K. Kim, J. H. Lee, Q. Y. Kong, E. Pontecorvo, M. L. Russo, G. Schiró, A. Cupane, M. Wulff, and H. Ihee. "Impulsive solvent heating probed by picosecond x-ray diffraction". In: *The Journal of Chemical Physics* 124 (2006), p. 124504. DOI: 10.1063/1.2176617.

- [Can+15] S. E. Canton, K. S. Kjær, G. Vankó, T. B. van Driel, S.-i. Adachi, A. Bordage, C. Bressler, P. Chabera, M. Christensen, A. O. Dohn, A. Galler, W. Gawelda, D. Gosztola, K. Haldrup, T. Harlang, Y. Liu, K. B. Møller, Z. Németh, S. Nozawa, M. Pápai, T. Sato, T. Sato, K. Suarez-Alcantara, T. Togashi, K. Tono, J. Uhlig, D. a. Vithanage, K. Wärnmark, M. Yabashi, J. Zhang, V. Sundström, and M. M. Nielsen. “Visualizing the non-equilibrium dynamics of photoinduced intramolecular electron transfer with femtosecond X-ray pulses”. In: *Nature Communications* 6 (2015), p. 6359. DOI: 10.1038/ncomms7359.
- [Cap+14] G. Capano, M. Chergui, U. Rothlisberger, I. Tavernelli, and T. J. Penfold. “A Quantum Dynamics Study of the Ultrafast Relaxation in a prototypical Cu(I)-phenanthroline”. In: *The journal of physical chemistry. A* 118 (2014), pp. 9861–9869.
- [Cap+15] G. Capano, C. J. Milne, M. Chergui, U. Rothlisberger, I. Tavernelli, and T. J. Penfold. “Probing wavepacket dynamics using ultrafast x-ray spectroscopy”. In: *Journal of Physics B: Atomic, Molecular and Optical Physics* 48 (2015), p. 214001. DOI: 10.1088/0953-4075/48/21/214001.
- [Cas+98] M. E. Casida, C. Jamorski, K. C. Casida, and D. R. Salahub. “Molecular excitation energies to high-lying bound states from time-dependent density-functional response theory: Characterization and correction of the time-dependent local density approximation ionization threshold”. In: *The Journal of Chemical Physics* 108 (1998), pp. 4439–4449. DOI: 10.1063/1.475855.
- [Cha+05] J. Chaboy, A. Muñoz-Páez, F. Carrera, P. Merkling, and E. Marcos. “Ab initio x-ray absorption study of copper K-edge XANES spectra in Cu(II) compounds”. In: *Physical Review B* 71 (2005), p. 134208. DOI: 10.1103/PhysRevB.71.134208.
- [Cha00] J. Charles P. Poole, ed. *Handbook of superconductivity*. Academic Press, 2000.
- [Che+02] L. X. Chen, G. Jennings, T. Liu, D. J. Gosztola, J. P. Hessler, D. V. Scaltrito, and G. J. Meyer. “Rapid excited-state structural reorganization captured by pulsed x-rays”. In: *Journal of the American Chemical Society* 124 (2002), pp. 10861–10867. DOI: 10.1021/ja017214g.
- [Che+03] L. X. Chen, G. B. Shaw, I. Novozhilova, T. Liu, G. Jennings, K. Attenkofer, G. J. Meyer, and P. Coppens. “MLCT State Structure and Dynamics of a Copper (I) Diimine Complex Characterized by Pump - Probe X-ray and Laser Spectroscopies and DFT Calculations”. In: *Journal of American Chemical Society* 125 (2003), pp. 7022–7034.
- [Che+13] J.-L. Chen, X.-F. Cao, J.-Y. Wang, L.-H. He, Z.-Y. Liu, H.-R. Wen, and Z.-N. Chen. “Synthesis, Characterization, and Photophysical Properties of Heteroleptic Copper(I) Complexes with Functionalized 3-(2'-Pyridyl)-1, 2, 4-triazole Chelating Ligands”. In: *Inorg. Chem.* 52 (2013), pp. 9727–9740. DOI: 10.1021/ic4002829.
- [Che01] L. X. Chen. “Capturing a Photoexcited Molecular Structure Through Time-Domain X-ray Absorption Fine Structure”. In: *Science* 292 (2001), pp. 262–264. DOI: 10.1126/science.1057063.
- [Chr+09] M. Christensen, K. Haldrup, K. Bechgaard, R. Feidenhans'l, Q. Kong, M. Cammarata, M. L. Russo, M. Wulff, N. Harrit, and M. M. Nielsen. “Time-Resolved X-ray Scattering of an Electronically Excited State in Solution. Structure of the  $^3A_{2u}$  State of Tetrakis- $\mu$ -pyrophosphitodiplatinate(II)”. In: *J. Am. Chem. Soc.* 131 (2009), pp. 502–508. DOI: 10.1021/ja804485d.
- [Cic09] A. di Cicco, ed. *GNXAS. Extended suite of programs for advanced X-ray absorption data analysis: methodology and practice*. 2009.

- [Con06] R. R. Conry. "Copper: Inorganic and Coordination Chemistry". In: *Encyclopedia of Inorganic Chemistry*. Wiley, 2006. DOI: 10.1002/0470862106.ia052.
- [CT14] Y. Y. Chia and M. G. Tay. "An insight into fluorescent transition metal complexes." In: *Dalton transactions* 43 (2014), pp. 13159–68. DOI: 10.1039/c4dt01098a.
- [CY15] R. Czerwieniec and H. Yersin. "Diversity of copper(I) complexes showing thermally activated delayed fluorescence: Basic photophysical analysis". In: *Inorganic Chemistry* 54 (2015). DOI: 10.1021/ic503072u.
- [CZS14] L. X. Chen, X. Zhang, and M. L. Shelby. "Recent advances on ultrafast X-ray spectroscopy in the chemical sciences". In: *Chem. Sci.* 5 (2014), pp. 4136–4152. DOI: 10.1039/c4sc01333f.
- [Dam97] N. H. Damrauer. "Femtosecond Dynamics of Excited-State Evolution in  $[\text{Ru}(\text{bpy})_3]^{2+}$ ". In: *Science* 275 (1997), pp. 54–57. DOI: 10.1126/science.275.5296.54.
- [DBW11] L. Decaria, I. Bertini, and R. J. P. Williams. "Copper proteomes, phylogenetics and evolution". In: *Metallomics* 3 (2011), pp. 56–60. DOI: 10.1039/c0mt00045k.
- [Dea+10] J. C. Deaton, S. C. Switalski, D. Y. Kondakov, R. H. Young, T. D. Pawlik, D. J. Giesen, S. B. Harkins, A. J. M. Miller, S. F. Mickenberg, and J. C. Peters. "E-type delayed fluorescence of a phosphine-supported  $\text{Cu}_2(\mu\text{-NAr}_2)_2$  diamond core: Harvesting singlet and triplet excitons in OLEDs". In: *Journal of the American Chemical Society* 132 (2010), pp. 9499–9508. DOI: 10.1021/ja1004575.
- [DeB+01] S. DeBeer George, M. Metz, R. K. Szilagyi, H. Wang, S. P. Cramer, Y. Lu, W. B. Tolman, B. Hedman, K. O. Hodgson, and E. I. Solomon. "A Quantitative Description of the Ground-State Wave Function of  $\text{Cu}_A$  by X-ray Absorption Spectroscopy: Comparison to Plastocyanin and Relevance to Electron Transfer". In: *Journal of the American Chemical Society* 123 (2001), pp. 5757–5767. DOI: 10.1021/ja004109i.
- [Dic+17] B. Dicke, A. Hoffmann, J. Stanek, M. Rampp, B. Grimm-Lebsanft, A. Wetzels, F. Biebl, D. Rukser, B. März, D. Göries, M. Naumova, M. Biednov, S. Hofmann, P. Roedig, A. Meents, J. Bielecki, J. Andreasson, C. Bressler, K. Beyerlein, H. N. Chapman, W. Zinth, M. Rübhausen, and S. Herres-Pawlis. "Transferring the entatic state concept into photochemistry." In: *Submitted to Nature Chemistry* (2017).
- [Dic13] B. Dicke. "Time-Resolved Pump-Probe X-ray Absorption Fine Structure Spectroscopy of  $\text{Gaq}^3$ ". PhD thesis. Hamburg University, 2013.
- [Dok+09] K. M. Dokken, J. G. Parsons, J. McClure, and J. L. Gardea-Torresdey. "Synthesis and structural analysis of copper(II) cysteine complexes". In: *Inorganica Chimica Acta* 362 (2009), pp. 395–401. DOI: 10.1016/j.ica.2008.04.037.
- [Duc+98] V. Ducros, A. Brzozowski, K. Wilson, S. Brown, P. Ostergaard, P. Schneider, D. Yaver, A. Pedersen, and G. Davies. "Crystal structure of the type-2 Cu depleted laccase from *Coprinus cinereus* at 2.2 Å resolution". In: *Nature structural biology* 5 (1998), pp. 310–316.
- [Dun89] T. H. Dunning. "Gaussian basis sets for use in correlated molecular calculations. I. The atoms boron through neon and hydrogen". In: *The Journal of Chemical Physics* 90 (1989), pp. 1007–1023. DOI: 10.1063/1.456153.
- [El +13] A. El Nahhas, R. M. van der Veen, T. J. Penfold, V. T. Pham, F. A. Lima, R. Abela, A. M. Blanco-Rodriguez, S. Zális, A. Vlček, I. Tavernelli, U. Rothlisberger, C. J. Milne, and M. Chergui. "X-ray absorption spectroscopy of ground and excited rhenium-carbonyl-diimine complexes: evidence for a two-center electron transfer." In: *The journal of physical chemistry A* 117 (2013), pp. 361–9. DOI: 10.1021/jp3106502.

- [Fah77] R. C. Fahey. "Biologically Important Thiol-Disulfide Reactions and the Role of Cyst(E)ine in Proteins: an Evolutionary Perspective". In: *Protein Crosslinking: Biochemical and Molecular Aspects*. Ed. by M. Friedman. Boston, MA: Springer US, 1977, pp. 1–30. DOI: 10.1007/978-1-4684-3282-4\_1.
- [For06] L. S. Forster. "Intersystem crossing in transition metal complexes". In: *Coordination Chemistry Reviews* 250 (2006), pp. 2023–2033. DOI: 10.1016/j.ccr.2006.01.023.
- [Fox+00] S. Fox, R. T. Stibrany, J. A. Potenza, S. Knapp, and H. J. Schugar. "Copper(II) and nickel(II) complexes of binucleating macrocyclic bis(disulfide)tetramine ligands". In: *Inorganic Chemistry* 39 (2000), pp. 4950–4961. DOI: 10.1021/ic000380p.
- [Fra+14] K. A. Fransted, N. E. Jackson, R. Zong, M. W. Mara, J. Huang, M. R. Harpham, M. L. Shelby, R. P. Thummel, and L. X. Chen. "Ultrafast structural dynamics of Cu(I)-bicinchoninic acid and their implications for solar energy applications". In: *Journal of Physical Chemistry A* 118 (2014), pp. 10497–10506. DOI: 10.1021/jp504294j.
- [Fri+09] M. J. Frisch, G. W. Trucks, H. B. Schlegel, G. E. Scuseria, M. A. Robb, J. R. Cheeseman, G. Scalmani, V. Barone, B. Mennucci, G. A. Petersson, H. Nakatsuji, M. Caricato, X. Li, H. P. Hratchian, A. F. Izmaylov, J. Bloino, G. Zheng, J. L. Sonnenberg, M. Hada, M. Ehara, K. Toyota, R. Fukuda, J. Hasegawa, M. Ishida, T. Nakajima, Y. Honda, O. Kitao, H. Nakai, T. Vreven, J. A. Montgomery, J. E. Peralta, F. Ogliaro, M. Bearpark, J. J. Heyd, E. Brothers, K. N. Kudin, V. N. Staroverov, R. Kobayashi, J. Normand, K. Raghavachari, A. Rendell, J. C. Burant, S. S. Iyengar, J. Tomasi, M. Cossi, N. Rega, J. M. Millam, M. Klene, J. E. Knox, J. B. Cross, V. Bakken, C. Adamo, J. Jaramillo, R. Gomperts, R. E. Stratmann, O. Yazyev, A. J. Austin, R. Cammi, C. Pomelli, J. W. Ochterski, R. L. Martin, K. Morokuma, V. G. Zakrzewski, G. A. Voth, P. Salvador, J. J. Dannenberg, S. Dapprich, A. D. Daniels, Farkas, J. B. Foresman, J. V. Ortiz, J. Cioslowski, and D. J. Fox. *Gaussian 09, Revision B.01*. Wallingford CT, 2009.
- [Fro+09] R. Fromme, Y. Bukhman-deRuyter, H. Mi, and P. Fromme. *Crystal Structure of the double mutant D44A D45A Plastocyanin from Phormidium laminosum*. 2009. DOI: 10.2210/pdb3bqv/pdb.
- [Gam+98] D. R. Gamelin, D. W. Randall, M. T. Hay, R. P. Houser, T. C. Mulder, G. W. Canters, S. de Vries, W. B. Tolman, Y. Lu, and E. I. Solomon. "Spectroscopy of Mixed-Valence Cu<sub>A</sub>-Type Centers: Ligand-Field Control of Ground-State Properties Related to Electron Transfer". In: *Journal of the American Chemical Society* 120 (1998), pp. 5246–5263. DOI: 10.1021/ja973161k.
- [Gas+88] Z. Gasyna, A. Zelazowski, A. Rae Green, E. Ough, and M. J. Stillman. "Luminescence decay from copper(I) complexes of metallothionein". In: *Inorganica Chimica Acta* 153 (1988), pp. 115–118. DOI: 10.1016/S0020-1693(00)83868-2.
- [Gaw+05] W. Gawelda, C. Bressler, M. Saes, M. Kaiser, A. Tarnovsky, D. Grolimund, S. L. Johnson, R. Abela, and M. Chergui. "Picosecond Time-Resolved X-Ray Absorption Spectroscopy of Solvated Organometallic Complexes". In: *Physica scripta* T115 (2005), pp. 102–106.
- [Gaw+07] W. Gawelda, V.-T. Pham, M. Benfatto, Y. Zaushitsyn, M. Kaiser, D. Grolimund, S. L. Johnson, R. Abela, A. Hauser, C. Bressler, and M. Chergui. "Structural Determination of a Short-Lived Excited Iron(II) Complex by Picosecond X-Ray Absorption Spectroscopy". In: *Physical Review Letters* 98 (2007). DOI: 10.1103/physrevlett.98.057401.

- [Gaw+09] W. Gawelda, V.-T. Pham, R. M. van der Veen, D. Grolimund, R. Abela, M. Chergui, and C. Bressler. "Structural analysis of ultrafast extended x-ray absorption fine structure with subpicometer spatial resolution: Application to spin crossover complexes". In: *The Journal of Chemical Physics* 130 (2009), p. 124520. DOI: 10.1063/1.3081884.
- [Gaw+16] M. B. Gawande, A. Goswami, F.-X. Felpin, T. Asefa, X. Huang, R. Silva, X. Zou, R. Zboril, and R. S. Varma. "Cu and Cu-Based Nanoparticles: Synthesis and Applications in Catalysis". In: *Chemical Reviews* 116 (2016), pp. 3722–3811. DOI: 10.1021/acs.chemrev.5b00482.
- [Gaw06] W. Gawelda. "Time-Resolved X-Ray Absorption Spectroscopy of Transition Metal Complexes". PhD thesis. École Polytechnique Fédérale de Lausanne, 2006.
- [Gaž+76] J. Gažo, I. Bersuker, J. Garaj, M. Kabešová, J. Kohout, H. Langfelderová, M. Melník, M. Serátor, and F. Valach. "Plasticity of the coordination sphere of copper(II) complexes, its manifestation and causes". In: *Coordination Chemistry Reviews* 19 (1976), pp. 253–297. DOI: 10.1016/S0010-8545(00)80317-3.
- [Gen+11] M. Gennari, J. Pécaut, S. DeBeer George, F. Neese, M.-N. Collomb, and C. Duboc. "A Fully Delocalized Mixed-Valence Bis- $\mu$ (Thiolato) Dicopper Complex: A Structural and Functional Model of the Biological Cu<sub>A</sub> Center". In: *Angewandte Chemie International Edition* 50 (2011), pp. 5662–5666. DOI: 10.1002/anie.201100605.
- [GF83] J. M. Guss and H. C. Freeman. "Structure of oxidized poplar plastocyanin at 1.6 Å resolution". In: *Journal of Molecular Biology* 169 (1983), pp. 521–563. DOI: 10.1016/S0022-2836(83)80064-3.
- [GGJ03] N. M. Giles, G. I. Giles, and C. Jacob. "Multiple roles of cysteine in biocatalysis". In: *Biochemical and Biophysical Research Communications* 300 (2003), pp. 1–4. DOI: 10.1016/S0006-291X(02)02770-5.
- [Gil95] H. F. Gilbert. "[2] Thiol/disulfide exchange equilibria and disulfide bond stability". In: *Methods in Enzymology*. Elsevier BV, 1995, pp. 8–28. DOI: 10.1016/0076-6879(95)51107-5.
- [Gio+14] F. Giordanino, E. Borfecchia, K. A. Lomachenko, A. Lazzarini, G. Agostini, E. Gallo, A. V. Soldatov, P. Beato, S. Bordiga, and C. Lamberti. "Interaction of NH<sub>3</sub> with Cu-SSZ-13 catalyst: A complementary FTIR, XANES, and XES study". In: *Journal of Physical Chemistry Letters* 5 (2014), pp. 1552–1559. DOI: 10.1021/jz500241m.
- [Gla01] P. Glatzel. "X-Ray Fluorescence Emission Following K Capture and 1s Photoionization of Mn and Fe in Various Chemical Environments". PhD thesis. Hamburg University, 2001.
- [Gne+15] T. Gneuß, M. J. Leitzl, L. H. Finger, N. Rau, H. Yersin, and J. Sundermeyer. "A new class of luminescent Cu(I) complexes with tripodal ligands - TADF emitters for the yellow to red color range". In: *Dalton Transactions* 44 (2015), pp. 8506–8520. DOI: 10.1039/C4DT02631D.
- [Goe+16] D. Goeries, B. Dicke, P. Roedig, N. Stübe, J. Meyer, A. Galler, W. Gawelda, A. Britz, P. Geßler, H. Sotoudi Namin, A. Beckmann, M. Schlie, M. Warmer, M. Naumova, C. Bressler, M. Rübhausen, E. Weckert, and A. Meents. "Time-Resolved Pump and Probe X-ray Absorption Fine Structure Spectroscopy (XAFS) at Beamline P11 at PETRA III in Hamburg". In: *Review of Scientific Instruments* 87 (2016), p. 053116. DOI: 10.1063/1.4948596.

- [Gon+16] J. M. González-Pérez, D. Choquesillo-Lazarte, A. Domínguez-Martín, E. Vílchez-Rodríguez, I. Pérez-Toro, A. Castiñeiras, O. K. Arriortua, M. E. García-Rubiño, A. Matilla-Hernández, and J. Niclós-Gutiérrez. "Metal binding pattern of acyclovir in ternary copper(II) complexes having an S-thioether or S-disulfide NO<sub>2</sub>S-tripodal tetradentate chelator". In: *Inorganica Chimica Acta* 452 (2016), pp. 258–267. DOI: 10.1016/j.ica.2016.05.005.
- [Gon+17] J. Gong, K. Sumathy, Q. Qiao, and Z. Zhou. "Review on dye-sensitized solar cells (DSSCs): Advanced techniques and research trends". In: *Renewable and Sustainable Energy Reviews* 68, Part 1 (2017), pp. 234–246. DOI: <http://doi.org/10.1016/j.rser.2016.09.097>.
- [Gör14] D. Göries. "Photoinduced Charge Transfer in a Transition Metal Complex Investigated by Time-Resolved X-ray Absorption Fine Structure Spectroscopy: Setup and Experiment". PhD thesis. Hamburg University, 2014.
- [GRP06] B. Geffroy, P. le Roy, and C. Prat. "Organic light-emitting diode (OLED) technology: materials, devices and display technologies". In: *Polymer International* 55 (2006), pp. 572–582. DOI: 10.1002/pi.1974.
- [Hat] K. Hatada. <https://www.inf.infn.it/theory/CondensedMatter/fpms.html>, accessed 05.02.2017.
- [Hat+10] K. Hatada, K. Hayakawa, M. Benfatto, and C. R. Natoli. "Full-potential multiple scattering theory with space-filling cells for bound and continuum states". In: *Journal of Physics: Condensed Matter* 22 (2010), p. 185501. DOI: 10.1088/0953-8984/22/18/185501.
- [Hat84] B. J. Hathaway. "A new look at the stereochemistry and electronic properties of complexes of the copper(II) ion". In: *Structure and Bonding* 57 (1984), pp. 55–118. DOI: 10.1007/BFb0111454.
- [Hau05] M. Haumann. "Photosynthetic O<sub>2</sub> Formation Tracked by Time-Resolved X-ray Experiments". In: *Science* 310 (2005), pp. 1019–1021. DOI: 10.1126/science.1117551.
- [Hof+14] A. Hoffmann, S. Binder, A. Jesser, R. Haase, U. Flörke, M. Gnida, M. Salomone Stagni, W. Meyer-Klaucke, B. Lebsanft, L. E. Grünig, S. Schneider, M. Hashemi, A. Goos, A. Wetzel, M. Rübhausen, and S. Herres-Pawlis. "Catching an entatic state – a pair of copper complexes". In: *Angewandte Chemie (International ed. in English)* 53 (2014), pp. 299–304. DOI: 10.1002/anie.201306061.
- [Hou+95] R. P. Houser, J. A. Halfen, V. G. Young Jr., N. J. Blackburn, and W. B. Tolman. "Structural Characterization of the First Example of a Bis( $\mu$ -thiolato)dicopper(II) Complex. Relevance to Proposals for the Electron Transfer Sites in Cytochrome c Oxidase and Nitrous Oxide Reductase". In: *Journal of the American Chemical Society* 117 (1995), pp. 10745–10746. DOI: 10.1021/ja00148a018.
- [HS12] R. K. Hocking and E. I. Solomon. "Ligand field and molecular orbital theories of transition metal X-ray absorption edge transitions". In: *Structure and Bonding* 142 (2012), pp. 155–184. DOI: 10.1007/430.
- [Hsu+11] C.-W. Hsu, C.-C. Lin, M.-W. Chung, Y. Chi, G.-H. Lee, P.-T. Chou, C.-H. Chang, and P.-Y. Chen. "Systematic Investigation of the Metal-Structure - Photophysics Relationship of Emissive d<sup>10</sup>-Complexes of Group 11 Elements : The Prospect of Application in Organic Light Emitting Devices". In: *Journal of the American Chemical Society* 133 (2011), pp. 12085–12099.

- [Hua+15] L. Hua, M. Iwamura, S. Takeuchi, and T. Tahara. "The substituent effect on the MLCT excited state dynamics of Cu(I) complexes studied by femtosecond time-resolved absorption and observation of coherent nuclear wavepacket motion." In: *Physical chemistry chemical physics : PCCP* 17 (2015), pp. 2067–77. DOI: 10.1039/c4cp03843f.
- [Hub65] J. Hubbel. "Common volume of two intersecting cylinders". In: *Journal of research of the National Bureau of Standards – C. Engineering and Instrumentation*. 69C (1965), pp. 139–143.
- [Hus+10] N. Huse, T. K. Kim, L. Jamula, J. K. McCusker, F. M. F. de Groot, and R. W. Schoenlein. "Photo-Induced Spin-State Conversion in Solvated Transition Metal Complexes Probed via Time-Resolved Soft X-ray Spectroscopy". In: *Journal of the American Chemical Society* 132 (2010), pp. 6809–6816. DOI: 10.1021/ja101381a.
- [Hus+11] N. Huse, H. Cho, K. Hong, L. Jamula, F. M. F. de Groot, T. K. Kim, J. K. McCusker, and R. W. Schoenlein. "Femtosecond Soft X-ray Spectroscopy of Solvated Transition-Metal Complexes: Deciphering the Interplay of Electronic and Structural Dynamics". In: *The Journal of Physical Chemistry Letters* 2 (2011), pp. 880–884. DOI: 10.1021/jz200168m.
- [HYT96] R. P. Houser, V. G. Young, and W. B. Tolman. "A Thiolate-Bridged, Fully Delocalized Mixed-Valence Dicopper(I, II) Complex That Models the Cu<sub>A</sub> Biological Electron-Transfer Site". In: *Journal of the American Chemical Society* 118 (1996), pp. 2101–2102. DOI: 10.1021/ja953776m.
- [IB13] M. Ilbert and V. Bonnefoy. "Insight into the evolution of the iron oxidation pathways". In: *Biochimica et Biophysica Acta (BBA) - Bioenergetics* 1827 (2013). The evolutionary aspects of bioenergetic systems, pp. 161–175. DOI: <http://dx.doi.org/10.1016/j.bbabi.2012.10.001>.
- [Ihe+10] H. Ihee, M. Wulff, J. Kim, and S.-i. Adachi. "Ultrafast X-ray scattering: structural dynamics from diatomic to protein molecules". In: *International Reviews in Physical Chemistry* 29 (2010), pp. 453–520. DOI: 10.1080/0144235X.2010.498938.
- [Ihe05] H. Ihee. "Ultrafast X-ray Diffraction of Transient Molecular Structures in Solution". In: *Science* 309 (2005), pp. 1223–1227. DOI: 10.1126/science.1114782.
- [Ihe09] H. Ihee. "Visualizing Solution-Phase Reaction Dynamics with Time-Resolved X-ray Liquidography". In: *Accounts of Chemical Research* 42 (2009), pp. 356–366. DOI: 10.1021/ar800168v.
- [INF01] S. Itoh, M. Nagagawa, and S. Fukuzumi. "Fine tuning of the interaction between the copper(I) and disulfide bond. Formation of a bis( $\mu$ -thiolato) dicopper(II) complex by reductive cleavage of the disulfide bond with copper(I)". In: *Journal of the American Chemical Society* 123 (2001), pp. 4087–4088. DOI: 10.1021/ja0157200.
- [ITT07] M. Iwamura, S. Takeuchi, and T. Tahara. "Real-time observation of the photoinduced structural change of bis(2,9-dimethyl-1,10-phenanthroline)copper(I) by femtosecond fluorescence spectroscopy: A realistic potential curve of the Jahn-Teller distortion". In: *Journal of the American Chemical Society* 129 (2007), pp. 5248–5256. DOI: 10.1021/ja069300s.
- [IUC] IUCr. <http://it.iucr.org/>, accessed on the 18.02.2017.
- [Iwa+11] M. Iwamura, H. Watanabe, K. Ishii, S. Takeuchi, and T. Tahara. "Coherent Nuclear Dynamics in Ultrafast Photoinduced Structural Change of Bis(diimine)copper(I) Complex". In: *Journal of the American Chemical Society* 133 (2011), pp. 7728–7736. DOI: 10.1021/ja108645x.

- [Iwa+95] S. Iwata, C. Ostermeier, B. Ludwig, and H. Michel. "Structure at 2.8 Å resolution of cytochrome c oxidase from *Paracoccus denitrificans*". In: *Nature* 376 (1995), pp. 660–669. DOI: 10.1038/376660a0.
- [Jac+03] C. Jacob, G. I. Giles, N. M. Giles, and H. Sies. "Sulfur and Selenium: The Role of Oxidation State in Protein Structure and Function". In: *Angewandte Chemie International Edition* 42 (2003), pp. 4742–4758. DOI: 10.1002/anie.200300573.
- [Jen+91] R. Jenkins, R. Manne, R. Robin, and C. Senemaud. "IUPAC—nomenclature system for x-ray spectroscopy". In: *X-Ray Spectrometry* 20 (1991), pp. 149–155. DOI: 10.1002/xrs.1300200308.
- [Jen99] R. Jenkins. *X-Ray Fluorescence Spectrometry*. Wiley-Blackwell, 1999. DOI: 10.1002/9781118521014.
- [Jer+09] T. Jerphagnon, M. G. Pizzuti, A. J. Minnaard, and B. L. Feringa. "Recent advances in enantioselective copper-catalyzed 1,4-addition". In: *Chemical Society Reviews* 38 (2009), p. 1039. DOI: 10.1039/b816853a.
- [Kar+91] B. Karlsson, M. Nordling, T. Pascher, L.-C. Tsai, L. Sjölin, and L. G. Lundberg. "Cassette mutagenesis of Met121 in azurin from *Pseudomonas aeruginosa*". In: *Protein Engineering, Design and Selection* 4 (1991), pp. 343–349. DOI: 10.1093/protein/4.3.343.
- [Kau+87] L. S. Kau, D. J. Spira-Solomon, J. E. Penner-Hahn, K. O. Hodgson, and E. I. Solomon. "X-ray absorption edge determination of the oxidation state and coordination numbers of copper: application to the type 3 site in *Rhus vernicifera* laccase and its reaction with oxygen". In: *Journal of the American Chemical Society* 109 (1987), pp. 6433–6442. DOI: 10.1021/ja00255a032.
- [KHR08] S. Kelly, D. Hesterberg, and B. Ravel. In: *Methods of soil analysis. Part 5: Mineralogical Methods*. Ed. by A. Klute. American society of agronomy. Madison, WI., 2008. Chap. Analysis of soils and minerals using X-ray absorption spectroscopy, pp. 387–463.
- [Kim+] K. H. Kim, J. Kim, J. H. Lee, and H. Ihee. "Topical Review: Molecular reaction and solvation visualized by time-resolved X-ray solution scattering: structure, dynamics, and their solvent dependence". In: *Structural Dynamics* 1 (), p. 011301. DOI: 10.1063/1.4865234.
- [Kim+06] T. K. Kim, M. Lorenc, J. H. Lee, M. L. Russo, J. Kim, M. Cammarata, Q. Kong, S. Noel, A. Plech, M. Wulff, and H. Ihee. "Spatiotemporal reaction kinetics of an ultrafast photoreaction pathway visualized by time-resolved liquid x-ray diffraction". In: *Proceedings of the National Academy of Sciences* 103 (2006), pp. 9410–9415. DOI: 10.1073/pnas.0601958103.
- [Kim+12] J. Kim, J. H. Lee, J. Kim, S. Jun, K. H. Kim, T. W. Kim, M. Wulff, and H. Ihee. "Structural Dynamics of 1, 2-Diiodoethane in Cyclohexane Probed by Picosecond X-ray Liquidography". In: *The Journal of Physical Chemistry A* 116 (2012), pp. 2713–2722. DOI: 10.1021/jp2078314.
- [Kjæ+13] K. S. Kjær, T. B. van Driel, J. Kehres, K. Haldrup, D. Khakhulin, K. Bechgaard, M. Cammarata, M. Wulff, T. J. Sørensen, and M. M. Nielsen. "Introducing a standard method for experimental determination of the solvent response in laser pump, X-ray probe time-resolved wide-angle X-ray scattering experiments on systems in solution." In: *Physical chemistry chemical physics : PCCP* 15 (2013), pp. 15003–16. DOI: 10.1039/c3cp50751c.

- [KM05] M. Klessinger and J. Michl. *Excited States and Photo-Chemistry of Organic Molecules*. Wiley-VCH, 2005.
- [Kno+92] D. M. Knotter, G. Blasse, J. P. M. Van Vliet, and G. Van Koten. "Luminescence of copper(I) arenethiolates and its relation to copper(I) luminescence in other complexes". In: *Inorg. Chem.* 31 (1992), pp. 2196–2201. DOI: 10.1021/ic00037a038.
- [Kra79] M. O. Krause. "Atomic radiative and radiationless yields for K and L shells". In: *Journal of Physical and Chemical Reference Data* 8 (1979), pp. 307–327. DOI: 10.1063/1.555594.
- [Krü] P. Krüger. <http://www.msnano.org/?p=284>, accessed on 05.02.2017.
- [Kui+16] B. E. V. Kuiken, H. Cho, K. Hong, M. Khalil, R. W. Schoenlein, T. K. Kim, and N. Huse. "Time-Resolved X-ray Spectroscopy in the Water Window: Elucidating Transient Valence Charge Distributions in an Aqueous Fe(II) Complex". In: *The Journal of Physical Chemistry Letters* 7 (2016), pp. 465–470. DOI: 10.1021/acs.jpcllett.5b02509.
- [Kui+17] B. E. V. Kuiken, M. R. Ross, M. L. Strader, A. A. Cordones, H. Cho, J. H. Lee, R. W. Schoenlein, and M. Khalil. "Picosecond sulfur K-edge X-ray absorption spectroscopy with applications to excited state proton transfer". In: *Structural Dynamics* 4 (2017), p. 044021. DOI: 10.1063/1.4983157.
- [Lak06] J. R. Lakowicz. *Principles of fluorescence spectroscopy. Third edition*. Springer, 2006.
- [Lei+13] M. J. Leitzl, F. R. Kuchle, H. A. Mayer, L. Wesemann, and H. Yersin. "Brightly blue and green emitting Cu(I) dimers for singlet harvesting in OLEDs". In: *Journal of Physical Chemistry A* 117 (2013), pp. 11823–11836. DOI: 10.1021/jp402975d.
- [Lin+10] C. L. Linfoot, P. Richardson, T. E. Hewat, O. Moudam, M. M. Forde, A. Collins, F. White, and N. Robertson. "Substituted [Cu(I)(POP)(bipyridyl)] and related complexes: Synthesis, structure, properties and applications to dye-sensitised solar cells". In: *Dalton Transactions* 39 (2010), p. 8945. DOI: 10.1039/c0dt00190b.
- [Loc+10] J. V. Lockard, S. Kabehie, J. I. Zink, G. Smolentsev, A. Soldatov, and L. X. Chen. "Influence of ligand substitution on excited state structural dynamics in Cu(I) bisphenanthroline complexes". In: *Journal of Physical Chemistry B* 114 (2010), pp. 14521–14527. DOI: 10.1021/jp102278u.
- [LS13] B. G. Lowe and R. A. Sareen. *Semiconductor X-Ray Detectors*. CRC Press, 2013.
- [Luo+12] S.-P. Luo, E. Mejia, A. Friedrich, A. Pazidis, H. Junge, A.-E. Surkus, R. Jackstell, S. Denurra, S. Gladiali, S. Lochbrunner, and M. Beller. "Photocatalytic Water Reduction with Copper-Based Photosensitizers: A Noble-Metal-Free System". In: *Angewandte Chemie International Edition* 52 (2012), pp. 419–423. DOI: 10.1002/anie.201205915.
- [LYP88] C. Lee, W. Yang, and R. G. Parr. "Development of the Colle-Salvetti correlation-energy formula into a functional of the electron density". In: *Physical Review B* 37 (1988), pp. 785–789. DOI: 10.1103/physrevb.37.785.
- [Mal09] A. Maldotti. "Photochemistry and photophysics of transition-metal complexes". In: *Photochemistry* 37 (2009), pp. 240–299. DOI: 10.1039/9781847559937.
- [MDD12] D. M. P. Mingos, P. Day, and J. P. Dahl, eds. *Molecular Electronic Structures of Transition Metal Complexes I*. Springer, 2012. DOI: 10.1007/978-3-642-27370-4.
- [MFC15] M. W. Mara, K. A. Fransted, and L. X. Chen. "Interplays of excited state structures and dynamics in copper(I) diimine complexes: Implications and perspectives". In: *Coordination Chemistry Reviews* 282–283 (2015), pp. 2–18. DOI: 10.1016/j.ccr.2014.06.013.

- [Miy+80] K. Miyoshi, Y. Sugiura, K. Ishizu, Y. Iitaka, and H. Nakamura. "Crystal structure and spectroscopic properties of violet glutathione-copper (II) complex with axial sulfur coordination and two copper sites via a disulfide bridge". In: *Journal of the American Chemical Society* 102 (1980), pp. 6130–6136. DOI: 10.1021/ja00539a027.
- [Miz97] Y. Mizutani. "Direct Observation of Cooling of Heme Upon Photodissociation of Carbonmonoxy Myoglobin". In: *Science* 278 (1997), pp. 443–446. DOI: 10.1126/science.278.5337.443.
- [MPC14] C. Milne, T. Penfold, and M. Chergui. "Recent experimental and theoretical developments in time-resolved X-ray spectroscopies". In: *Coordination Chemistry Reviews* 277-278 (2014), pp. 44–68. DOI: 10.1016/j.ccr.2014.02.013.
- [MS85] R. A. Marcus and N. Sutin. "Electron transfers in chemistry and biology". In: *Biochimica et Biophysica Acta (BBA) - Reviews on Bioenergetics* 811 (1985), pp. 265–322. DOI: 10.1016/0304-4173(85)90014-x.
- [MW97] A. McNaught and A. Wilkinson, eds. *IUPAC. Compendium of Chemical Terminology, 2nd ed.* Blackwell Scientific Publications, Oxford, 1997. DOI: 10.1351/goldbook.
- [NAB86] G. E. Norris, B. F. Anderson, and E. N. Baker. "Blue copper proteins. The copper site in azurin from *Alcaligenes denitrificans*". In: *Journal of the American Chemical Society* 108 (1986), pp. 2784–2785. DOI: 10.1021/ja00270a064.
- [NBD86] C. R. Natoli, M. Benfatto, and S. Doniach. "Use of general potentials in multiple-scattering theory". In: *Physical Review A* 34 (1986), pp. 4682–4694. DOI: 10.1103/physreva.34.4682.
- [Neu+11] A. Neuba, U. Flörke, W. Meyer-Klaucke, M. Salomone-Stagni, E. Bill, E. Bothe, P. Höfer, and G. Henkel. "The Trinuclear Copper(I) Thiolate Complexes  $[\text{Cu}_3(\text{NGuaS})_3]^{0/1+}$  and their Dimeric Variants  $[\text{Cu}_6(\text{NGuaS})_6]^{1+/2+/3+}$  with Biomimetic Redox Properties". In: *Angewandte Chemie (International ed. in English)* 50 (2011), pp. 4503–7. DOI: 10.1002/anie.201008076.
- [Neu+12] A. Neuba, R. Haase, W. Meyer-Klaucke, U. Flörke, and G. Henkel. "A halide-induced copper(I) disulfide/copper(II) thiolate interconversion." In: *Angewandte Chemie (International ed. in English)* 51 (2012), pp. 1714–8. DOI: 10.1002/anie.201102714.
- [Neu+15] A. Neuba, M. Rohrmüller, R. Hölscher, W. G. Schmidt, and G. Henkel. "A panel of peralkylated sulfur-guanidine type bases: Novel pro-ligands for use in biomimetic coordination chemistry". In: *Inorganica Chimica Acta* 430 (2015), pp. 225–238. DOI: 10.1016/j.ica.2015.03.015.
- [Neu09] A. Neuba. "Biomimetische Kupferkomplexe mit Schwefel-Guanidinliganden". PhD thesis. Paderborn University, 2009.
- [Neu11] A. Neuba. *Cambridge Crystallographic Data Centre. Reference 809966*. 2011.
- [New04] M. Newville. *Fundamentals of XAFS*. [http://xafs.org/Tutorials?action=AttachFile&do=get&target=Newville\\_xas\\_fundamentals.pdf](http://xafs.org/Tutorials?action=AttachFile&do=get&target=Newville_xas_fundamentals.pdf). Accessed: 19.02.2017. 2004.
- [Nic+93] J. Niclos-Gutiérrez, E. Abarca-Garcia, B. Viossat, D. Nguyen-Huy, A. Busnot, and J. F. Hemidy. "Structure of  $\mu$ -[cystamine-N,N,N',N'-tetraacetato(4-)]-bis(5-methylimidazole)dicopper(II) dihydrate". In: *Acta Crystallographica* C49 (1993), pp. 19–22. DOI: 10.1107/S0108270192004682.
- [NIS] NIST. <http://physics.nist.gov/PhysRefData/Xcom/html/xcom1.html> (accessed 04.02.2017).

- [Och+17] M. Ochmann, I. von Ahnen, A. A. Cordones, A. Hussain, J. H. Lee, K. Hong, K. Adamczyk, O. Vendrell, T. K. Kim, R. W. Schoenlein, and N. Huse. "Light-Induced Radical Formation and Isomerization of an Aromatic Thiol in Solution Followed by Time-Resolved X-ray Absorption Spectroscopy at the Sulfur K-Edge". In: *Journal of the American Chemical Society* 139 (2017), pp. 4797–4804. DOI: 10.1021/jacs.6b12992.
- [Oht+00] T. Ohta, T. Tachiyama, K. Yoshizawa, T. Yamabe, T. Uchida, and T. Kitagawa. "Synthesis, structure, and H<sub>2</sub>O<sub>2</sub>-dependent catalytic functions of disulfide-bridged dicopper(I) and related thioether-copper(I) and thioether-copper(II) complexes." In: *Inorganic chemistry* 39 (2000), pp. 4358–69.
- [Ols+98] M. H. M. Olsson, U. Ryde, B. O. Roos, and K. Pierloot. "On the relative stability of tetragonal and trigonal Cu(II) complexes with relevance to the blue copper proteins". In: *Journal of Biological Inorganic Chemistry* 3 (1998), pp. 109–125. DOI: 10.1007/s007750050212.
- [Ord+14] E. C. M. Ording-Wenker, M. van der Plas, M. A. Siegler, S. Bonnet, F. M. Bickelhaupt, C. Fonseca Guerra, and E. Bouwman. "Thermodynamics of the Cu(II)- $\mu$ -thiolate and Cu(I)-disulfide equilibrium: A combined experimental and theoretical study". In: *Inorganic Chemistry* 53 (2014), pp. 8494–8504. DOI: 10.1021/ic501060w.
- [OTo+89] T. R. O'Toole, J. N. Younathan, B. P. Sullivan, and T. J. Meyer. "1,2-difluorobenzene: a relatively inert and noncoordinating solvent for electrochemical studies on transition-metal complexes". In: *Inorg. Chem.* 28 (1989), pp. 3923–3926.
- [Pen+13] T. J. Penfold, S. Karlsson, G. Capano, F. A. Lima, J. Rittmann, M. Reinhard, M. Rittmann-Frank, O. Braem, E. Baranoff, R. Abela, I. Tavernell, U. Rothlisberger, C. J. Milne, and M. Chergui. "Solvent-Induced Luminescence Quenching: Static and Time-Resolved X-ray Absorption spectroscopy of a Copper(I) Phenantroline Complex". In: *The journal of physical chemistry A* 117 (2013), pp. 4591–4601.
- [Pen05] J. E. Penner-Hahn. In: *Comprehensive Coordination Chemistry II*. Vol. 2. Elsevier, 2005. Chap. X-ray Absorption Spectroscopy. Pp. 159–186. DOI: 10.1038/npg.els.0002984.
- [Per+92] J. P. Perdew, J. A. Chevary, S. H. Vosko, K. A. Jackson, M. R. Pederson, D. J. Singh, and C. Fiolhais. "Atoms, molecules, solids, and surfaces: Applications of the generalized gradient approximation for exchange and correlation". In: *Physical Review B* 46 (1992), pp. 6671–6687. DOI: 10.1103/physrevb.46.6671.
- [RA00] J. J. Rehr and R. C. Albers. "Theoretical approaches to x-ray absorption fine structure". In: *Rev. Mod. Phys.* 72 (3 2000), pp. 621–654. DOI: 10.1103/RevModPhys.72.621.
- [RA90] J. J. Rehr and R. C. Albers. "Scattering-matrix formulation of curved-wave multiple-scattering theory: Application to x-ray-absorption fine structure". In: *Phys. Rev. B* 41 (12 1990), pp. 8139–8149. DOI: 10.1103/PhysRevB.41.8139.
- [Ram+06] W. Rammal, C. Belle, C. Béguin, C. Duboc, C. Philouze, J.-L. Pierre, L. L. Pape, S. Bertaina, E. Saint-Aman, and S. Torelli. "Multifrequency EPR and Redox Reactivity Investigations of a Bis( $\mu$ -thiolato)-dicopper(II, II) Complex". In: *Inorganic Chemistry* 45 (2006), pp. 10355–10362. DOI: 10.1021/ic0612606.
- [Ran+00] D. W. Randall, S. DeBeer George, B. Hedman, K. O. Hodgson, K. Fujisawa, and E. I. Solomon. "Spectroscopic and Electronic Structural Studies of Blue Copper Model Complexes. 1. Perturbation of the Thiolate-Cu Bond". In: *Journal of the American Chemical Society* 122 (2000), pp. 11620–11631. DOI: 10.1021/ja001591w.

- [RN05] B. Ravel and M. Newville. "ATHENA, ARTEMIS, HEPHAESTUS: Data analysis for X-ray absorption spectroscopy using IFEFFIT". In: *Journal of Synchrotron Radiation* 12 (2005), pp. 537–541. DOI: 10.1107/S0909049505012719.
- [Roh+15] M. Rohrmüller, A. Hoffmann, C. Thierfelder, S. Herres-Pawlis, and W. G. Schmidt. "The Cu<sub>2</sub>O<sub>2</sub> torture track for a real-life system: [Cu<sub>2</sub>(btm<sub>2</sub>gp)<sub>2</sub>O<sub>2</sub>]<sup>2</sup> oxo and peroxo species in density functional calculations". In: *Journal of Computational Chemistry* 36 (2015), pp. 1672–1685. DOI: 10.1002/jcc.23983.
- [Ror04] D. B. Rorabacher. "Electron Transfer by Copper Centers". In: *Chemical Reviews* 104 (2004), pp. 651–698. DOI: 10.1021/cr020630e.
- [Roy+09] N. Roy, S. Sproules, E. Bothe, T. Weyhermüller, and K. Wieghardt. "Polynuclear Complexes Containing the Redox Noninnocent Schiff Base Ligand 2-[(E)-2-Mercaptophenyl-imino]methyl-4,6-di-*tert*-butylphenolate(2-)]". In: *European Journal of Inorganic Chemistry* 2009 (2009), pp. 2655–2663. DOI: 10.1002/ejic.200900168.
- [Ryd+96] U. Ryde, M. H. Olsson, K. Pierloot, and B. O. Roos. "The Cupric Geometry of Blue Copper Proteins is not Strained". In: *Journal of Molecular Biology* 261 (1996), pp. 586–596. DOI: 10.1006/jmbi.1996.0484.
- [Sae+03] M. Saes, C. Bressler, R. Abela, D. Grolimund, S. L. Johnson, P. A. Heimann, and M. Chergui. "Observing Photochemical Transients by Ultrafast X-Ray Absorption Spectroscopy". In: *Physical Review Letters* 90 (4 2003). DOI: 10.1103/PhysRevLett.90.047403.
- [Sal+10] L. Salassa, E. Borfecchia, T. Ruiu, C. Garino, D. Gianolio, R. Gobetto, P. J. Sadler, M. Cammarata, M. Wulff, and C. Lamberti. "Photo-Induced Pyridine Substitution in *cis*-[Ru(bpy)<sub>2</sub>(py)<sub>2</sub>]Cl<sub>2</sub>: A Snapshot by Time-Resolved X-ray Solution Scattering". In: *Inorganic Chemistry* 49 (2010), pp. 11240–11248. DOI: 10.1021/ic102021k.
- [Sal09] G. Salvato-Vallverdu. <http://www.texample.net/tikz/examples/the-perrin-jablonski-diagram/> Accessed 08.03.2016. 2009.
- [San+14] M. Sandroni, A. Maufroy, M. Rebarz, Y. Pellegrin, E. Blart, C. Ruckebusch, O. Poizat, M. Sliwa, and F. Odobel. "Design of Efficient Photoinduced Charge Separation in Donor–Copper(I)–Acceptor Triad". In: *The Journal of Physical Chemistry C* 118 (2014), pp. 28388–28400. DOI: 10.1021/jp507984s.
- [San+84] M. Sano, T. Maruo, Y. Masuda, and H. Yamatera. "Structural Study of Copper(II) Sulfate Solution in Highly Concentrated Aqueous Ammonia by X-ray Absorption Spectra". In: *Inorganic chemistry* 23 (1984), pp. 4466–4469.
- [Sar+07] R. Sarangi, S. DeBeer George, D. J. Rudd, R. K. Szilagyi, X. Ribas, C. Rovira, M. Almeida, K. O. Hodgson, B. Hedman, and E. I. Solomon. "Sulfur K-edge X-ray absorption spectroscopy as a probe of ligand-metal bond covalency: Metal *vs* ligand oxidation in copper and nickel dithiolene complexes". In: *Journal of the American Chemical Society* 129 (2007), pp. 2316–2326. DOI: 10.1021/ja0665949.
- [Sar+08] R. Sarangi, J. T. York, M. E. Helton, K. Fujisawa, K. D. Karlin, W. B. Tolman, K. O. Hodgson, B. Hedman, and E. I. Solomon. "X-ray absorption spectroscopic and theoretical studies on (L)<sub>2</sub>[Cu<sub>2</sub>(S<sub>2</sub>)<sub>n</sub>]<sup>2+</sup> complexes: disulfide versus disulfide(·1-) bonding". In: *Journal of the American Chemical Society* 130 (2008), pp. 676–686. DOI: 10.1021/ja0762745.
- [Sar+11] R. Sarangi, L. Yang, S. G. Winikoff, L. Gagliardi, C. J. Cramer, W. B. Tolman, and E. I. Solomon. "X-ray Absorption Spectroscopic and Computational Investigation of a Possible S··S Interaction in the [Cu<sub>3</sub>S<sub>2</sub>]<sup>3+</sup> Core". In: *Journal of the American Chemical Society* 133 (2011), pp. 17180–17191. DOI: 10.1021/ja111323m.

- [Sca+06] G. Scalmani, M. J. Frisch, B. Mennucci, J. Tomasi, R. Cammi, and V. Barone. "Geometries and properties of excited states in the gas phase and in solution: Theory and application of a time-dependent density functional theory polarizable continuum model". In: *The Journal of Chemical Physics* 124 (2006), p. 094107. DOI: 10.1063/1.2173258.
- [Sch+05] B. Schulz, J. Bäckström, D. Budelmann, R. Maeser, M. Rübhausen, M. V. Klein, E. Schoeffel, A. Mihill, and S. Yoon. "Fully reflective deep ultraviolet to near infrared spectrometer and entrance optics for resonance Raman spectroscopy". In: *Review of Scientific Instruments* 76 (2005), p. 073107. DOI: 10.1063/1.1946985.
- [Sch04] T. Schönherr, ed. *Optical Spectra and Chemical Bonding in Transition Metal Complexes*. Springer-Verlag Berlin Heidelberg, 2004.
- [Sch13] M. Schlie. "Time-resolved studies at PETRA III with a highly repetitive synchronized laser system." PhD thesis. Hamburg University, 2013.
- [Sid+03] Z. A. Siddique, Y. Yamamoto, T. Ohno, and K. Nozaki. "Structure-Dependent Photophysical Properties of Singlet and Triplet Metal-to-Ligand Charge Transfer States in Copper(I) Bis(diimine) Compounds". In: *Inorganic chemistry* 42 (2003), pp. 6366–6378.
- [Sie99] H. Sies. "Glutathione and its role in cellular functions". In: *Free Radical Biology and Medicine* 27 (1999), pp. 916–921. DOI: 10.1016/s0891-5849(99)00177-x.
- [Sin+15] W. Sinha, M. G. Sommer, N. Deibel, F. Ehret, M. Bauer, B. Sarkar, and S. Kar. "Experimental and Theoretical Investigations of the Existence of Cu<sup>II</sup>, Cu<sup>III</sup>, and Cu<sup>IV</sup> in Copper Corrolato Complexes". In: *Angewandte Chemie International Edition* 54 (2015), pp. 13769–13774. DOI: 10.1002/anie.201507330.
- [SKY92] M. Sano, S. Komorita, and H. Yamatera. "XANES spectra of copper(II) complexes: correlation of the intensity of the 1s→3d transition and the shape of the complex". In: *Inorg. Chem.* 31 (1992), pp. 459–463.
- [SL93] E. Solomon and M. Lowery. "Electronic structure contributions to function in bioinorganic chemistry". In: *Science* 259 (1993), pp. 1575–1581. DOI: 10.1126/science.8384374.
- [SLR98] E. I. Solomon, L. B. LaCroix, and D. W. Randall. "Electronic structure contributions to function in bioorganic chemistry: The blue copper active site". In: *Pure and Applied Chemistry* 70 (1998). DOI: 10.1351/pac199870040799.
- [Smi+85] T. A. Smith, J. E. Penner-Hahn, M. A. Berding, S. Doniach, and K. O. Hodgson. "Polarized X-ray Absorption Edge Spectroscopy of Single-Crystal Copper(II) Complexes". In: *Journal of the American Chemical Society* 107 (1985), pp. 5945–5955.
- [Sol+04] E. I. Solomon, R. K. Szilagyi, S. Debeer George, and L. Basumallick. "Electronic Structures of Metal Sites in Proteins and Models : Contributions to Function in Blue Copper Proteins Electronic Structures of Metal Sites in Proteins and Models : Contributions to Function in Blue Copper Proteins". In: *Chemical reviews* 104 (2004), pp. 419–458. DOI: 10.1021/cr0206317.
- [Sol+14] E. I. Solomon, D. E. Heppner, E. M. Johnston, J. W. Ginsbach, J. Cirera, M. Qayyum, M. T. Kieber-Emmons, C. H. Kjaergaard, R. G. Hadt, and L. Tian. "Copper Active Sites in Biology". In: *Chemical Reviews* 114 (2014), pp. 3659–3853. DOI: 10.1021/cr400327t.
- [Sou00] T. Soulimane. "Structure and mechanism of the aberrant *ba*<sub>3</sub>-cytochrome *c* oxidase from *Thermus thermophilus*". In: *The EMBO Journal* 19 (2000), pp. 1766–1776. DOI: 10.1093/emboj/19.8.1766.

- [SS15] G. Smolentsev and V. Sundström. "Time-resolved X-ray absorption spectroscopy for the study of molecular systems relevant for artificial photosynthesis". In: *Coordination Chemistry Reviews* (2015). DOI: 10.1016/j.ccr.2015.03.001.
- [SSC08] G. Smolentsev, A. V. Soldatov, and L. X. Chen. "Three-dimensional local structure of photoexcited Cu diimine complex refined by quantitative XANES analysis". In: *Journal of Physical Chemistry A* 112 (2008), pp. 5363–5367. DOI: 10.1021/jp801410a.
- [SSF98] R. E. Stratmann, G. E. Scuseria, and M. J. Frisch. "An efficient implementation of time-dependent density-functional theory for the calculation of excitation energies of large molecules". In: *The Journal of Chemical Physics* 109 (1998), pp. 8218–8224. DOI: 10.1063/1.477483.
- [SSL71] D. Sayers, E. A. Stern, and F. Lytle. "New Technique for Investigating Noncrystalline Structures: Fourier Analysis of the Extended X-Ray Absorption Fine Structure". In: *Physical Review Letters* 27 (1971), p. 1204. DOI: 10.1103/physrevb.10.3027.
- [SSM96] E. I. Solomon, U. M. Sundaram, and T. E. Machonkin. "Multicopper Oxidases and Oxygenases." In: *Chemical reviews* 96 (1996), pp. 2563–2606. DOI: 10.1021/cr950046o.
- [SSR95] D. T. Sawyer, A. Sobkowiak, and J. L. Roberts. *Electrochemistry for chemists, 2nd ed.* Wiley, 1995.
- [Ste74] E. A. Stern. "Theory of the extended x-ray-absorption fine structure". In: *Physical Review B* 10 (1974), pp. 3027–3037. DOI: 10.1103/physrevb.10.3027.
- [Syk85] A. G. Sykes. "Tilden Lecture. Structure and electron-transfer reactivity of the blue copper protein plastocyanin". In: *Chemical Society Reviews* 14 (1985), p. 283. DOI: 10.1039/cs9851400283.
- [Tao+03] J. Tao, J. P. Perdew, V. N. Staroverov, and G. E. Scuseria. "Climbing the Density Functional Ladder: Nonempirical Meta-Generalized Gradient Approximation Designed for Molecules and Solids". In: *Physical Review Letters* 91 (2003). DOI: 10.1103/physrevlett.91.146401.
- [Thi+74] J. A. Thich, D. Mastropaolo, J. Potenza, and H. J. Schugar. "Crystal and Molecular Structure of Bis[copper(II) D-penicillamine disulfide] Nonahydrate, a derivative of Copper(II) Cystinate". In: *Journal of the American Chemical Society* 96 (1974), pp. 726–731.
- [TMC05] J. Tomasi, B. Mennucci, and R. Cammi. "Quantum Mechanical Continuum Solvation Models". In: *Chemical Reviews* 105 (2005), pp. 2999–3094. DOI: 10.1021/cr9904009.
- [Tsu+95] T. Tsukihara, H. Aoyama, E. Yamashita, T. Tomizaki, H. Yamaguchi, K. Shinzawa-Itoh, R. Nakashima, R. Yaono, and S. Yoshikawa. "Structures of metal sites of oxidized bovine heart cytochrome *c* oxidase at 2.8 Å". In: *Science* 269 (1995), pp. 1069–1074. DOI: 10.1126/science.7652554.
- [Ura+05] A. I. Uraev, I. S. Vasilchenko, V. N. Ikorskii, T. A. Shestakova, A. S. Burlov, K. A. Lyssenko, V. G. Vlasenko, T. A. Kuz'menko, L. N. Divaeva, I. V. Pirog, G. S. Borodkin, I. E. Uflyand, M. Y. Antipin, V. I. Ovcharenko, A. D. Garnovskii, and V. I. Minkin. "Copper(II) dimers with ferromagnetic intra- and intermolecular exchange interactions". In: *Mendeleev Communications* 15 (2005), pp. 133–135. DOI: 10.1070/mc2005v015n04abeh002144.
- [UTI02] Y. Ueno, Y. Tachi, and S. Itoh. "Interconversion between Bis( $\mu$ -thiolato)dicopper(II) and disulfide-bridged dicopper(I) complexes mediated by chloride ion". In: *Journal of the American Chemical Society* 124 (2002), pp. 12428–12429. DOI: 10.1021/ja027397m.

- [Van+06] G. Vankó, T. Neisius, G. Molnár, F. Renz, S. Kárpáti, A. Shukla, and F. M. F. de Groot. "Probing the 3d Spin Momentum with X-ray Emission Spectroscopy : The Case of Molecular-Spin Transitions". In: *Journal of Physical Chemistry B* 110 (2006), pp. 11647–11653.
- [Van+10] G. Vankó, P. Glatzel, V.-T. Pham, R. Abela, D. Grolimund, C. N. Borca, S. L. Johnson, C. J. Milne, and C. Bressler. "Picosecond Time-Resolved X-Ray Emission Spectroscopy : Ultrafast Spin-State Determination in an Iron Complex". In: *Angewandte Chemie International Edition* 49 (2010), pp. 5910–5912. DOI: 10.1002/anie.201000844.
- [Van+15] G. Vankó, E. Bordage, M. Pápai, K. Haldrup, P. Glatzel, A. M. March, G. Doumy, A. Britz, A. Galler, T. Assefa, D. Cabaret, T. B. V. Driel, K. S. Kjær, A. Dohn, K. B. Møller, H. T. Lemke, E. Gallo, M. Rovezzi, J. Uhlig, V. Sundstro, M. M. Nielsen, L. Young, S. H. Southworth, C. Bressler, and W. Gawelda. "Detailed Characterization of a Nanosecond-Lived Excited State: X - ray and Theoretical Investigation of the Quintet State in Photoexcited  $[\text{Fe}(\text{terpy})_2]^{2+}$ ". In: *The journal of physical chemistry C* 119 (2015), pp. 5888–5902. DOI: 10.1021/acs.jpcc.5b00557.
- [Vee+09] R. M. van der Veen, C. J. Milne, A. El Nahhas, F. A. Lima, V.-T. Pham, J. Best, J. A. Weinstein, C. N. Borca, R. Abela, C. Bressler, and M. Chergui. "Structural Determination of a Photochemically Active Diplatinum Molecule by Time-Resolved EXAFS Spectroscopy". In: *Angewandte Chemie International Edition* 48 (2009), pp. 2711–2714. DOI: 10.1002/anie.200805946.
- [Vee+11] R. M. van der Veen, A. Cannizzo, F. van Mourik, A. Vlček Jr., and M. Chergui. "Vibrational Relaxation and Intersystem Crossing of Binuclear Metal Complexes in Solution". In: *Journal of the American Chemical Society* 133 (2011), pp. 305–315. DOI: 10.1021/ja106769w.
- [Vlč00] A. Vlček Jr. "The life and times of excited states of organometallic and coordination compounds". In: *Coordination Chemistry Reviews* 200-202 (2000), pp. 933–977.
- [VW68] B. L. Vallee and R. J. Williams. "Metalloenzymes: The entatic nature of their active sites". In: *Proceedings of the National Academy of Sciences of the United States of America* 59 (2 1968), pp. 498–505.
- [WA05] F. Weigend and R. Ahlrichs. "Balanced basis sets of split valence, triple zeta valence and quadruple zeta valence quality for H to Rn: Design and assessment of accuracy". In: *Physical Chemistry Chemical Physics* 7 (2005), p. 3297. DOI: 10.1039/b508541a.
- [Wei06] F. Weigend. "Accurate Coulomb-fitting basis sets for H to Rn". In: *Physical Chemistry Chemical Physics* 8 (2006), p. 1057. DOI: 10.1039/b515623h.
- [Wer+15] P. Wernet, K. Kunnus, I. Josefsson, I. Rajkovic, W. Quevedo, M. Beye, S. Schreck, S. Grübel, M. Scholz, D. Nordlund, W. Zhang, R. W. Hartsock, W. F. Schlotter, J. J. Turner, B. Kennedy, F. Hennies, F. M. F. de Groot, K. J. Gaffney, S. Techert, M. Odelius, and A. Föhlisch. "Orbital-specific mapping of the ligand exchange dynamics of  $\text{Fe}(\text{CO})_5$  in solution". In: *Nature* 520 (2015), pp. 78–81. DOI: 10.1038/nature14296.
- [Wet+16] A. Wetzel, F. Biebl, K. R. Beyerlein, J. Stanek, L. Gumprecht, A. Hoffmann, S. Herres-Pawlis, S. Bajt, H. N. Chapman, B. Grimm-Lebsanft, D. Rukser, and M. Rübhausen. "Jet delivery system for Raman scattering on bio-inorganic compounds". In: *Applied Physics Letters* 109 (2016), p. 213502. DOI: 10.1063/1.4967476.
- [Wil95] R. J. P. Williams. "Energised (entatic) States of Groups and of Secondary Structures in Proteins and Metalloproteins". In: *European Journal of Biochemistry* 234 (1995), pp. 363–381. DOI: 10.1111/j.1432-1033.1995.363\_b.x.

- [Win91] D. R. Winge. "Copper Coordination in Metallothionein". In: *Methods in Enzymology* 205 (1991), pp. 458–469.
- [Wit+16] M. Witte, U. Gerstmann, A. Neuba, G. Henkel, and W. G. Schmidt. "Density functional theory of the Cu<sub>A</sub>-like Cu<sub>2</sub>S<sub>2</sub>diamond core in Cu<sub>2</sub>(II)(NGuaS)<sub>2</sub>Cl<sub>2</sub>". In: *Journal of Computational Chemistry* 37 (2016), pp. 1005–1018. DOI: 10.1002/jcc.24289.
- [WOS74] L. G. Warner, T. O. R. Ottersen, and K. Seff. "Synthesis and Crystal Structure of a Polymeric Copper(I) Aliphatic Disulfide Complex. Bis[2-(2-pyridyl)ethyl]disulfide copper(I) Perchlorate". In: *Inorganic chemistry* 8 (1974), pp. 2819–2826.
- [Wul+02] M. Wulff, A. Plech, L. Eybert, R. Randler, F. Schotte, and P. Anfinrud. "The realization of sub-nanosecond pump and probe experiments at the ESRF". In: *Faraday Discussions* 122 (2002), pp. 13–26. DOI: 10.1039/b202740m.
- [XAF] XAFS\_spectral\_library. <http://cars.uchicago.edu/xaslib/search/Cu>, accessed 20.02.2017.
- [YBT05] J. T. York, E. C. Brown, and W. B. Tolman. "Characterization of a Complex Comprising a {Cu<sub>2</sub>(S<sub>2</sub>)<sub>2</sub>}<sup>2+</sup> Core: Bis(μ-S<sub>2</sub><sup>2-</sup>)dicopper(III) or Bis(μ-S<sub>2</sub><sup>-</sup>)dicopper(II)?" In: *Angewandte Chemie International Edition* 44 (2005), pp. 7745–7748. DOI: 10.1002/anie.200503134.
- [Yer+11] H. Yersin, A. F. Rausch, R. Czerwieniec, T. Hofbeck, and T. Fischer. "The triplet state of organo-transition metal compounds. Triplet harvesting and singlet harvesting for efficient OLEDs". In: *Coordination Chemistry Reviews* 255 (2011), pp. 2622–2652. DOI: 10.1016/j.ccr.2011.01.042.
- [Zai+96] I. Zaitseva, V. Zaitsev, G. Card, K. Moshkov, B. Bax, A. Ralph, and P. Lindley. "The X-ray structure of human serum ceruloplasmin at 3.1 Å: nature of the copper centres". In: *Journal of Biological Inorganic Chemistry* 1 (1996), pp. 15–23. DOI: 10.1007/s007750050018.
- [Zha+16] X. Zhang, M. Pápai, K. B. Møller, J. Zhang, and S. E. Canton. "Characterizing the Solvated Structure of Photoexcited [Os(terpy)<sub>2</sub>]<sup>2+</sup> with X-ray Transient Absorption Spectroscopy and DFT Calculations". In: *Molecules* 21 (2016), p. 235. DOI: 10.3390/molecules21020235.
- [Zin+13] D. M. Zink, D. Volz, T. Baumann, M. Mydlak, H. Flügge, J. Friedrichs, M. Nieger, and S. Bräse. "Heteroleptic, Dinuclear Copper(I) Complexes for Application in Organic Light-Emitting Diodes". In: *Chemistry of Materials* 25 (2013), pp. 4471–4486. DOI: 10.1021/cm4018375.

# Acknowledgements

First of all I would like express my sincere gratitude to Prof. Gerald Henkel, who invited me to take part in the 100 pixel HpGe detector project, which was the beginning of my PhD work in DESY. Additionally the time spent in Paderborn university working in the synthetic lab, where I learned about the diverse world of biomimetic copper-sulfur chemistry, was very valuable. I am very grateful for his support when my work took the time-resolved direction and brought me into the group of Prof. Michael Rübhausen in CFEL. My deepest gratitude I express to Michael for cosupervising my PhD from this point on, for catching enthusiasm, valuable discussions and for widening my world in the field of optical spectroscopies.

I am thankful to Prof. Matthias Bauer from Paderborn University, for his interest in this work, for measuring EXAFS spectra in ANKA and ESRF and for agreeing to be a member of my PhD defence committee. I also express my gratitude to Prof. René Wilhelm for agreeing to be the head of the defence committee.

In this work I had a chance to collaborate with many groups in order to answer questions of structural dynamics we put before us. To work with so many people, from different groups, places and scientific and cultural backgrounds, was truly exciting.

I am very grateful to people from Petra Extension beamlines P64 and P65 – Wolfgang Caliebe and Edmund Welter, as well as other beamline staff, for bringing me into the world of X-rays and building experimental hutches. Particular thanks to Vadim Murzin for valuable XAS measurements, and to Ligia Martín, with whom we started the work together, for everything.

I would like to thank my whole AP-OG group in CFEL – Benjamin Dicke, Florian Biebl, Mykola Biednov, Benjamin Grimm-Lebsanft, Dieter Rukser, Lewis Akinsinde, Malwin Paufler, Bastian Besner, Philipp Bremer, Gerd Neuber, Alina Wetzels, Calvin Brett, Stephanie Baer. Special thanks go to the P11 subteam lead by Benni, with whom we spent many long shifts at P11 until this moment was coming – transient! Double transient all the way!

I'm indebted to Adam Neuba and Jochen Ortmeyer who synthesised the compound used in the experiment in this work. I'd also like to acknowledge other people from Prof. Henkel's group with whom I had a chance to work two months doing synthesis in Paderborn, in particular Alexander Oppermann, Catharina Hollmann and Regina Dick, for helping me there.

I'm very grateful to Martin Rohrmüller, from group of Prof. W.G. Schmidt, who patiently calculated DFT and as patiently explained to me what the results mean.

Roland Schoch led the away team to ESRF where we performed the EXAFS experiment and further analysed the data together. I keep ExCurve in mind, and I intend to use it. I'm also grateful to the beamline staff of ID23 and other members of Prof. M. Bauer's group who took part in the experiment.

An important part of the work was performed together with people from ELI beamlines in Prague. My very big thanks to Mateusz Rebarz, Miroslav Kloz and Shirly Espinoza from the group of Prof. Jakob Andreasson who made the transient absorption measurements happen, building the setup and making it work in just two days. Particular thanks to Mateusz, who introduced me into the details of TA and performed the data analysis.

Scientific work of Prof. Christian Bressler and his group was for me an inspiring example

and guide in the time-resolved X-ray field. Very big thanks to Dmitry Khakhulin for interest in my sample with its two copper atoms in the first place, for introducing me into wide-angle X-ray solution scattering, for taking care of the experiment in ESRF and performing the data analysis. Special thanks to Alexander Britz and Tadesse Abebaw Assefa, for all scientific discussions in the past years, which were really important for my work. I would also like to thank other participants of the beamtime in ESRF and the beamline ID09B staff.

I am very thankful to the beamline staff and PhD students of P11 beamline of Petra – Alke Meents, Dennis Goeries, Philip Roedig, Anja Burkhart, Olga Lorbeer, Saravanan Panneerselvam, Jan Meyer, for creating and supporting pump-probe XAS experiments.

I am grateful to Keisuke Hatada and E-COST MP1306 for giving me an opportunity to take part in the Multiple scattering codes school in Rennes.

I would like to thank Joe Doyle, from group of Prof. Arwen Pearson, for being my local contact in questions of chemical nomenclature, and Marta Sans Vals, for providing access to their chemistry lab. I would also like to thank Prof. Nils Huse, for very interesting insights into excited states of molecules, as well as Prof. Sonja Herres-Pawlis, for putting so much energy into scientific life of our DFG collaboration.

Besides that, there have been people with whom I hadn't had a direct contact, but who had an impact on my work and whom I'd like to acknowledge for doing right things: all contributors of matplotlib gallery, for plotting everything one could think of; Bruce Ravel, for putting so much effort into support of the EXAFS community; Eliezer Judkowski for lesswrong.com; and the sci-hub project.

My very big gratitude I owe to all people who took time to proofread some parts of my thesis, gave me valuable comments and significantly increased its volume by putting all missing definite and indefinite articles: Carsten Richter, Oleg Gorobtsov, Benjamin Dicke, Benjamin Grimm-Lebsanft, Dmitry Khakhulin, Mateusz Rebarz, Matthias Ruppert, Joe Doyle, Florian Biebl, Alexander Britz and Niko Höppel. Special thanks to Niko for translating the abstract to German in one night shift.

DESY was a very nice place to come to every day thanks to many people already mentioned, and many more people who became my friends besides work. Getting to know the campus started in the DESY summer school 2011, which was a great experience and brought me here for my PhD.

At the end I'd like to thank Carsten, for the great time together, and, besides that, for many things he taught me during the years in DESY about proper data analysis and for accelerating transition of my programming style from "make it work" to "make it right" to "make it fast".

And, finally, I'd like to thank all my family, both in Russia and Ukraine, my brother, and my parents, mathematicians in word and deed, who gave me all opportunities to follow my interests which finally brought me here. This work is devoted to them.